THE PRODUCTION AND PROPERTIES OF TCO COATINGS PREPARED BY PULSED MAGNETRON SPUTTERING FROM POWDER TARGETS

Yanwen Zhou

Institute of Materials Research

School of Computing, Science & Engineering

The University of Salford, Salford, UK

Submitted in Partial Fulfilment of the Requirements of the Degree of Doctor of Philosophy, January 2005

TABLE OF CONTENTS

LIST OF FIGURES

LIST OF PICTURES

LIST OF TABLES

LIST OF EQUATIONS

Acknowledgements

First of all I would like to thank my supervisor Dr. Peter James Kelly for giving me this precious chance to study in the UK, and for his continuous help throughout the project.

Many thanks must go to all my colleagues in the lab, especially Alan Postill, for their friendship and help, (with the rig modifications) which made my life in the UK fruitful and enjoyable. Special thanks must go to Professor Derek Arnell for his advice on my midterm report. Thanks must also go to Geoff France for all his help with the SEM work in this project.

I would like to thank Richard Pilkington of the Physics Department for the advice on the theory of semiconductors. Also, the thanks should go to Prof. David Cameron of Dublin University for discussion with us for zinc oxide films.

I would like to dedicate this thesis to my husband to express my appreciation of his love, encouragement and supports.

I would also like to dedicate this thesis to my parents to thank them for giving me this beautiful life.

Abstract

With their unique transparent and conductive properties, TCO (transparent conductive oxide) coatings are becoming increasingly studied. These commercially important coatings have a promising future due to their various applications as components in optoelectronic devices, photovoltaic solar cells, flat panel displays, electroluminescent devices, etc. Their high transmittance and low resistivity are generally achieved through the use of specific dopant materials, whilst adjustments are made to the deposition processes to improve the structure of the coatings.

TCO coatings are commonly deposited by the magnetron sputtering process. Sputtering normally takes place from a solid plate, known as the target, of the material to be deposited. Clearly, each solid target can only be of a single composition. Thus, to change the compositions of the coatings, the whole target has to be replaced. Furthermore, alloy, or doped targets can be very expensive and the choice of available compositions is likely to be limited.

In this project, instead of using solid targets, metal or ceramic powder blends were used as the targets. The powder blends were spread across the surface of a magnetron and lightly tamped down to produce a smooth surface. The benefits of this approach are that any material that is available in powder form can be considered as a target material and alloy or multi-component compositions can be readily blended.

The basic aim of this project, therefore, was to produce novel TCO coatings by magnetron sputtering from powder targets. The coatings were deposited in a specially designed rig with a number of important features, including a pulsed DC power supply and a closed magnetic field. The project concentrated on the production of

commercially useful zinc oxide–based TCO coatings. Coatings were produced with different dopant materials and concentrations, and their optical and electrical properties were measured. After the coatings were annealed at 500°C for 2 hours in vacuo, aluminum and gallium doped zinc oxide coatings showed their low resistivity, which were no larger than $5.19\times10^{-3}\Omega cm$, and the lowest resistivity was obtained from 3at% Al-doped ZnO coating; $1.95\times10^{-3}\Omega cm$. The average transmittance in the visible range of the ZnO coatings was 90%. From this, optimal compositions were identified. For comparison purposes, coatings were also produced of the TCO material most commonly used at present; namely ITO (indium tin oxide). The results showed that ITO coatings generally had lower resistivity and visible transmittance, ($4\text{-}6\times10^{-4}\Omega cm$ and 80-85%), than doped ZnO coatings. Also, the electrical and optical properties of ITO coatings were very sensitive to the content of oxygen in the deposition atmosphere. Finally, the flexibility offered by this approach was exploited through the use of multi-component target compositions to produce TCO coatings with tailored optical and electrical properties.

1. INTRODUCTION

Transparent conductive oxide (TCO) coatings, with their unique optical and electrical properties, are becoming increasingly important in the optical, electronic and semi-conductive industries. TCO coatings, deposited on glass or polymeric substrates, form components integral to many applications, including optoelectronic devices, photovoltaic solar cells, flat panel displays and electroluminescent devices [1-4]. Besides tin-doped indium oxide (ITO) coatings (the most commonly used TCO material at present), doped zinc oxide coatings, with their wide band gap energy, high transparency, reasonably low resistivity, stable properties and, importantly, very competitive price are attracting increasing interest. Another trend in the study of TCO coatings is the move from single dopant composition to multi-dopant and multi-component materials to prepare novel coatings with tailored properties [5-11].

Many techniques can be used to produce TCO coatings, such as physical vapour deposition (PVD), chemical vapour deposition (CVD) and sol-gel, etc [12]. Of the PVD techniques, magnetron sputtering takes the major role. Normally sputtering takes place from a solid plate, or target, which only allows a single composition per target. Thus, to investigate the effect of dopants and their concentrations on film properties requires many targets. This is not only inconvenient, but also very expensive. To overcome this problem, in this project targets were prepared from mixed powder blends, which required no further treatment, such as sintering. The advantages of preparing targets in this way are that any material that is available in powder form can be considered and alloy or multi-component compositions can be readily blended. This approach offers great flexibility to identify film compositions, which combine optimum optical and electrical properties.

The magnetron sputtering technique has risen to its current prominent position amongst deposition techniques due to the introduction of a number of important

developments, including the unbalanced magnetron, closed field multiple magnetron systems and the pulsed magnetron sputtering process [13-19]. This project takes advantage of each of these developments in a specifically designed deposition system – the unbalanced rare earth magnets under target forms closed magnetic field with the dummy magnets on top of the chamber; Advanced Energy Pinnacle Plus pulsed DC as power supply to sputter the target; the copper back-plate of targets was recessed to support powder or their mixture as targets.

The basic aim of this project, therefore, was to prepare novel TCO coatings by pulsed magnetron sputtering from blended powder targets. Firstly, this project concentrated on the production of commercially useful zinc oxide–based TCO coatings. The flexibility offered by the use of powder targets was exploited to investigate the effectiveness of a range of dopant materials and dopant concentrations on the optical and electrical properties of the films. Then, for comparison purposes, tin-doped indium oxide coatings were prepared by the same method. Finally, the production of TCO coatings with tailored properties was investigated through the use of new multi-dopant and multi-component target compositions.

This thesis has been divided into a number of sections, detailed below:

Chapter 2 reviews the background of Physical Vapour Deposition (PVD) processes from initial glow discharge plasmas to film formation, and finally to the development of the magnetron sputtering process.

Chapter 3 concentrates on the basic concepts of semiconductors and the principles of transparent conductive oxide (TCO) coatings.

Chapter 4 describes the modification of an existing powder coating rig. This work included the installation of mass flow controllers for the process gases, a Radio Frequency (RF) bias supply, a heater system for substrate annealing and a number of

safety devices.

Chapter 5 briefly explains the analytical techniques used in this project for measuring film properties, including the four point probe, Van der Pauw's technique, spectrophotometry, scanning electron microscopy (SEM), Auger Electron Spectroscopy (AES), X-ray Photoelectron Spectroscopy (XPS), Rutherford Backscattering Spectrometry (RBS)< Secondary Ion Mass Spectrometry (SIMS), X-ray diffraction, scratch testing and surface profilometry.

Chapter 6 states and discusses the experimental techniques used in this project.

Chapter 7 describes the effect of changing process parameters, such as pulse frequency and duty, target-to-substrate separations and magnetron configurations, on the operating characteristics of the rig, thickness and properties of the coatings.

Chapter 8 shows the results of all coatings prepared in this project. This is sub-divided into the following sections:

1. An investigation into powder mixing and target production techniques, and the determination of 'standard' operating conditions for regular, reproducible Al-doped ZnO (ZAO) film production, thus demonstrating the viability of depositing coatings from powder targets via pulsed magnetron sputtering.
2. Investigating the effect of annealing temperature, time and atmosphere on the electrical and optical properties of Al-doped ZnO films, and identification of the optimum conditions.
3. An investigation of the influence of other dopant materials and concentrations on the properties of zinc oxide coatings. Ga, In, Sn and Sb were chosen as dopants following a literature review (chapter 3).
4. A study of the influence of process parameters on the structure and properties of the coatings.
5. Preparation of ITO coatings by the same approach as the production of ZnO

coatings, to compare their optical and electrical properties.

6. A study of multi-dopant compositions to optimize film properties.
7. Comparison of the results of ZAO, ITO and multi-component coatings.

Chapter 9 discusses the results of the coatings prepared above, and considers the success of the project in terms of its aims.

Chapter 10 draws the conclusions of this project, and chapter 11 considers future work that might be undertaken.

At the beginning of this project, a study was carried out into the effectiveness of a number of cleaning techniques for glass substrates. The results of this study have been included in this thesis as Appendix A.

Appendix B explains a few terms of semiconductor physics, which help to describe band gap theory.

2. PHYSICAL VAPOUR DEPOSITION

2.1 Definition of Physical Vapour Deposition

Physical vapour deposition is a branch of surface engineering. It is appropriate, therefore, to first consider a definition of *surface engineering*: The design of surface and substrate together as a system to give cost effective performance enhancement of which neither is capable on its own [20].

Surface modification techniques and surface coating techniques are two major members in the surface engineering family. Processes, such as heat treatment, implantation, carburizing and nitriding etc. belong to the surface modification group. The surface coating group includes vapour phase processes (e.g. physical vapour deposition, and chemical vapour deposition), solution state processes (e.g. electroplating) and fusion processes (e.g. thermal spraying) [21-22].

Thus, a definition can now be given for *physical vapour deposition (PVD)*: a generic term for a number of processes used to deposit coatings, or films from by the vapour phase from solid sources under a partial vacuum [21-22].

Vacuum evaporation, ion plating and sputtering are three common PVD processes [23]. In evaporation processes, atoms are removed from the source by thermal means, whereas in ion plating processes the growing film is subjected to concurrent ion bombardment. In sputtering processes, such as that used in this project, atoms are ejected from the surface of a solid target by the impact of gaseous ions and then deposited on the surface of the substrate as a thin film. This process will be detailed later in this chapter.

Vacuum evaporation, also called *thermal evaporation,* refers to a group of PVD

processes in which a vapour flux is created by heating the surface of a source material to a sufficiently high temperature in vacuum. The vapour flux can then condense onto a substrate as a thin film.

Vacuum evaporation is the oldest, but still widely used PVD process, which began in the middle of 19th century and developed in the first half of 20th century [24]. The operating pressure is not higher than $1x10^{-2}$Pa, with the mean free path (MFP, the average distance between collisions occuring between species) no smaller than 5m [25]. The evaporated atoms undergo essentially collisionless transport from the source onto the substrate. The basic configuration of a vacuum evaporation system is shown in figure 2.1.

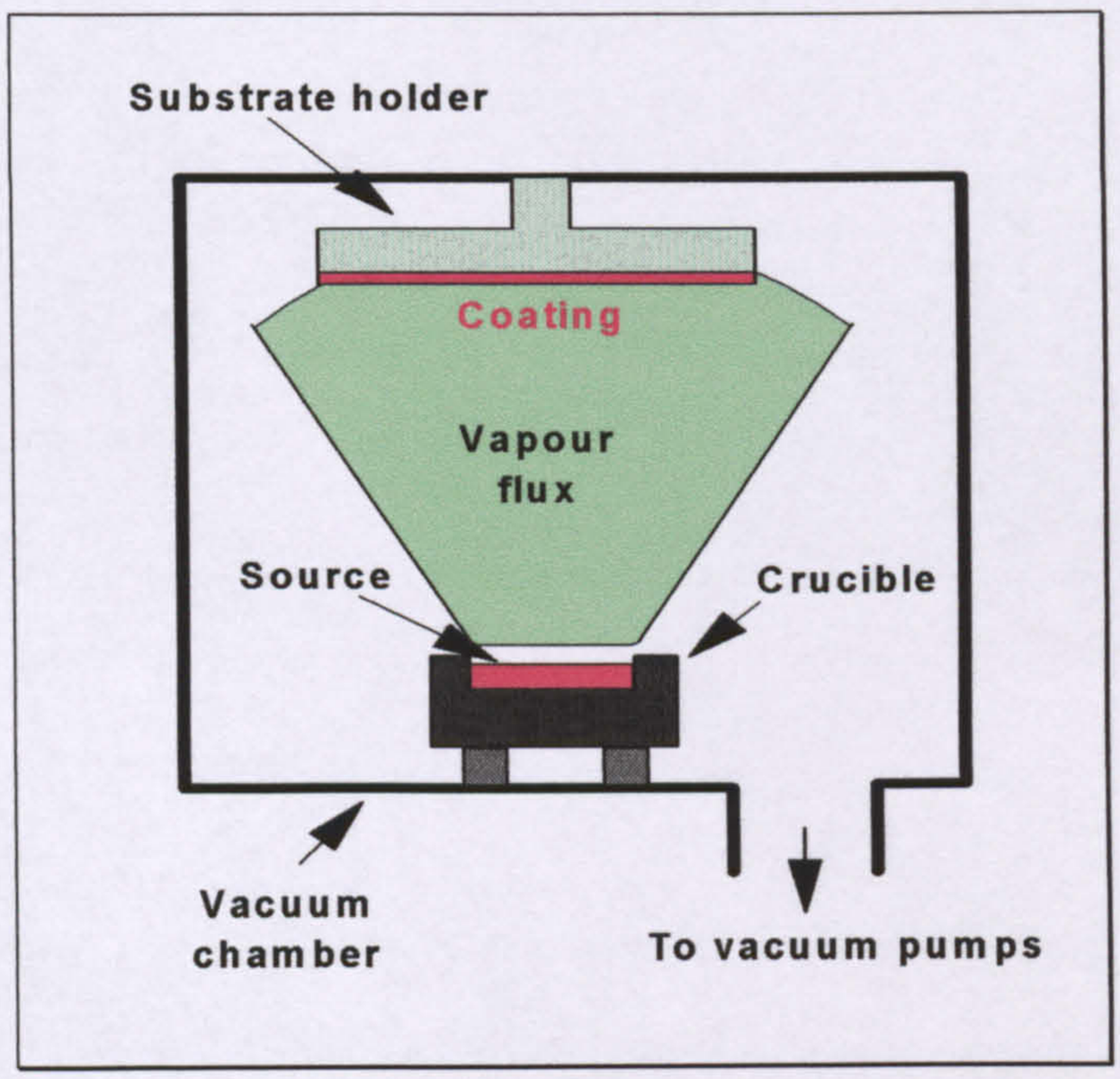

Figure 2.1 schematic representation of a vacuum evaporation system

(Typical operating pressure: 0.01Pa; Deposition rate:≤ μm/min; Mostly metallic coatings with low energy-porous columnar structures)

There are a number of ways to evaporate or sublimate the source, the most common of which are *resistance heating, electron-beam gun heating* and *laser heating* [26]. The limitations of resistance heating are that metallic source materials are needed for

direct resistive heating, and crucible contamination is possible due to the source material reacting with the walls of the crucible. Electron-beam guns eliminate the possible contamination effects caused by resistance heating and allow the deposition of dielectric films due to the incidence of high energetic electrons creating very high temperatures at the surface of the source. Laser heating has a similar principle to electron-beam heating, but can be located outside of the process environment. The disadvantage of it is the small heating point of which is easy to cause source spitting.

At normal operating pressures, such as 0.01Pa, evaporation processes are essentially 'line-of-sight' deposition processes. This can lead to non-uniform coating thicknesses on complex components due to shadowing. This problem can be reduced by the introduction of a low partial pressure of an appropriate working gas to cause gas phase scattering of the vapour flux. If the working gas is a reactive gas (e.g. oxygen, or nitrogen) then compounds can be deposited (i.e., oxides, or nitrides) and the process is called reactive evaporation [26].

Ion plating: a group of PVD processes in which the substrate is bombarded by a flux of high-energy ions sufficient to cause appreciable sputtering on the surface of the substrate before and during film growth [27].

Ion plating, firstly reported in 1960s by Mattox [24], is a process in which a glow discharge is created close to the surface of the substrate by applying a DC or RF bias to the substrate. Ions from this discharge bombard the surface of the substrate before and during deposition. The source material is vaporized in the similar way to that of vacuum evaporation process, but the evaporated atoms pass through the gaseous glow discharge on their way to the substrate, which causes some of the vaporized atoms to be ionized. Before deposition, ion bombardment of the surface can clean and modify the substrate surface on an atomic scale, which results in improved adhesion of the film to the substrate and reduces the point stresses creating by defects on the surface [28]. Ion bombardment during film growth helps to create denser films with the

densities closer to that of the bulk materials [29]. Figure 2.2 shows the schematic representation of the ion plating process.

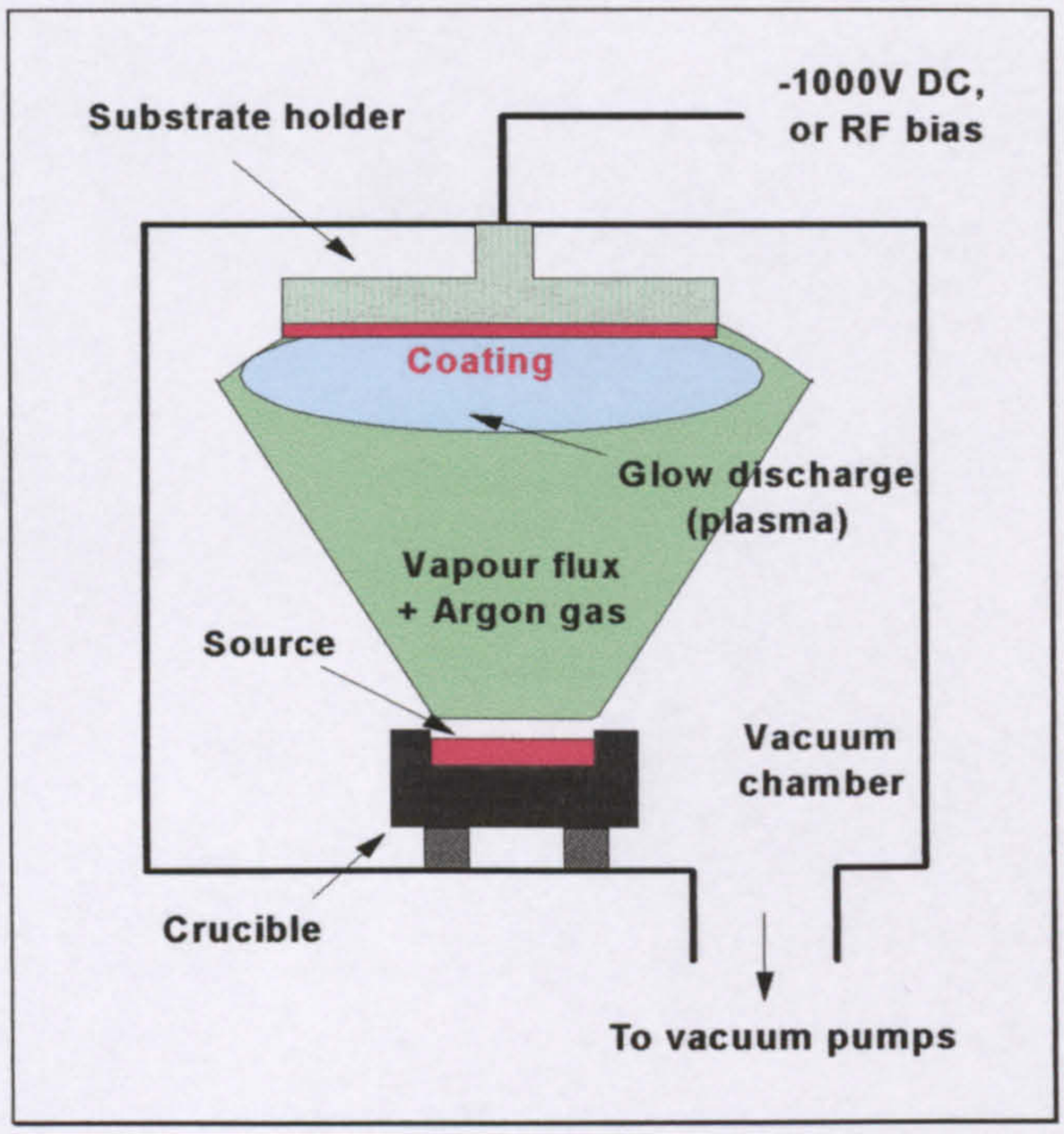

Figure 2.2 schematic representation of an ion plating system

(Typical operating pressure: 1-0.1Pa; Deposition rate: μm/min; Ion bombardment of growing films; Metallic or ceramic coatings)

The ion plating process can be carried out at gas pressures in the range of 1-0.1 Pa, which is needed to sustain a glow discharge as well as scatter the vapour particles in all directions through numerous collisions to improve the overall coating of the substrate during film growth [27]. The energy of ions is crucial in the ion plating process to modify the growing film. Low (a few eV) energy ions cannot provide sufficient energy to overcome the lattice binding energies and substrate atoms will not be sputtered away, thus the substrate surface will not be cleaned completely. Ions with too high energy will cause excessive sputtering and damage of the growing films, which results in film defects and excessive film stresses. D.M. Mattox [30] showed in his study that ion energies in the range 50-300eV provide benefits to films, and any beyond to this range will cause detrimental effects. In general, films structure can be

dense, and adhesion to the substrate etc. be increased by suitable employment of the ion plating process over basic evaporation processes.

The process can be enhanced by the addition of a filament; extra electrons with high energy collide with gas atoms, to increase the level of ionisation of the gas. Reactive gases (e.g. oxygen and nitrogen) can be introduced into the chamber in order to produce ceramic films (e.g. oxides and nitrides) from metallic sources [26]. Moreover, the development of ion plating processes also includes the sputter ion plating process, which will be described in more detail later.

Another evaporation process worthy of mention is *cathodic arc evaporation*, a technique where the coating flux is generated by creating an arc that travels across the surface of the target [26]. At each point where the arc strikes, metal atoms and small droplets of target material are ejected from the target and can condense on the substrate as a coating. It is very different to normal vacuum evaporation because a large proportion of the metal atoms become ionised, so they can arrive at the substrate with high energy, which promotes the formation of dense coatings. The problem is that the droplets can result in defects in the films. Also arc evaporation can take place in any direction, whereas normal evaporation must take place upwards. It is an important industrial technique, but is not normally used for optical coatings because of the problems with defects.

To describe in detail other PVD processes, such as sputtering, it is necessary to have a basic knowledge of plasmas and the theory of film growth. The following section will, therefore, give a description of sputtering processes.

2.2 Plasmas

2.2.1 Glow discharge plasmas

Plasmas were characterized in the mid-1920s by I. Langmuir [24] as a result of his development of small-area plasma probes, although a glow discharge was noted by J. Picard as early as 1678 and widely studied from the mid-1800s. The term of 'plasma' can be defined as:

A plasma is a gas in which enough ions and electrons are contained to be able to conduct a current and sustain glow discharge when a voltage is applied between two electrodes [26].

Or

A plasma is a partially ionised gas containing ions, electrons and atoms, produced by glow discharge processes under reduced pressure. These plasmas are generally created by applying an external electric field, with typical ionisation rates in the order of 0.1% [31-32].

There are many PVD processes in which plasmas are created and sustained, such as ion plating, DC, RF sputtering etc. All these techniques rely on the ionization of a working gas (most commonly argon) by energetic electrons in the chamber under suitable pressure. Therefore, it is necessary to detail plasmas from the initial discharge, formation and characteristics.

The discharge can be initiated by applying a DC voltage between two electrodes in a vacuum chamber containing a gas under suitable pressure, usually greater than 0.1 Pa with a DC type device. Electrons close to the cathode will be accelerated away and may collide with a gas atom. Under the correct conditions of pressure, the atom may

be ionised:

$$Ar + e^- \rightarrow Ar^+ + 2e^- \qquad \text{... eq. 2.1}$$

Collisions, which take place without sufficient energy to cause ionization, may lead to excitation of the gas atoms, with the release of photons, giving the characteristic glow to the plasma:

$$Ar + e^- \rightarrow Ar^* + e^- \qquad \text{... eq. 2.2}$$

and then,

$$Ar^* \rightarrow Ar + h\nu \qquad \text{...eq. 2.3}$$

The processes of ionization and glowing of the plasma are visualized in the following figures 2.3 and 2.4.

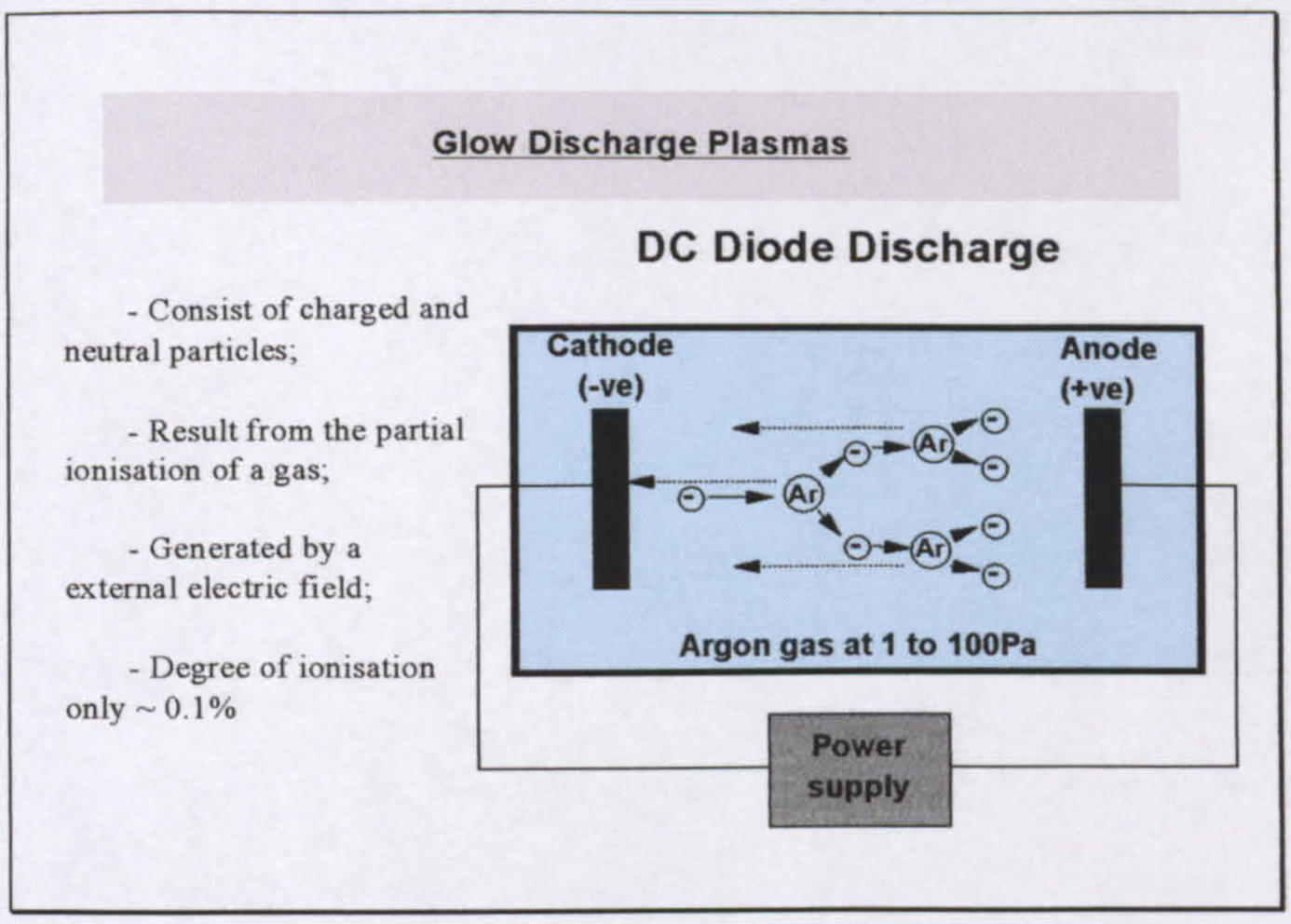

Figure 2.3 schematic representation of ionization and formation of the glow discharge plasma

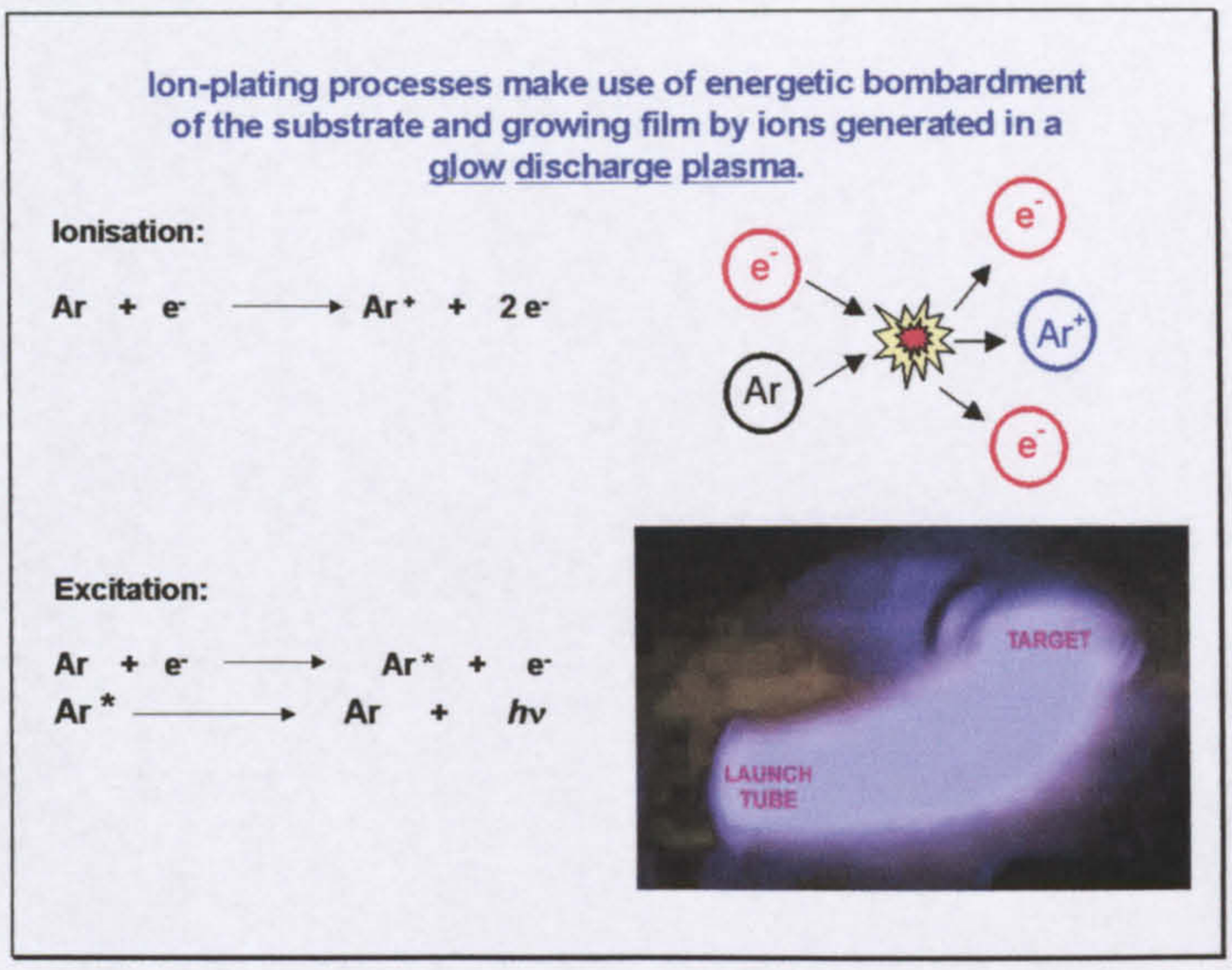

Figure 2.4 the formation of the visible glow discharge plasma in an ion-plating process

The discharge usually includes three distinct regions, shown in Figure 2.5 [33]. The first region is called the 'Townsend discharge'. At low voltage, little current is drawn because the electrons have insufficient energies and only a few ionized particles exist. As the voltage is increased, electrons gain enough energy to ionize more argon atoms creating charged particles, leading to a linear growth of the current. As the voltage is increased further, ion bombardment of the cathode takes place and secondary electrons are released. The released secondary electrons are accelerated, in turn, away from the cathode to collide with the residual gas atoms and molecules until a self-sustaining discharge is achieved. This region is called the 'breakdown region'.

Following that comes the 'glow region'. At the beginning, the gas starts to glow, which is combined with a decrease of the voltage and an abrupt increase of the current, known as 'normal glow discharge'. The electrons, which sustain the discharge, come basically from the secondary electron emission due to ion bombardment of the cathode. The typical yield of secondary electrons for most of materials is about 0.1 per incident ion [34]. Therefore, the energy of each secondary electron must be high enough to create ten ions to enable the discharge to be self-sustaining.

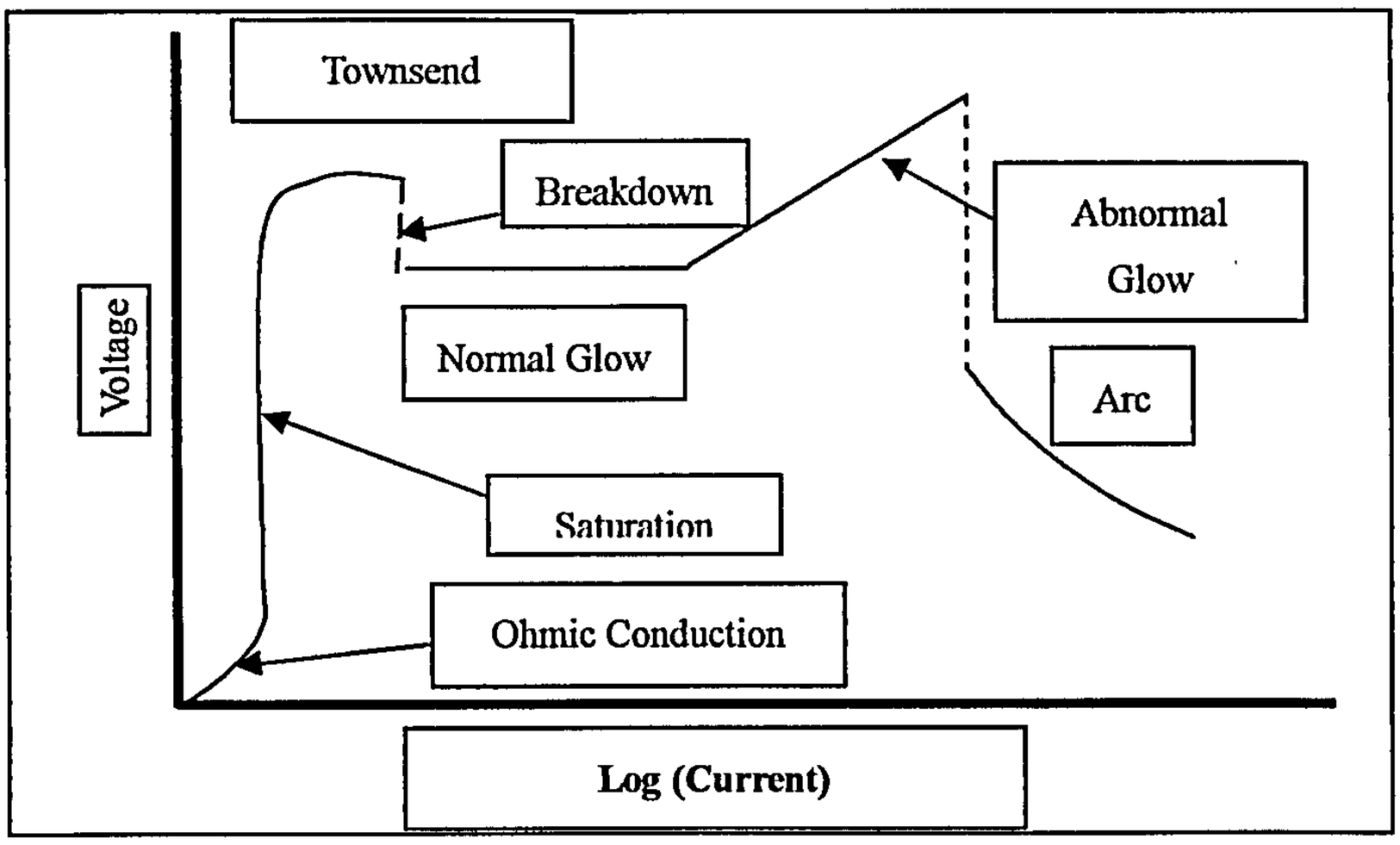

Figure 2.5 Graph of applied voltage vs current for a DC discharge

In the normal glow region, the ion bombardment of the cathode can be characterized as non-uniform and concentrated at the edges. By further increasing the voltage, the bombardment gradually covers the cathode and the current density eventually becomes uniform. This is named the 'abnormal glow discharge' region, in which the current intensity becomes a function of the voltage at a constant pressure. This is the region where sputtering and ion plating processes are normally carried out. Arcing and target breakdown can happen if the current is increased beyond this point with the corresponding phenomenon of the voltage suddenly reducing.

2.2.2 Plasma characteristics

A plasma has a number of unique characteristics. First, the *plasma potential* has to be understood. In plasmas, electrons tend to reach the boundaries of the plasma (i.e the chamber walls and installed components) faster than the ions because they have much less mass and in turn much higher mobility than ions. This results in the plasma bulk acquiring a net positive charge, restricting further losses of electrons. Eventually, a stable state would be reached, where the plasma potential is positive enough to keep the loss rate of electrons the same as the loss rate of ions. This characteristic of the

plasma can also be called 'quasi-neutrality'. The plasma potential normally is about several volts more positive than the grounded surfaces connected with the plasma. Figure 2.6 [33] shows the potential drop graph across a DC diode set-up.

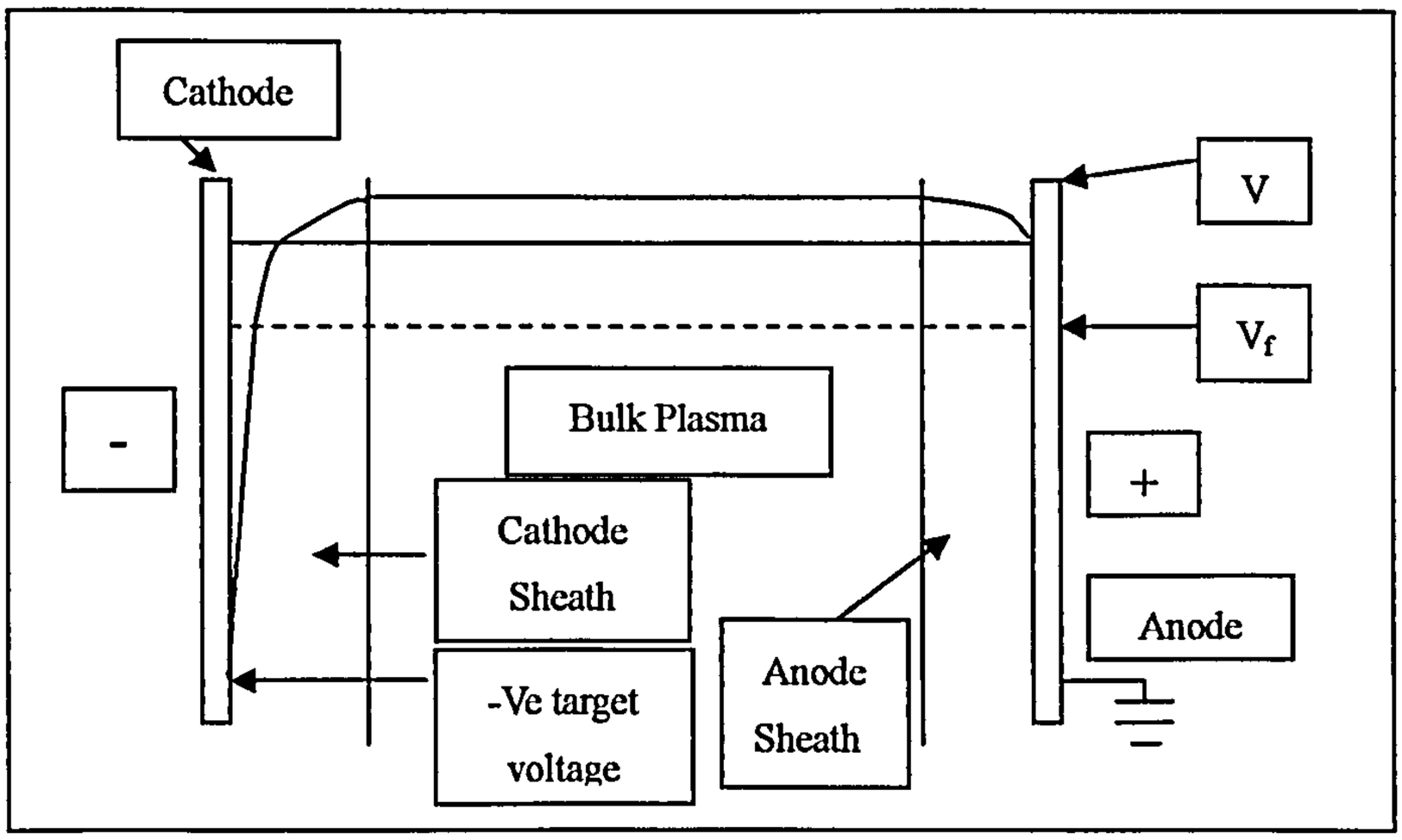

Figure 2.6 Potential drop across a DC diode set-up (not to scale)

There are special regions, called *sheaths* (see figure 2.6), which form between the bulk plasma and the surfaces connected with the edges of plasma (chamber walls, substrates, targets, etc.). In the sheath, the voltage drops significantly and the electron density is extremely low due to their high mobility. Consequently, gas species are exited in very low levels, and hence the sheath regions appear dark. In the example of the figures (2.5 and 2.6) mentioned above, it can be said that the *cathode sheath* is a plasma creation region or a process from Townsend discharge to glow discharge. The anode sheath is the region where the plasma potential drops down to anode potential within a short distance.

Another term to characterize plasmas is *Debye shielding or Debye length.* Plasmas can respond to the changes in potential due to their conductive property. The distance over which a small potential can disturb plasmas is called *the Debye length or Debye shielding,* which is proportional to the square root of electron energy and inverse to

the square root of electron density and charge [31-32]. In a typical magnetron discharge the Debye length is of the order of 0.5mm to 0.02mm [35].

The plasmas used in sputtering or ion plating processes are described as low temperature plasmas and are formed by partially ionising a gas at a reduced pressure, with normally about an ionization fraction of 10^{-5} to 10^{-1} [25]. The electron energy is in the range of 1-10 eV and ion energy 0.02-0.1 eV [36-37]. The electron temperature is actually extremely high, but they contribute little to the temperature because the majority of the plasma is made up of neutrals, which are at low temperatures. The result of this low plasma temperature allows many substrate materials to be used in this relative cold deposition process.

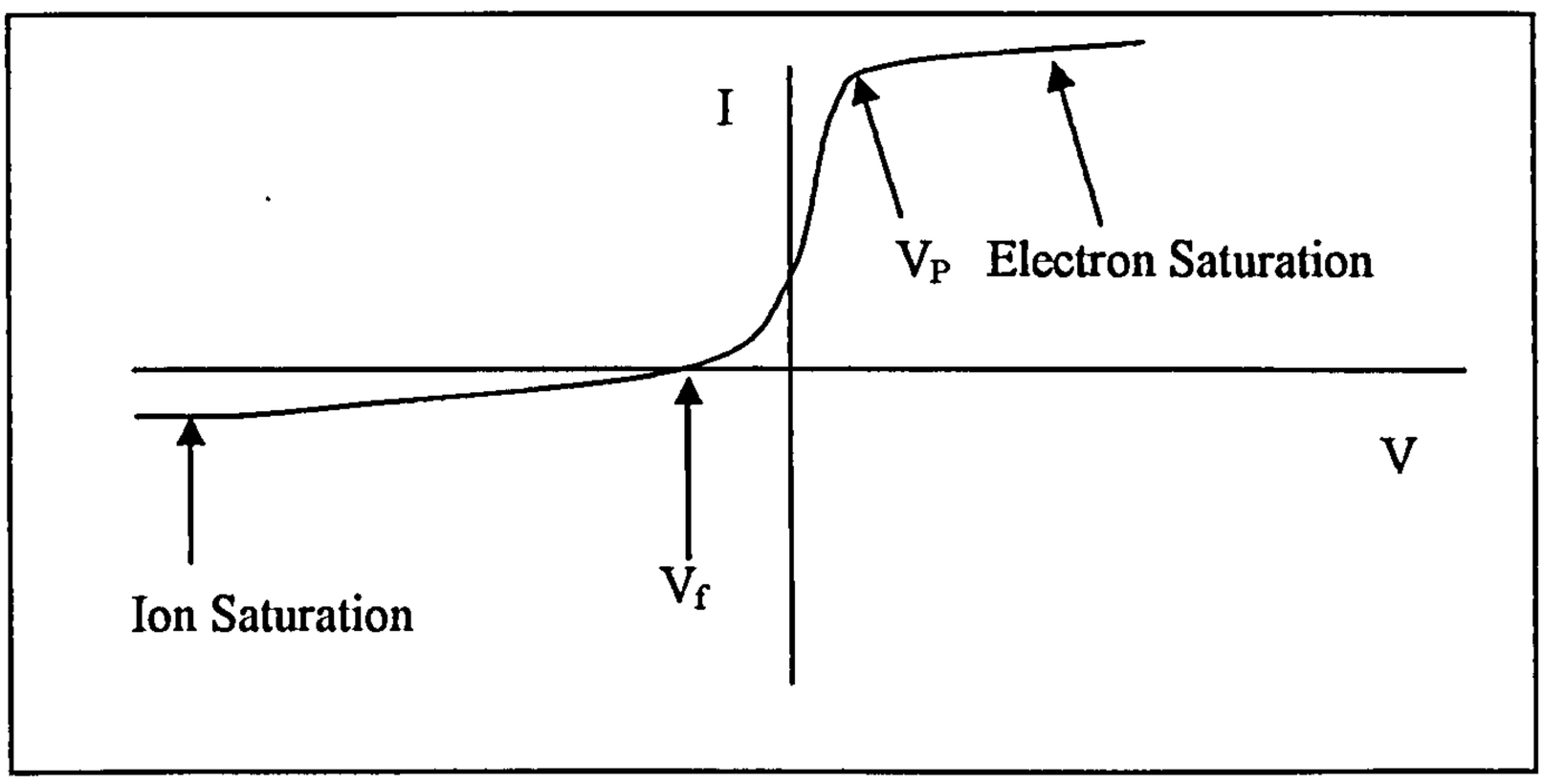

Figure 2.7 Characteristics Langmuir probe current-voltage plot

Plasma potential can be measured by using a Langmuir probe and described by a current (I) and voltage (V) plot (see figure 2.7). As the potential increases in the positive direction, the ratio of different charge species change from ion saturation to electron saturation. There are two points that need to be mentioned: one is the point at which the current equals zero, i.e. zero net current flows. This is the *floating potential* point (V_f) which occurs at a negative potential of, typically, –20 to –30V in a magnetron system. Another is the *plasma potential* point (V_p) at which the rate of increase of the electron current slows, which means the plasma voltage is high enough

to stop the further losses of electrons and keep the lost rate of ions the same as that of electrons [38]. In a plasma, electrons are more mobile than ions and other species. Therefore, an electrically floating surface in contact with the plasma will rapidly charge negative. This negative charge will repel further electron flow, then the flux of ions and electrons will be equal. At this point the negative charge on the surface is known as the *floating potential*. For the same reason, a plasma will suppress the highly mobile electrons from escaping from it by the increase of its potential, known as the *plasma potential*.

The DC diode plasma can be divided into several regions, which are shown in figure 2.8 [25]. There are three glowing areas with the *cathode glow* being located at the region closest to the cathode, where excitation ions are neutralised at the surface of the cathode. The very thin luminous region is very difficult to see normally. *Negative glow* is in the middle of plasma, a bright luminous region with roughly equal densities of electrons and ions. The third bright region is called the *positive column,* the result of electrons accelerated by local electric fields. Three dark areas are termed the Aston Dark Space, *Crookes dark space* and *Faraday dark space*. The former is located between target surface and Cathode Glow. This very thin area appears dark because the electrons have just been emitted from cathode and have very low energy. The Crookes Dark Space is located between the cathode glow and negative glow regions, in which secondary electrons from the cathode surface are accelerated by applying high electric fields. The high ionization and excitation rate of the species are the characteristics of this region. The Faraday dark space, located between the negative glow and positive column, is formed due to electrons losing their energy too much that glow or excitation are not able to continue after negative glow. The electrons can be accelerated again by the positive potential at the anode after the Faraday dark, and this region is known as the positive column. The Faraday dark space and positive column is obstructed if the anode is placed in the negative glow region, which is very common in deposition systems.

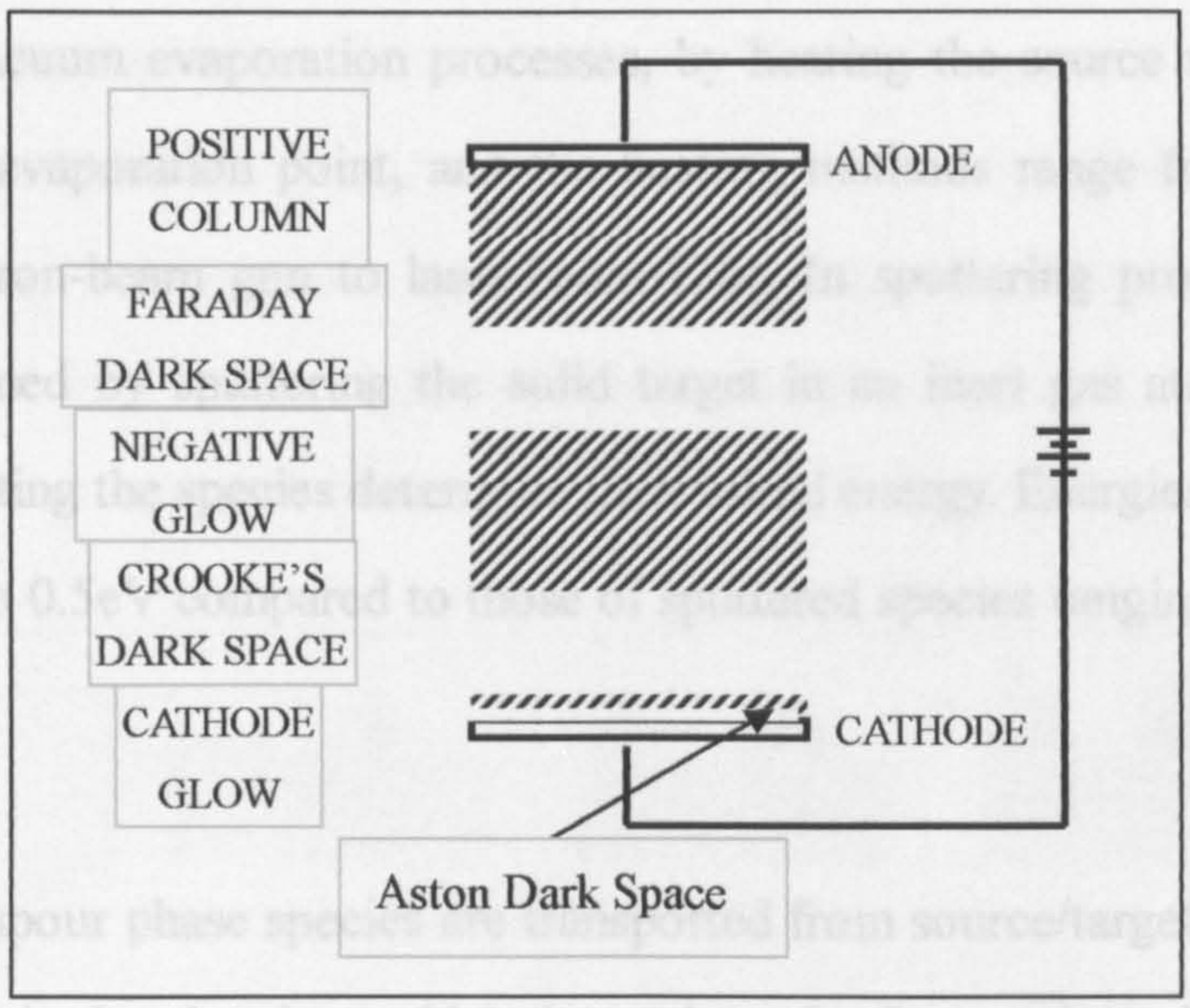

Figure 2.8 the regions of DC plasma discharge

2.3 Film Formation and Growth

There are generally three steps for film formation in all PVD processes. See the schematic figure 2.9 below.

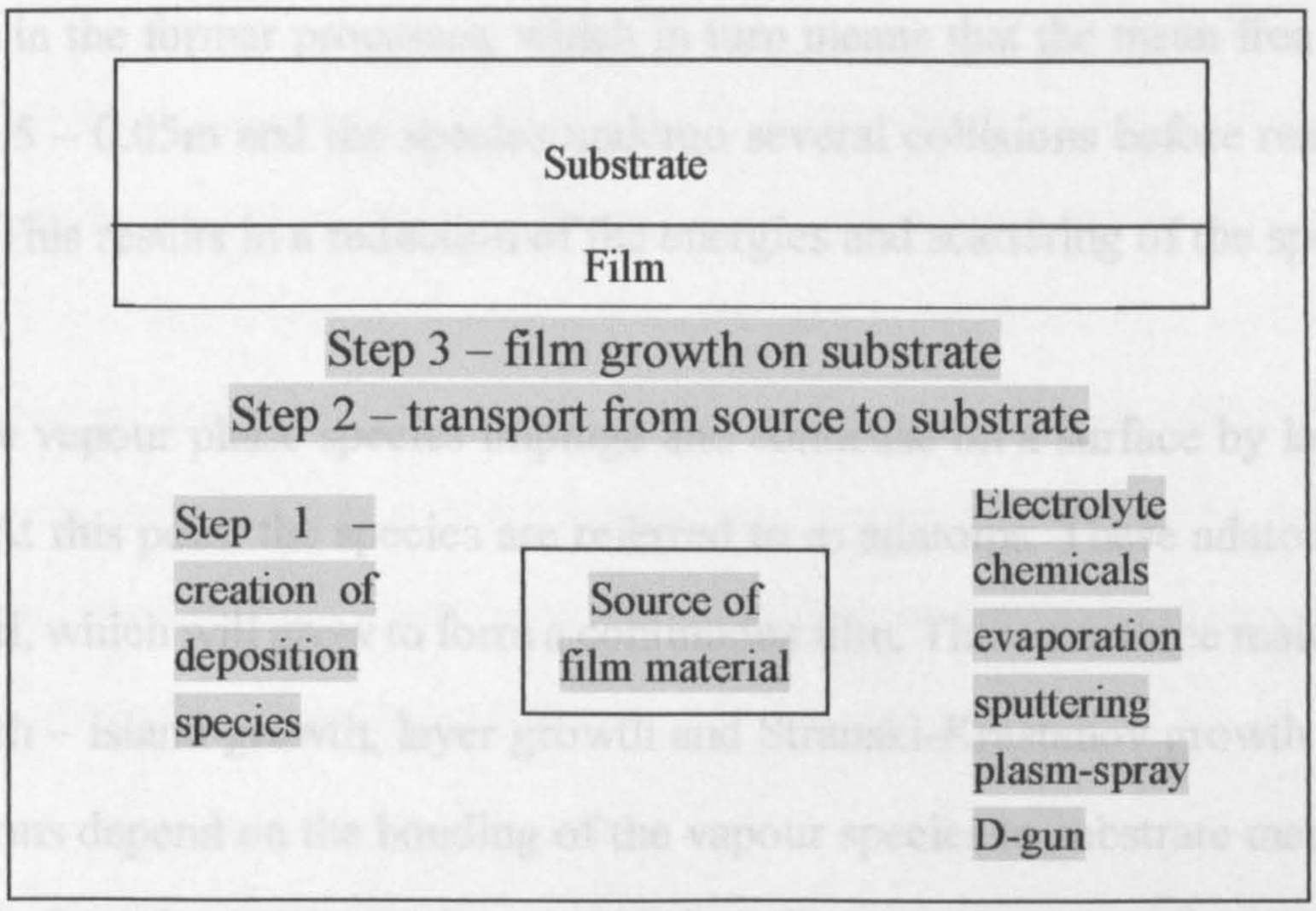

Figure 2.9 the three steps in film deposition [25]

First, the depositing species, or vapour phase species are created in the vacuum chamber from a source/target by energy transfer. The vapour phase species are generated, in vacuum evaporation processes, by heating the source materials to its sublimation or evaporation point, and the heating methods range from resistance, induction, electron-beam gun to laser-beam [26]. In sputtering processes, vapour species are formed by sputtering the solid target in an inert gas atmosphere. The methods of creating the species determine their initial energy. Energies of evaporated species are up to 0.5eV compared to those of sputtered species ranging from 1-40eV [38].

Secondly, the vapour phase species are transported from source/target to substrate in partial pressures in the chamber, which determines the flow regime characterization. The mean free path (λ) of a gas is dependant on the molecular diameter of the gas and the pressure in the chamber. For argon, $\lambda = 5.7 \times 10^{-2}/P$ (m), in which the unit of pressure, P, is Pascal [39]. In evaporation processes, the low gas pressures (no higher than 10^{-2} Pa) results in mean free paths (no shorter than 5m) greater than the source-to-substrate distances. Therefore, collisionless transport of the species occurs. In contrast, gas pressures in sputtering processes are normally higher (0.1 to 1 Pa) than those in the former processes, which in turn means that the mean free paths are between 0.5 – 0.05m and the species undergo several collisions before reaching the substrate. This results in a reduction of the energies and scattering of the species.

Finally, the vapour phase species impinge and condense on a surface by losing their energies. At this point the species are referred to as adatoms. These adatoms in turn form nuclei, which will grow to form a continuous film. There are three main forms of film growth – island growth, layer growth and Stranski-Krastanov growth [40]. The growth forms depend on the bonding of the vapour species to substrate materials and themselves. Island growth can be seen if the adherence is greater between vapour species. Therefore small groups of adatoms accumulate on the surface of substrate and then coalesce to form the film. This can lead to the formation of porous films.

Growth is in three dimensions if the adherence between species and substrate is greater. In this case the films will grow layer by layer, the way of layer growth. Then the films will be desirably dense coatings. The third growth way is called Stranski-Krastanov growth, which combines both forms mentioned above. In this way, the adatoms begin to accumulate and form islands after an initial layer has grown. Lewis and Anderson [166] developed the concept of nuclei growth and formation in their studies of the evaporated films.

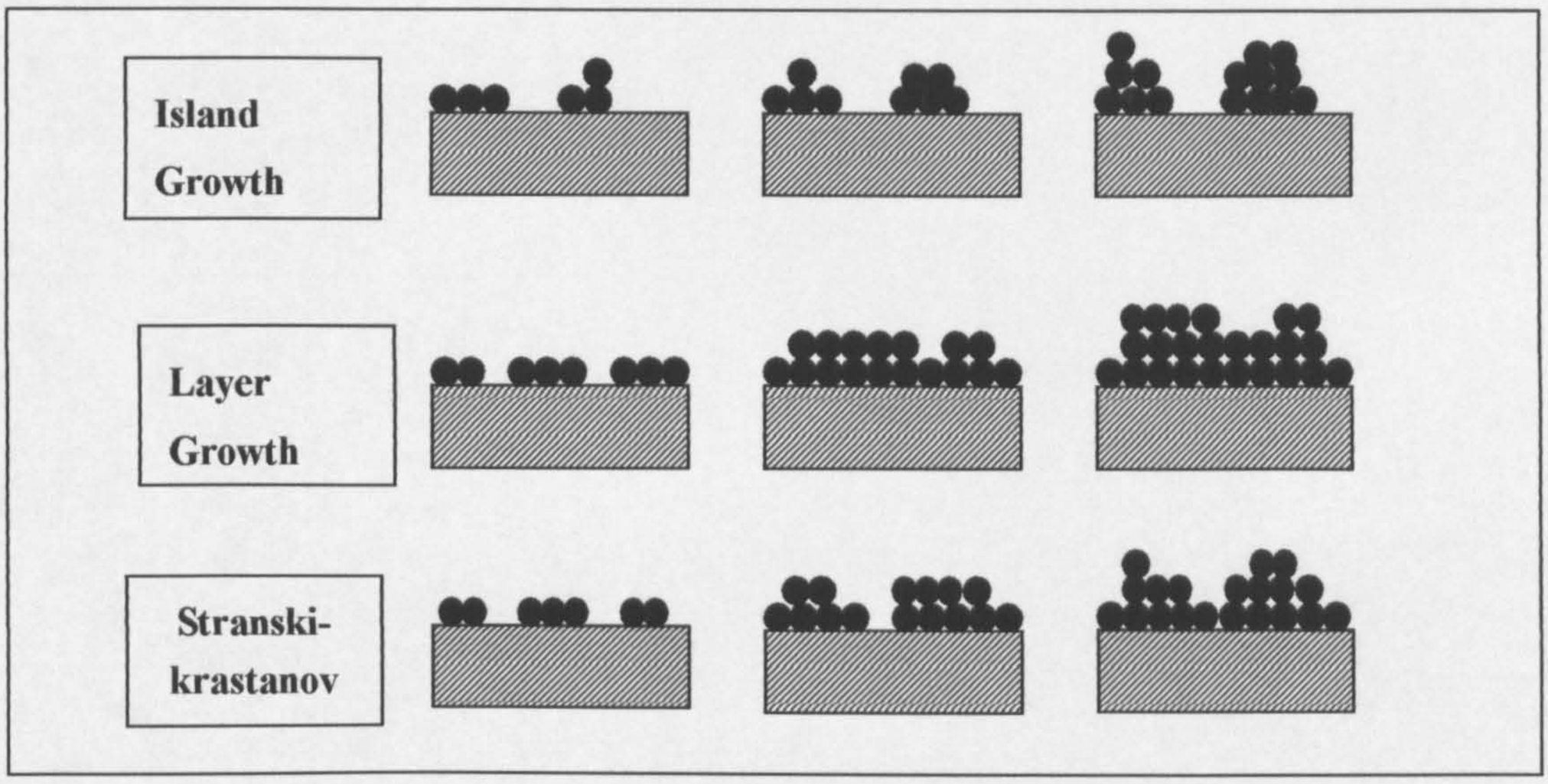

Figure 2.10 Basic growth mechanisms [33]

The film formation processes are controlled by many factors, such as the nature and roughness of the substrate surface, the substrate temperature whilst depositing, the deposition rates, the angle of incidence of the species and the gas pressure in the vacuum chamber, and the substrate bias. Gas pressure, in particular, affects the energy of the adatoms, which is a key factor in controlling adatom mobility on the substrate surface. Adatoms with high-energies are likely diffuse across the substrate surface and possibly diffuse into the substrate material.

Understanding the types of film growth is important because they affect the formation of film structures, which is going to be discussed in the following section.

2.4 Film Structure

In the late 1960s, Movchan and Demchisin [41] began to study the effect of substrate temperature on the formation of film structure, and created the famous three zones model for evaporation deposition processes, see figure 2.11 [23, 27]. The relationship of film structure and the ratio of the substrate surface temperature (T) to the melting point of the deposited material (T_m) were established in the model. Three zones formed as the ratio (T/T_m), known as homologous temperature, increased. Zone (1) takes place at the ratio lower than 0.3, at which the adatom energies are not high enough to overcome the shadowing effects from substrate irregularities, causing insufficient surface diffusion. The film growth is in turn dominated by the island type mode, and therefore porous columnar structures are formed in the growing film. In zone (2) the ratio (T/T_m) is range form 0.3 to 0.5. The substrate surface appears to have a more regular morphology with a smooth, matt appearance as the substrate temperature increases. Adatom surface diffusion now dominates the film growth process, and denser columnar crystalline structures represent the characteristics of the coating. As the substrate temperatures further increase, the zone (3) region can be reached, where bulk diffusion processes, such as annealing and recrystallisation, take the main role in film growth process, and determine the final structure of the coating. It is described that, in zone (3), equi-axed grains are the representative structure, similar to those of a fully annealed metal.

In the 1970s, Thornton [42-43] extended this work by adding an additional axis to account for the effects of gas pressure in sputter deposition processes, shown in figure 2.12. A transition zone (T) was introduced between zones (1) and (2). The film structure with dense poorly defined fibrous grains is dominant in this zone. Zone (T) structure is more likely to form on a smooth surface at lower T/T_m ratio, which provides fewer barriers for adatom diffusion and needs relatively lower adatom energies to overcome the barriers. On the other hand, to form zone (T) structure on a

rough substrate surface needs higher energy for adatom to fill the voids, which requires higher T/T_m ratio. In the Thornton structure zone model, the formation of zone (T) is also apparently affected by gas pressure. The region of zone (T) is wider at lower gas pressure and T/T_m ratio. Zone (T) structures become difficult to see as gas pressure increases (i.e. zone 1 predominates), which is probably because the vapour species from source/target collide with each other resulting in energy losses.

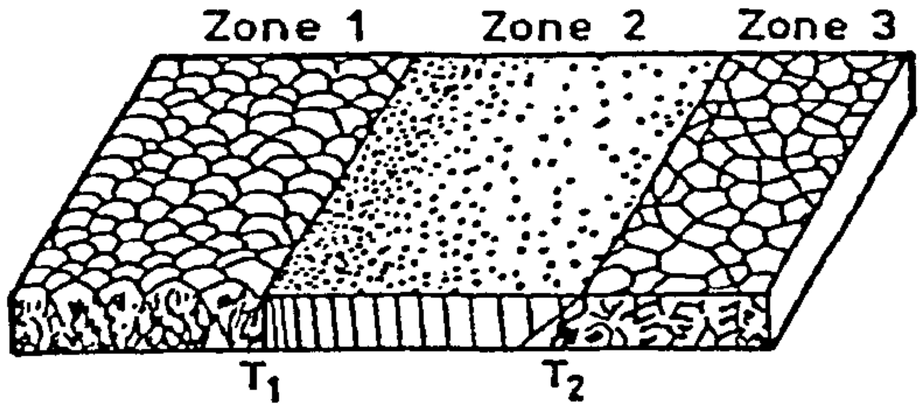

	Zone 1	Zone 2	Zone 3
Metals	$<0.3\ T_m$	$0.3-0.45\ T_m$	$>0.45\ T_m$
Oxides	$<0.26\ T_m$	$0.26-0.45\ T_m$	$>0.45\ T_m$

Figure 2.11 Movchan and Demchishin structure zone model [41]

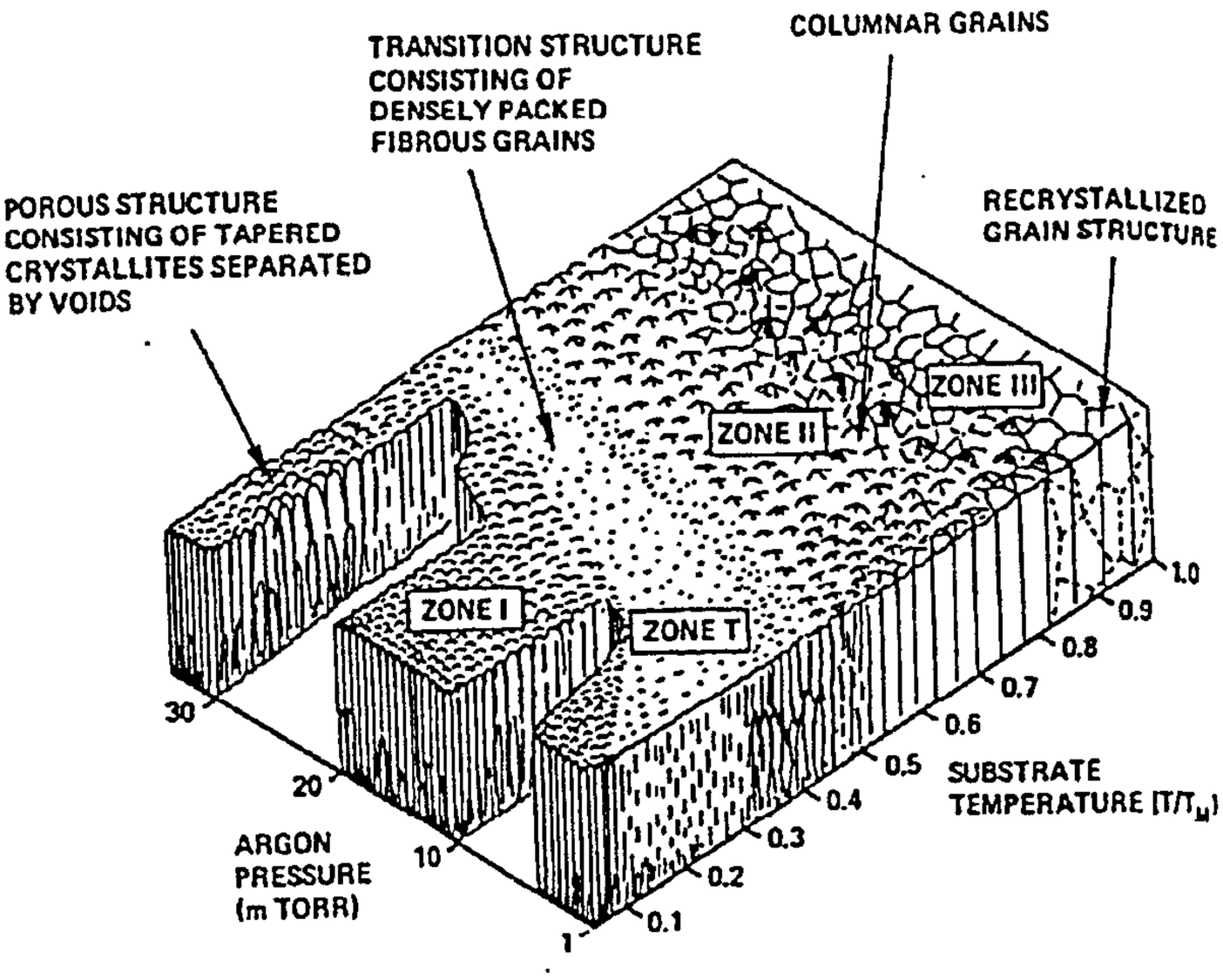

Figure 2.12 Thornton structure zone model [42]

Following the studies of Thornton, the dense equi-axed grains were produced at high bias conditions in ion-plated coatings [44-45]. Messier et al. [46-47] suggested that the bias voltage axis should be introduced to replace the pressure axis in the SZM structure models. Moreover, Fountzoulas and Nowak [48], Musil and Kadlec [49-52] introduced other versions of SZM (structure zone model) models by using total energy axis of ions or combined energy of ions as a parameter.

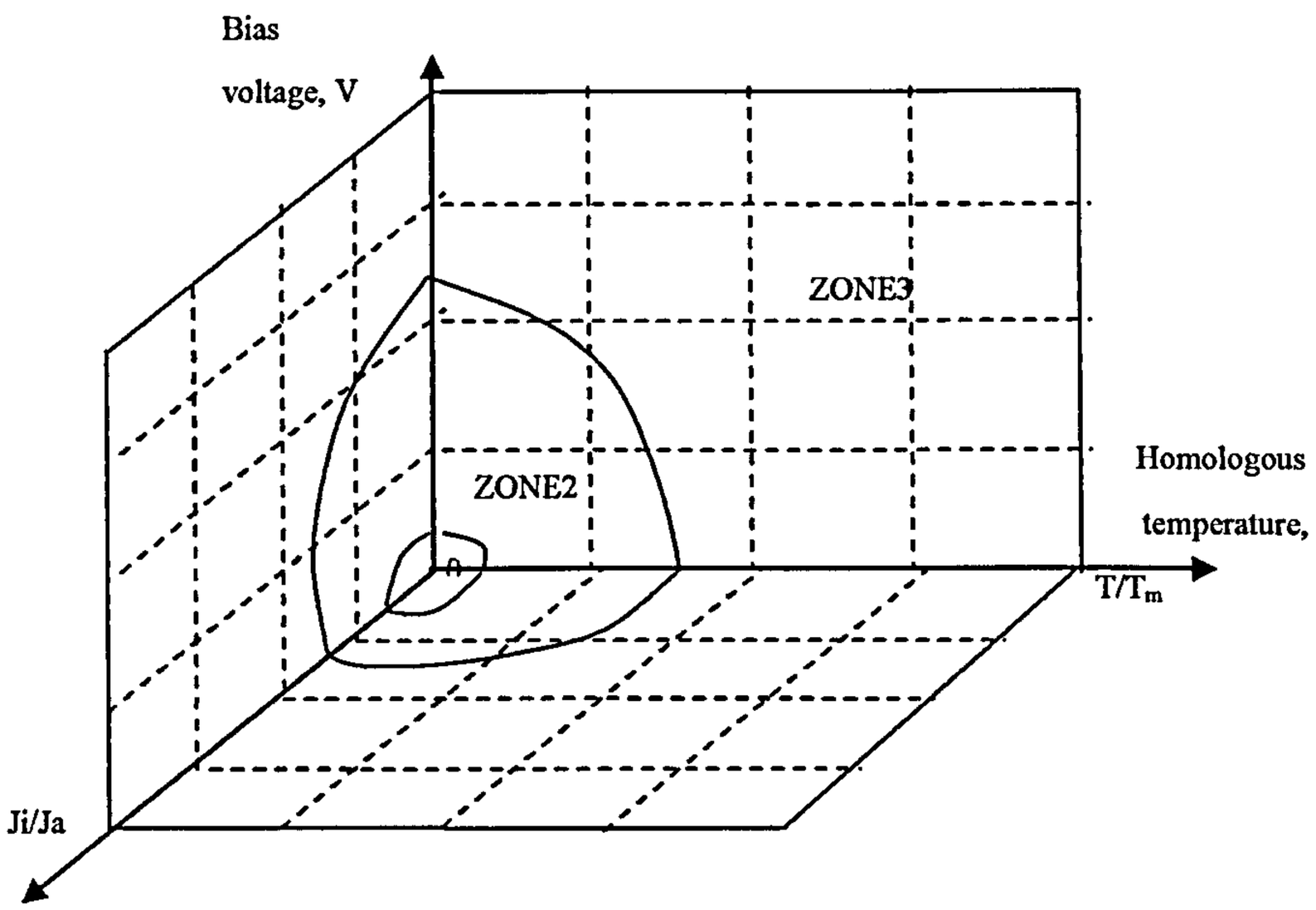

Figure 2.13 P.J. Kelly and R.D. Arnell structure zone model [53]

More recently Kelly and Arnell have proposed a structure zone model to describe closed field unbalanced magnetron sputtering (CFUBMS) [53] by taking into account the homologous temperature T/T_m, the bias voltage on the substrate and the ion to neutral ratio J_i/J_n. In their experiments, zone (2) appeared within the homologous temperature range from 0.13 to 0.43, and zone (3) from 0.43 to 0.68. It is clearly shown in the three dimensions figure 2.13 that zone (2) structures appear in the region with relative low homologous temperature, ion to atom ratio and bias voltage except the very small region near zero point of three axes. This structure zone model describes the ability of CFUBMS systems to form fully dense columnar structures at low deposition temperatures.

Structure is an important factor in determining film properties. It is important, therefore, to control factors, such as ion bombardment of the substrate, that affect film structure. In general zone 1 structures are unsuitable for engineering applications due to their poor mechanical properties, hence the interest in processes capable of producing zone 2 and zone 3 structures. The figures below are typical scanning electron micrographs showing examples of the three types of structures [53].

Zone 1 – Porous Columnar Structure

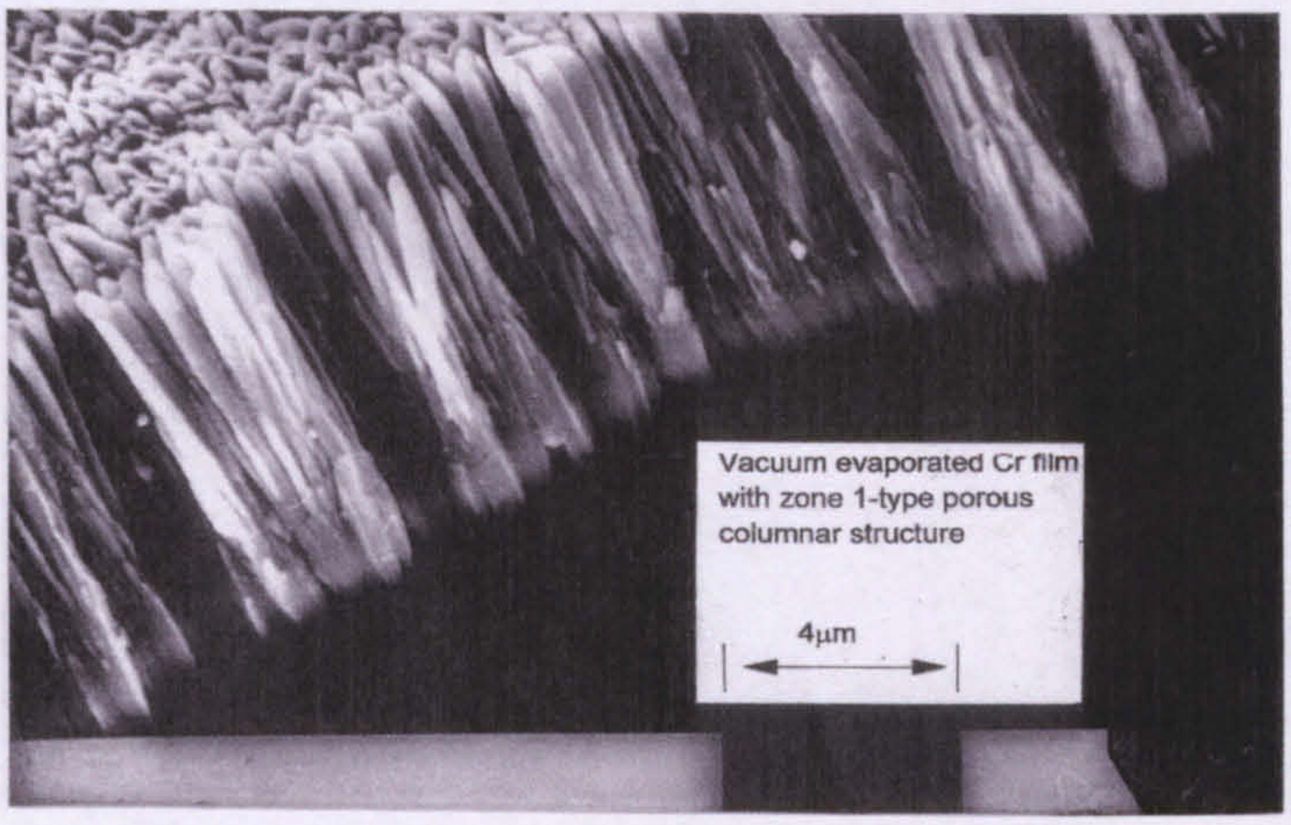

Zone 2 – Dense Columnar Structure

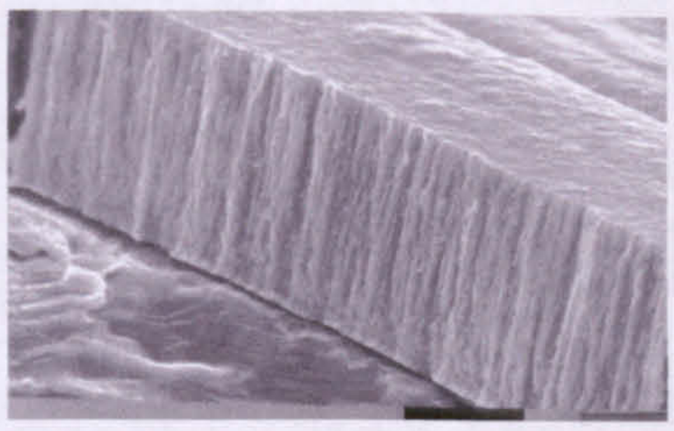

SEM micrograph of W coating deposited by CFUBMS, showing typical zone 2-type structure

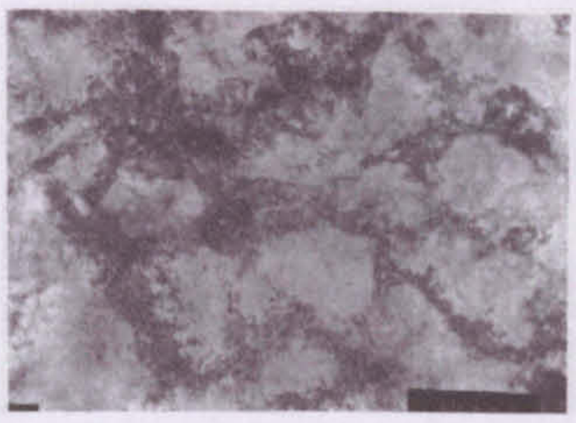

Through thickness TEM micrograph of W coating deposited by CFUBMS, showing typical zone 2-type structure

Zone 3 – Fully Dense Structure

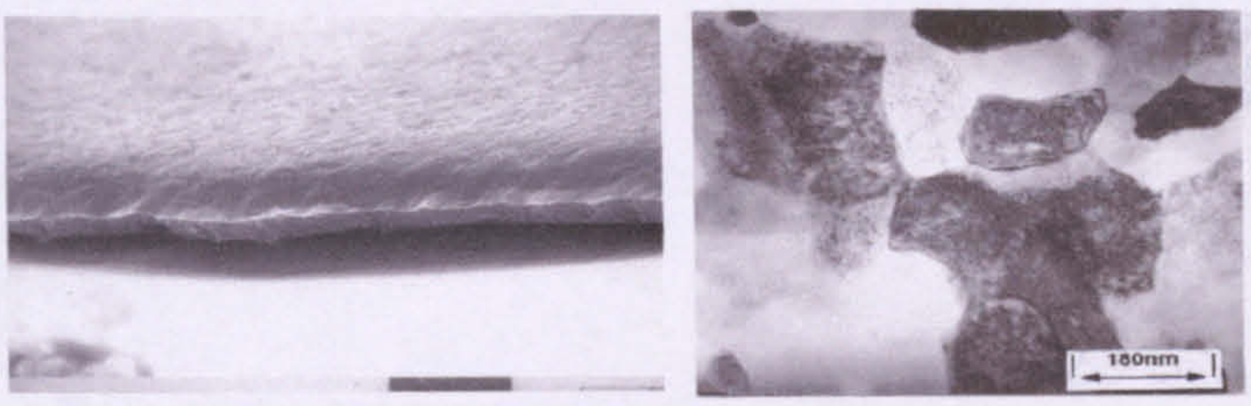

SEM micrograph of Al coating deposited by CFUBMS, showing typical zone 3-type structure

Through thickness TEM micrograph of Al coating deposited by CFUBMS, showing typical zone 3-type structure

Picture 2.1 SEM and TEM micrographs showing three types of coating structures, as described in structure zone models [53]

2.5 Sputter Ion Plating

Sputter ion plating is a process using a sputtering target as the source in the ion plating system. Unlike the evaporation processes the source vapour is no longer created by thermal methods, but by ion impact on the target. The species created by sputtering normally have energies in the range from 4.0-10eV, which is higher than thermally evaporated species (typically, 0.1-0.6eV). Figure 2.14 shows the schematic representation of a basic sputter ion plating system.

Sputtering is a process whereby individual atoms escape from the target surface due to atomic collision cascades by suitable high energy ion bombardment [54-55].

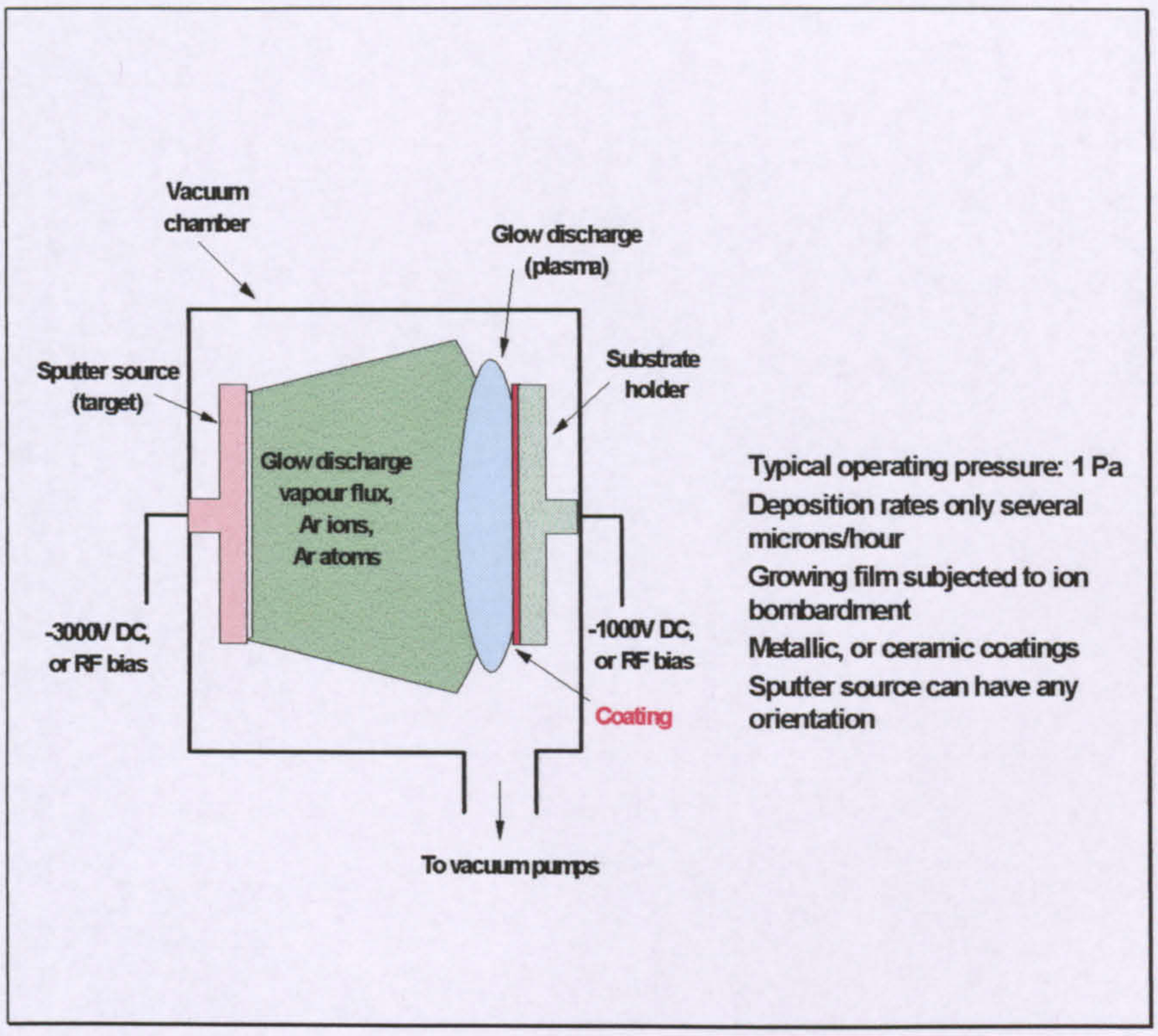

Figure 2.14 Basic sputter ion plating graph

(Typical operating pressure: 1Pa; Deposition rate: microns/h; Ion bombardment of growing film; Metallic or ceramic coatings; Any orientation of sputter source)

The common method of providing the energetic ions is to evacuate the chamber to the pressure lower than 10^{-3} Pa and backfill it by inert gas, normally argon to a pressure of about 1Pa (higher than 0.05 Pa for magnetron sputtering). Then ignite an electric discharge so that the working gas is partially ionized and ready to bombard the target. A number of processes can occur at the target surface, in addition to the sputtering of target atoms, and they are summarised in Figure 2.15.

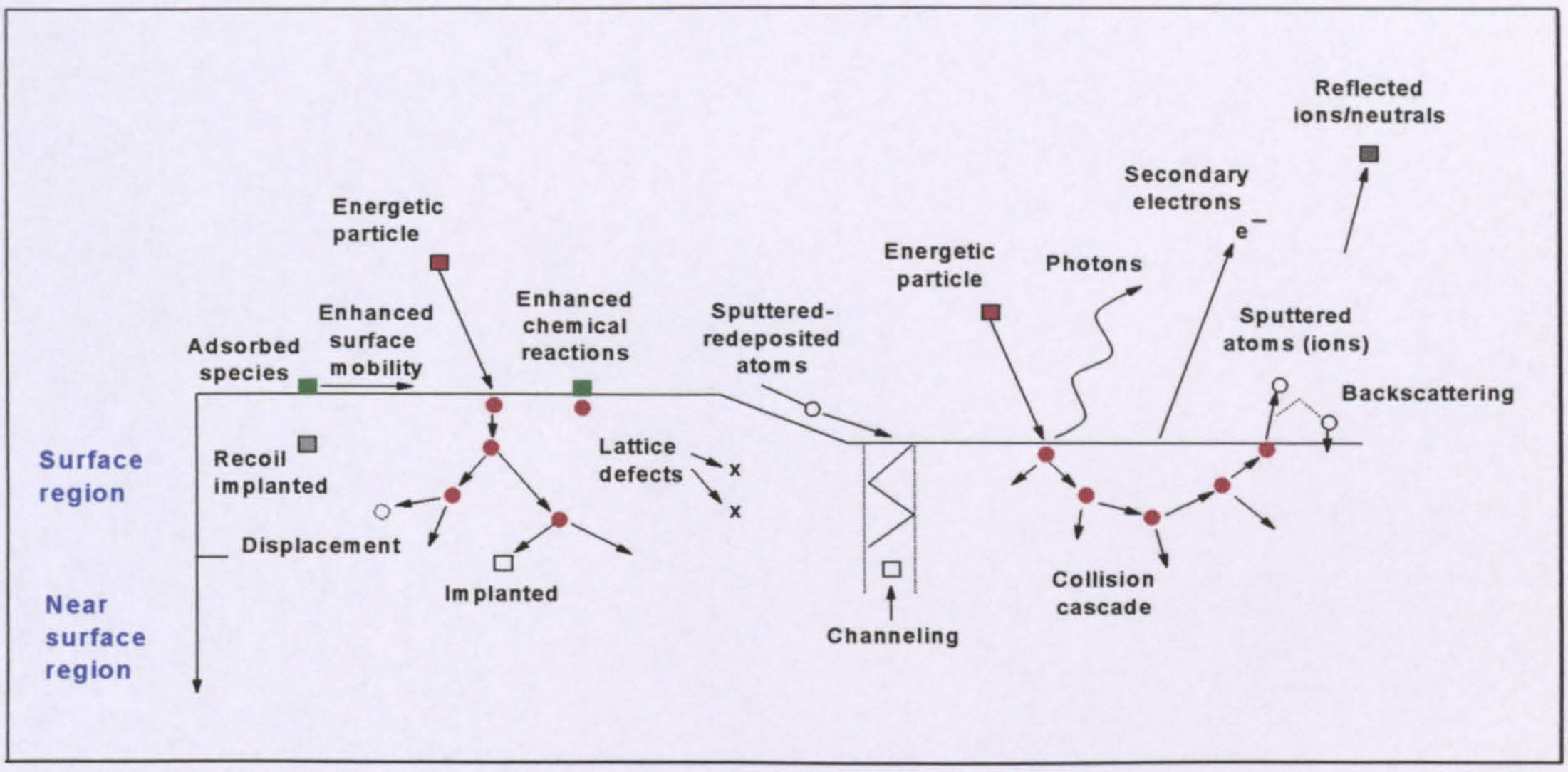

Reactions: collision cascade – sputtering ions and secondary electron;

Channelling -- redepositions; Enhanced surface mobility -- implantation

Figure 2.15 Possible reactions at the target surface [12]

If the impinging ion has enough energy, it will strike the atoms in the near surface region of the target and eventually impart sufficient energy to a surface atom, through a 'collision cascade' for it to be ejected from the target. Generally sputtered particles are neutral, but a small fraction may be ions. The collision may cause 'implantation' or 'gas trapping' if the result of collision is to displace atoms from their lattice positions and create lattice defects. In the momentum transfer process, the transfer mechanism are not only the collision cascade and implantation processes, but also:

- Secondary electron emission
- Surface modification
- Particle backscattering
- Surface atom sputtering
- Photon or X-ray emission

- Gas desorption
- Re-deposition of sputtered species due to the atoms colliding in the plasma and being attracted back to the surface of the target.

Sputtering can be driven by many kinds of power supply. DC supplies cannot sputter poorly conducting materials, due to the excessively high target voltages that would be required to initiate the discharge. The alternative supplies (mid-frequency pulsed DC and radio frequency RF) can be used to overcome this problem. For RF (normally @ 13.56MHz) processes, sputtering works because the target self-biases to a negative potential, which is based on the fact that electrons are considerably more mobile than ions and have little difficulty in following the periodic change in the electric field, whereas, the slower ions cannot respond at these frequencies. As RF power is applied, a large initial electron current is drawn to the target during the positive half of the cycle. However, only a small ion current is drawn during the second half of the cycle. Therefore, since the power supply is capacitively coupled, the target acquires a negative potential, capable of sustaining sputtering. Moreover, there is a formula about voltages of electrodes and their areas:

$$\frac{V_t}{V_s} = \left(\frac{A_s}{A_t}\right)^4 \qquad \text{... eq. 2.4}$$

in which V_t is the voltage of the target, V_s is the voltage of the substrate and system ground (including substrate holders, chamber walls, etc.). A_t is the area of the target, and A_s is the area of substrate and system ground. The fact that A_s is much larger than A_t causes V_s to be too small to sputter the substrate, which is very important for the deposition of films by RF, as it can prevent film contamination [28].

Pulsed DC power (20-350 kHz) is a promising choice for depositing partially insulating materials. Different from RF, pulsed DC frequencies allow both ions and electrons to respond to the changing potential. The high negative potential during the "pulse on" period results in sputtering of the target by positive ion bombardment. The small positive potential during "pulse off" period discharges any build-up of positive charge from the previous period by electron bombardment. The deposition process is

controlled by adjusting pulse parameters, such as pulse frequency and duty (i.e., the length of the pulse on time in proportion to the full pulse cycle pulse). Another advantage of pulsed DC supply is it does not need to be tuned like RF, which means it is much more stable and scalable than RF driven systems.

Another function in sputter ion plating is ion bombardment on the surface of the substrate and therefore on the growing film by biasing the substrate. Bombardment of the substrate surface before deposition can generally clean the surface of the substrate by removal of contamination, resulting in surface modification at the atomic scale. Bombardment of the surface of the substrate during the film growth can produce high density films, but may result in very low deposition rates because of re-sputtering of the films. The bias power and vacuum pressure are two critical factors [30]. High intrinsic stresses can arise in the coatings if the bias voltage is too high. Suitable gas pressure will improve the ion-to-atom ratio and species with appropriate energy by controlling the number of collisions during their transport from the target to the substrate. In general, both the degree of ionization and deposition rate is low in sputter ion plating processes compared to magnetron sputtering, which is going to be discussed in the next section.

Many of the limitations of the basic sputtering process have been overcome through the development of magnetron sputtering, which brought about a new era in PVD.

2.6 Magnetron Sputtering

From the well-known equation, a charged particle is subject to a Lorenz force, F_m, if it is located in a magnetic field.

$$\vec{F}_m = q\vec{v} \times \vec{B} \qquad \text{...eq. 2.5}$$

Where q is the charge on the particle, v is the velocity, and B is the strength of the magnetic field. If the force subjected on the charged particle is perpendicular to a

magnetic field, the charged particle will change its initial track and move in an orbital path around the magnetic field line. The orbit radius can be determined by the formula as follow:

$$R = \frac{mv_{\perp}}{qB} \qquad \text{... eq. 2.6}$$

Where m is the mass of the particle and $v_{\perp}$ is the component of the velocity perpendicular to the magnetic field. From the relationship above, it can be seen that the heavier the mass of the charged particle, the larger the radius of the orbital circle of the movement at a constant magnetic field at the same charge and velocity. Considering that the mass of an electron is much less than that of an ion, the radius for an ion around the magnetic field line will be more than 1000 times larger compared to that of an electron at the same conditions. Therefore, it can be said that magnetic fields have a significant influence on charged particles within the plasma, also the degree of effect is dependent on the mass of the charged particle when the other parameters are the same. In a plasma, the effect of the magnetic field on electrons is normally considered, and on ions ignored.

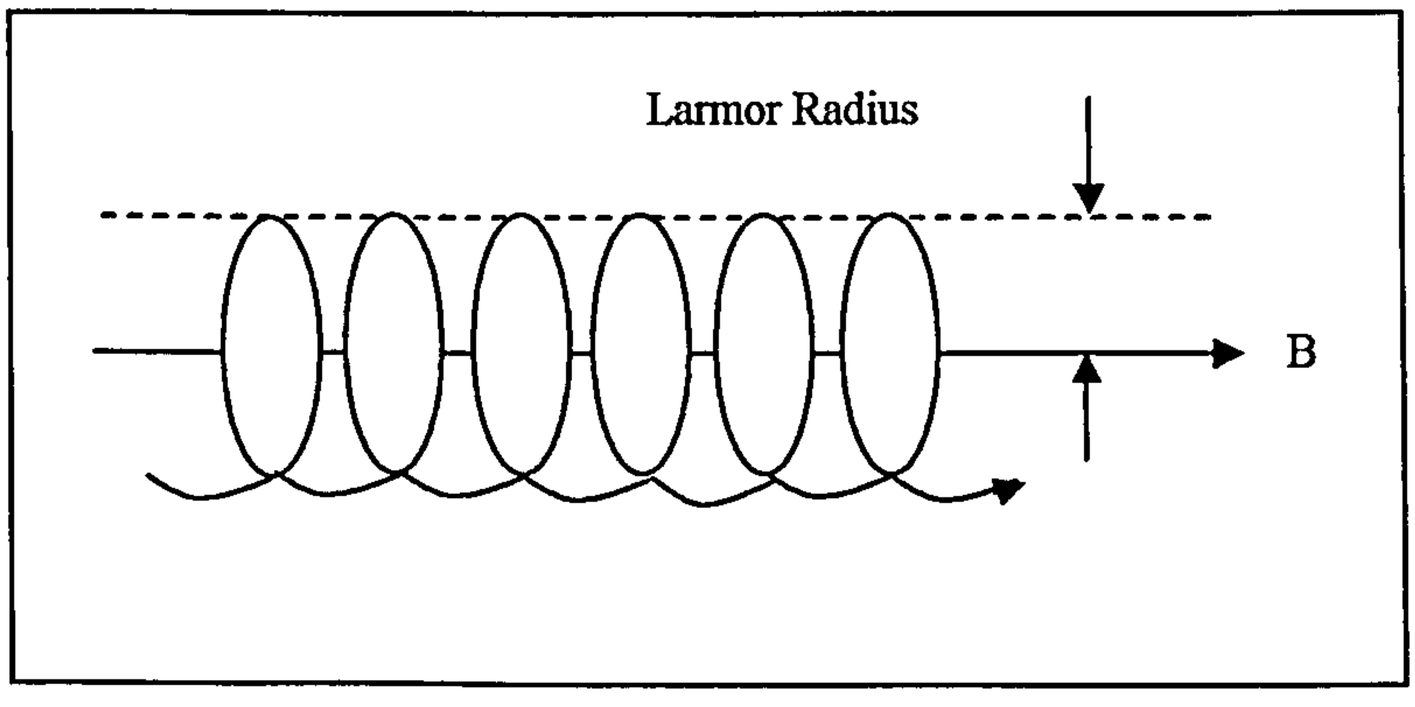

Figure 2.16 The trajectory of a charged particle moving in a constant magnetic field [33]

By the application of a magnetic field parallel to an electric field (figure 2.16), based on the concept that they interact with each other, the electrons move in a helical way along the magnetic field lines towards the anode. This movement prevents electron

losses from the plasma, therefore provides the electrons with a chance to collide with the atoms as they pass through the plasma to the anode.

By applying a magnetic field perpendicular to an electric field, the electrons will move in a cycloidal way, on which the electrons are accelerated when they move in the direction of the electric field and they are deflected less by the magnetic field. On the other hand, electrons are accelerated when they move in the direction against the electric field on the other half of the cycle, they are affected more by the magnetic field and result in greater deflections. Figure 2.17 shows the electron's movement with the combination of electric and magnetic fields.

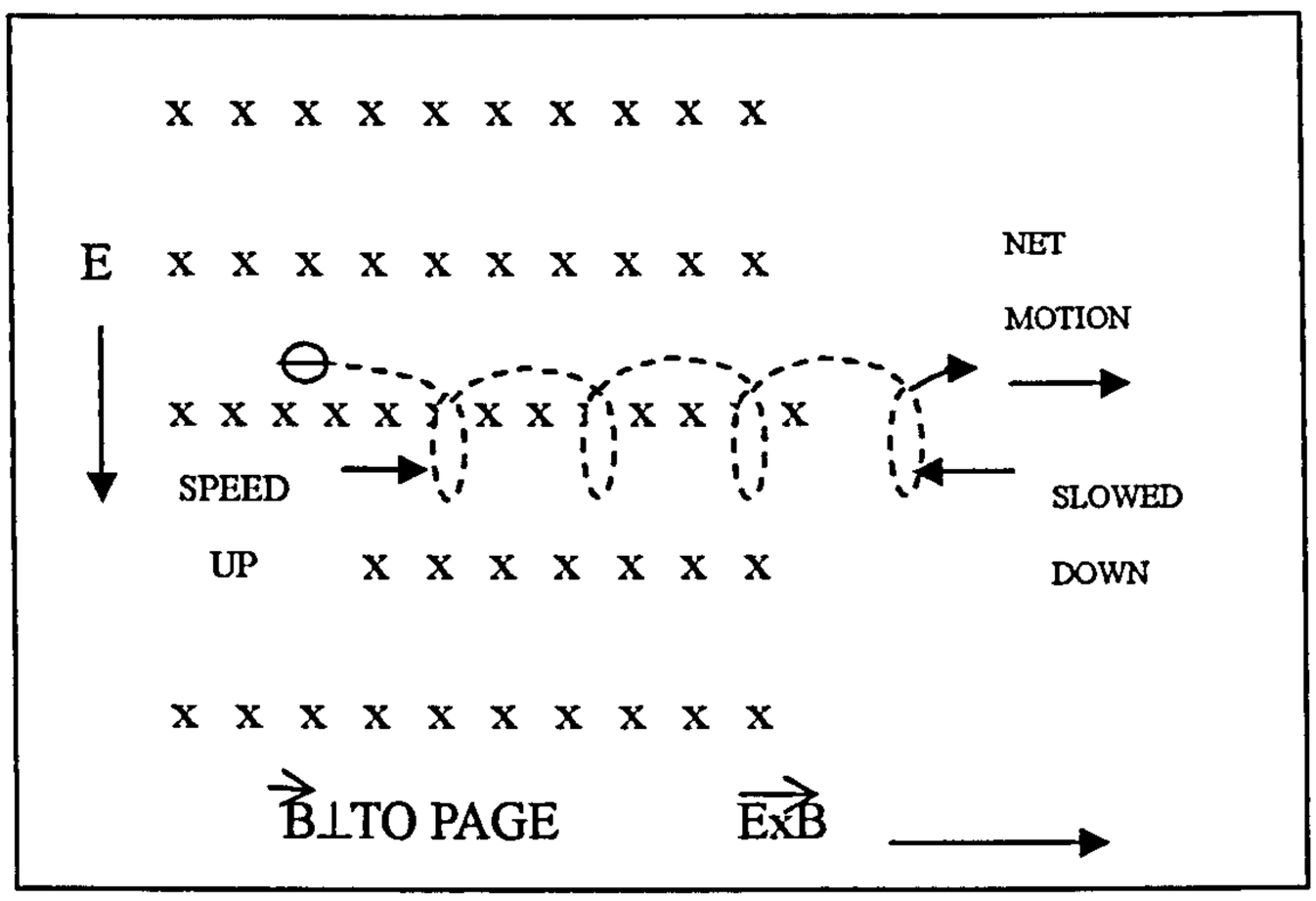

Figure 2.17 The motion of an electron in combined electric and magnetic fields.

Magnetrons were developed for use in sputtering processes in the 1970s [56] to take advantage of the effect on electron movement of the interaction between magnetic and electric fields, detailed above. Figure 2.18 is the layout of a typical conventional magnetron configuration, and figure 2.19 shows the electron movement in the region of space in front of the target with the magnetic and electric fields. By placing magnets in this configuration behind the target as shown in the figure 2.18, the magnetic field lines travel from north pole to south pole through the target material

and form a region in the shape of a closed loop. Electrons spiral along the magnetic field lines and are confined close to the target. This results in a closed current loop formed above the target and the sputtering species are generally ejected away from the current circle region into the plasma. The electron path length is significantly increased due to this motion, meaning they can undergo many collisions before they are lost to ground. Then the secondary electrons produced from the target into the plasma will be attracted by magnetic field lines again and confined to the region near the target. This entrapment increases the amount of ionization in the plasma, creating a dense plasma in front of the target. In turn, more ions from the plasma are accelerated across the cathode sheath and bombard the target in that confined region at the full discharge potential. This technique allows the sputtering and deposition at a reduced discharge voltage, dc bias and gas pressure in the chamber compared to the basic sputtering process. Discharge voltages in the range of –500 to -1000V are sufficient to create energy-efficient sputtering of many useful materials compared to about -3000V in basic sputtering. The reduced pressure, which is up to 100 times less than conventional sputtering [57], allows the sputtering species to travel with very little gas scattering and hence the deposition rate is increased and the coating flux arrives with greater energy. In practice, an erosion path created within the closed loop region, known as the racetrack, is formed on the target, as shown in figure 2.19. Consequently, the typical utilization of the target is only 30%.

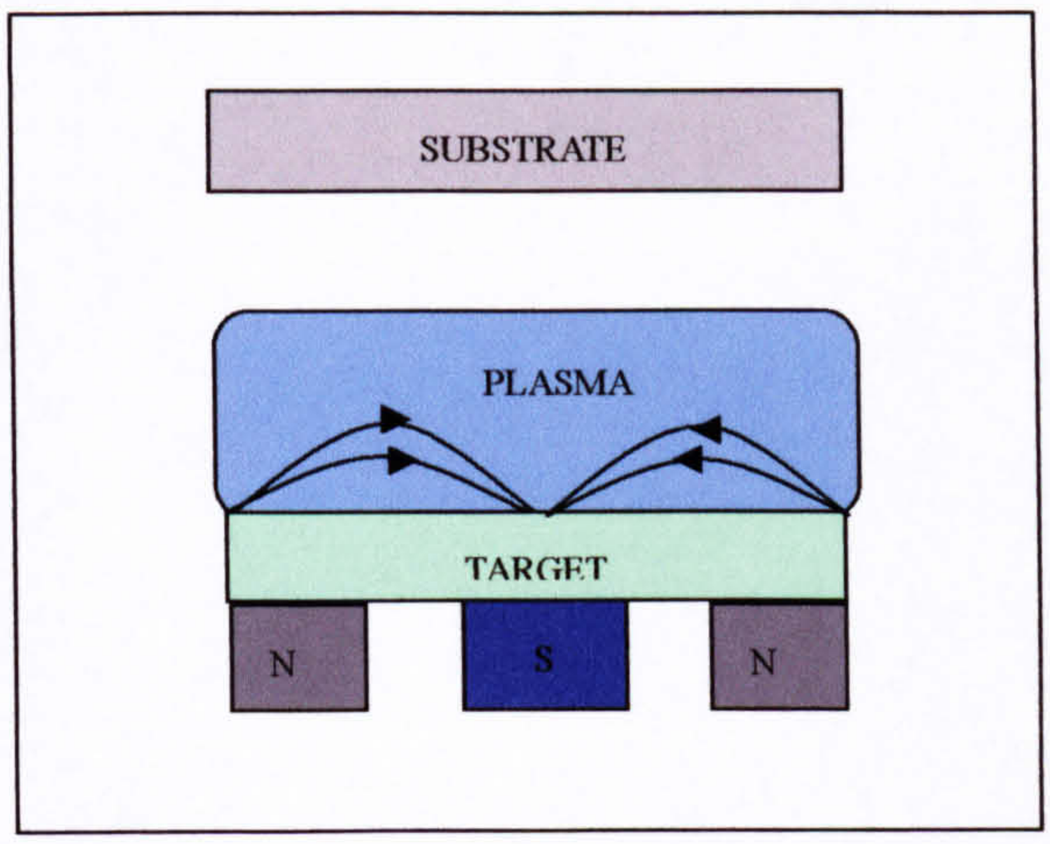

Figure 2.18 Vertical graph of conventional magnetron

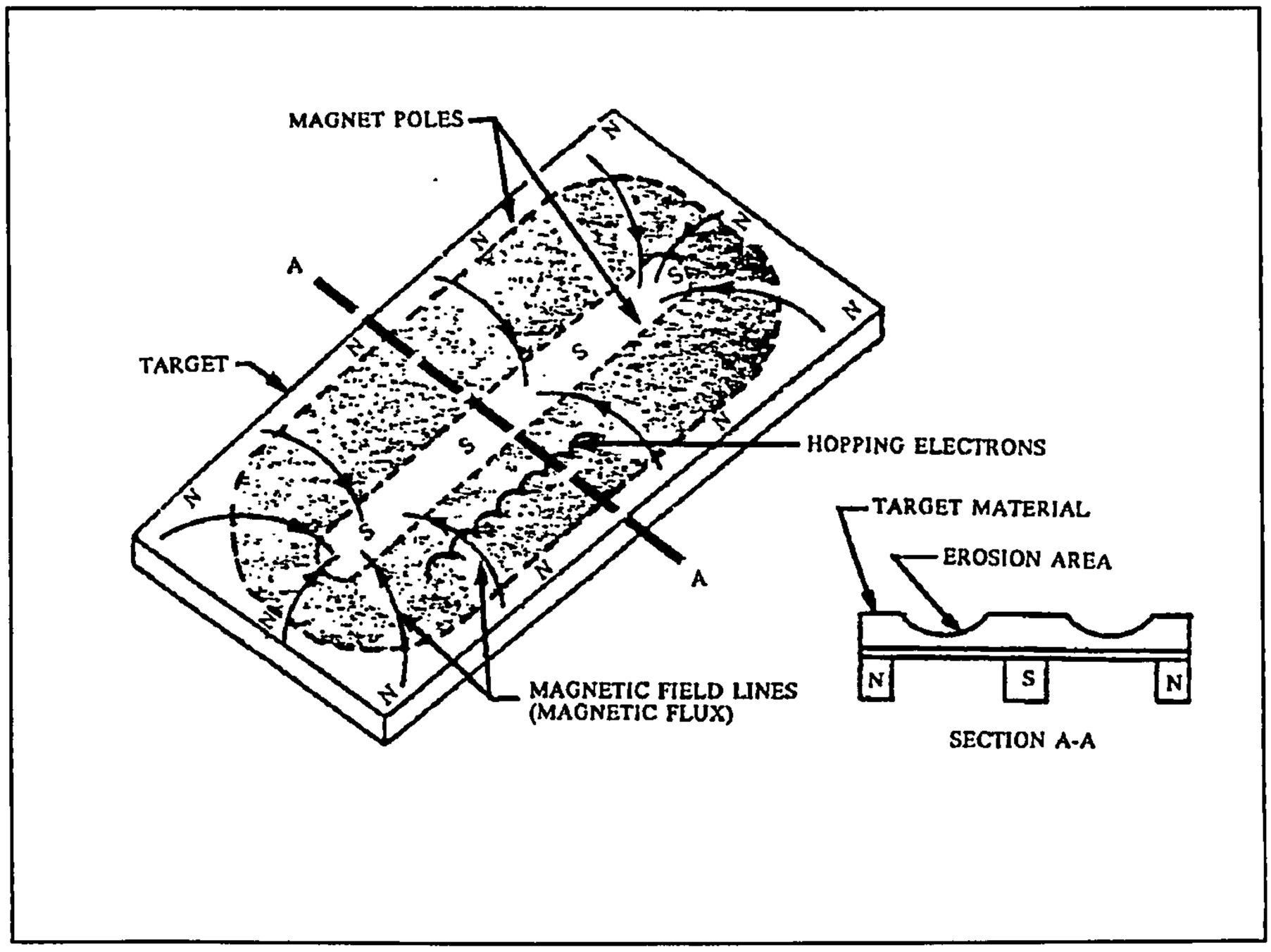

Figure 2.19 Rectangular planar magnetron [25]

A water-cooled system is needed in this technique to dissipate the target heating by heavy ion bombardment. The system normally is arranged by clamping the target directly onto the magnetron body. Moreover, the magnetrons can be arrayed in a variety of different ways besides the rectangular planar mentioned above, such as circular, cylindrical [58] and rotating. Rotating magnetrons can enhance the utilization [59] of the target up to 80% by rotating the tubular target around the magnetic array.

A drawback of the conventional magnetron sputtering is that the dense plasma is confined very near to the surface of the target. If the substrate is located any further the target, the growing film has no chance to be modified because of very little ion bombardment on the surface of substrate and the growing film, which is known to improve both physical and chemical properties of the film [60]. This problem was tackled by improving magnetron configuration in the 1980s by Window and Savvides

[13-15], who changed the 'balanced' magnetic array to a so-called 'unbalanced' array, and many researchers have studied this configuration since then [61-64].

.

2.7 Unbalanced Magnetron Sputtering

Window and Savvides made a prominent development in the 1980s in sputtering systems by changing the design of the magnetron. As detailed above, the strength of both inner and outer magnetic arrays in conventional balanced magnetron (CBM) sputtering systems are approximately equal and the magnetic flux is directed from north to south pole without significant losses. In Window and Savvides' design, the strength of either the outer or inner magnetic array was increased with respect to the other and therefore the magnetic flux was no longer completely confined to the near target region—this design is called the unbalanced magnetron (UBM).

There were two types of unbalanced design. By increasing the strength of the outer magnetic array, with respect to the inner array, the type II unbalanced magnetron system can be formed (following the nomenclature of Window and Savvides). Therefore, part of the magnetic flux does not close on the target, but is directed towards the substrate. Some of the secondary electrons will escape the trap near the target and follow these field lines, causing ionisation of atoms in the substrate region. The result is a dense plasma extending out towards the substrate and the ion bombardment of the growing film is increased. In Window and Savvides' findings, the magnitude of this increased ion bombardment was dependent on the degree of unbalance as well as other deposition conditions, such as the gas pressure, target power and substrate bias etc. More than 5mA cm^{-2} ion current could be drawn on the substrate according to studies by R.P. Howson, W.D. Sproul etc.[62-63]. A study in Salford [65] comparing the ion current in different magnetron configuration showed that the ion current was 0.9 mA cm^{-2} in type II unbalanced magnetron system, whilst using the same conditions, it was 0.54 mA cm^{-2} and 0.1 mA cm^{-2} in balanced and type

I unbalanced magnetron system, respectively. In general, the UBM design extends the region of dense plasma and increases ion current at the substrate, allowing high ion-to-atom ratios to be achieved at larger target to substrate distances and, therefore improving coating properties. Figure 2.20 shows the type II unbalanced magnetron design.

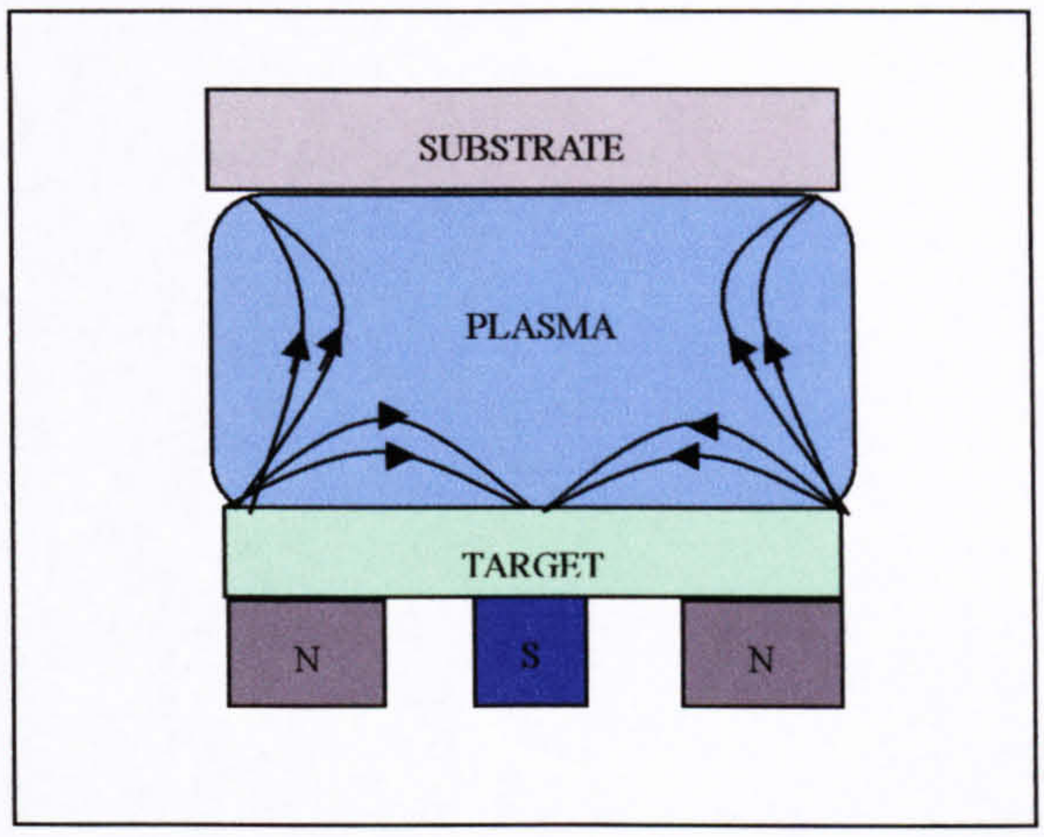

Figure 2.20 Graph of a type II unbalanced magnetron

The Type I configuration was designed by increasing the strength of the inner magnetic array in respect to the outer array, which caused the magnetic field lines to be directed towards the chamber walls rather than the substrate. Very low ion current densities at the substrate were found for this kind of magnetron configuration. In fact, this type of unbalanced magnetron is not often used due to its low deposition rate and low energetic ion bombardment. However, it was found useful for producing porous and chemically reactive films [64]. The schematic representation is shown in figure 2.21.

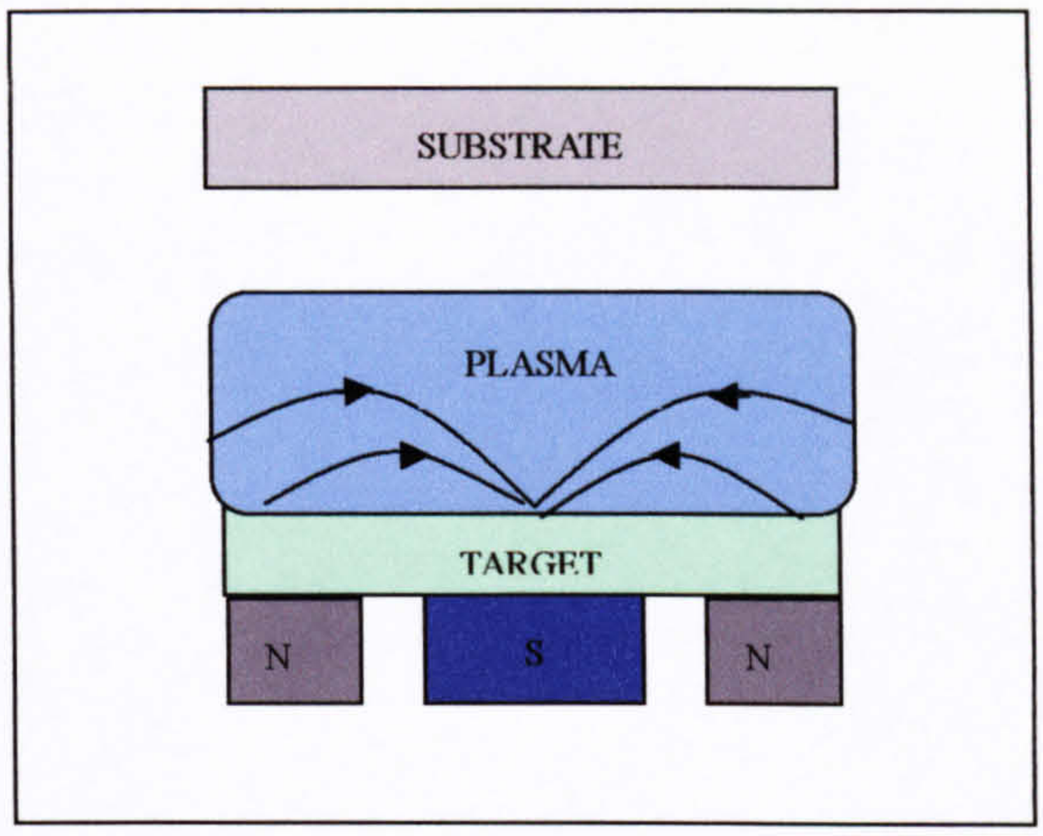

Figure 2.21 Graph of type I unbalanced magnetron

The drawback of UBM design is that it is difficult to deposit a coating with uniform thickness at high deposition rate using a single UBM system. This problem was tackled by developing another magnetron design – the closed field unbalanced magnetron sputtering (CFUBMS) system.

2.8 Closed-Field Unbalanced Magnetron Sputtering

The introduction of multiple magnetron systems [16] — closed-field unbalanced magnetron sputtering (CFUBMS) systems further advanced the magnetron sputtering process. CFUBMS systems normally arrange alternate magnetrons with opposite magnetic polarity; therefore the field lines are linked from target to target. As with UBM sputtering, the film deposited in CFUBMS systems also tend to have dense columnar structures, which can be achieved at lower substrate temperatures. The early work about CFUBMS was begun by Teer Coatings Ltd. [16], and Rohde et al carried out similar work consisting of two unbalanced magnetrons in both mirrored and closed field configurations [66]. Further study and use have being continued by Kelly and Arnell at the University of Salford [17-19]. Two models of the CFUBMS system are shown in figure 2.22 below.

There are a number of factors affecting the ion to atom arrival ratio at the substrate. Varying the magnetron configuration from UBM to CFUBMS is one of them. The ratio could be up to 60 times by changing the configuration from mirrored to closed field [67], which represents the increasing ion bombardment and the amount of energy available. The benefit from that would be modifying film structure and promoting adhesion between the substrate and the film, possibly by diffusion of the film into the substrate. Moreover, the study at Salford proved that zone 2 and 3 film structures could be formed at lower substrate temperatures, without excessive substrate bias or heating.

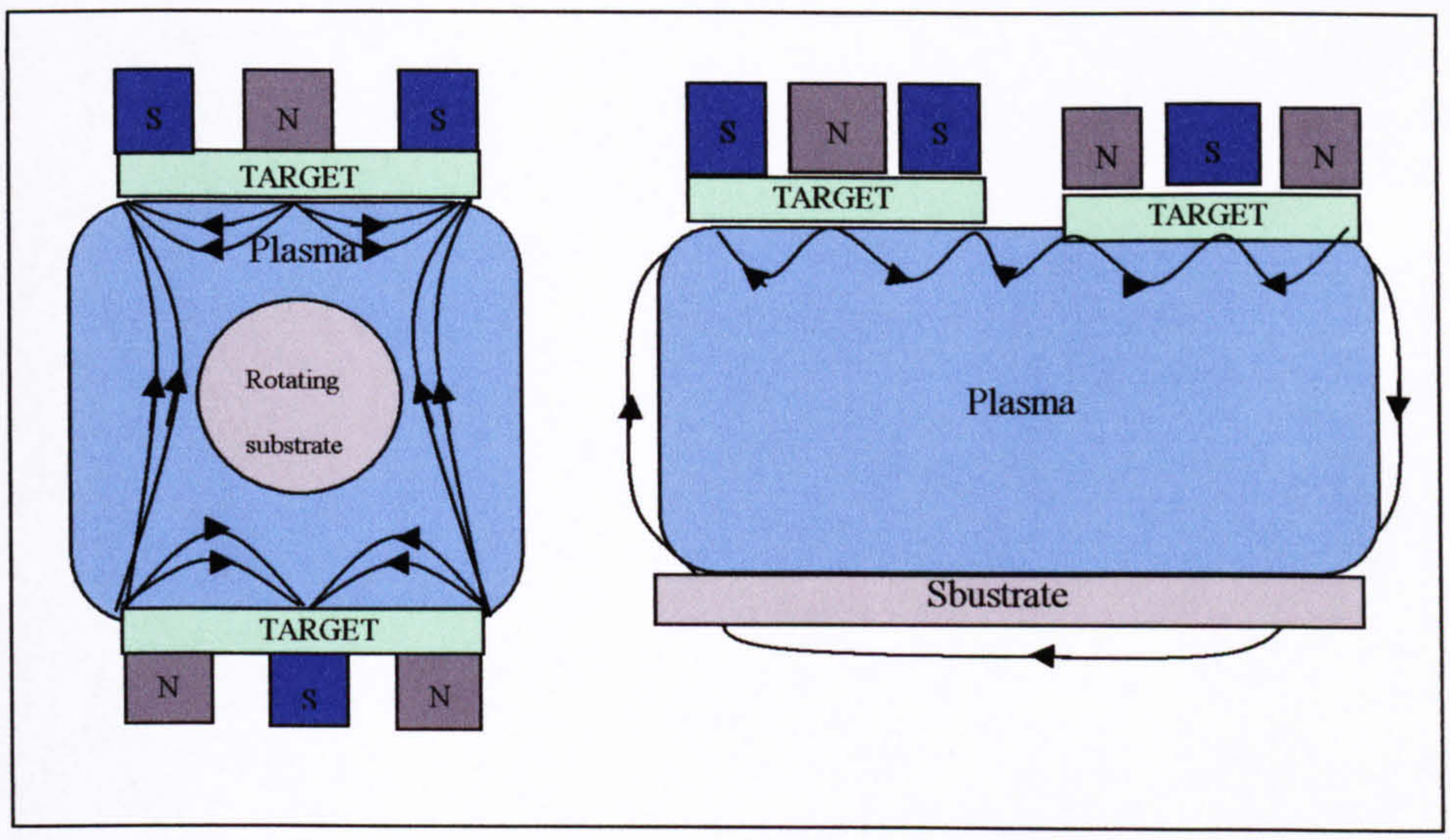

Figure 2.22 closed field configurations –vertically opposed and co-planar.

In summary the sputtering processes were developed by using magnetron, promoted by changing the configuration to be unbalanced, and further improved by the introduction of the CFUBMS system. Also, the development of the sputtering system and configuration of the magnetron made it possible to coat the materials from pure metal to ceramic, the substrate from simple to complex and the coating from single layer to multi-layers, as well as competitive qualities.

3. SEMICONDUCTOR AND TCO COATINGS

3.1 Concepts of Semiconductor

3.1.1 Semiconductor

A *semiconductor* is a substance, whose conductivity is between a conductor and an insulator. Considering the difference between a metal conductor and an insulator, the former has free electrons to respond an applied field easily, the later has too large a band gap for electrons to jump from the valence band into the conduction band. The electrons in a semiconductor have to gain energy, such as from temperature, to overcome the relatively narrow band gap to conduct electricity. Refer to Appendix II.

The reason that a semiconductor can perform a conductive function is that electron and hole pairs exist in it. The number of electrons and holes are same in an intrinsic semiconductor. By adding suitable dopants or impurities, a semiconductor may be called n-type, in which case the number of electrons is greater than the number of holes; or called p-type, in which case the opposite is true - the number of holes is greater than the number of electrons. An *n-type* semiconductor carries current mainly in the form of negatively charged electrons, in a manner similar to the conduction of current in a wire. In a *p-type* semiconductor the charge carriers are positive electric charge holes, equal and opposite to the charge on electrons, of which the flow occurs in a direction opposite to the flow of electrons. The conductive properties of a semiconductor can be changed dramatically by doping.

3.1.2 Free charge carriers and their effective masses in semiconductors

There are several particular technology names in semiconductor physics. The concept of a 'hole' is one of them. In a semiconductor electrons carry out the conduction when

an external electric field is applied as a kind of free charge carriers, which are negative. It is also possible to find vacant states in the valence band at a finite temperature, which contribute to the conductivity of a semiconductor and have the same amount of charge as electrons but positive. The positive vacant states are called *holes* in semiconductor physics.

The holes travel in the same direction as the applied electric field, i.e., the opposite direction to the electrons. Take silicon as an example. Providing that there is a vacant state in the valence band, there must be a bond incomplete, see figure 3.1 (a) [68]. Then one of the electrons is attracted by the vacant state and moves closer to its position when an electric field is applied, see 3.1 (b). This process is going to continue again and again 3.1 (c), so that the electron moves towards the positive end of the solid body and the hole towards to the negative end.

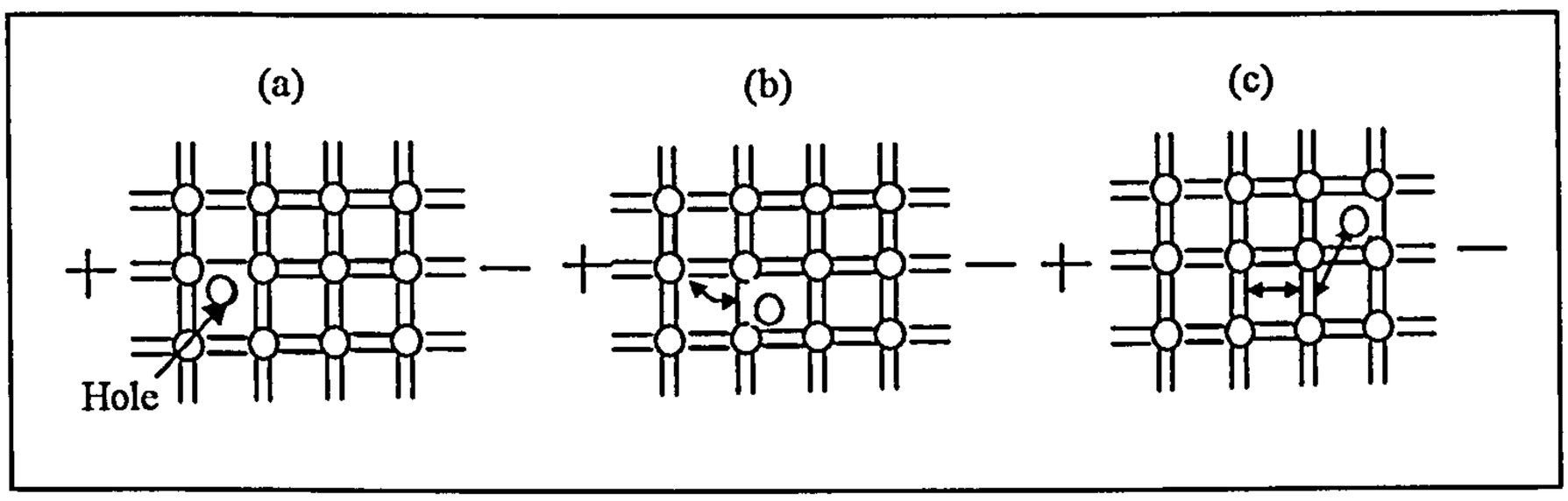

Figure 3.1 (a) A vacant state (or hole) in the valence band corresponds to an incomplete bond. (b) The charge carriers move in an applied electric field. (c) The continuous process.

Another concept in semiconductor physics is the *effective mass*, which is introduced because an electron has a quite different mass in a solid than in a vacuum. It is assumed that an electron in a solid experiences the interaction with other particles, such as ions and other valence electrons, whilst a free electron in vacuum does not. A free electron in a magnetic field will be obliged to move by the magnetic force on the electron corresponding to the following formula:

$$v_c = \frac{B_e}{2\pi m_e} \qquad \text{...eq (3.1)}$$

in which v_c refers to frequency of electrons in vacuum, B_e the strength of magnetic field and m_e the mass of the electron in vacuum. The above formula will never be correct for the same electron in a solid. Then it is suggested that there is a different electron mass, notated as m_e^*, so that the above formula can be used:

$$v_e = \frac{B_e}{2\pi m_e^*} \qquad \text{...eq (3.2)}$$

in which m_e^* is called the electron effective mass.

The electron effective mass, m_e^*, in E-*k* relationship (E, energy of the electron; *k*, momentum of the particle) is defined as $m_e^* = \hbar^2(d^2E / dk^2)^{-1}$ ($\hbar = h / 2\pi$, Plank's constant $h=6.63*10^{-34}$J, d represents the symbol of differential) [69], which is therefore determined by the radius of curvature of the energy curve line at the given level and is the result of the effects of both internal potential and external force. For electrons in the lowest conduction band, m_e^* is positive because the curve is concave.

Let us consider an electron in the highest valence band. Near the convex top of the valence band, the effective electron mass would be negative. In the same way that the concept of the 'hole' was introduced, a positive effective mass, hole effective mass is assigned and can be written as:

$$m_h^* = - m_e^* \qquad \text{...eq (3.3)}$$

when the electron occupies an empty state in the valence band.

It has to be mentioned that the electron effective mass in conduction band is not normally equal to the hole effective mass in the amount in the valence band because

the width of two parabolas are not normally equal.

3.1.3 Intrinsic and extrinsic semiconductors

An intrinsic semiconductor refers to a semiconductor with a perfect crystal structure containing no impurities or lattice defects. In this kind of semiconductor, there are no charge carriers at absolute zero. The electron-hole pairs are generated at a certain temperature as explained in the figure A3 in the Appendix II. If we use n_i to represent the *intrinsic carrier concentration*, n, *the electron concentration* in the conduction band and p, *the hole concentration* in the valence band, it can be said that

$$n_i = n = p \qquad \text{...eq (3.4)}$$

which is the particular feature of an intrinsic semiconductor.

There is a recombination process in a semiconductor to balance the generation of electron-hole pairs. It is possible that when an electron is removed from the conduction band in a direct band-gap semiconductor, that it will recombine with a hole in the valence band [69]. This process is called *direct* or *radiative recombination*, because a *photon* may be emitted as the way to release energy when this transition takes place, refer to Appendix II. The *indirect recombination* process is the common recombination way in an indirect band gap semiconductor, although direct recombination could happen. The indirect recombination will take place when an electron drops into a localized state in the forbidden gap, known as *recombination centre*, and recombines with a hole in the same localized, known as *trapping*, and phonons are given up as the energy form. Figure 3.2 [70] shows the schematic representation of the recombination processes. The recombination process can be very fast, say as short as 10^{-7}s, also slow, say many seconds, depending on the semiconductor. This feature of semiconductors can be used in practice, such as making luminescence long after excitation in some phosphorescent materials used.

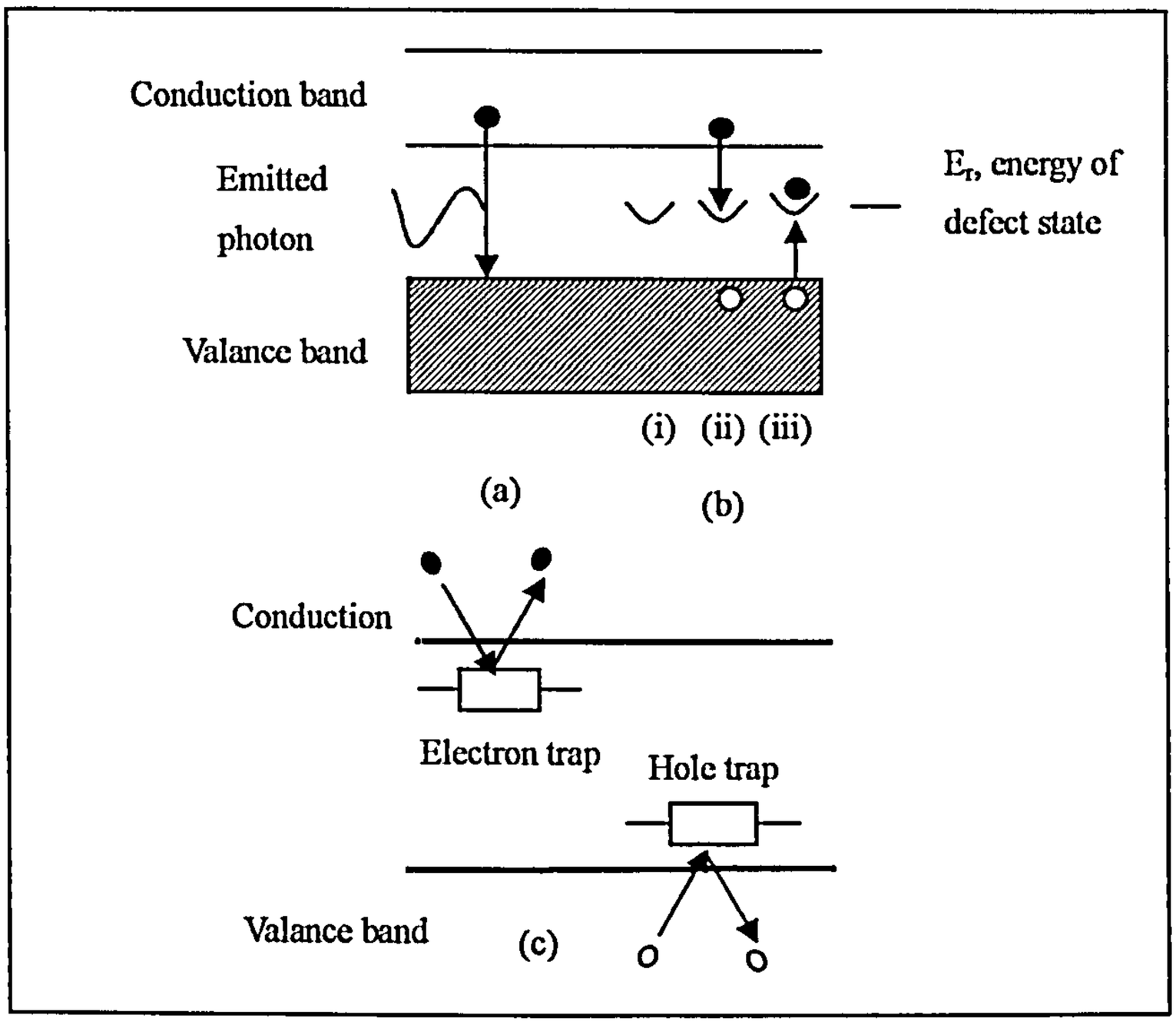

Figure 3.2 (a) Direct recombination, (b) Sequence of events in the indirect recombination process (i) localized state or trap centre; (ii) trapping of an electron; (iii) capture a hole, and (c) Trapping in semiconductors and the electron and hole leaving the centre ready for another recombination.

By adding only small concentrations of a suitable impurity (max. 0.0001%, typically one in every hundred million atoms), the charge carriers in a semiconductor may increase, and this in turn leads to a dramatic change in its conductivity [68]. This semiconductor is called an *extrinsic semiconductor*, the impurity is called a *dopant*, and the process *doping*. If the free electrons are the majority charge carriers, the semiconductor is *n-type*, and the dopant is named as a *donor*. On the other hand, if the holes are the majority charge carriers, the semiconductor is *p-type*, and the dopant is named as an *acceptor*.

How can a semiconductor be made an n-type? Take silicon as an example. A silicon atom has four valence electrons, so impurities from column V in the periodic table such as phosphorus can be used as donors to produce an n-type semiconductor. The phosphorus atoms in the silicon solid are obliged to sit in the position of silicon atoms

and form four covalent bonds. Therefore there is an extra fifth electron weakly bound to its parent phosphorus atom without bonding with any silicon atom. This electron is easily freed, and easily elevated into the conduction band. This means there are more free electrons in the silicon doped with phosphorus, thus an n-type semiconductor is created.

Similarly, by adding impurities from column III in the periodic table into intrinsic silicon, a p-type semiconductor will be produced. Suppose the silicon is doped with boron, the boron atoms will occupy the sites of silicon atoms. Because there are only three valence electrons in the outer-shell of a boron atom, one electron from a silicon atom will not be able to complete a covalent bond. Electrons from neighbouring silicon atoms may move to the boron atom to complete the bonding, which in turn leaves a vacant state in the valence band – an additional hole is created.

3.1.4 Band gap in real semiconductors

In a semiconductor, adding of a donor results in the addition of a new allowed energy state of a level E_d in the forbidden gap, which is slightly underneath the bottom of the conduction band, E_c. At very low temperatures, the extra donor electrons are attached to their parent atoms and accommodated in the E_d energy level. In this case the Fermi energy level (refer to appendix II) is half way between E_d and E_c. Since the donor atoms are relatively far apart (low concentration) and not continuous, they do not affect each other. As the temperature increases to about 100K, the thermal energy is sufficient to be absorbed by the electrons of donors and enable to occupy the conduction band and carry current. On the other hand, the addition of an acceptor into a semiconductor equates to addition of an allowed energy level E_a slightly above the valence band, which in turn puts the Fermi level on the half way at the mid-point between E_a and E_v. Again at temperatures around 100K, the electrons originally in the fully filled valence band are able to transfer to those states in E_a and leave holes behind. Figure 3.3 [71] shows the effect of donors on the semiconductor band gap

energy.

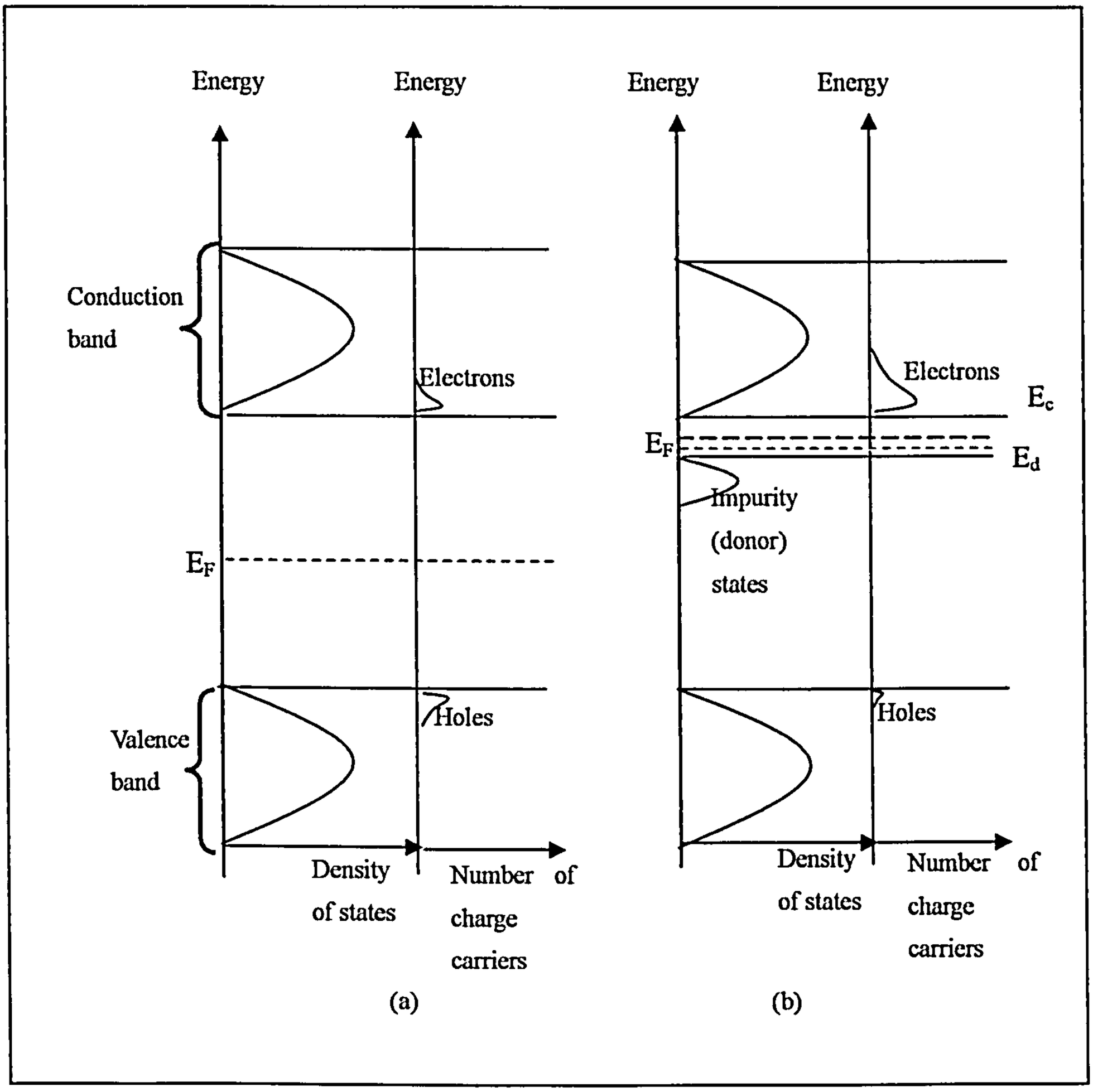

Figure 3.3 the effect of donor on a semiconductor band gap: (a) intrinsic density of states and number of charge carriers versus energy; (b) effect of dopant on the density of states and number of charge carriers versus energy [71].

For the undoped semiconductor the Fermi level is located halfway between the conduction and valence bands. For a low doped semiconductor, depending on n-type or p-type, the Fermi level lies halfway between the minimum conduction band and donor's energy level or the maximum valence band and acceptor's energy level at very low temperature, because the occupation probability of E_d or E_a is 1 and E_c or E_v is 0. By increasing the donor density in a semiconductor, such as tin doped indium oxide, the donor states can merge with the conduction band at a certain critical density,

in turn the Fermi level will be determined by the highest occupied energy level, which is related with the density of charge carriers (e.g. $E_F \propto n_e^{2/3}/m_e^*$ for a n-type, n_e the concentration of free electrons, m_e^* the electron effective mass) [72]. This phenomenon is also known as *band gap widening* or *Burstein-Moss shift,* which corresponds to the increase of the concentration of charge carriers. Figure 3.4 [72] shows the undoped and heavily doped indium oxide energy bands. A shift of the bands is apparent from the figure. E_{g0} represents the band gap energy of undoped indium oxide and E_g that of doped indium oxide. The occupied states are shown in the shaded area in the figure. Moreover, a heavily doped semiconductor is called a *degenerate semiconductor*, because the classic Maxwell-Boltzmann statistics no longer apply to the energy distribution and Fermi-Dirac statistics must be used, which means the continuous increase of the carrier number will finally bring Fermi energy levels into the conduction band, as discussed above.

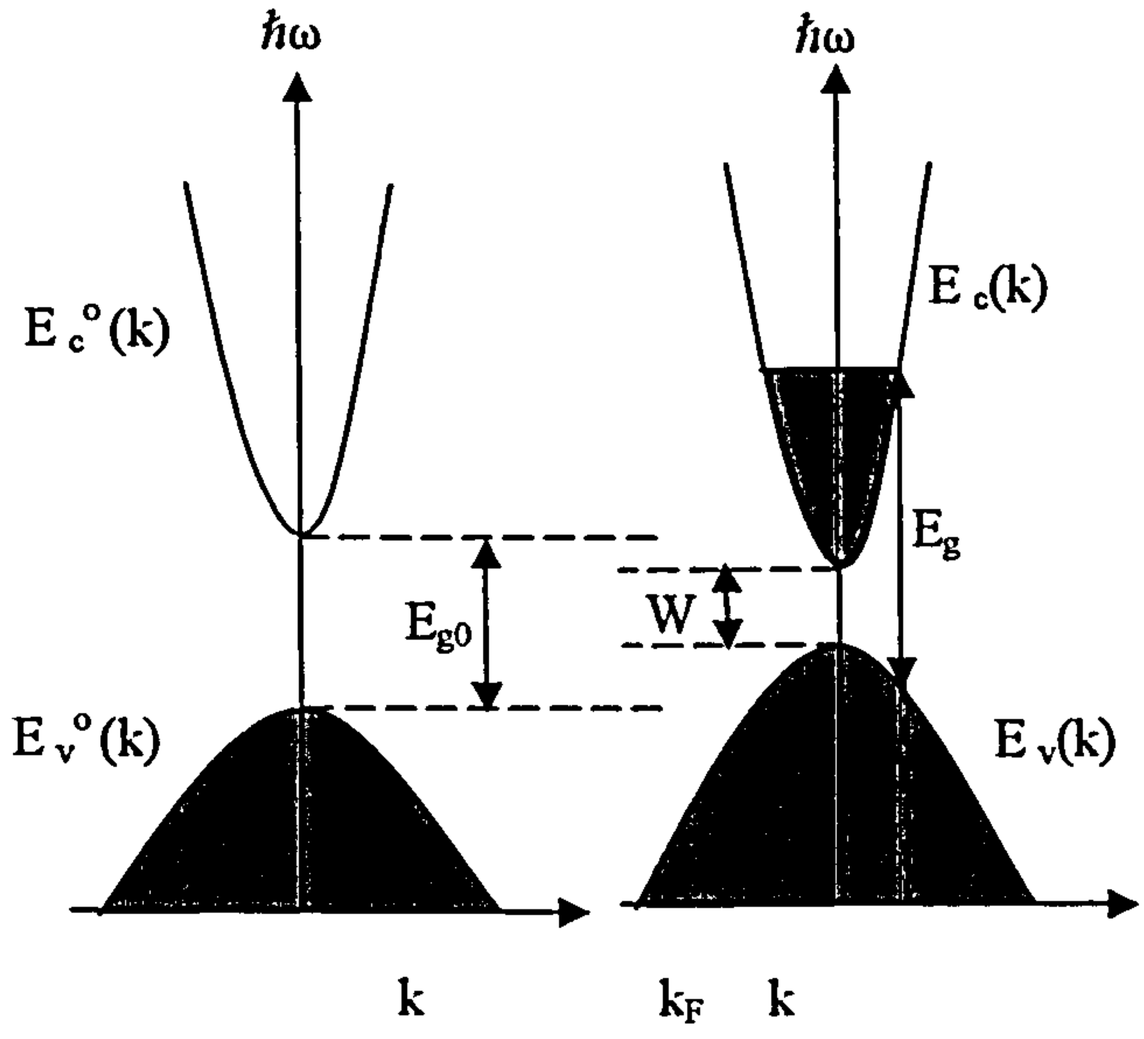

Figure 3.4 (a) The assumed band structure of undoped indium oxide; (b) The band structure heavily tin doped indium oxide [72].

In contrast, another effect of heavy doping in a semiconductor is that the dopant density fluctuates from point to point, which causes band energy fluctuations and distortion of the top of the valance band or the bottom of conduction band – also called *band 'tail'*. The band tail extends the allowed states into the forbidden band

gap, resulting in *band gap narrowing*, see figure 3.5 [73].

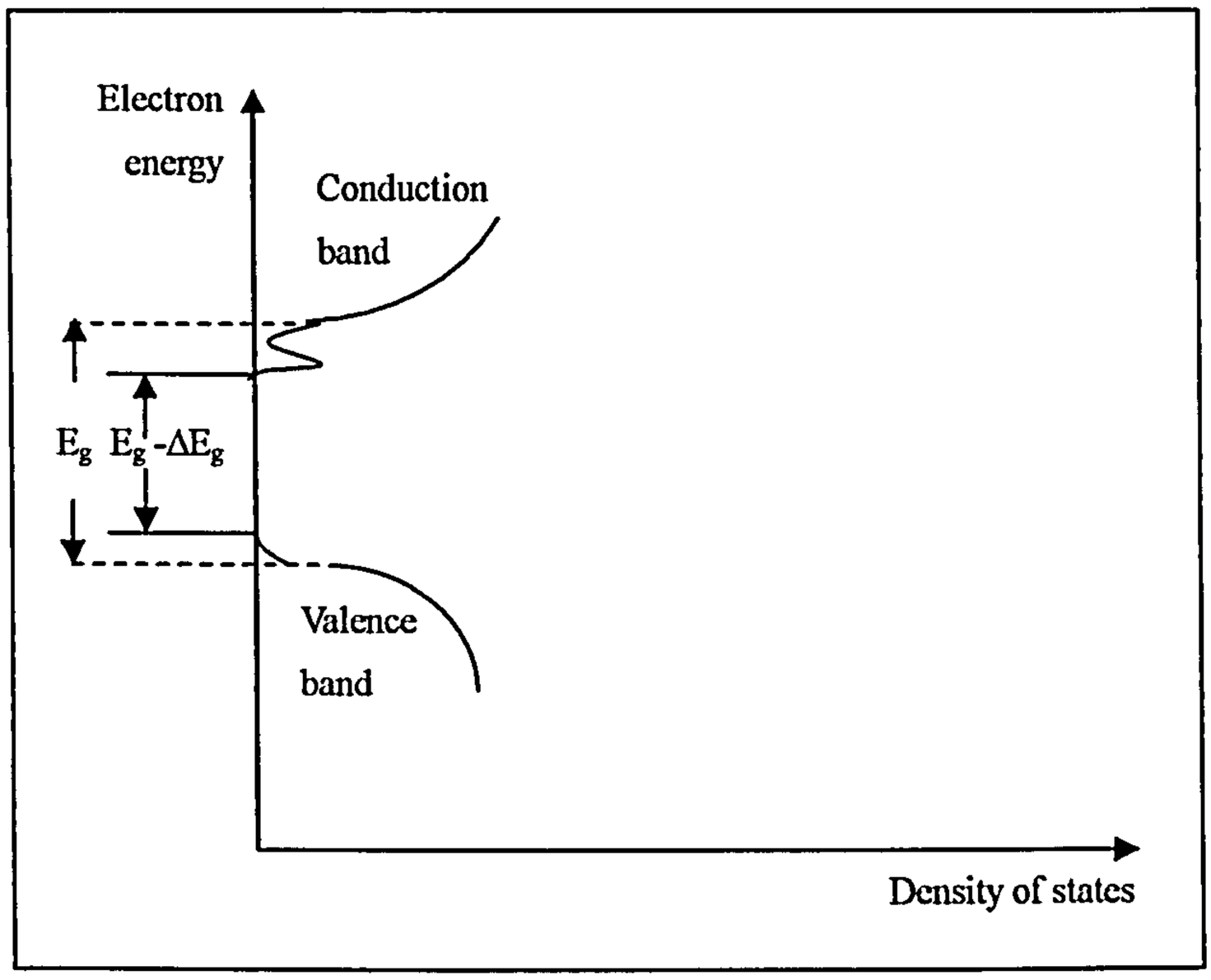

Figure 3.5 the schematic representation of band gap narrowing due to heavy doping level.

3.2 Optical and Electrical Properties of Transparent Conductive Oxide (TCO) Coatings

Transparent conductive oxides (TCO) belong to the group of wide band gap semiconductors, for example zinc oxide with the band gap larger than 3eV[12]. The large band gap of TCO materials contribute to the transparent property in the visible wavelength region, and intrinsic (defects) or extrinsic (dopants) charge carriers donate to the conductivity. The intrinsic charge carriers can be created by lattice defects, for example oxygen vacancies or metal atoms on substitutional lattice sites; and extrinsic carriers by either metal dopants with one additional conduction electron on the metal lattice sites, or halogen dopants with one additional electron on oxygen lattice sites.

There are many TCO materials available, see table 3.1 and 3.2. Among them, indium doped tin oxide (ITO) is currently the most commonly used transparent thin film

material which can be deposited by various methods on glass, polymers etc [12]. In recent years, however, zinc oxide (chapter 3) has emerged as one of most promising materials because of its optical and electrical properties as well as the abundance in nature, which makes it competitive both in practical uses and marketing development [12].

Table 3.1 Properties of some n-type TCO materials [12]

Property	In_2O_3	SnO_2	ZnO
Mineral name	-	cassiterite	Zincite
Band gap E_g(eV)	3.75	3.7	3.4
Melting point (°C)	≅2000	>1930*	1975
Heat of formation (eV)	9.7	6.0	3.6
Density ($g.cm^{-3}$)	7.12	6.99	5.67
Relative permittivity	9	9	8.1
Effective electron mass m^*/m_e	0.3	0.28	0.28
Dopants	Sn, Ti, Zr, F, Cl	Sb, As, P, F, Cl	B, Al, In, Ga, Si, Sn, F, Cl
Crystal structure	Cubic	Tetragonal, rutile	Hexagonal, wurtzite
Lattice parameters (nm)	a:1.012	a:0.474 c:0.319	a:0.325 c:0.5207
Thermal expansion α (300K) (K^{-1})	6.7	‖ c:3.7 ⊥c:4.0	‖c:2.92 ⊥c:4.75
Property	In_2O_3	SnO_2	ZnO
Melting point of the metal (°C)	157	232	420
Average amount of the metal in the earth's crust (ppm)	0.1	40	132

** Decomposition into SnO and O_2 at 1500 ℃.*

Table 3.2 Other types of TCO materials

Multi-component TCO materials		p-type TCO
Components of materials	Combined n-type TCO	
CdO, SnO_2, ZnO, In_2O_3, Ga_2O_3 and Y_2O_3	In_2O_3-SnO_2-ZnO (ZITO), In_2O_3-SnO_2-Ga_2O_3 (GITO), In_2O_3-SnO_2-Y_2O_3, ZnO coated-SnO_2 $MgIn_2O_4$, $CdGa_2O_4$, Cd_2SnO_4, $CdSnO_2$, $CdSb_2O_6$:Y, Zn_2SnO_4, $ZnSnO_3$, $Zn_2In_2O_5$, $ZnGa_2O_4$, $In_4Sn_3O_{12}$ $GaInO_3$,	$CuMO_2$ (M = Al, Ga, Sr, and Ln = lanthanides;) in which Cu acts as dopant. Or M_2O_3:Cu In_2O_3:Ag ZnO: (Ga and N) (co-doped)

3.2.1 Optical properties of TCO coatings

For metals, when incident light strikes the surface, electrons are excited and move to higher energy levels where they undergo collisions with lattice ions, and the extra energy is dissipated in the form of phonons. Then the lattice is heated, which is called absorption. The emission occurs and the light is reflected when the electrons drop back to a lower energy level. Transparency in some relevant portion of the electromagnetic spectrum is the essential common feature of dielectric optical materials, because the bonding characteristics ranging from ionic to covalent are represented in these materials, which means the energy from some part of spectrum can not be absorbed by overcoming the band gap energy and therefore is transmitted through. Also, the optical transmission is limited again when wavelengths become longer because the absorption occurs due to the vibration of lattice ions in resonance with the incident radiation.

Transparent conductors are an interesting class of materials, which exhibit both optical properties of metals and dielectric materials. The most prominent feature of transparent conductors is the significant change in absorption at the *cutoff wavelength* λ_c. For wavelengths larger than λ_c, they show transparent properties because no electrons can be excited to higher energy level. However, electrons can be stimulated into the conduction band when wavelengths are shorter than λ_c, then they behave like metals. With the same principle of band gap energy, E_g, the cut-off point ($\lambda_c = 1.24 / E_g$, in which λ_c in the unit of μm and E_g in eV) can moved to shorter wavelengths with increasing of number of carriers, see the formula: $\lambda_c \propto m_c^*/N^{2/3}$.

Another interesting feature of transparent conductors is the decrease in the optical transmission in the infrared due to collective plasma oscillations of the conducting carriers — anions and cations. A term introduced here is *plasma wavelength,* λ_p, which corresponds to the plasma frequency ω_p ($\omega_p = 2\pi c/\lambda_p$) when optical properties change radically. The relationship between λ_p and carrier concentration can be expressed as $\lambda_p \sim (m^*/N)^{1/2}$, in which N is the carrier concentration and m* is the effective mass of the charge carrier [40, 74-75]. When $\lambda > \lambda_p$, the film exhibits reflectance properties, whereas at $\lambda < \lambda_p$ the high transparency occurs. However, λ_p moves to shorter wavelengths with the increase of carrier density or concentration.

In general, transparent conductors show transparent properties in a certain region of the spectrum; they exhibit metal-like reflection in the region of wavelength shorter than λ_c and longer than λ_p. The λ_c and λ_p of transparent conductors depend on the carrier concentration in the conductive band and IR regions, respectively.

The index of refraction (n) and absorption coefficient (k) [refer to appendix II] of a semiconductor can be affected by the film structure and deposition processes. For many applications, it is important to have films with higher refractive index and lower absorption coefficient in the visible range; high transmittance is essential as well. The

values of n in films normally are lower than those in bulk because n increases with the increase of the density, which is commonly greater in bulk than in thin films. The packing density P for an optical columnar film is about 0.907, assuming a columnar grain structure with an array of close-packed cylindrical columns of identical diameter. P is lower in unevenly contracting columns and larger when columns expand into a hexagonal shape. For deposition processes, the substrate temperature has an important effect on n. Apart from the influences of purity of the target, cleaning of the substrate and controlling the atmosphere etc., the value of n increases as the substrate temperature is raised. Also, deposition rate, pressure and can strongly influence it. In general, the refractive index of the film increases if a dense, even columnar structure can be formed under the deposition processes.

3.2.2 Electrical properties of TCO coatings

The conductivity of a semiconductor comes from the energy absorbed by electrons when light or photons strike it and cause the carriers to transit between the valence and conduction bands. The special spectra of light with energy larger than E_g or wavelength shorter than λ_c can be absorbed or emitted by the semiconductor and contribute to the conductivity.

The resistivity or sheet resistivity, ρΩcm or R Ω/□ ($\rho = R / d$, d represents the thickness of the film, refer to chapter 5), of a conductive material is contributed to by various electron scattering processes [72]. One factor that affects resistivity is electron collisions with vibrating atoms, which are displaced from their equilibrium lattice position. Impurity atoms, defects and grain boundaries are the other factors that affect the resistivity by locally disrupting the periodic electric potential of the lattice. This means the resistivity can become lower with a higher degree of crystallinity (more periodic lattice), smaller crystal peak shift (equilibrium lattice position), and larger grain sizes (fewer grain boundaries). Also, the resistivity of a semiconductor can be decreased markedly by adding some impurity atoms together with suitable post

treatment, because they provide free high mobility electrons. The result is a merger of the impurity band with the host conduction band forming a free electron gas, which culminates in a significant change in the band states, Burstein-Moss or blue shift [76]. The shift energy, the distance of the Fermi level from the bottom of the conduction band, can be expressed as $\Delta E \propto N^{2/3}/m_c^*$, in which N represents the number of charge carriers, and m_c^* the electron effective mass.

3.2.3 Dopant functionality in TCO coatings

The main function of dopants in TCO coatings studied in this project, is as impurities in semiconductors to provide charge carriers by substitution on the lattice sites of the metal atoms or oxygen atoms. As Al-doped ZnO will be the main oxide semiconductor studied in this project, it will be taken as the example in the following description. Dopants for Zinc oxide can be divided into two groups: metals and halogens. Studies of the effects of different dopants in zinc oxide coatings, such as Al, In, Ga, Cd, Sn, Sb, V, Mg, F and S have been published [5, 77-83]. Also, it is widely believed that the conductivity, transparency (cut-off point) and stability of the coating are very sensitive to the amount of oxygen and the concentration of dopants in the films. The mechanism of dopants contributing to the conductivity of a semiconductor is by providing the charge carriers. The charge carriers are introduced when impure elements (or dopants) substitute on the lattice sites, providing extra electrons. In zinc oxide, the metal ions of dopants normally replace the ions of zinc and extra electrons are produced. But the metal dopant ions also tend to combine with oxygen to form oxides instead of substitutional lattice sites of zinc ions if excess oxygen is supplied. As a result, the mobility of charge carriers is decreased and resistivity becomes higher. On the other hand, oxygen deficiency may create dangling bonds in the semiconductor, and the charge carriers are trapped by localized states in the forbidden band, therefore the mobility of charge carriers is reduced. The ions of halogen dopants replace the oxygen ions in the zinc oxide lattice, rather than taking the places of zinc ions. They contribute electrons, reducing the resistivity. Another advantage of

halogen elements is they do not react with oxygen, which may mean that the amount of oxygen present will not require strict control.

It has been proved by Ellmer and his colleagues [12] that the electrical properties of zinc oxide films depend on the crystallographic perfection (grain size, strain) of the films. Larger grain sizes and lower strains decrease the boundary energy of a crystal material, therefore leading to higher mobility of the charge carriers. The size of the impurity ions can also, therefore, influence the resistivity. Dopant ions of similar size to zinc or oxygen are able to avoid lattice distortions, this minimising film stresses. However, the amount of dopants should be limited in the films, because the ions of dopants tend not only to substitute host ions, but also to take up interstitial positions, distorting the crystal lattice. Higher strains increase the potential barrier between the grains, leading to lower mobility of the charge carriers.

Additionally, dopants in the film can make the transparency line shift to higher energies of the band gap, which is correlated to the increase of the carrier concentration [74] – Burstein-Moss shift. This is also in conformity with the study of Al-doped zinc oxide in this project. This blue shift can be useful for some electric devices, such as emission displays [84].

Another effect of dopants is on the stabilization of the properties of coatings. The mechanism of dopants to decrease the resistivity and enlarge the band gap energy of TCO coating is to provide extra electrons by substitution on the host lattice sites, which is much more stable than the deficiency of oxygen because there are more metal atoms in the film, which tend to be re-oxidized in the oxygen atmosphere, resulting in higher resistivity.

3.2.4 Doped zinc oxide coating

Zinc Oxide is a ceramic material with wurtzite crystallinity. Zincite, the mineral name

of zinc oxide, is known for its very rich storage in the earth's crust, which makes zinc oxide easy and cheap to be obtained. The properties of zinc oxide can be referred from the beginning of section 3.2 in table 3.1.

Zinc oxide coatings can be prepared by many deposition techniques, such as thermal evaporation [85], chemical vapour deposition (CVD) [86], chemical spray [82], sol-gel [1], electron beam evaporation [87], pulsed laser deposition [88] and magnetron sputtering [89-93]. The optical and electrical properties of TCO coatings depend on the film composition, structure, crystallinity, defect density, surface roughness and dopant concentration [3, 94-95]. These properties are, in turn, strongly dependant on the deposition processes, or parameters. The new development tool of pulsed magnetron sputtering from powder targets has been used in this project to produce high quality TCO coatings.

During magnetron sputtering, there are three key parameters that must be controlled. Firstly, the control of the doping materials and their amount in the target gives the possibility of achieving lower resistivity due to electrons provided by the substitutional effect of dopants in the zinc oxide. Secondly, the deposition atmosphere, especially the concentration of oxygen, must be controlled. The resistivity of zinc oxide films varies with the amount of oxygen in the plasma. Oxygen deficiency in the films may cause a decrease in transparency and an instability in the resistivity of the coatings due to the trend of rich zinc atoms combining with oxygen when exposed in air or suitable atmosphere, reducing the mobility of free electrons. An excess of oxygen during or after the deposition will cause a loss of the substitutional effect of dopants on the lattice sites (the carriers mobility decreases due to oxidization of the metal dopants). Finally, the temperature of the substrate and the flux and energy of particles incident at the substrate will also influence the properties of zinc oxide coatings. Following deposition, the properties of the films can be further modified by annealing treatments under conditions of varying time, temperature and atmosphere.

Magnetron sputtering can be driven by DC, pulsed DC, MF or RF power supplies. For the deposition of doped-zinc oxide coatings, in the DC case, the commonly used commercial method is reactive magnetron sputtering of alloyed metallic targets [2, 12, 105 and 107]. Although some research [93, 136 and 158] claims that ceramic zinc oxide and alumina targets, sintered in nitrogen and hydrogen or argon above 1000°C, were used. For the RF case, sintered ceramic targets are the common route, because RF power supplies are able to sputter ceramic targets without arcing problems [3, 87 and 92]. MF or AC power supplies are also used in reactive magnetron sputtering, especially in large area commercial industries [4, 90, 159-160]. Also, Jin and Hamberg in their research [105] combined RF and DC power supplies in a double magnetron sputtering process to produce the ZnO:Al thin films, in which the zinc oxide ceramic target was connected to a RF supply and a metallic aluminium target was connected to a DC supply. In most cases, the Al-doped zinc oxide thin films were found to have resistivities in the order of $10^{-2}\Omega$cm to $10^{-4}\Omega$cm, and transmittances of 80-83%. In one exceptional case, Chang etc. [94] reactively sputtered a metallic target using a RF supply, but the results showed no significant differences, compared to those from the above examples. The doping concentrations studies in all the cases referred to here varied from 1 – 10 at%, and within this range, it has been claimed [90] that 3-5at% doping concentration gives the optimum electrical and optical properties.

In reactive sputtering, the main effort was paid on the control of the partial pressure of the reactive gas. Research by Von Ardenne Anlagentechnik [159-160] showed that the possible process window for obtaining enhanced deposition rates with good TCO properties during the reactive sputtering of ZnAl alloy targets was much narrower than that for metallic zinc targets, and at low target powers a low partial pressure of the reactive gas was necessary. To avoid the complicated processing in reactive magnetron sputtering, RF power supply becomes a good choice to sputter the ceramic targets.

Apart from the doping concentration and the partial pressure of reactive gas, there are another two ways in magnetron sputtering to achieve the desired electrical properties: control of the substrate temperature; and control of the post annealing process. For example, substrates have been heated up to 250°C to 500°C before deposition [90, 92, 94], and ZnO:Al thin films have been post annealed at above 400°C for 1-2hours in controlled atmospheres, such as vacuo, or mixtures of nitrogen and hydrogen gas [3, 87].

Most studies of ZnO:Al thin film are on glass substrates [90-94], although reports of the use of polymeric/organic materials [106] and silicon wafers [161] as the substrate were given. In the polymer case, the resistivity of the ZnO:Al films were only about $3.6\times10^{-2}\Omega$cm with an average transmittance of 83%. The reason for the relatively high resistivity was that the temperature of the substrate had to be controlled no higher than 150°C and no post annealing process could be performed. The properties of the films on silicon wafers were comparable to those on glass slides. Care had to be taken when the silicon was used was that the initial deposition power had to be low to minimise the surface damage on the silicon wafer due to energetic particle bombardment from the plasma.

Not many researchers report the use of pulsed DC power in the magnetron sputtering processes, which may be because this is still a relatively new technique in laboratory and industrial use. One report from the Journal of the Korean Ceramic Society in 2004 mentioned the use of pulsed DC power in the production of ZnO:Al coatings. Another, by Delahoy etc. [162], claimed that the features of the method were high plasma density, high deposition rate, arc-free operation, easy and controllable deposition of insulating materials, etc. Therefore, the combination of pulsed DC, closed magnetic field and powder targets appears to be a new tool in the magnetron sputtering processes.

It is well known, and has already been demonstrated in this project (refer to chapter 8),

that doping zinc oxide with aluminium can change the optical property (enlarge the band gap energy) and improve the conductivity (decrease the resistivity after suitable post-treatment). For example, the resistivity of Al-doped zinc oxide films decreased to the order of $10^{-3}\,\Omega\,cm$ compared to that of pure ZnO film ($1.4x10^{-1}\,\Omega\,cm$) after annealing under a pressure of 10^{-5} mbar, at a temperature of 470℃ for 2 hours, although both as-deposited pure ZnO and Al-doped zinc oxide coatings deposited under argon and oxygen atmosphere are insulating before the annealing treatment.

The details above concentrated on aluminium doped zinc oxide coatings. In practical uses, a wide range of dopant materials can be chosen dependent on the applications. The functions of different dopants in zinc oxide are various, which depend on the applications of the doped zinc oxide. For example, ZnO:Er thin films are used for a blue luminescence [96]; Al, In, Cu, Fe, Sn and Sb are used as dopants in ZnO films for sensors [97-98]; Cu and N co-doped ZnO are used as a p-type TCO [99-100]. Also, Ga [31, 77, 101], In [102], F [82], Se [103] and V [81] elements have all been studied as dopants in zinc oxide films, in addition to the wide investigation of Al as a dopant [4, 104-106].

There are many kinds of applications for ZnO coatings, which are related to different principles. For instance, ZnO coatings used in photoluminescence (PL) detectors or emission displays utilizing the higher PL intensity or band edge emission at the wavelength of about 380 nm when laser light with the wavelength of 351 nm comes through the photomultiplier tube detector [86-88]. Zinc oxide films can be used in ozone sensors because they exhibit conductive sensitivity by changing resistivity by several orders of magnitude after exposure to an ozone atmosphere [107]. The high reflectance function in the range of infrared wavelengths of ZnO is an important property for architectural and automotive applications. ZnO piezoelectric coatings used in an optical fibre laser were also reported recently [108, 163]. Zinc oxide coatings, as transparent conductive oxides, are mainly used as electrodes in solar cells, or in displays, such as cathode ray tubes (CRT), liquid crystal displays (LCD), thin

film transistors (TFT) and plasma display panels (PDP), etc [109]. As a TCO coating, zinc oxide has the dual roles of acting as a window layer and as an electrically conducting contact layer. Figure 3.6 shows a typical application of the ZnO coating acting as a transparent conductive oxide.

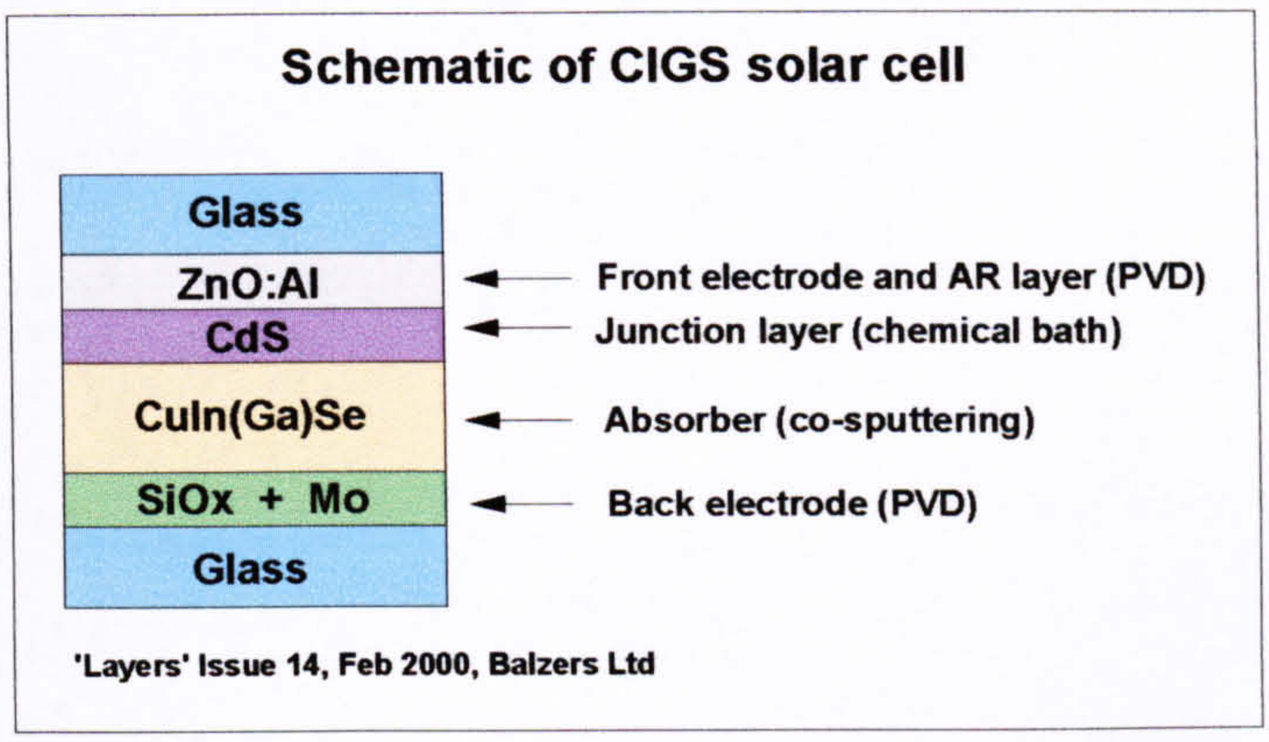

Figure 3.6 Typical application of TCO coatings

3.2.5 ITO and multi-component TCO coatings

Tin-doped indium oxide (ITO) coatings are the most widely used transparent conductive oxide coatings in applications, such as optoelectronic components, photovoltaic solar cells, flat panel displays and electroluminescent devices [1,105, 121-123], which have been studied for more than forty years [110]. The preparation techniques include DC, pulsed DC and RF magnetron sputtering [112-118], evaporation [119-120], sol-gel [1, 121], CVD [122] and spray pyrolysis [123], ect. Post-annealing treatments e.g. thermal heating [115], electron plasma annealing [124] and excimer laser annealing [125], and various annealing atmospheres [1, 123-124] have also been studied. The optical and electrical properties of ITO coatings are sensitive to process parameters and depend on control of film composition, structure, crystallinity, defect density, and dopant concentration [126-128], which were proved in this project.

Both alloy metallic [114, 126] and ceramic [112, 125] targets were used in DC and

MF magnetron sputtering. The doping concentrations of the targets varied from 3-14at%, with about 5at% Sn doping proving to be optimum [125] to obtain the desirable properties of the coatings. May compared metallic and ceramic targets, DC and MF powers and single and dual magnetron configurations in her work [114]. The coatings had maximum transmittances of 89% and resistivities in the order of x $10^{-4}\Omega$cm. There was no need to heat the substrate when a metallic target was used, but post annealing under controlled atmosphere, such as in vacuo, was required. The best result was obtained by DC/DC sputtering the ceramic targets with the substrate pre-heated to about 300°C. This resulted in coatings in which the resistivity was slightly lower than those obtained by MF sputtering. The advantages of using ceramic targets were high deposition rate and no post annealing or reactive gas control was required. Also, it was proved that the dual magnetron sputtering produced the coatings with the most uniform properties.

ITO coatings have also been produced by using RF power supplies and ceramic targets [115-116]. As above, either heating the substrate or post annealing was required to achieve the low resistivities of the coatings. The lowest resistivities of ITO coatings could be in the order of $10^{-5}\Omega$cm, but more commonly $10^{-4}\Omega$cm, with transmittances of 80-85% [110]. Pulsed DC power supplies have also been reported for sputtering ceramic targets to produce ITO coatings [113], but this work was only begun recently.

Besides commonly used glass, polymers were also used as the substrate [115]. Due to the restriction of the operating temperature, the resistivities of the coatings were still too high, such as 250 Ω/□ to be practical applications.

There are many factors affecting the properties of the films, such as oxygen partial pressure in the plasma, power supplied to the targets, substrate temperatures, annealing treatments, even the thickness of the films, etc. The studies Morikawa and his colleagues [124] showed that tin in amorphous films was not only unable to

provide free charge carriers, but also contributed to scattering of the carriers, which led to an increase of the resistivity. Tin atoms were ionised in crystalline ITO films, which provided free charge carriers to reduce the resistivity of the films. Another interesting study [164] showed that the resistivities of ITO coatings decreased as the substrate temperatures increased, and the power from DC supply decreased. HO-Chul Lee etc. [165] showed in their study that the carrier concentration increased and mobility decreased as the thickness of the film increased. The resistivity of the film increased rapidly when the thickness of the film was below 50nm [110].

Recent studies of ITO coatings have gone deep into theoretical understanding [128], although this understanding is still limited. The review by Granqvist [128] stated that three s-like symmetry impurity bands may be formatted when a tin atom replaces an indium atom, and one of these bands overlaps the conduction band of indium oxide, in which the Fermi level of ITO is located. That is the reason of the free-electron-like properties of the ITO film. Also, the substitution of tin atoms did not change significantly the shape of the density of states around the bottom of the conduction band, which meant that the electron scatterings did not serious affect the resistivity of the film.

Recently, Minami et al, used magnetron sputtering to study a new family of transparent conductive coatings using ternary compounds ranging from multi-component zinc oxide and indium oxide to zinc, tin and indium oxide, magnesium and indium oxide, gallium and indium oxide etc. [5-11]. Naghavi et al, also, investigated multi-component zinc and indium oxide coatings, this time using pulsed laser deposition [129-133]. Toshihiro Miyata et al [81, 134-136] reported on TCO coatings doped with multiple materials and prepared by a variety of deposition techniques. It is believed that the structures and properties of these ternary-compound films can be controlled by varying their compositions.

The effects of the different co-dopants varied. For instance, the chemical stability of

Al-doped zinc oxide coating could be improved by using Cr or Co co-dopants. Sn and Zn doped In_2O_3 coating exhibited good electrical, optical and chemical properties. $(Zn_2In_2O_5)_x$-$(MgIn_2O_4)_{1-x}$ multi-component oxide thin films showed stable sensitivity as gas sensors, which could be controlled by altering the composition. Moreover, the preparation of multi-component oxides such as $Zn_2In_2O_5$ –$In_4Sn_3O_{12}$ were reported as well [137].

4. THE POWDER RIG

4.1 Design and Commissioning of the Rig

The distinct characteristic of the so-called powder rig is that, instead of conventional solid plates, powders or mixtures of powders can be used as targets without the need for further processing. Powders can be mixed according to the requirement of composition by blending appropriate quantities in a rotating drum for several hours. Then a single composition powder or the mixture of several different kinds of powders is evenly distributed across the surface of the copper backing plate on the magnetron to form a target – the 'powder' target. Although sintered powder targets have been used elsewhere [135-137], the author has not found any references to other researchers using powder targets prepared in this way. The reasons for adopting this technique are that they can offer many advantages over solid targets for certain applications.

Firstly, the use of powder targets can be more convenient and cheaper than that of solid targets. For example in solid targets, only a small amount of the target material is consumed – the 'racetrack' area – before the target must be replaced. Sintered ceramic targets also have a disadvantage that they can be quite delicate and fragile and may crack under a high sputtering power, thus limiting deposition rates. Also, the processes of sintering targets are expensive and require long lead times. The introduction of powder targets solves these problems. The powder can be re-spread again and again after sputtering, therefore the target material is used more efficiently, and the mixing process for powder blends is much easier than that of sintering, and more convenient to obtain the targets.

Secondly, the powder target can be a very useful tool for seeking an optimum

composition of coating materials to pursue the optimum combination of coating properties. Because it is easy to mix the blends and form the targets, the compositions of the targets can be changed very conveniently. Therefore, there is no need to order many different target compositions to complete an experimental array. It is only necessary to order the main powder materials and mix them together in the appropriate quantities according to the required compositions or atomic ratios of the powders. In this project, five dopant materials were selected and each was used at three doping levels, covering the doping range presented in most of the public literature [3, 85, 90-95]. If conventional solid targets had been used, 23 targets with different compositions would have been required to be ordered or manufactured by sintering. When forming the powder targets, the powders were blended to the desired doping level, mixed in a rotating drum for several hours and then spread on the backing plate as targets. Not only doped ZnO runs but also the tin-doped indium oxide (ITO) runs and multi-component runs are good examples of the use of powder targets to select the optimum coating compositions.

4.1.1 The design of the powder rig

The rig was built specifically for use with powder targets. Therefore, the magnetron in this system was designed to face upward in order to hold the loose powder as a target. Pictures 4.1a, b and c show the targets in on-work (sputtering) situation, off-work (target changing) situation and the micrograph of the powder blend's surface of a target respectively. A powder or powder blend can be spread evenly over the magnetron backing plate, which was recessed to a depth of approximately 2mm, then gently tamped to form a target with an even, smooth surface. The upward facing magnetron was unbalanced with the strength of outer north ring stronger than that of inner south pole. Another dummy magnetron containing only an outer ring of south magnets was positioned directly above the unbalanced magnetron, which in turn formed a closed magnetic field around the substrate holder. High field strength rare earth magnets were specified for both magnetrons, with a maximum field strength of

2.2kG at the target surface in the unbalanced magnetron.

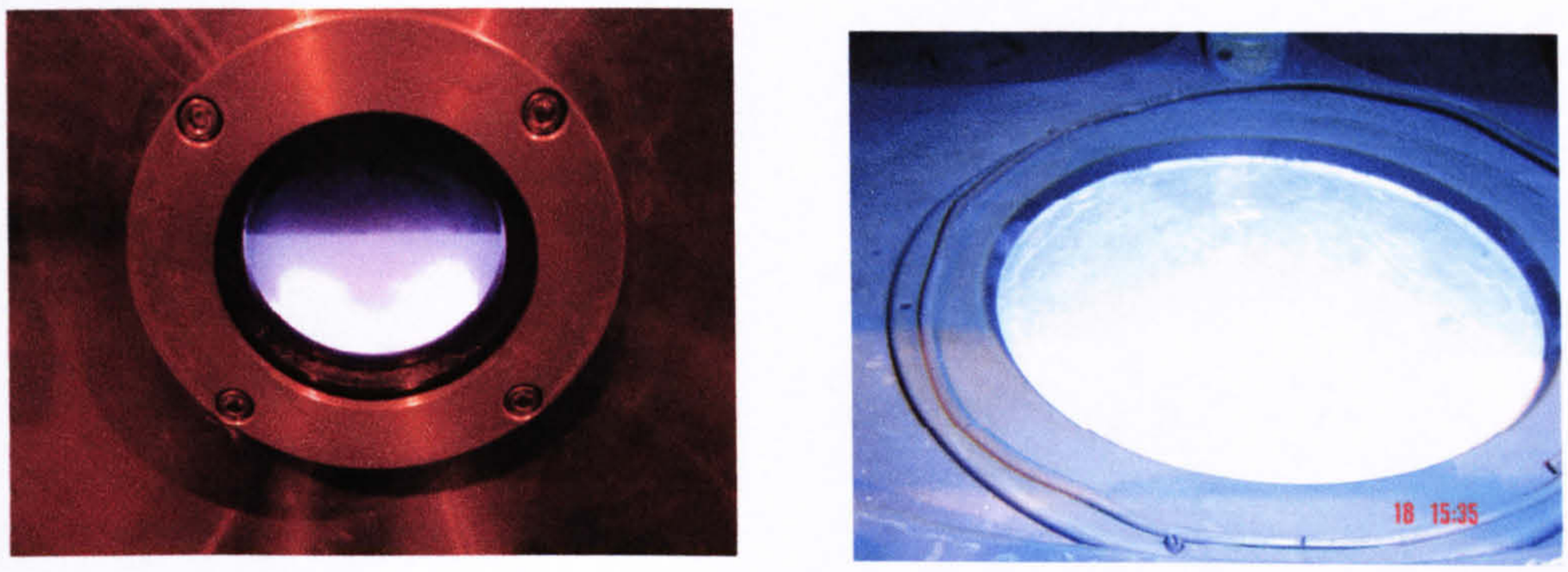

(a) on-work target (b) off-work target

(c) ZnO-4wt% Al_2O_3 powder blend for use in target production (SEM)

Picture 4.1 the macro- and micro- graphs of the powder targets

The substrate holder was positioned above the target, and could be adjusted to allow the optimization of the substrate position within the plasma in the range from 50mm to 250mm above the target. All of those were mounted in the chamber.

The chamber, originally a Nordiko 255 system, was fabricated from stainless steel and had dimensions of approximately 750mm diameter x 325mm deep. The top and bottom plate were made from aluminum alloy and attached by high tensile cap head screws. A 500mm x 290mm rectangular door in front of the chamber allows access to the chamber. The bottom plate is provided with three 180mm diameter ports, one of which was used for installing the magnetron, and an outlet port to the diffusion pump. The top plate is provided with three ports of 160mm diameter (the one directly facing the magnetron port on the bottom was used to mount the dummy magnetron), and two

of 50mm. One of these ports was used to mount the chamber Pirani and Penning gauges, and the other for the Baratron gauge. Picture 4.2 gives a general view of the rig.

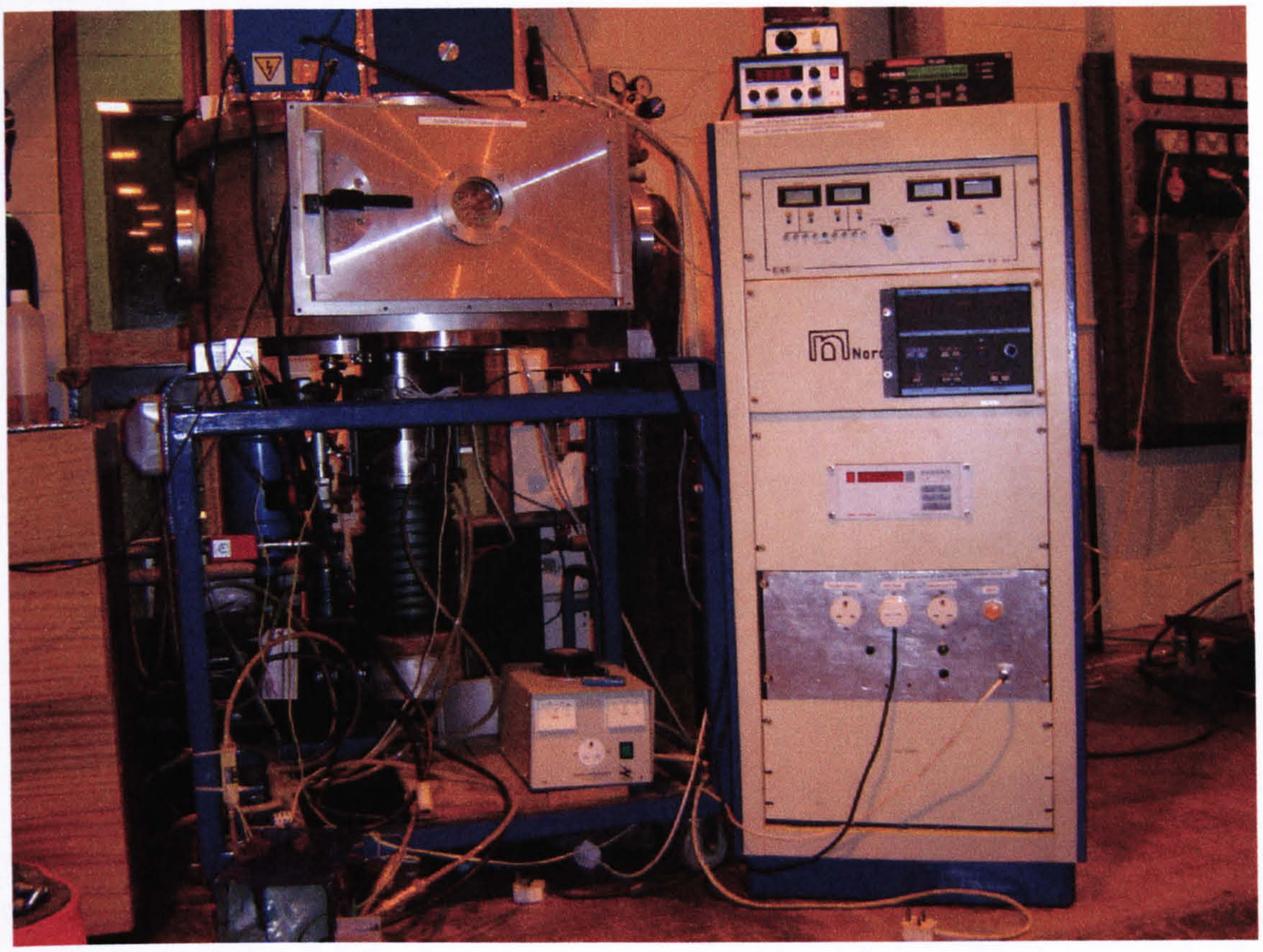

Picture 4.2 the general view of the powder rig in the Surface Engineering Lab in the University of Salford

The schematic pumping system can be seen in figure 4.1 [138]. In the system, a Varian VHS 250 diffusion pump is backed by a Leybold Trivac-60A rotary pump, which work together and allow the system to be evacuated to the pressure lower than $1x10^{-5}$mbar or 10^{-3}Pa. The working range of the Pirani gauge is pressures above $5x10^{-3}$mbar or 0.5Pa, and that of the Penning gauge is pressures between $1x10^{-3}$mbar or 0.1Pa and $1x10^{-6}$mbar or 10^{-4}Pa. The Baratron gauge is used between these ranges: 10^{-2} –10^{-4} mbar or 1 – 0.01Pa.

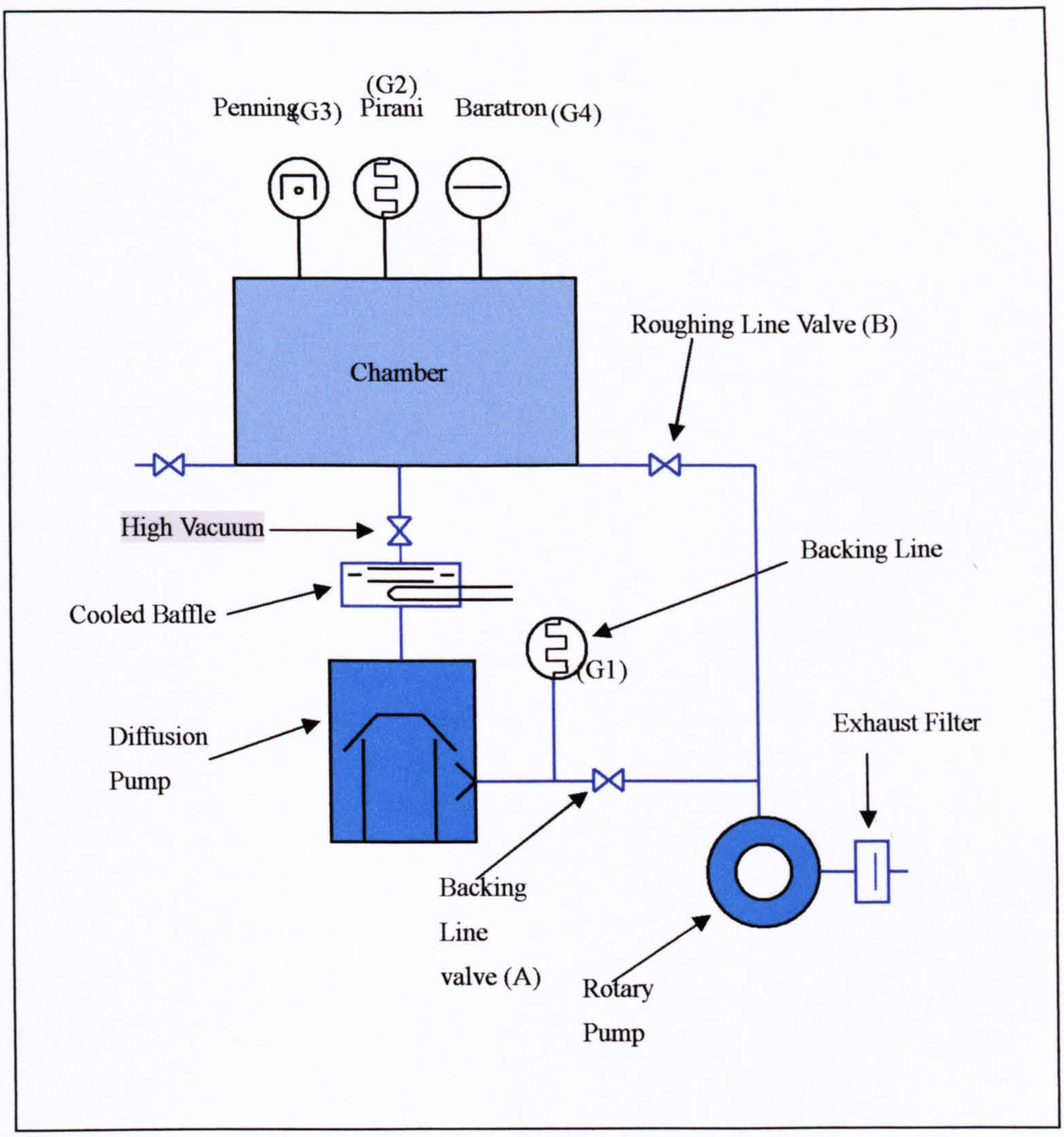

Figure 4.1 the schematic representation of the pumping system of the powder rig.

There are many factors influencing the evacuation speed of the pumping system. For example, water vapour condensed on the chamber walls, which exists all the time while the chamber is opened to atmosphere; contaminants such as grease and trapped gas present in the chamber; and small leaks within the chamber and pumping pipes, which can only be minimized, but never completely eliminated. The powder rig is adequate in respect of the pumping speed, in that it can be pumped down practically to 10^{-3}Pa within three hours.

The water cooling system is an important part of the rig. The cold water supplies the magnetron to prevent the target from overheating. It also supplies the diffusion pump and the cold trap above the diffusion pump to improve the pumping efficiency of the diffusion pump, and to reduce the back streaming of pump oil into the chamber. Figure 4.2 shows the schematic representation of the cooling system of the rig. Flow switches were installed to shut down the electrical supply either to the magnetron power supply or diffusion pump in case of failure of the water supply. The water flow rate to the cooling system is controlled by a flow control valve, which is situated in the inlet supply line.

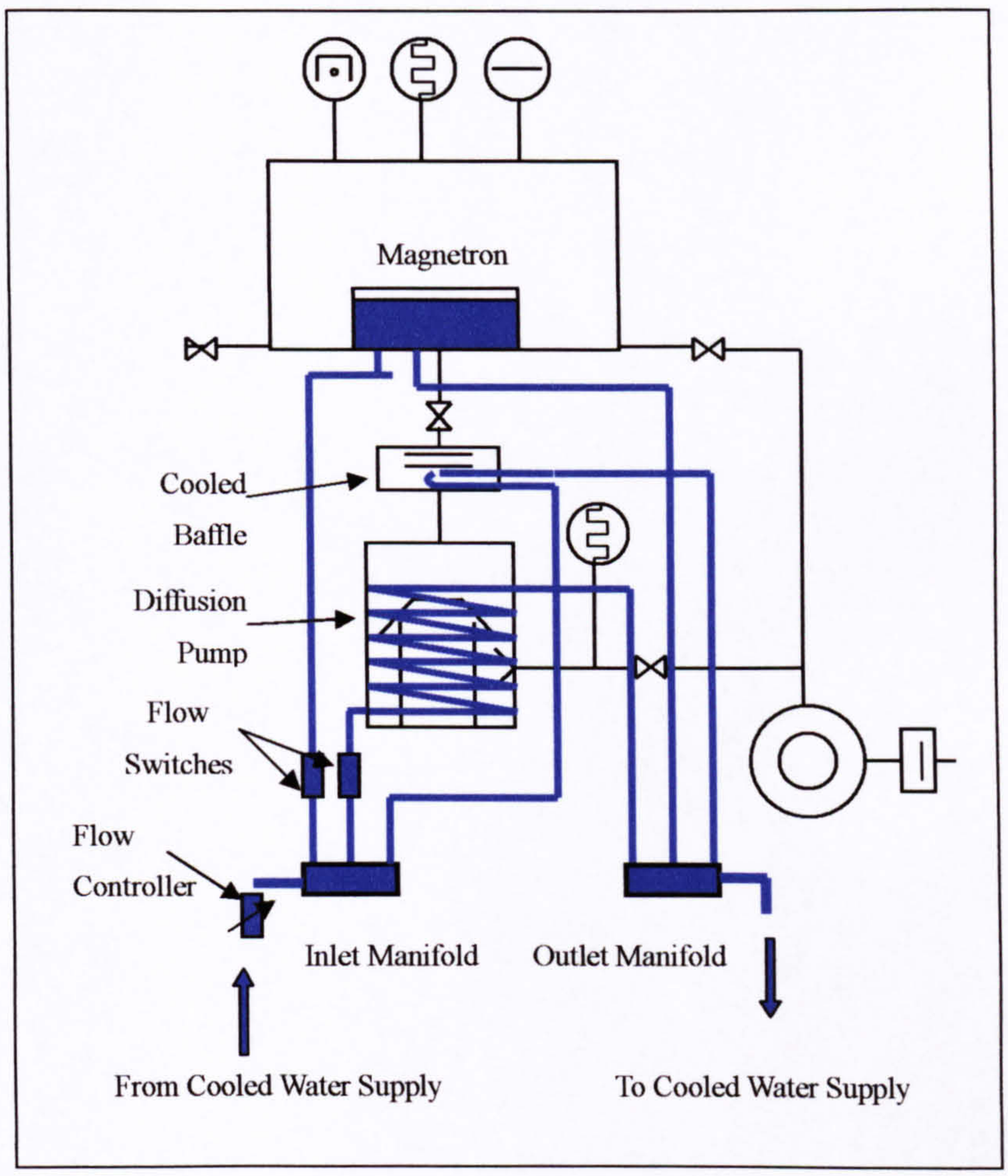

Figure 4.2 the schematic representation of water cooling system of the powder rig

All deposition work in this project was carried out using Advanced Energy Pinnacle

Plus DC power supply. The Pinnacle Plus supply offered a large range of options in terms of deposition parameters, with the pulse frequency ranging from 5 to 350kHz, duty cycle from 50% to 97.5% and power output up to 10kW. The supply can operate in current, voltage, or power regulation modes.

4.1.2 The commissioning of the powder rig

A commissioning exercise was carried out to demonstrate that all aspects of the powder rig were functioning as required. The substrates used in this project were soda lime and BK7 (Borosilicate) glass slides, and the main powder used was doped zinc oxide. Therefore, alumina and zinc oxide powders will be given as examples in the following description.

For target preparation, single materials can be spread directly onto the backing plate. For mixed blends, e.g. Al-doped ZnO, the weight of alumina required to produce the desired atomic dopant ratio (usually in the range 1-10 at%) must be calculated. It was proved in this project that the compositions of the coatings are the same or very similar to those of the target blends. Both powders (or more in the case of multi-dopant compositions) were then measured (to 0.01g) using electronic scales and mixed together. The mixture was then put into a bottle that was located on a rotary drum for several hours. Finally, the blends could be evenly spread on the backing plate, as for the pure materials. A cylindrical stainless steel block was adopted to lightly tamp the surface of the powder to form a target with evenly smooth surface.

For safety reasons, a mask and a pair of gloves were worn during the whole process from measurement of the powder to tamping the powder to form a target. The risk and potential hazards associated with the use of each new powder must be assessed.

The next step was to clean the substrate. Numerous cleaning techniques and materials are available for glass substrates. A detailed investigation of cleaning techniques was,

therefore, carried out at the beginning of this project and the results are given in Appendix I.

The pumping system of the powder rig is fully manual in operation. Beginning from cold, the start-up procedure is as follows (in reference to figure 4.1):

1. Switch on rotary pump with valve A (the backing line) open and all the other valves closed till the diffusion pump and the backing line is pumped out to a pressure below 0.1Pa (Gauge G1).
2. Switch on the cooling water system.
3. Switch on the diffusion pump and allow about 20 minutes for it to heat up.
4. Close valve A (backing line) and open valve B (roughing line) to rough-pump the chamber until the pressure is below 10Pa (Gauge G2).
5. Close valve B and re-open valve A and gradually open valve C (high vacuum valve) to continue pumping the chamber down to base pressure (gauge G3) by both the diffusion pump and rotary pump.

The chamber is then backfilled with an inert gas, usually argon, or both inert and reactive gases if needed, to the required coating pressure (gauges G3 and G4), which is typically 0.4 and 0.2Pa, respectively, in this system. At this pressure the plasma can be ignited and the deposition process initiated.

The Advanced Energy Pinnacle Plus pulsed DC power supply was connected to the target. The connection point was covered by a box, which was grounded to earth, to protect the operator's safety.

In this project, the pulsed DC power supply was operated in current regulation mode (asymmetric bipolar pulse waves). The duty cycle and pulse frequency were changed in certain study runs, although they were fixed on 62% and 350kHz, respectively in most of the research runs. The deposition parameters will be discussed in chapter 6.

The operation procedure were are as follows:

1. Connect the power supply to the magnetron.
2. Turn on the Pinnacle Plus.
3. Adjust the operation conditions, such as asymmetric pulsed mode, and set up parameters, e.g. frequency, duty cycle and current.

Make sure that the pressure in the chamber and the operation parameters from pulsed power supply etc. are all in the right states. Finally press the 'power on' button to begin a deposition run.

The time of a deposition run depends on the thickness of the coating required. Also, it varies with the deposition process (magnetron configuration, reactive or non-reactive, etc.) and the material to be deposited.

After deposition, the power supply was switched off first. Then the high vacuum valve was left open until the coated substrate had fully cooled down to room temperature. Secondly, the Baratron and Penning gauges must be switched off to protect them from damage. Finally, make sure the valve A on backing line is open and valve B on the roughing line and high vacuum valve C are closed, then the vent valve can be opened to allow the chamber up to atmosphere. Open the chamber door when the pressure inside the chamber is balanced with the air pressure outside, and take out of the coated samples. The coating then is ready to be checked to assess its properties.

If the rig needs to be completely checked, such as cleaned or repaired, then the pumps have to be switch off. In this case, switch off the diffusion pump first, and leave it to cool down at least half an hour before the rotary pump is turned off.

4.2 The Modification of the Powder Rig

4.2.1 The gas flow control units

Following the successful commissioning of the powder rig, it was decided to make several modifications to improve the coating properties and enlarge the research fields. One of the modifications was to be able to accurately measure the gas flow (argon and oxygen) input into the chamber. This is important to achieve reproducible coating conditions, and also to compensate for losses of oxygen in the plasma. Oxygen atoms are more easily lost than the metal atoms and argon atoms due to their lighter weight than those of the others (the free mean path of oxygen is larger than that of argon or some metal atoms.). Moreover, the properties of oxide coatings, especially the optical and electrical properties of transparent conductive oxide films are very sensitive to the oversupply or deficiency of oxygen in the deposition atmosphere. [12]

Two surplus Brooks 5850TR mass flow controllers were, therefore, installed on the rig. Both instruments were checked and recalibrated by Flotech Solutions of Stockport to meet the proposed experimental conditions. One of them was set to deliver argon flow in the range between 0.7 and 35mls/min (or sccm), the other was set to control oxygen flow in the range between 0.2 to 10mls/min (sccm). The range of the argon flow controller was sufficient to supply argon gas to adjust the pressure of the chamber from 10^{-3} to 0.6 Pa. Also, the range of the oxygen flow controller was accurate enough to deliver the small amounts of oxygen necessary to maintain coating stoichiometry.

4.2.2 RF bias power supply

The second modification for the rig was to connect a 600W Advanced Energy RFX600 power supply to the substrate holder, which allowed the power levels to be set and the incident power to be tuned conveniently. The matching box was mounted

the top of the chamber, as close as possible to the substrate holder.

There were two reasons for adding a RF power unit to the rig. One is to use RF to sputter clean the glass substrate in-situ, prior to deposition. With a large flat metallic substrate holder (as an extended inductance), the RF tuning can be controlled well. For 250W incident RF power, the reflected power normally can be tuned within 30-50W. In fact, the effectiveness of plasma cleaning by RF power supply has been proved in the investigation of glass substrate cleaning techniques. The experiments and conclusions of this study are detailed in Appendix I. The conclusion was that the adhesion of the coating to the substrate was improved by in-situ cleaning by this technique.

The second reason is to RF bias the substrate, if required, during deposition. Dr. Peter J. Kelly [139] studied the influence of bias voltage on the adhesion of coating to substrate and properties of coatings in his PhD thesis. It was concluded that the appropriate bias voltage was very important to obtain the required properties of the coatings and better adhesion. Figure 4.3 shows the schematic representation of the rig after modification [140].

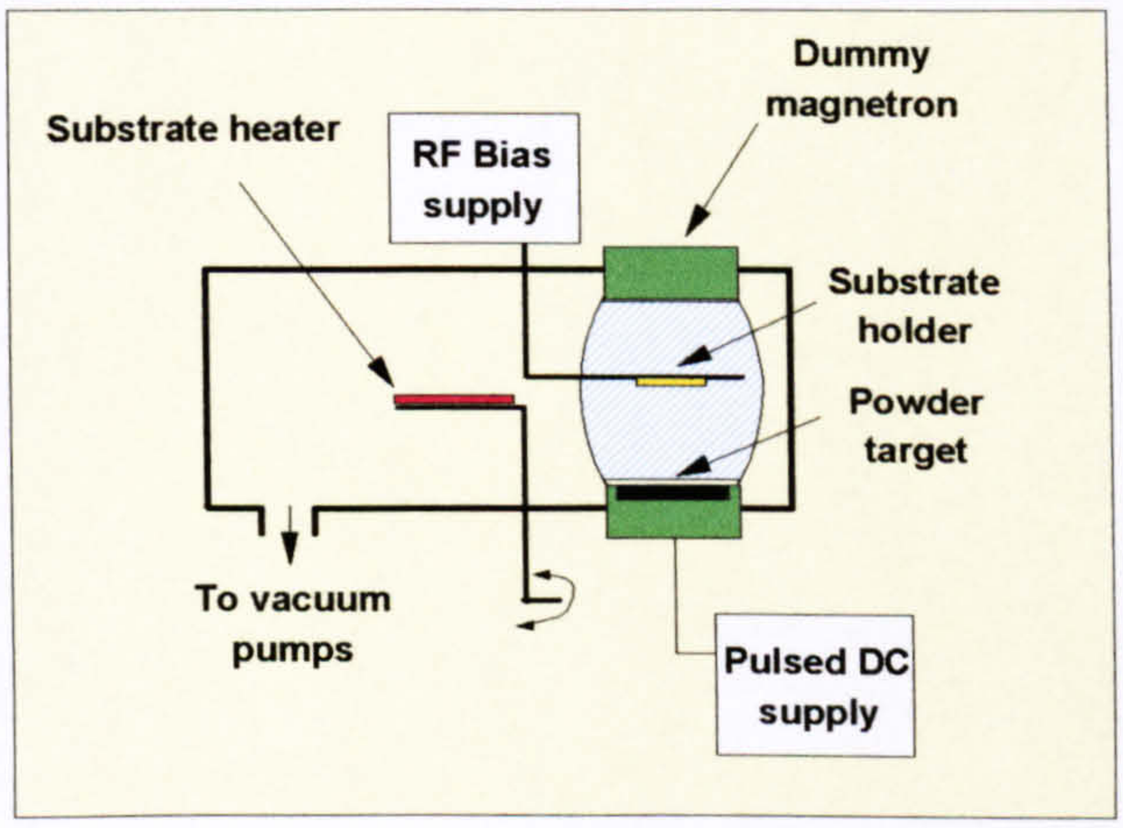

Figure 4.3 the schematic representation of the modified powder rig.

4.2.3 In-situ heater

In order to achieve satisfactory values for the electrical properties of transparent conductive oxide coatings, it is necessary to anneal the coating in a controlled atmosphere at temperatures of the order of 500° C [1, 89]. The vacuum chamber presented an opportunity to anneal the coatings in a controlled atmosphere, with the added advantage that removal of the substrate sample for annealing would not be necessary. It was decided, therefore, to add an annealing facility to the chamber.

Two quartz infrared heating elements were mounted on a pivot system beneath the substrate. The elements can be moved beneath the substrate from outside of the chamber during annealing using a shaft feed through. See schematic diagram in figure 4.3 [140] and picture 4.3, which shows the general view of the heater in the chamber. The power for the heater is supplied by a “Varatran" voltage controller with the capability of supplying 0 to 1000watts.

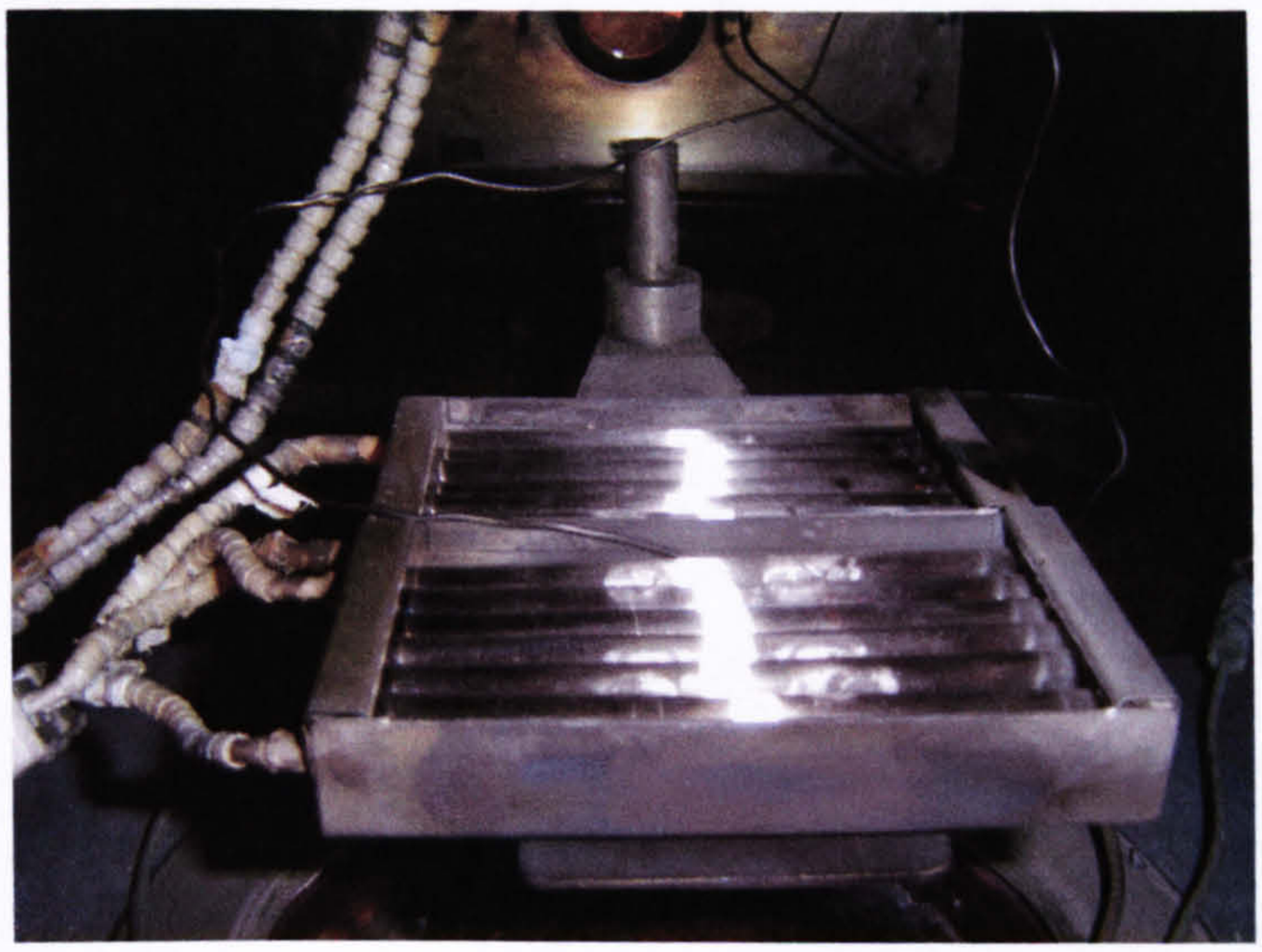

Picture 4.3 a general view of the heater in the chamber.

During annealing, the heater is moved beneath the substrate and set at a distance of approximately 20mm. One thermocouple is attached to the centre of the heater and another one underneath the substrate. The chamber is pumped down to a base pressure

of lower than $3x10^{-3}$Pa, then annealing takes place, either in the vacuum or using nitrogen at pressures up to 4Pa. The heater supply increased gradually until the substrate thermocouple indicates the required temperature. The powers of the heaters are controlled to lower than 850W, which can allow heater temperatures of up to 700°C and that of the substrate up to 650°C, to keep within the upper operating limit of the heater elements. With this facility in the chamber, post-annealing processes were carried out successfully.

5. ANALYTICAL TECHNIQUES

It is important to analyze the characteristics and properties of thin films in practical applications. For TCO coatings, the techniques to analyze the electrical and optical properties involve the four point probe, Van der Pauw's method and spectrophotometry. The structural and compositional analysis techniques for thin films include scanning electron microscopy (SEM), electron probe micro-analysis (EPMA), X-ray diffraction (XRD), Auger electron spectroscopy (AES), Rutherford Backscattering Spectrometry (RBS), Secondary Ion Mass Spectrometry (SIMS) and X-ray photoelectron spectroscopy (XPS). The adhesion between film and substrate, and thickness of the films can be measured by scratch testing and surface profilometry, respectively.

5.1 Analysis of Electrical Properties

5.1.1 Basic concepts of the electrical properties of semiconductor materials

The basic electrical semiconductor parameters are the conductivity, σ, or resistivity, ρ, the majority carrier concentration (n), the type (N or P) and the mobility, μ, the diffusion constant and lifetime. There are several laboratory techniques for measuring those parameters. In this chapter, two of them; the four point probe and Van der Pauw's techniques, will be discussed to measure the former four parameters.

Electrical *conductivity* is a measure of how well a material accommodates the transport of charge carriers, which are movable and flow when a difference of electrical potential is applied across the material, with units ohm.m^{-1}.

The *resistivity* is the reciprocal of the conductivity, the basic parameter of the conductive property of a semi-conductive material, with units ohm-cm (Ω m).

There is another parameter, *sheet resistivity,* to refer to the conductive property of thin film materials. It represents the resistance between two sides of a square and is independent on the area of the square if the area is much larger than the thickness of the thin film.

Both resistivity and sheet resistivity are dependent on the material itself, not like the resistance, which refers to the capability of a material to pass the current and may be affected by the shapes of different samples.

Since different materials can have the same resistivity, and also a given material might exhibit different values of resistivity, depending upon how it was synthesized, the definitions of carrier density and mobility are introduced which are capable of further understanding the electric properties of a material, especially a semiconductor. The definitions of carrier density and mobility involve the concept of Lorentz force and the interaction of electric and magnetic fields.

Lorentz force refers the force **F** that an electron experiences when it moves along a direction perpendicular to an applied magnetic field **B** (Wm^{-2}). The force is normal to both directions of the electron movement and magnetic field.

The force acts on the charge carriers, such as electrons in an n-type semiconductor, moving at a drift velocity **v**, opposite to the conventional current direction. The electrons will be pushed along the force direction, whilst in turn the semiconductor loses its local neutrality; the side opposite to the force direction becomes depleted of electrons, and the other side receives an excess of electrons. This gives a measurable voltage V_H, called the *Hall voltage*, see figure 5.1. For p-type semiconductors, even if the charge carriers (holes) move in the same direction as the current, the force will also be in the same direction as in the figure, and there will be a polarity of V_H in the reverse direction. This phenomenon is called *Hall effect*, discovered by E. Hall in 1874.

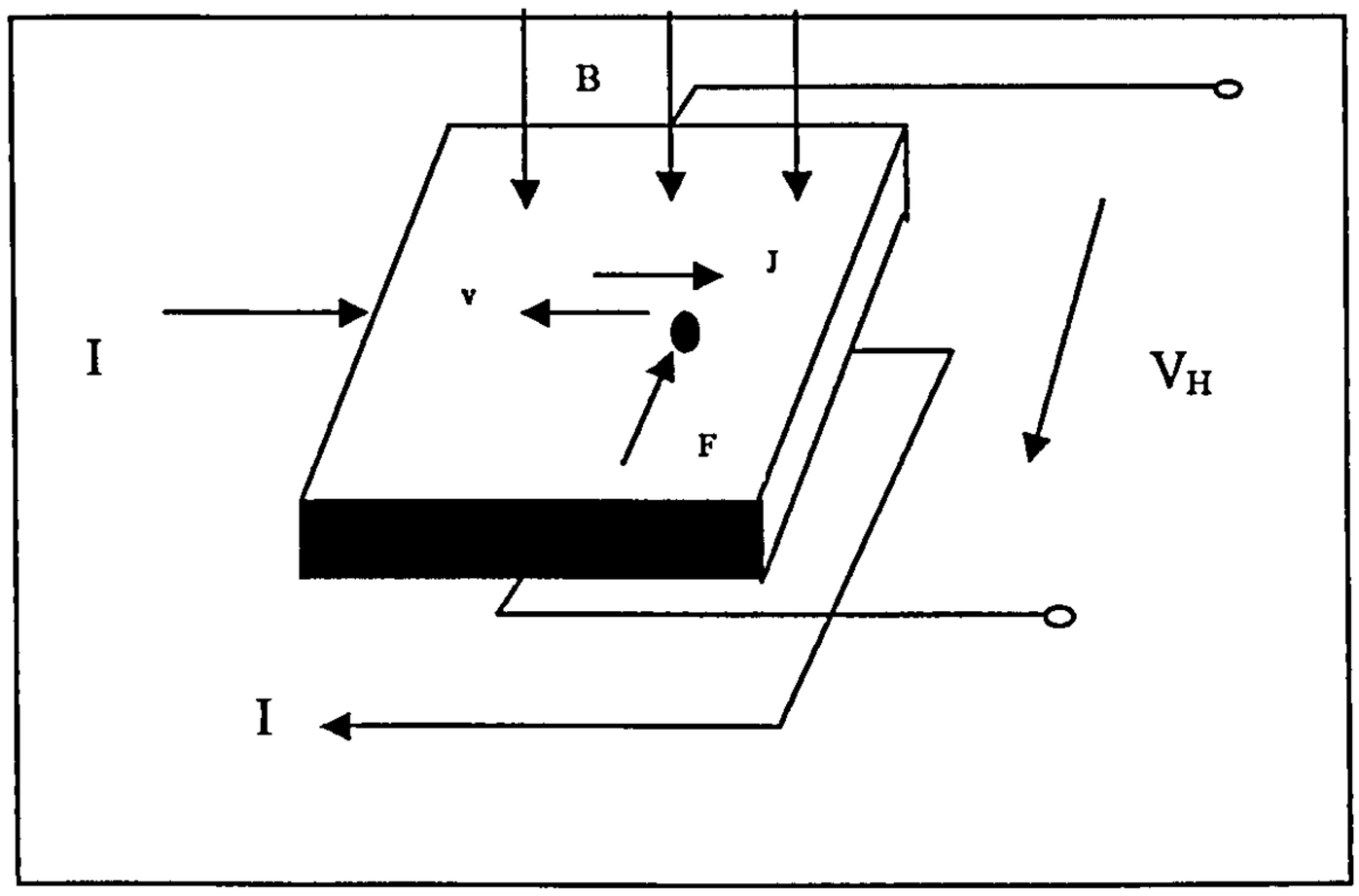

Figure 5.1 the Hall effect on an n-type semiconductor with current density J in a normal magnetic field B, results the force F acting on the electron q carrying the current [73]

We assume that a constant current, *I,* flows along the x-axis from left to right in the presence of a z-directed magnetic field, B. The sample thickness is d and q represents the elementary charge (1.602×10^{-19} C) of an electron, n is the charge carrier concentration. Then the transverse hall voltage can be expressed as follow:

$$V_H = \frac{IB}{qnd} \qquad \text{...Eq (5.1)}$$

In some cases, it is convenient to use sheet carrier density ($n_s = nd$) instead of bulk carrier density. One then obtains the equation:

$$n_s = \frac{IB}{q|V_H|} \qquad \text{...Eq(5.2)}$$

The sheet resistance, R_S, of the semiconductor can be conveniently determined by use of the Van der Pauw resistivity measurement technique or four point probe method, which will be discussed in the following sections.

The mobility of charge carriers measured by the Van der Pauw's technique is called *Hall mobility,* which is related to sheet resistance and sheet density, and can be expressed by the following formulation:

$$\mu = \frac{|V_H|}{R_s IB} = \frac{1}{qn_s R_s} \qquad \text{...Eq (5.3)}$$

5.1.2 Four-point probe

Four-point probe – calculates the resistivity of the coating by measuring the voltage between two inner probes whilst a current is passed between the outer two.

Figure 5.2 (a) shows the basic measurement principle, in which the constant current is forced to pass through points A to B and the difference of the potential between point C and D is measured by a voltmeter with a high input impedance compared to the measured value. The high input impedance voltmeter draws negligible current, which means the metal-semiconductor contact resistance at C and D do not affect the results. The current is constant and forced through the material. Therefore, it is not affected by the material itself and the resistances at points A and B. The resistivity of the material, according to the definition will be:

$$\rho = \left(\frac{Wd}{L}\right) \times \left(\frac{V}{I}\right) \qquad \text{...Eq (5.4)}$$

in which W, d and L represent, respectively, the width, the thickness and the length; V and I, the voltage (difference of the potentials between point C and D) and current through points A and B. This formula is true only in the case that the current flows in parallel lines.

The commercially obtainable probe is a more practical and simpler way to measure the resistivity, see figure 5.2 (b). There are four springy metal points, arranged in a

line, usually less than 1mm apart, which can be lowered onto the semiconductor surface. The constant current is forced to pass through the two outer points and voltage is measured from the two inner points. The current density in this case is not uniform but it is found that this problem can be corrected by following formulas. For a semiconductor wafer, if the thickness of the wafer d is much bigger than the distance s between points, the formula will be [73]

$$\rho = \frac{2\pi s V}{I}(\Omega cm) \qquad \text{...Eq (5.5)}$$

On the other hand, if the thickness is much less than s, then:

$$\rho = \left(\frac{\pi}{\ln 2}\right) \times \left(\frac{Vd}{I}\right) = \frac{4.53Vd}{I}(\Omega cm) \qquad \text{...Eq (5.6)}$$

This method is very useful for thin semiconductor films. For a doped semiconductor, the resistivity will change if the dopant atoms of another type of impurity are allowed to diffuse at high temperature, but not uniform in depth. Therefore the sheet resistivity, R_s, which measured in ohms per square is better to describe the layer conductive property than the average one.

$$R_s = \frac{\rho}{d} = \frac{4.53V}{I}\ (\Omega\square^{1}) \qquad \text{...Eq (5.7)}$$

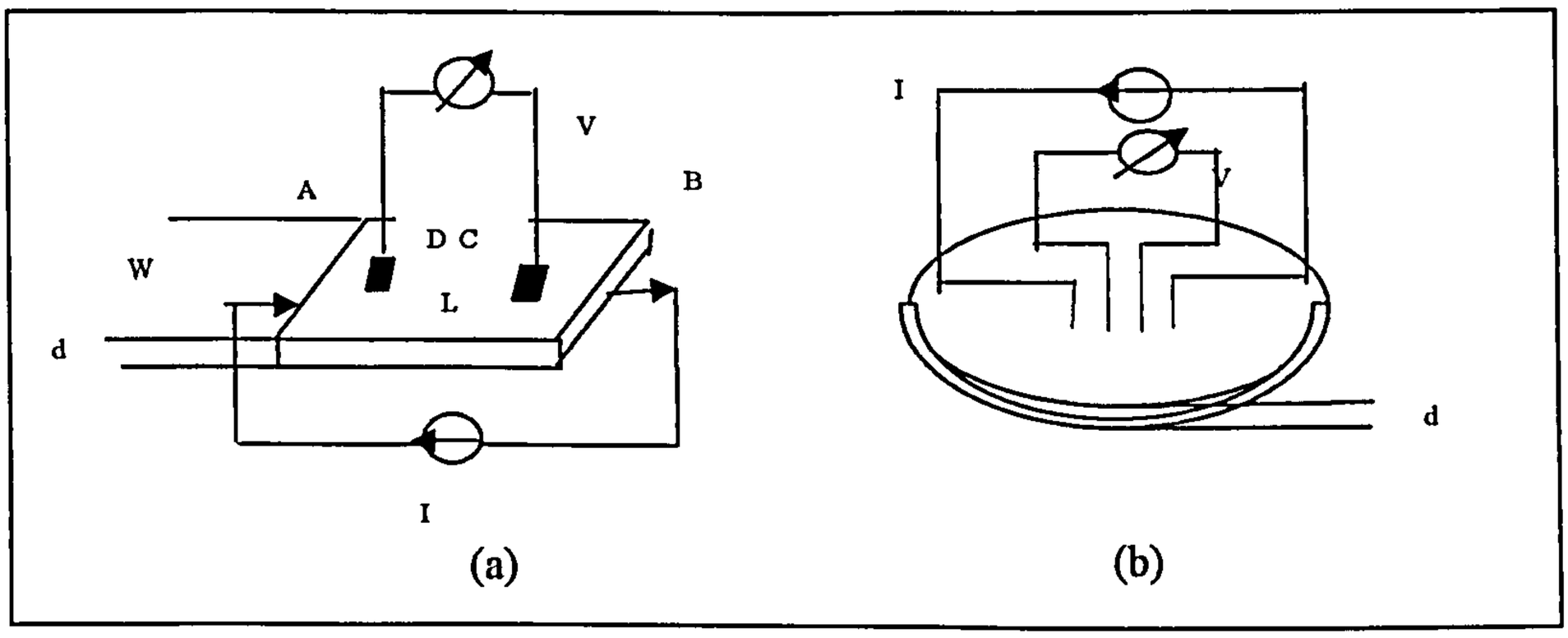

Figure 5.2 (a) the four contact method; (b) the four point probe to measure the resistivity. [73]

5.1.3 Van der Pauw's technique

Van der Pauw's technique – to obtain the electrical resistivity (ρ), the type, the Hall mobility (μ) and the carrier concentration (n) of the semiconductor films by doing four probe and Hall measurements.

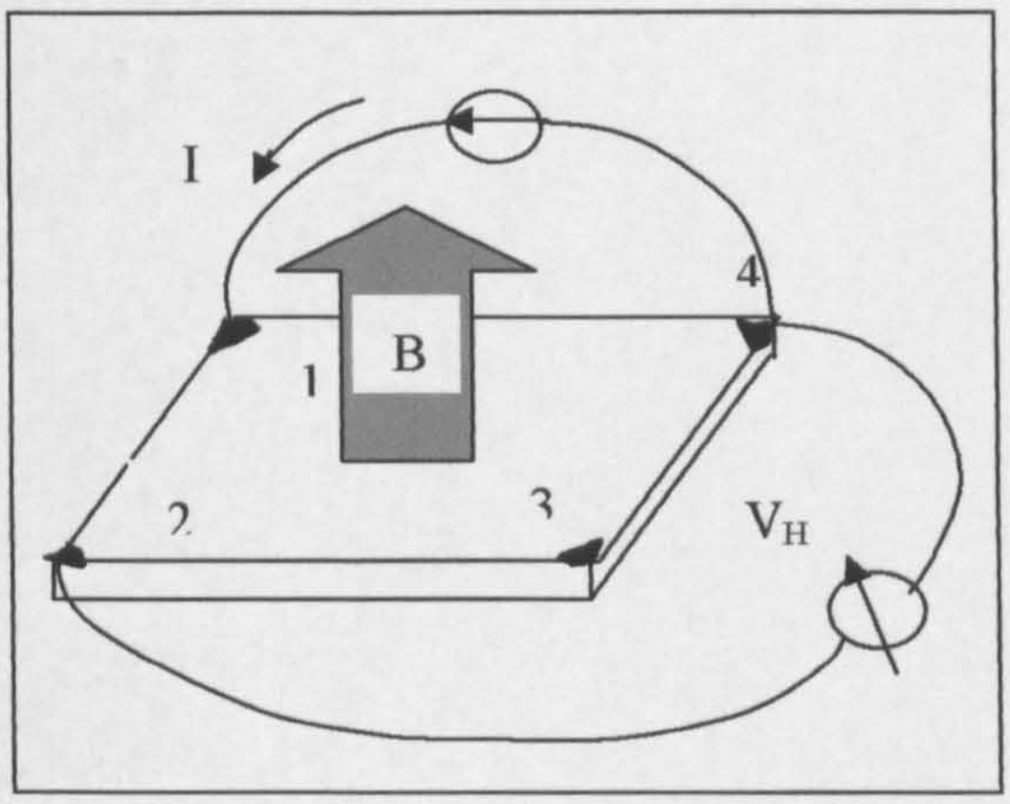

Figure 5.3 schematic representation of a Van der Pauw configuration used in the determination of the Hall voltage, V_H

The sample geometry used to carry out the Van der Pauw measurement is shown in figure 5.3, which is suitable for measuring thin films of semiconductor materials. The thickness, d, of the sample must be much smaller than the distance between the contacts, L.

For resistivity measurements, four leads are connected to the four metal contacts on the sample. These are labelled 1, 2, 3, and 4, counterclockwise as shown in figure 5.3. It is important to use the same batch of wire for all four leads in order to minimize thermoelectric effects. Similarly, all four ohmic contacts should consist of the same material.

Then apply current from contact 1 to 2 to get the positive current I_{12} and measure the voltage from contact 4 to 3, V_{43}. Reverse the current to obtain another current and

voltage group I_{21} and V_{34}. Using the same method, I_{23}, I_{34}, I_{41}, I_{14}, I_{43}, I_{32} and V_{23}, V_{41}, V_{21}, V_{14}, V_{32} can be measured.

Eight measurements of voltage yield the following eight values of resistance, all of which must be positive [71]:

$$R_{21,34} = \frac{V_{34}}{I_{21}}, R_{12,43} = \frac{V_{43}}{I_{12}}, \quad R_{32,41} = \frac{V_{41}}{I_{32}}, R_{23,14} = \frac{V_{14}}{I_{23}}$$

$$R_{43,12} = \frac{V_{12}}{I_{43}}, R_{34,21} = \frac{V_{21}}{I_{34}}, \quad R_{14,23} = \frac{V_{23}}{I_{14}}, R_{41,32} = \frac{V_{32}}{I_{41}} \quad \textit{...Eq (5.8)}$$

The sheet resistance R_S can be determined from the two characteristic resistances by the formula [71]:

$$\exp\left(-\frac{R_A}{R_S}\right) + \exp\left(-\frac{R_B}{R_S}\right) = 1 \qquad \textit{...Eq (5.9)}$$

$$R_A = \frac{R_{21,34} + R_{12,34} + R_{43,12} + R_{34,21}}{4} \quad \textit{and}$$

$$R_B = \frac{R_{32,41} + R_{32,14} + R_{14,23} + R_{41,32}}{4} \qquad \textit{...Eq (5.10)}$$

If the conducting layer thickness d is known, the bulk resistivity $\rho = R_S\, d$ can be calculated from R_S.

The most common way of performing Hall measurements is to acquire two sets of Hall measurements, one for positive and one for negative magnetic field direction. The current passed into lead 1 and taken out of lead 3 is termed I_{13}. Likewise for I_{31}, I_{42}, I_{24}. The Hall voltage measured between leads 2 and 4 with magnetic field positive for I_{13} is termed V_{24P}. Likewise for V_{42P}, V_{13P}, and V_{31P}. Similar definitions for V_{24N}, V_{42N}, V_{13N}, V_{31N} apply when the magnetic field B is reversed.

Then the Hall calculation is as follows:

$$V_C = V_{24P} - V_{24N}, \quad V_D = V_{42P} - V_{42N},$$

$$V_E = V_{13P} - V_{13N}, \quad V_F = V_{31P} - V_{31N} \qquad \text{...Eq (5.11)}$$

The sample type is determined from the polarity of the voltage sum $V_C + V_D + V_E + V_F$. If this sum is positive (negative), the sample is *p*-type (*n*-type).

The sheet carrier density (in units of cm^{-2}) is calculated from [71]

$$n_s = \left| \frac{8 \times 10^{-8} IB}{q(V_C + V_D + V_E + V_F)} \right| \qquad \text{...Eq (5.12)}$$

where B is the magnetic field in gauss (G) and I is the dc current in amperes (A).

The bulk carrier density (in units of cm^{-3}) can be determined by $n = n_s/d$ if the conducting layer thickness d of the sample is known.

The Hall mobility [71]

$$\mu = \frac{1}{qn_s R_s} (cm^2 V^{-1} s^{-1}) \qquad \text{...Eq (5.13)}$$

is calculated.

5.2 Analysis of optical properties

Spectrophotometry – to measure the transmittance and reflectance of the films, and derive the optical constants n and k, via modeling.

Spectrophotometry is the quantitative measurement of the reflection or transmission properties of a material as a function of wavelength. Depending on the machine used, measurements of reflectance and transmittance can be performed in the ultraviolet (UV), visible, and near-infrared (IR) spectral regions (250 nm to 2500 nm). The

schematic representation shows the basic structure of a spectrophotometer, see figure 5.4.

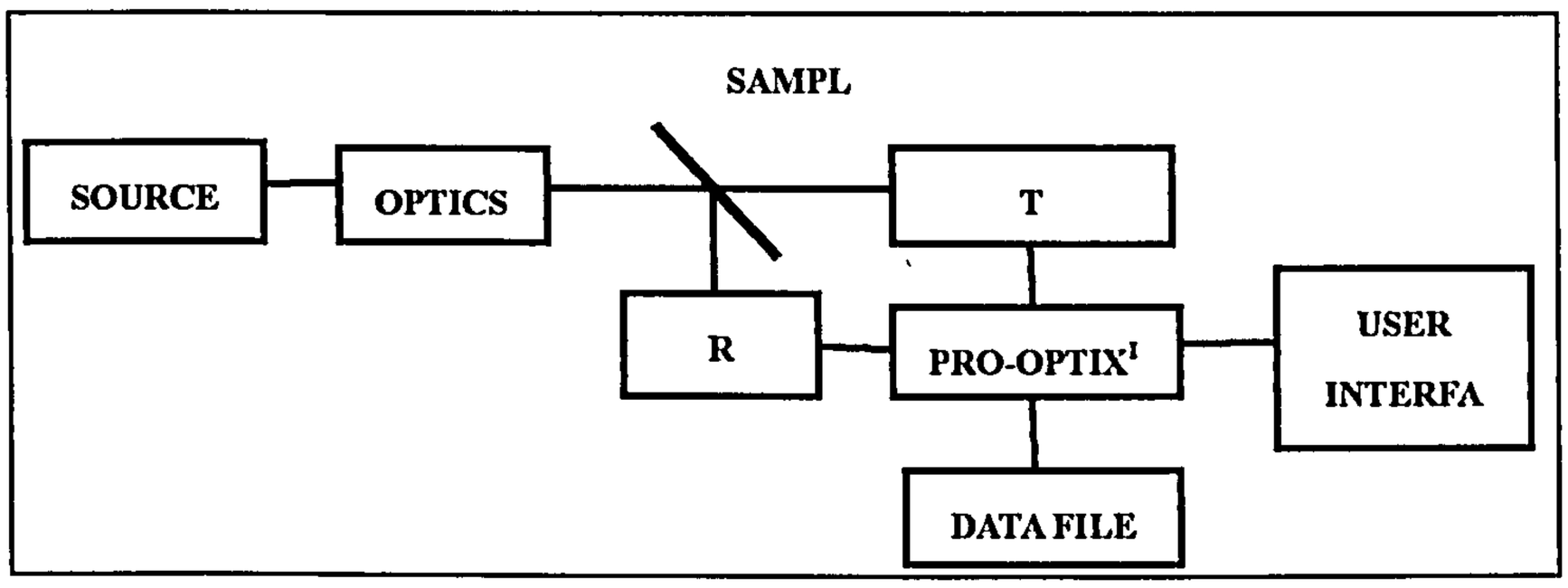

Figure 5.4 the schematic representation of a basic structure of a spectrophotometer.

The light from the source is transferred by optics in the instrument and strikes the surface of the sample, where the light is divided into three parts – transmission (T), reflection (R) and absorption (A). The sum of the three parts should be equal to the input light. Therefore, a formula can be written, as follows if we assume the sum of input light is 1

$$T + R + A = 1 \qquad \text{...Eq (5.14)}$$

Absorption refers that light is absorbed by an atom, ion or molecule, taking it to a higher energy state. There are three kinds of energy transitions: electronic, which normally occurs in UV and Visible ranges of the light, and vibrational and rotational, which happen in IR range of the light.

When a spectrophotometer is employed to measure the amount of light that a sample absorbs, the instrument operates by passing a beam of light through a sample and measuring the intensity of light reaching a detector.

The beam of light consists of a stream of photons. When a photon encounters an analyte (in this project the analyte is a molecule of the thin film on the glass slide), there is a chance the analyte will absorb the photon. This absorption reduces the number of photons in the beam of light, thereby reducing the intensity of the light beam. In fact, a glass slide, as the substrate of a thin film, also has the chance to absorb the photons and reduce the light intensity. The absorption of the film can be accurately calculated by taking the intensity of light beam through the uncoated substrate into account.

The nkd 8000 made by Aquila Instruments Ltd was used in this project. First, the intensity of light (I_0) passing through a reference glass sample will identify the system error or incoherence from the instrument and light beam. Then the glass slide that is identical to the sample substrate is analyzed by the system, which provides the absorption of light by the glass slide. Second, the intensity of light (T) transmitted through the coated sample and the intensity of light (R) reflected from the coated sample are measured. Third, the experimental data --the transmittance (T) and the reflectance (R) are used to calculate the absorbance (A), absorption coefficient (k), refractive index (n), band gap (E_g) and film thickness (d) by modelling and calculation using the company's system software.

5.3 Structural Analysis

5.3.1 Scanning electron microscope

Scanning electron microscopy (SEM) [26] – indicates the morphology of the structure (discussed in chapter 2) and thickness of the films, and also gives information on adhesion, by visualizing the surface, fracture edges and coating/substrate interface regions of a coated sample.

In a SEM, a focused high energetic electron beam is rastered over the surface of an electrically conductive material, which in turn causes the ejection of secondary electrons from the first 10-20 atomic layers of the surface. These secondary electrons are collected by the detector in the SEM and then reproduced as a digital image according to their intensities as a function of positions. A thin film of gold on insulating coatings may be needed to make the surface of the coating sufficiently conductive to prevent the charging up of the area under investigation and the subsequent repulsion of the electron beam.

The digital image with a high resolution can be enlarged up to 150,000x times, with the typical magnifications of 20-50,000x. At a given magnification, it is impossible to obtain both the best resolution and depth-of-field at the same time, because good resolution needs a small beam dispersion of the electron beam with a small size exit aperture and a close working distance, in contrast, the maximum depth of field needs a long working distance as well as small exit aperture. Structural features, which are smaller than 100nm, are difficult to resolve because of the limited resolution.

SEMs can be used in the modes of energy dispersive X-ray spectrometry (EDX) or wavelength dispersive X-ray spectrometry (WDX) as an electron probe micro-analyzer (EPMA) to determine the chemical composition of the film. The principle of EPMA is to use X-rays to characterize the atoms by electron-atom collisions from the region up to a micron below the surface, which allows elemental chemical analysis.

5.3.2 X-Ray diffraction

X-ray diffraction (XRD) [149] – indicates the crystalline structure of the coating, and can also give information on texture, grain size and strain.

The atomic planes of a crystal cause an incident beam of X-rays (if the wavelength is

approximately the same magnitude as the interatomic distance) to interfere (constructively and destructively) with one another as they leave the crystal. The phenomonen is called *X-ray diffraction.* Diffraction can occur whenever Bragg's Law [151] is satisfied with monochromatic radiation. Practically this is done by using a range of X-ray wavelengths or rotating the crystal, or using a powder or polycrystalline specimen.

Bragg's Law can be expressed as

$$n\lambda = 2d\sin\theta \qquad \text{...Eq (5.15)}$$

in which λ is the wavelength of incident beam, d the spacing of planes of atoms and θ the angle of incidence of the beam. If a beam of coherent waves is incident on a multi-layer of regularly spaced atoms, such as in crystalline materials, diffraction occurs when the angles of incidence satisfy Bragg's Law (see the schematic representation in figure 5.5).

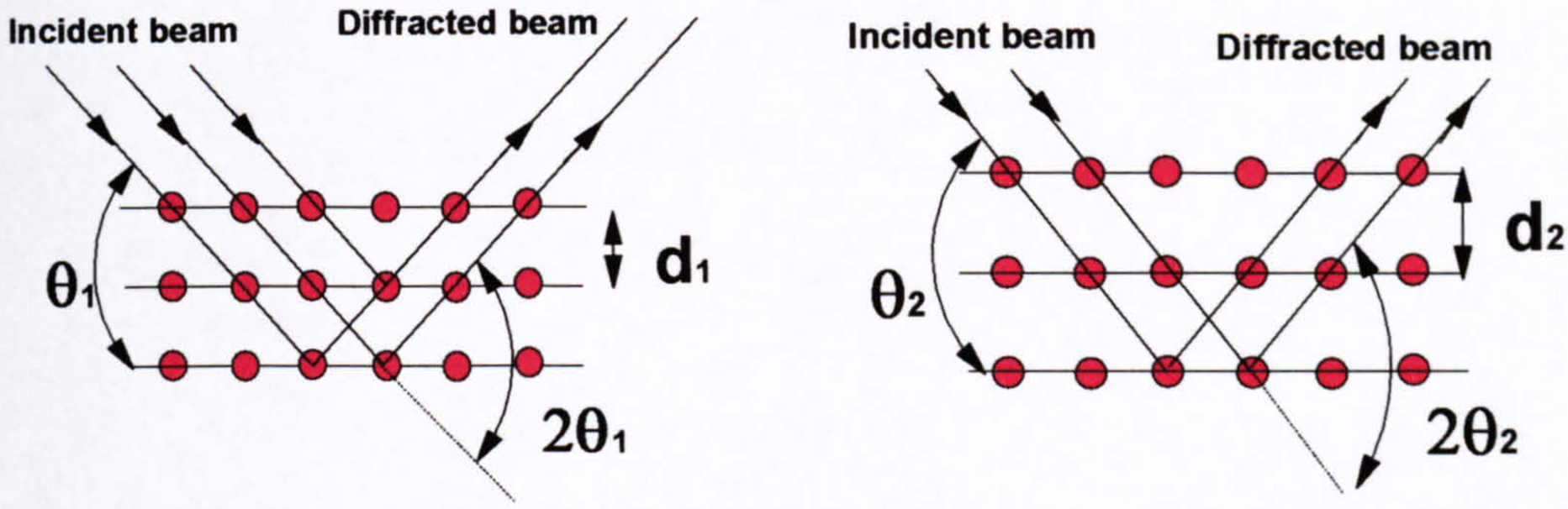

Figure 5.5 the schematic representation of X-ray diffraction [139]

The interatomic spacings in a crystalline material are a characteristic of that material. Thus, XRD traces can be used to identify materials through comparison with standard traces found in JCPDS cards (reference). The traces also give information on the texture (preferred orientation), grain size and strain present in a film through analysis of the positions, widths and heights of the peaks.

Coatings deposited by PVD methods normally display preferred orientations in the form of columnar microstructures due to the limited number of directions that the coating atoms approach the substrate. Therefore, the particular peaks will appear when the reflected X-rays correspond with Braggs Law. Each peak is unique to its lattice spacing for a material, which in turn can be used to identify the preferred orientations or textures of the coating.

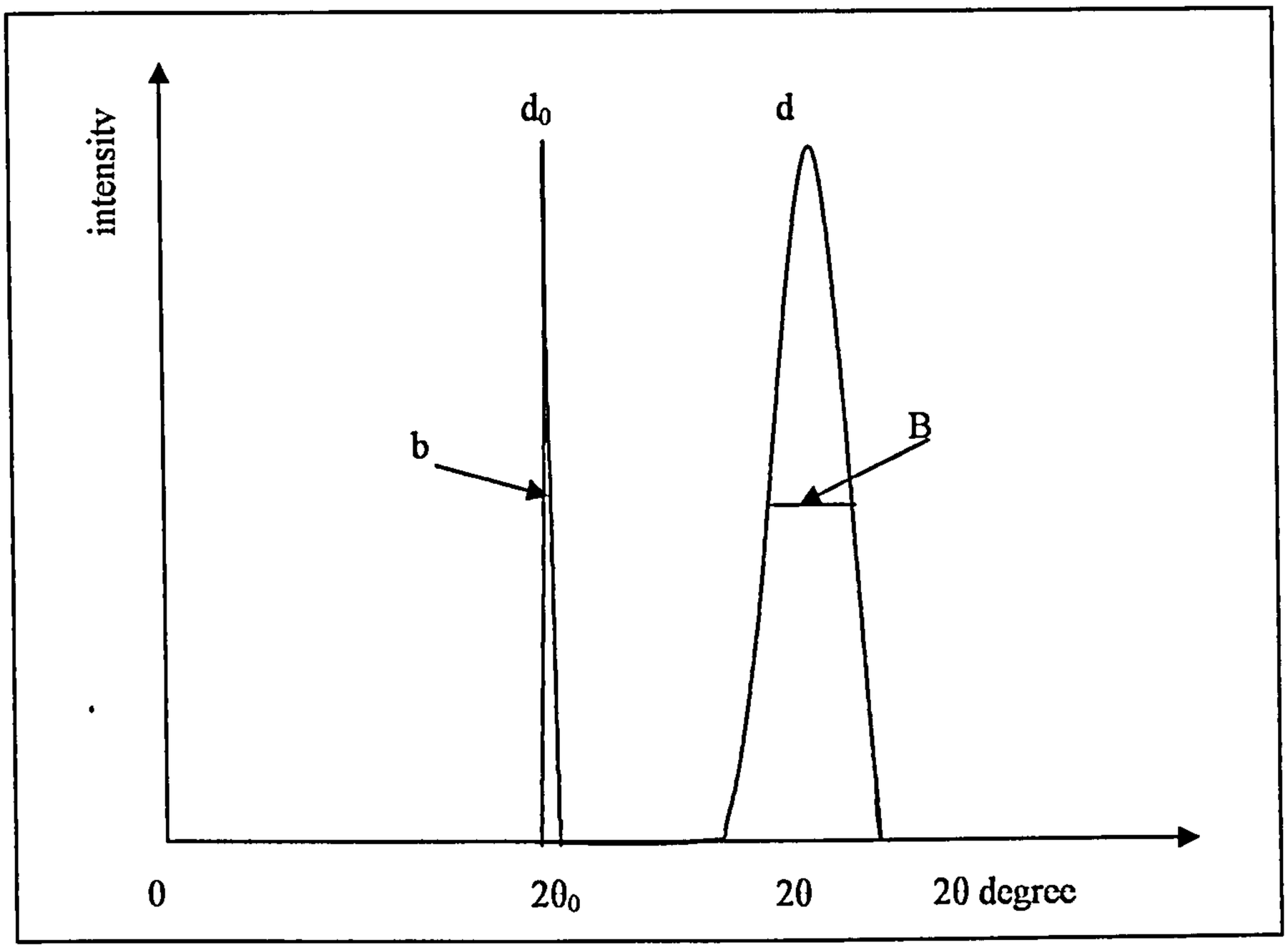

Figure 5.6 the schematic representation of the ideal diffraction peak (d_0) and practical peak (d)

The peaks for a polycrystalline material can also be shifted from their equilibrium positions $2\theta_0$ to 2θ (see figure 5.6) because of the elastically deformed lattice spacings, which can be used to estimate the strain in the coatings. A uniform tensile strain perpendicular to the reflecting plane can be written as follow:

$$\varepsilon_Z = \left(\frac{d - d_0}{d_0} \right) \qquad \text{...Eq (5.16)}$$

in which ε is the 'through-thickness' strain; d the coating lattice spacing and d_0 the equilibrium spacing of the coating material.

The line shape of a peak can give the information about the grain size of a coating or material. In a XRD system, several factors will cause peak line broadening, such as spectral broadening, instrumental broadening and physical broadening. Physical broadening (β) can be expressed as

$$\beta = B - b \qquad \text{...Eq (5.17)}$$

in which B is the observed FWHM (full width half maximum), the peak line broadening and b is the contribution due to instrument. The physical broadening is contributed by lattice strain (β_e) and crystallite size (β_b). Voigt function [142] gives a good way to separate them.

$$\varepsilon = \frac{\beta_e}{4(\tan\theta)} \qquad \text{...Eq (5.18)}$$

and

$$L = \frac{0.9\lambda}{\beta_g(\cos\theta)} \qquad \text{...Eq (5.19)}$$

where L is the crystallite size.

In this project, the SIEMENS D5000 X-ray diffraction machine was used in the θ-2θ mode using copper K_α radiation with λ 1.5418Å.

5.3.3 Auger Electron Spectroscopy (AES)

Auger Electron Spectroscopy (AES) [143] is a surface specific technique utilizing the emission of low energy electrons in the *Auger process* and is one of the most commonly employed surface analytical techniques to determine the composition of the surface layers of a sample.

The *Auger process* involves two steps – *ionization* of an atom by removal of a core electron, and *Auger emission* by emitting an Auger electron. First, a core hole is created by applying a beam of high energy electrons (2-10KeV) or soft-X-rays (1-2KeV) on the surface of the sample and removal of a core electron, which is called the ionization process. The ionization process retains the ionized atom in a highly exited state, which tends to relax back to a lower energy state by the second step; *Auger emission*. In the second step, the initial core hole is filled by a higher energy state electron accompanied by energy release. At the same time, a second electron obtains the liberated energy and overcomes the binding energy and is emitted as an

Auger electron. The result of the Auger process is to create holes in the atom by ejection of an Auger electron. The energy of the Auger electron can be written as, refers figure 5.6:

$$E_{auger} = E_K - (E_{L1} + E_{L23}) \qquad \text{...Eq (5.20)}$$

Providing the initial electron was ejected from K shell and the two final holes were created from L_1 and L_{23} shell, see figure 5.7.

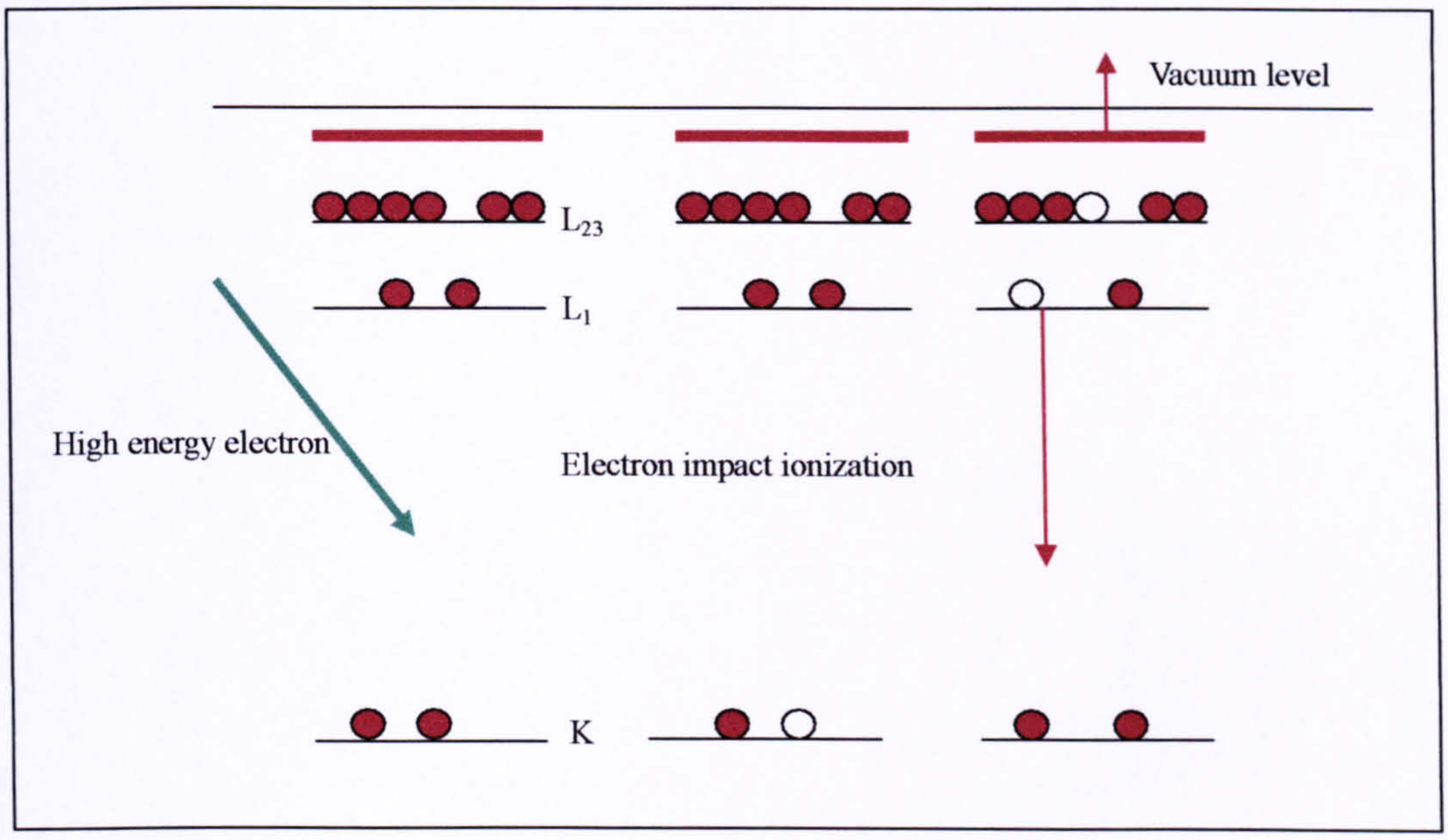

Figure 5.7 the schematic representation of a possible Auger emission.

In general, since the initial ionization event is non-selective and can happen in various shells, there will be many possible Auger transitions for a given element – some weak and some strong, which will show a characteristic spectrum of peaks at various kinetic energies. Therefore this technique can be used to determine the elements and the composition present at the surface of a sample.

AES can also be used to provide the compositional information as a function of depth

below the surface. It is realized by gradually removing material from the surface region being analysed whilst continuing to monitor and record the Auger spectra. The removal of the material is normally carried out by etching the analysed region by exposing the surface to an ion flux, which leads to sputtering of the surface atoms.

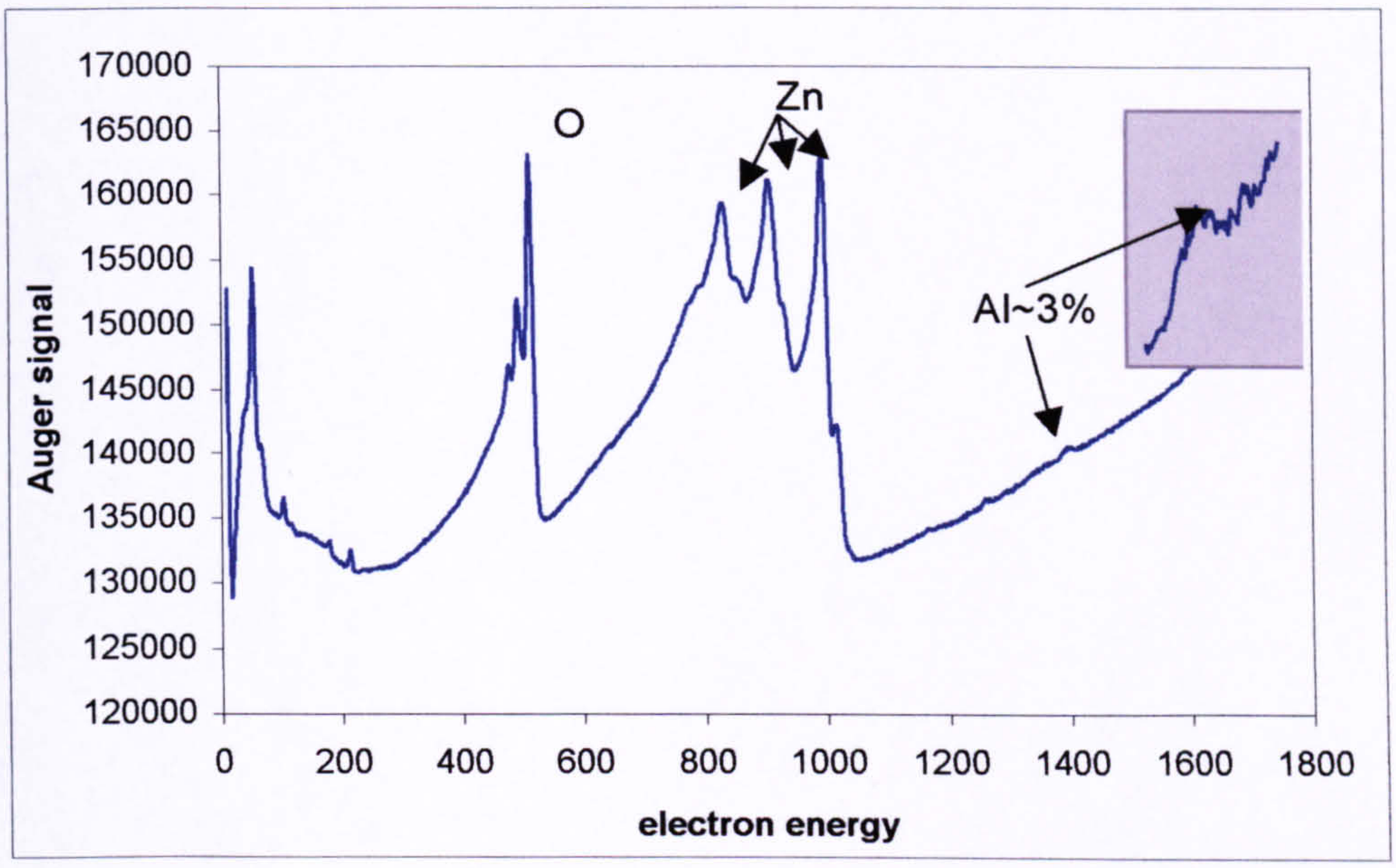

Figure 5.8 a typical auger spectrum

5.3.4 X-ray Photoelectron Spectroscopy (XPS)

Using the same principle as AES, the core electrons of the material from a sample are excited by soft X-rays, accompanied by the core electrons emitting [143]. These emitted electrons are called photoelectrons. The analysis of their kinetic energy allows the determination of their binding energies with the atoms of the analyzed material, which are unique to the material. Therefore, this analysis technique can be used to characterize the atoms by their core levels electron energy and to determine the chemical elements by defining their chemical bonds. Figure 5.9 shows the photoelectron emission process.

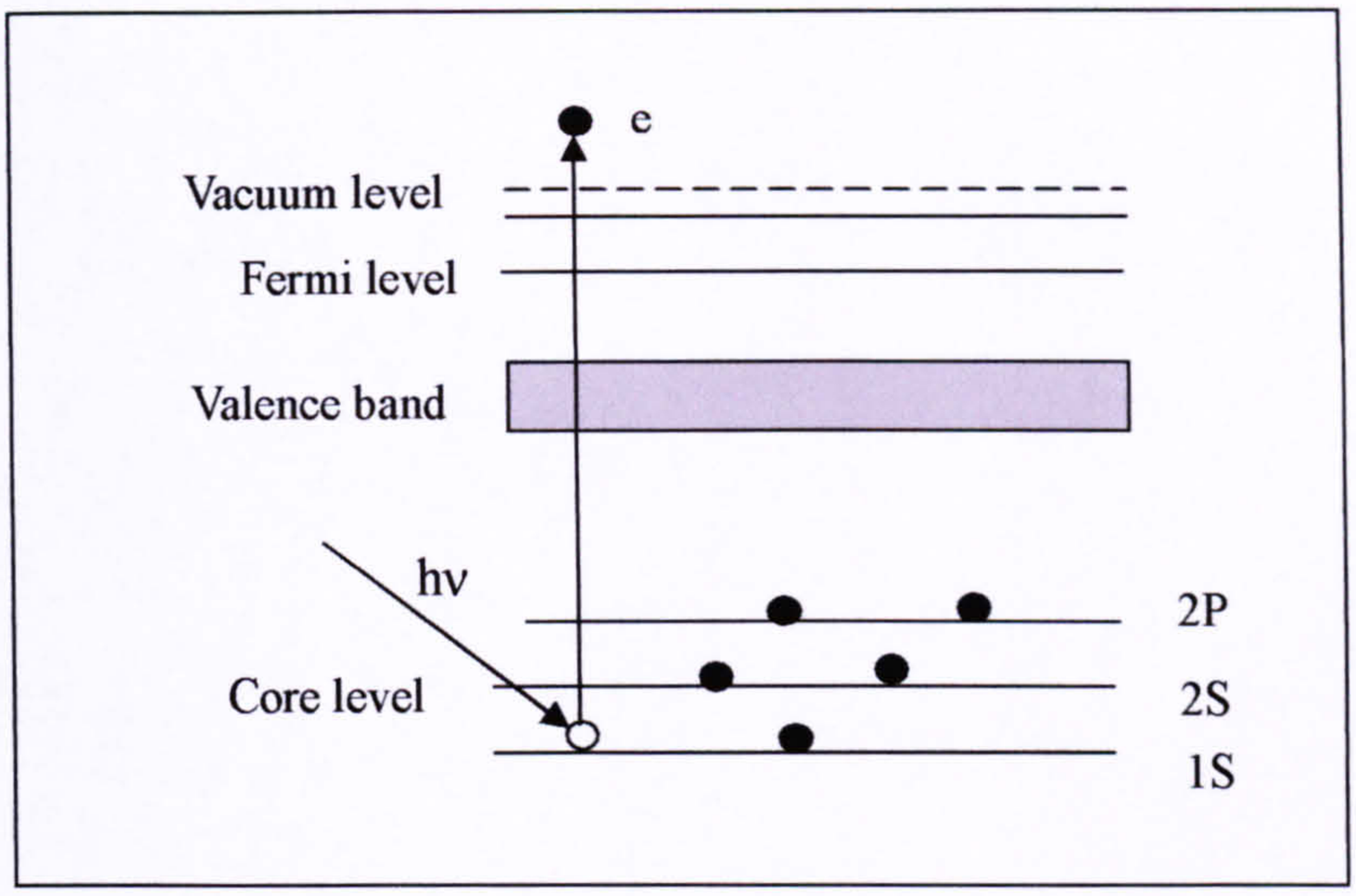

Figure 5.9 the process of a photoelectron emission [143]

When a X-ray photon ejects a core electron, the electron has to overcome the binding energy (E_b) to arrive the surface of the atom, see figure 5.10. Then the extra energy (E_{sp}) will be consumed for the electron escaping from the surface of atom to a conduction band. The whole energy that the core electron absorbs is the X-ray energy, hv. Therefore, we have the following formula to calculate the binding energy:

$$E_b = hv - E_c - E_{sp} \qquad \text{...Eq (5.21)}$$

in which E_c is photoelectron energy. Figure 5.10 shows the contributions of a photoelectron.

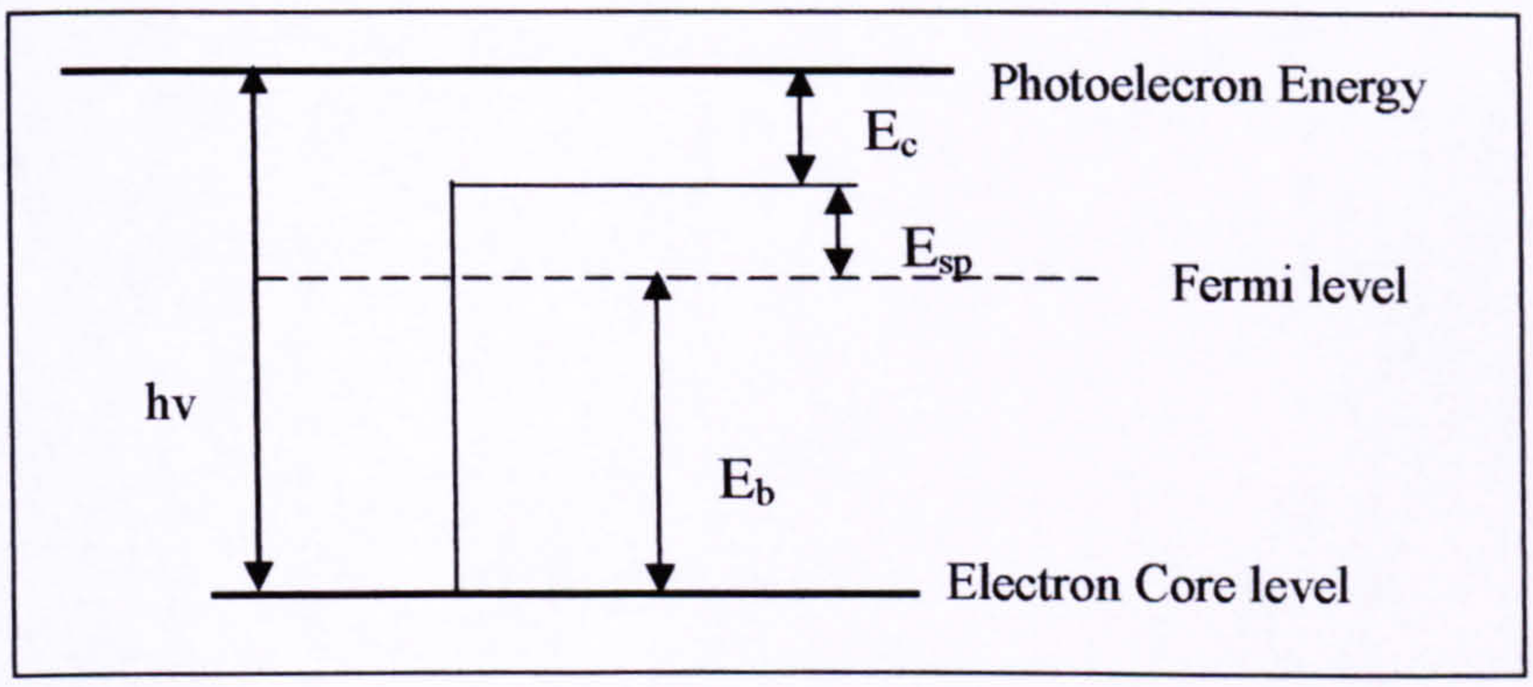

Figure 5.10 the energy constituents in the photoelectron emission process

Every XPS spectrum consists of a continuous line (see figure 5.11), resulting from the secondary electrons. The peaks are specific to the photoelectron, which will be analyzed. Every peak is named after the electronic level of which the photoelectron is emitted. Auger peaks may also appear in the spectrum.

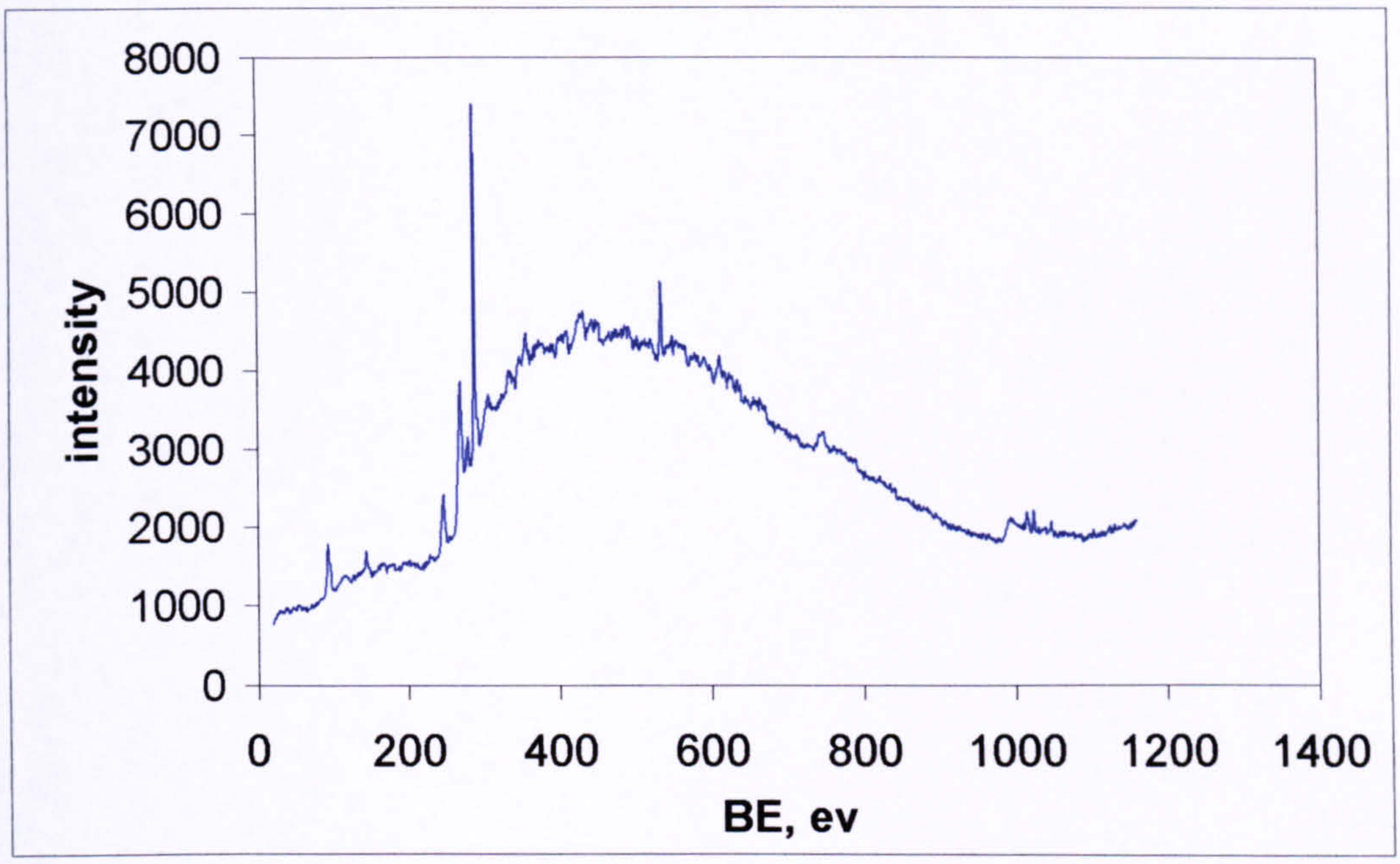

Figure 5.11 a typical XPS spectrum

5.3.5 Rutherford backscattering spectrometry (RBS)

It was found by Ernest Rutherford that high energy alpha particles (2MeV He^{2+}) could be elastically scattered back by the nuclei in the sample with the part of energy losses (website of the Centre for Industrial Technology Materials Analysis). The energy losses are dependent on the mass of the atoms from which the alpha particles are scattered, and the angle of the scattered particles, and the depth into the sample to which the particles travel before scattering. Thus, the backscattering alpha particles can be used to define the characterization of the heavier atoms in the sample and determine the elemental composition in the sample. Figure 5.9 shows a schematic RBS diagraph.

Backscattering can only occur form the atoms that are heavier than the helium ions.

For the atoms that are lighter than helium's will be elastic projected by helium ions. This measurement technique is called Elastic Recoil Detection (ERD).

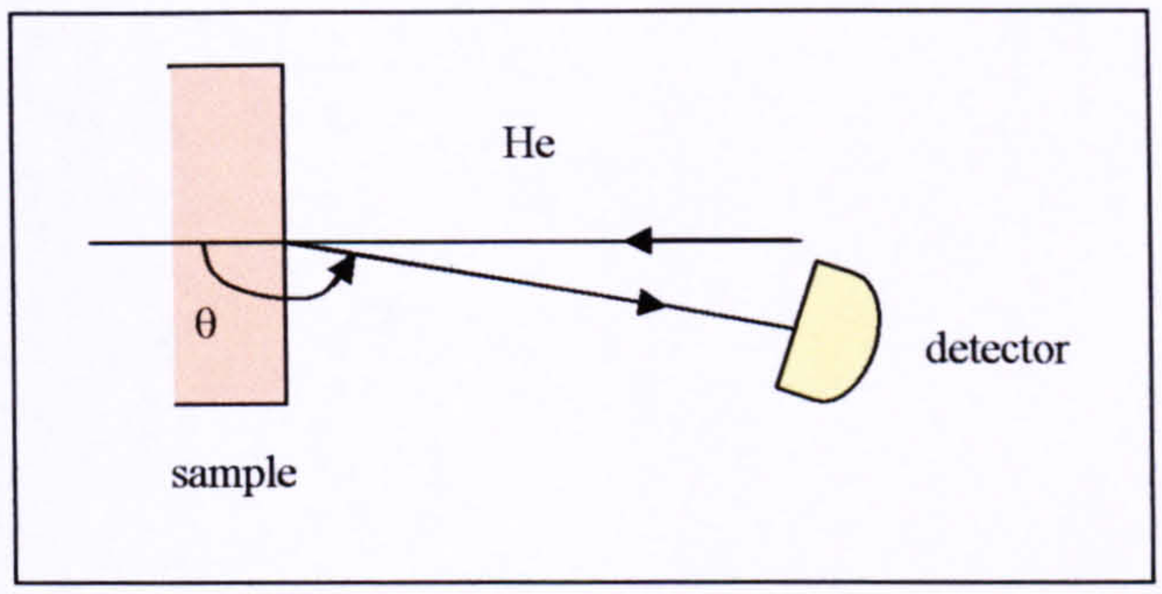

Figure 5.12 scattering geometry in a RBS (source from Centre for Industrial Technology Materials Analysis)

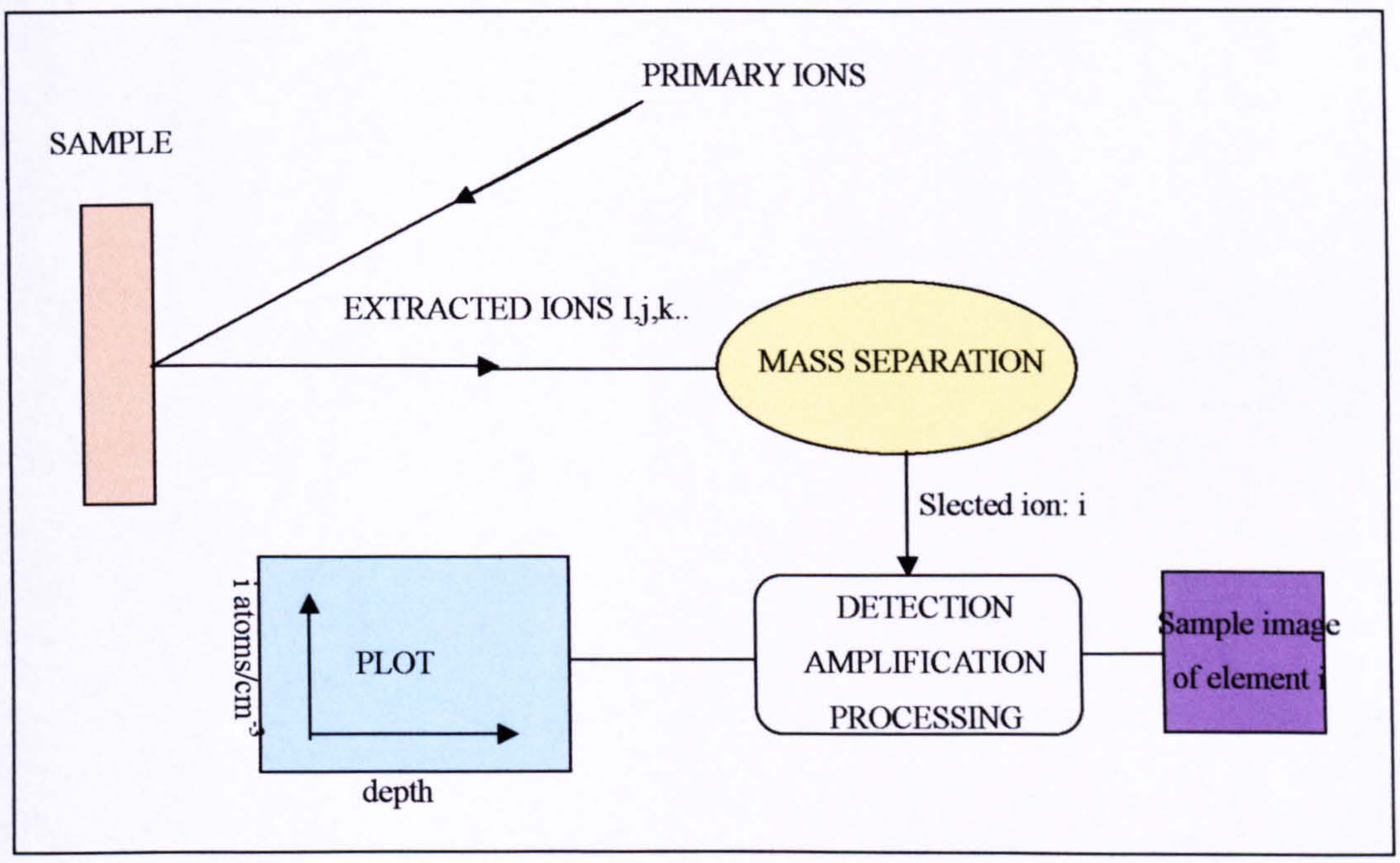

Figure 5.13 schematic representation of SIMS analysis (source from Centre for Industrial Technology Materials Analysis).

5.3.6 Secondary ion mass spectrometry (SIMS)

The principle of SIMS is shown in figure 5.13. SIMS is a technique used to obtain information on composition by bombarding the material with ions and identifying the

subsequent sputtered particles [143]. SIMS is a useful technique to study thin film compositions through depth. It can be seen that a primary ion beam sputters the sample surface to generate secondary ions, which are extracted from the sample. Then the extracted ions pass through the magnetic mass spectrometry to be separated. The signals of ions against depth, therefore are monitored in terms of ion-depth plots and ion elemental profiles. The further information on SIMS is not going to be detailed here because the analyses were carried out by Loughborough Surface Analysis Ltd.

5.4 Analysis of Coating Adhesion and Thickness

5.4.1 Scratch testing

Adhesion is the state in which two surfaces are held together by interfacial forces, such as valence forces (chemical bonding), interlocking forces (diffusion and pseudodiffusion etc.) or both. Adhesion can be measured either in terms of forces or work or energy. Scratch testing is a method used to measure the adhesion between the film and its substrate by measuring the maximum force per unit area exerted when the film and its substrate are separated.

A Teer Coatings ST-3001 Hardness, Scratch and Wear Tester was used to test the adhesions of the films to the substrates in this project. The basic processes of scratch testing are:

- Fixing the coated sample onto the moving sample table.
- Setting the loading rate and scratching speed to ensure that the critical load is reached. The loading rate and scratching speed depend on the substrate and film materials; a maximum load of 100N can be used on glass slides.
- Pulling a diamond indenter across the coated sample with the normal load gradually increasing until the coating spalls off. The frictional force via a load cell can be registered as the diamond scratches the surface. The load at the

spalling point is called critical load.

- The failure point can also be determined by acoustic emission monitoring, which detects cracking of the film. The point of cracking can be viewed with an integrated video camera.
- Repeating the above steps four times and calculating the average critical load.
- Pulling a diamond indenter with the constant load at the average critical load can be used to confirm the critical load.

A typical failure modes can be seen in figure 5.14 [28]. Six possible failure steps are included, whilst increasing the load onto the coated sample:

- Parallel cracks (1)
- Semi-circular cracks (2) along the parallel channel.
- External transverse cracks (3) at the edge of the scratch groove
- Coating chipping (4), which indicates that the cohesive failure of the coating occurs.
- Coating spalling (5) – the adhesive failure, and
- Coating breakthrough (6).

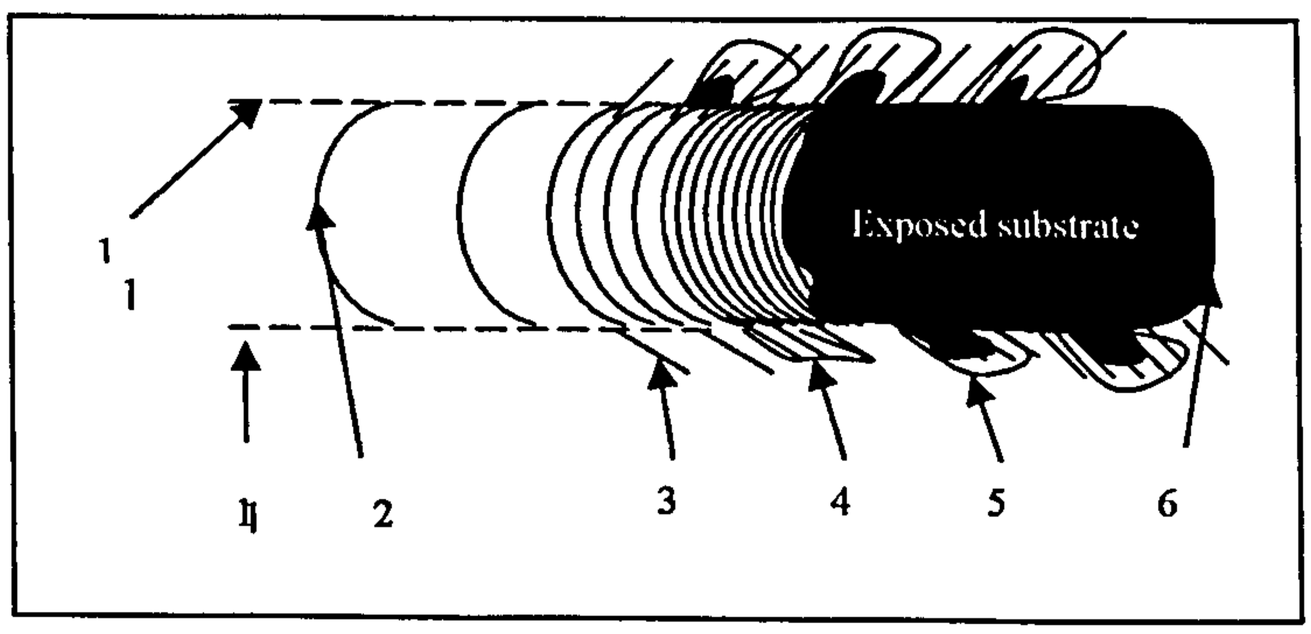

Figure 5.14 possible modes of scratch failure.

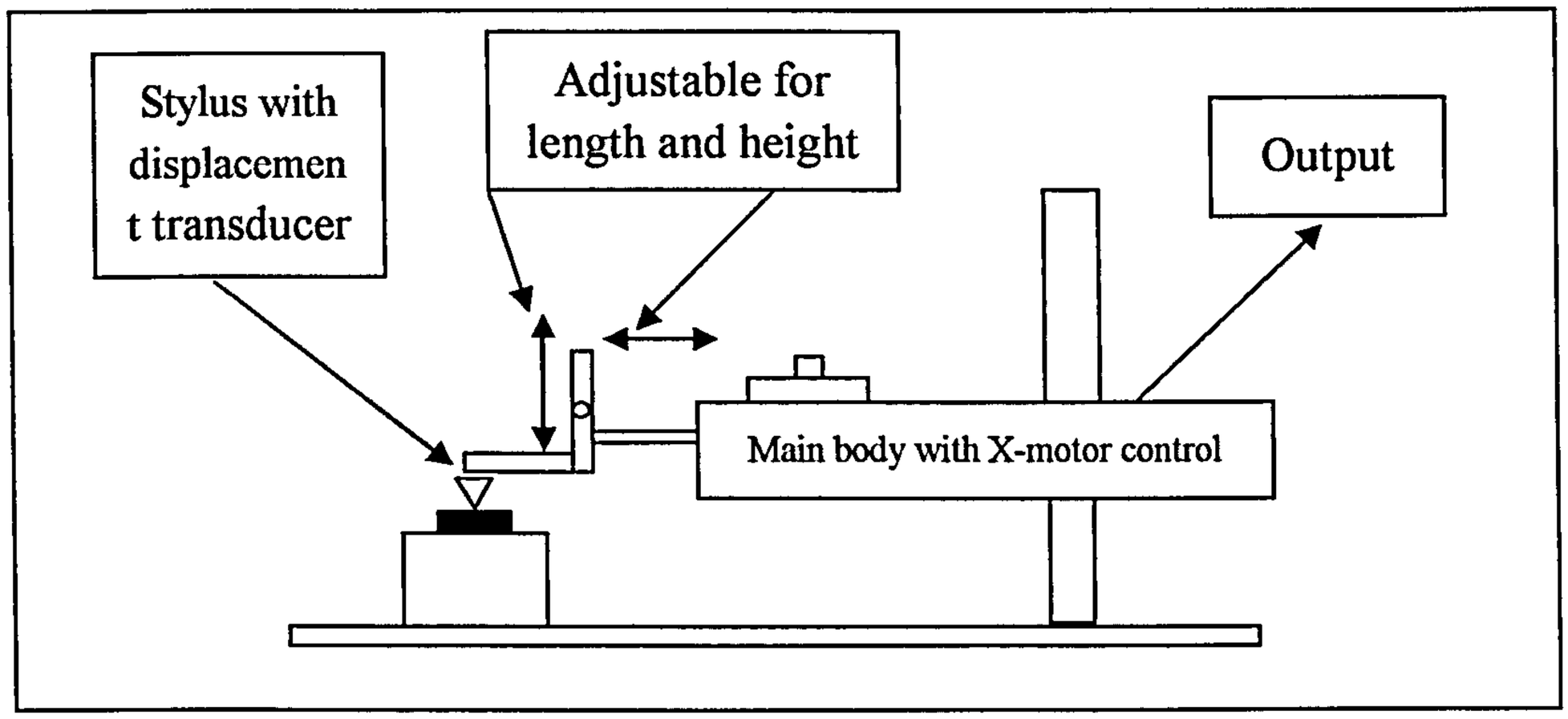

Figure 5.15 schematic representation of a Dektak

5.4.2 Surface profilometry (Talysurf/Dektak)

Surface profilometry (Talysurf/Dektak) is a technique in which a diamond stylus, in contact with a sample, can measure minute physical surface variations as a function of position to derive both surface roughness of the coating, and film thickness where partial masking is employed [28].

The Surface Engineering Group operates a Dektak^3 ST stylus surface profilometer for the measurement of surface topography. This instrument has the capability of measuring step height down to a few nm. The Dektak is controlled by a PC running Windows, making the system very easy to use. The software offers several data processing functions as well as image capture and storage. Figure 5.15 shows the schematically graph of a Dektak.

6. EXPERIMENTAL PROCEDURES

The aim of this project was to produce novel TCO coatings by magnetron sputtering from powder targets. In sputtering processes, the target is normally in the form of a solid plate of the material to be deposited onto a substrate as a film. Instead of using solid targets, metal or ceramic powder blends, which can be spread on the surface of a magnetron, are used as the targets. The first stage of the experimental works was to investigate the mixing method of the powders, and to produce the standard procedure of forming the targets.

The production of coatings, using zinc oxide and alumina powder as the targets, began with the investigation of the effective glass cleaning methods. The experimental arrays were designed using General Factorial and Central Composite design techniques to investigate cleaning techniques [144].

Secondly, to achieve the combined optimum electrical and optical properties of Al-doped ZnO coatings, Taguchi experimental arrays for annealing processes were designed and performed [145].

Thirdly, the traditional one variable method was used in the dopant runs, in which the different dopants and their compositions were chosen as the impurities of zinc oxide powder, and the effect of different dopants and their concentration on the coatings properties were studied.

General Factorial Design was then used again to characterize the voltage waveforms of the target and substrate, and to investigate the effects of pulse frequency and duty of the pulsed DC power supply on the thickness of coatings in the CFUBMS configuration rig. To further investigate the characteristics of this rig, the top dummy

magnetron was removed and ZnO:Al coatings were produced in UBMS configuration by both pulsed DC and DC power supplies. The effects of both magnetic configurations on the structure of the coatings were compared. Moreover, the ion saturation curves and self-bias voltages were measured in both CFUBMS and UBMS configurations.

ITO coatings were produced, using the same pulse parameters as ZnO coatings, by the traditional one variable method. Target compositions were chosen to match commercially available ITO films, such as 5at% and 10at% tin. The properties of the ITO coatings were analyzed and compared with those of the Al-doped ZnO coatings. As the blends were easy to mix and the powder targets were easy to prepare, further explorations were carried out to produce multi-component coatings, in which the experimental arrays were based on the one variable method.

In this chapter, therefore, the General Factorial Design, Response Surface Central Composite Design and Taguchi analysis technique will be briefly described. The methods and procedures used for target preparing, sample preparing or cleaning and coating producing will be detailed as well.

6.1 General Factorial Design, Response Surface Central Composite Design and Taguchi Analysis Technique

6.1.1 General Factorial Design

General Factorial Design is one of the Factorial Designs in the DX 6 Design Expert Package [146]. There can be 1 to 12 factors in this design where each factor may have a different number of levels. All factors in this design will be treated as categorical. Therefore, the response surface design may be chosen if some factors are numeric. This design technique was used in the parameter runs, which can be referred from

section 6.5.

6.1.2 Response Surface Central Composite Design

Response Surface Central Composite Design is one of the experimental designs in DX 6 Design Expert Package, which is based on Factorial Design. Five levels are needed per variable, which can be located on the surface of a sphere with the standard point at the centre. For two variables, the design can be in one block with 13 experimental runs or in two blocks with 14 experimental runs, depending on the number of replication runs at centre point. The array for two variables and five levels can be seen in the glass substrate cleaning runs [Appendix I]. The properties or characteristics of the coatings from the samples, we call responses in the design, can then be input into the statistics software to be analyzed, which will help to decide the most desirable run parameters.

6.1.3 Taguchi Analysis Technique

Taguchi analysis technique [145] is an experimental method in which fractional factorial arrays are developed from full factorial arrays (i.e. all possible combinations of variables) to reduce the number of experiments needed to be carried out, whilst obtaining an almost equal amount of information. The array may contain a number of variables, each at a number of levels. For example, a full factorial investigation of four variables at three different levels would require 3^4 experiments due to the possible combinations of the variables. By using of Taguchi design, there would be only nine experiments required. The reason for the large reduction in the number of experiments is that only main effects of each variable are investigated. The influence of each variable can be determined in terms of specific coating characteristics, we say responses in the design, by entering them into Taguchi analysis of variance software (ANOVA – TM). The level averages for each variable or factor for each response, e.g. resistivity as a response in this project, can be calculated and used to predict the optimum combination of variables. The level averages are simply the average value of

the response at each level (these can be numerical levels, i.e. 'low', 'medium', or 'high', or categorical levels) for each variable, or factor tested in the array (e.g. annealing time, annealing temperature, etc.). When expressed graphically for each response investigated, the significance of the factor becomes apparent from the gradient of the level average graphs, with the most significant factor having the largest gradient (positive, or negative). Zero, or low gradients means that the factor has no significant influence on the particular response. The optimum combination of factors to maximise, or minimise a response are selected on the basis of the level averages. Use was made of this experimental method in the annealing runs in this project, in the form of a L9 array, which can be referred from the section 6.3.2.

6.2 Sample Preparation

Standard commercial glass slides, both soda-lime and BK7 were used in this project. The experiment results for the substrate glass cleaning can be seen in Appendix I. The Factorial design and Central design were used in these experimental arrays, referred in Appendix I. In the following experiments in this project, the glass slides were polished by 'Windowlene' (a commercial window glass cleaner), or solvents, such as IPA or acetone, to smear free finish, followed by air blowing to remove the tissue dust. A pen line was drawn across the centre of the glass slide to prevent the coating sticking onto the substrate in this region. The removal of the pen line after the deposition run, using acetone or IPA, produced a step from which coating thickness measurements were made by surface profilometry.

The substrate was then fixed on the substrate holder, which was insulated from the dummy magnetron and connected to the radio frequency (RF) power supply. The chamber was pumped down to a base pressure lower than $2x10^{-3}$Pa (as measured on the Penning gauge). High purity argon was then introduced into the chamber to increase the pressure to 0.08Pa (Baratron gauge) and the substrate was RF sputter

cleaned to provide effective atomic scale cleaning. The RF power was set to 150W for 15min, which allowed contaminants on the surface of the substrate, such as grease, to be sputtered away.

6.3 Standard Deposition Parameters and Annealing Procedure

6.3.1 Standard deposition parameters

On completion of the in-situ substrate cleaning, the chamber pressure was further adjusted with high pure argon to 0.4Pa. At the same time, varying amounts of oxygen, depending on the specific run conditions, were also fed into the chamber to compensate for its loss during the deposition runs and, therefore, to maintain coating stoichiometry. As the main variable in this project was target composition, most of the deposition runs were carried out at constant values of substrate to target distance, chamber pressure, oxygen flow, target current, frequency and duty. The exception being one set of investigations that were particularly aimed at the deposition parameters. Table 6.1 shows the typical deposition conditions of a run.

Table 6.1 A typical conditions of a deposition run

<table>
<tr><td rowspan="2">Run number and date</td><td rowspan="2">Target (wt%) (g)</td><td colspan="3">Power supply</td><td rowspan="2">Time off (μs)</td><td rowspan="2">Run hours (h)</td></tr>
<tr><td>Current (A)</td><td>Voltage (V)</td><td>Frequency (KHz)</td></tr>
<tr><td>5
09/12/02</td><td>$ZnO+Al_2O_3$
3% (at)</td><td>2</td><td>300</td><td>350</td><td>1.1</td><td>1h</td></tr>
<tr><td rowspan="2">Bias voltage (V)</td><td rowspan="2">Argon (FRS)</td><td rowspan="2">Oxygen (FRS)</td><td colspan="4">Sputtering pressure</td></tr>
<tr><td>Basic (mbar)</td><td>After Ar and O_2 (mbar)</td><td>Sputtering (mbar)</td><td>mid run (mbar)</td></tr>
<tr><td rowspan="2">-</td><td rowspan="2">87</td><td rowspan="2">20</td><td>$2.4*10^{-5}$</td><td>$8.5*10^{-3}$</td><td>$1.0*10^{-2}$</td><td>$8.5*10^{-3}$</td></tr>
<tr><td>$8.0*10^{-5}$</td><td>$2.30*10^{-3}$</td><td>$1.6*10^{-2}$</td><td>$2.30*10^{-3}$</td></tr>
<tr><td colspan="7">Conditions: RF cleaning and heating: 150W (23-27) – 12min, the amount of argon is controlled to 35FRS, and the pressure is controlled within $2.34*10^{-3}$mbar ($8.5*10^{-4}$mbar by baratron gauge).

Problems:
Next step:</td></tr>
<tr><td colspan="7">Notes:
The distance between substrate and target is 135mm.
The pressure in the lower line is read from Baratron gauge. The pressure in the higher line is read from Penning gauge.</td></tr>
</table>

In the table, FRS is the full range scale of the gas flow controller. The cleaning conditions and any problems encountered during the run were also recorded in the table. Substrate to target distance and deposition pressure was fixed in most of the runs, which were recorded in the notes line in case there was any change.

The pulsed DC power supply was run in the constant current mode, so the target voltage was read from the power supply display, and current was set before the run began, see table 6.1. Moreover, the flow rates are 35sccm (ml/min) and 10sccm for the argon controller and oxygen controller, respectively, when both of the controllers are set up at full scales.

6.3.2 Annealing parameters

To further achieve the lower resistivity of the coating, annealing processes were investigated according to the Taguchi Analysis Technique. The annealing parameters chosen were atmosphere (mainly the amount of oxygen), temperature and time. Three levels were set per variable, see table 6.2. Table 6.3 shows the format of the Taguchi Arrays. To achieve the fixed chamber annealing pressure – 50Pa, pure nitrogen was backfilled besides partially backfilled oxygen, the amount of which were set according the conditions of experimental arrays.

Table 6.2 The annealing parameters and levels

Level	Time (h)	Temperature (°C, ±10)	Atmosphere (FRS)
Level 1	1	270	0
Level 2	2	360	24%
Level 3	3	470	98%

Note: temperature in the table indicates the substrate temperature.

Table 6.3 The Taguchi annealing arrays

Run No.	Time (h)	Temperature (°C, ±10)	Atmosphere (FRS=10sccm)
E1	L3	L3	L1
E2	L3	L2	L2
E3	L3	L1	L3
E4	L2	L3	L2
E5	L2	L2	L3
E6	L2	L1	L1
E7	L1	L3	L3
E8	L1	L2	L1
E9	L1	L1	L2

At least two substrates can be fixed onto the substrate holder in one run. Five runs were committed at same deposition parameters and conditions, and therefore ten as-deposited samples were obtained. One of the as-deposited samples was kept as comparison. The others were then fixed on the substrate holder again for annealing treatment according to the Taguchi arrays. The chamber was pumped down to

$2x10^{-3}$Pa again. According to the annealing conditions, different gases (nitrogen and oxygen) were fed into the chamber for the annealing runs. The substrate to heater separation was 30-40mm. There were two thermocouples in the chamber, one fixed on the heater, the other one near the surface of the substrate, to monitor the temperatures on both heater and substrate. The heater power was also monitored during annealing. Again, a typical annealing parameters chart is shown in table 6.4.

Table 6.4 A typical annealing conditions of annealing runs

RUN 9

Annealing: 5mbar<P<1atm;
Gas: 24% (FRS) O2 + N2
T (heater) = 500-510°C T (sub) = 256°C (from thermocouple)
300<T<335 (from crayon cream pencil)
V = 135-140V I = 2.7-2.9A
t = 1h (soaking)

Result:
transparency=0.9 (P)
Resistivity = $4.53*dV/I=4.53*5*10^{-5}*(1.2\text{-}9)*10^{-3}/0.01*10^{-6}$= 27-220 Ωcm (centre—edge)
(The thickness is measured by Dektak3ST)
Preferred direction:

Note:

Pink—grey at 295°C; light purple—grey at 320°C; yellow brown—red brown at 300°C; aqua green—did not change the colour (white buff at 360°C); dark violet—light violet at 320°C and did not change colour to white buff (at 460°C); organ brown—black at 245°C and did not change the colour to white buff (505°C)

The amount of O2 is 10* 24%*60(min)=144ml during annealing.

There was a problem during the annealing runs, which was that the heater frequently failed. The conclusion from the annealing runs was that the optimum annealing parameters were high temperature, certain annealing time and pure nitrogen atmosphere, i.e. without extra oxygen atmosphere. However, in order to avoid breaking the heater, the annealing was carried out, from the dopant runs, under vacuo instead of in nitrogen atmosphere to avoid any chance of re-oxide the wires in the heater. Table 6.5 shows a typical annealing parameters of dopant runs.

Table 6.5 A typical annealing conditions of a dopant run

Dopant annealing run 5
Annealing: Pbasis=$3.4*10^{-6}$ (0 mbar from baratron) ; T (heater) =600°C Ts= 500-515°C (from thermocouple) V = 165V I = 3.4 A t = 2h (soaking)
Result: Transparency = Resistivity = $4.53*dV/I=4.53*8*10^{-5}*\ 5.39*10^{-3}/1000*10^{-6}=1.95*10^{-3}$ Ωcm (The thickness is Dektak3ST)
Preferred direction:

6.4 Dopant Runs for Zinc Oxide Coatings

Several materials in terms of the positions at which they located in the periodical table of the elements were chosen to be dopants in the ZnO coatings. As a comparison with aluminium, gallium and indium, which belong to the same group III in the periodical table, were doped into zinc oxide coatings by mixing zinc oxide with gallium oxide, or indium oxide, respectively. Also, tin oxide and antimony oxide were used to compare with indium oxide because they are located in the same period in the periodical table. Three doping levels were set, i.e. 1at%, 3at% and 5at% of the metal element. Therefore, fifteen deposition runs were carried out under the deposition parameters, which were described in section 6.3. It should be noted that the deposition conditions were kept the same during all the fifteen runs.

Fifteen deposited samples, which were selected one from each run, were annealed under the same conditions. Therefore, the annealed coatings could be used to prove the influence of different dopants and their concentration on the properties of the films. As detailed before, the as-deposited samples were fixed on the substrate holder at a distance of 30-40mm from the heater. The chamber was then pumped to the pressure lower to $2x10^{-3}$Pa. The annealing was carried out in vacuo and the heater temperature

was set to a maximum of 600°C to avoid breaking the heater. The soaking time lasted for two hours, which was the optimum annealing parameter shown from annealing runs. All the parameters of the dopant annealing process can be referred from table 6.5.

6.5 General Factorial Design for Parameter Runs of Zinc Oxide Coatings

The aim of the parameter runs was to find out the influence of the deposition parameters on the coatings, specifically for the configuration of this powder rig. First, voltage waveforms at the powder target were used to monitor different settings of pulse frequency and duty. The Al-doped zinc oxide coatings were prepared at various frequencies and duties to investigate the effect of these variables on the properties of the coatings. TDK P5100 voltage probes were attached to the substrate and target and the voltage waveforms were monitored and recorded using a Tektronix TDS 3014 digital phosphor oscilloscope. This set of experiments was carried out according to the 3-level factorial design arrays with two replicates. Table 6.6 shows the array design. In the analyses of the results, the overshoot voltages on the powder target and the coatings thickness, which were identified as being the most significant effects of the pulsed parameters on the characteristic of the coatings. These responses were then analysed in more detail.

It was mentioned in chapter 2 that substrate self-bias potential and saturation ion current are two basic important physics terms of a plasma used in a deposition system. Concurrent bombardment of the growing film by a high flux of low energy ions is known to be beneficial in the production of dense coatings. In situations where no external bias supply is used, the substrate self-bias potential establishes the energy of the ions, and the saturation ion current drawn at the substrate is an indication of the ion flux. Consequently, the next part of the experiments in this project was designed for

the measurement and comparison of them under both closed field and single magnetron configurations.

Table 6.6 Two factors General factorial design arrays on the parameter runs

Std	Run	Block	Factor 1 Frequency kHz	Factor 2 Duty %	Response Thickness (nm)
3	1	Block 1	275	50	
17	2	Block 1	350	75	
15	3	Block 1	275	75	
11	4	Block 1	350	62	
5	5	Block 1	350	50	
9	6	Block 1	275	62	
7	7	Block 1	200	62	
13	8	Block 1	200	75	
1	9	Block 1	200	50	
18	10	Block 2	350	75	
6	11	Block 2	350	50	
8	12	Block 2	200	62	
10	13	Block 2	275	62	
14	14	Block 2	200	75	
16	15	Block 2	270	75	
12	16	Block 2	350	62	
2	17	Block 2	200	50	
4	18	Block 2	275	50	

The substrate self-bias potential is referred to as the probe or substrate voltage measured at the point of zero net current in the I-V characteristics curve, i.e., the point at which equal fluxes of ions and electrons arrive at the probe or substrate. In this project, the substrate self-bias potential was measured at the MDX DC bias supply with the magnetron operating and no bias voltage applied (i.e., the bias supply was acting as voltmeter). Measurements were made over a range of target currents and substrate-to-target separations in the 'normal' operating configuration, i.e., with the dummy magnetron installed to form the closed magnetic field, and the single magnetron configuration, with the dummy magnetron removed. Three levels of target current (1, 1.5 and 2A), and substrate-to-target separation (10, 15 and 40cm) were selected.

The saturation ion current can be determined by biasing the substrate because the probe theory assumes that all the electrons approaching the substrate will be repelled and the constant ion current can be measured if the negative bias is sufficiently large, over -100V in magnetron sputtering [13]. The measurements of the substrate current were actually carried out following the measurements of substrate self-bias potential at the same levels of variables and configurations. In each configuration and each substrate-to-target separation, the substrate bias voltage, supplied by the Advanced Energy MDX unit, was increased form -10v to -200V in steps. At each step, the total current drawn at the substrate was recorded from the MDX.

In this part of work, stainless steel (304) powder was used in these measurements, instead of the poorly conducting zinc oxide powder, to allow operation in DC mode. This was chosen to make the ion current measurements straightforward. In the experiments, the Advanced Energy Pinnacle Plus was connected to the target with the pulse frequency set to zero. The Advanced Energy MDX DC driver was connected to the substrate to supply the bias voltage and read the subsequent ion currents.

In order to show the effect of magnetron configuration and power supply on the structure and properties of the coatings, zinc oxide and alumina mixture was used again as the targets to deposit the Al-doped zinc oxide coatings. The first three runs were operated under UBM configuration by pulsed DC power supply with 3 different substrate-to-target separations. Then another two runs were operated under UBM and CFUBM configuration, respectively, by DC power supply. The results will be given in the next chapter.

6.6 ITO Coating Runs

The ITO coating runs were performed under the standard deposition conditions of pulse frequency, duty, current, and the argon flow rate. Only the oxygen flow rate was

chosen to be a variable. The powder targets were formed by mixing blends of indium oxide and tin oxide with tin contents of 5at% and 10at%. These compositions are commonly used for solid targets in commercial coatings. The blends of ITO were mixed in the same way as the zinc oxide and aluminium oxide powders.

In the runs, tin content in the targets or the coatings and the oxygen flow rate were the two variables, with 2 and 3 levels, respectively. Again, traditional one variable methods were used in this piece of work, which means six experiments were carried out. The resulting properties of the ITO coatings will be detailed in chapter 8 and the discussion will be given in chapter 9.

6.7 Multi-component Coating Runs

The multi-component coatings were also produced using the standard deposition parameters, and the oxygen flow was again chosen as a two-level variable.

The blends were mixed from ITO (5at% Sn) and ZAO (3at% Al) powder mixtures (these components were chosen on the basis of results from the previous sets of experiments). It has to be emphasized that the two kinds of the mixtures have significantly different characteristics. ITO powder was very loose, whereas the ZAO powder tended to be clumped together, making it very difficult to mix them uniformly. To solve this problem, ZAO powder was baked in an oven above 100^{O}C over night, and rolled by a ramp carefully before being poured into the ITO powder. Then a bottle with the mixture was put on a rotary drum for several hours, as before. This was not a perfect method to mix these two kinds of powders. Therefore, care was needed when the targets were formed, to ensure that the powder was carefully tamped to avoid non-uniformities as far as possible.

The coating blends were set at 4 levels, which were calculated by indium and zinc

atomic ratios. The four blends compositions were zinc oxide, aluminium oxide, indium oxide and tin oxide with the atom ratio of zinc: indium being 1:4; 2:3; 3:2 and 4:1, respectively. Therefore, four levels of the coatings or targets compositions at 2 levels of the oxygen flow amounted to 8 runs to complete this stage of the work, according to the traditional one variable method. Again, the results and discussion will be detailed in chapter 8 and 9.

6.8 Summary

In this project, the following parameters were varied or measured, as required. The variable parameters were not same in each set of design arrays. In total, they are:

- RF bias power,
- Time of RF sputter cleaning
- Coating annealing temperature,
- Coating annealing atmosphere - mainly the amount of oxygen,
- Coating annealing time,
- Dopant elements and their concentrations,
- Deposition atmosphere – oxygen content,
- Pulse frequency,
- Pulse duty,
- Magnetron configuration,
- Sputtering power – pulsed DC or DC
- Substrate-to-target separation,

The analysis of the coatings involved the following responses:

- Resistivity of the coatings,
- Transmittance of the coatings,

- Structure of the coatings,
- Orientation or texture of the coatings
- Lattice strain,
- Adhesion of the coatings to substrates,
- Deposition rate,
- Saturation ion current and I-V characteristics of the rig,

After all the investigations, the information provided from the experimental results or responses would help to understand the unique configuration of the powder rig – the CFUBMS and pulsed DC power. Also, the relationship of the properties of the coatings and deposition, annealing parameters would be understood.

7. RESULTS 1: CHARACTERISTICS OF THE POWDER RIG

As described in chapter 4, the powder rig was especially set up for the use of powder targets. The 'sputter-up' unbalanced magnetron used strong rare earth magnets to give a high field strength (2.2kG) at the target, and a dummy magnetron was used in the chamber roof to produce a closed magnetic field. Combined with the pulsed power supply, dense columnar, defect-free TCO coatings were prepared in this rig from powder targets. To understand the advantages of the powder rig, the effect of the configuration of the magnetron and the power supply has been investigated. The results are presented in this chapter.

7.1 The Characteristics of the Plasma in the Powder Rig

The substrate self-bias potential, V_{sb}, varied from –13V to –23V, appeared to depend on all the variables tested, except the target current (figure 7.2). The influence of the target-to-substrate separation and the magnetron configuration on the substrate self-bias potential is shown in figure 7.1. It can be seen that the target-to-substrate separation has a stronger influence on the substrate self-bias potential in the single drawn further away from the target in the closed-field magnetron configuration than the unbalanced one. In fact, the current on the substrate was too weak to be read no matter how high the bias voltage applied at the target-to-substrate separation of 40cm in the single magnetron configuration. Therefore, it can be assumed to be zero. Moreover, the self-bias potentials at the separation of 10cm are the same both in the double and single magnetron configuration conditions, this implies that the strength of the unbalanced magnetron dominates the ion flux arriving onto the substrate when the substrate is close to the target. This result confirms, as discussed in chapter 2, that the closed-field unbalanced magnetron configuration helps to prevent the losses of

electrons from the plasma and confines the electrons along the magnetic flux lines towards the substrate, therefore drawing the ions from the target and forming a dense unifom plasma further away from the target than in the single unbalanced magnetron configuration.

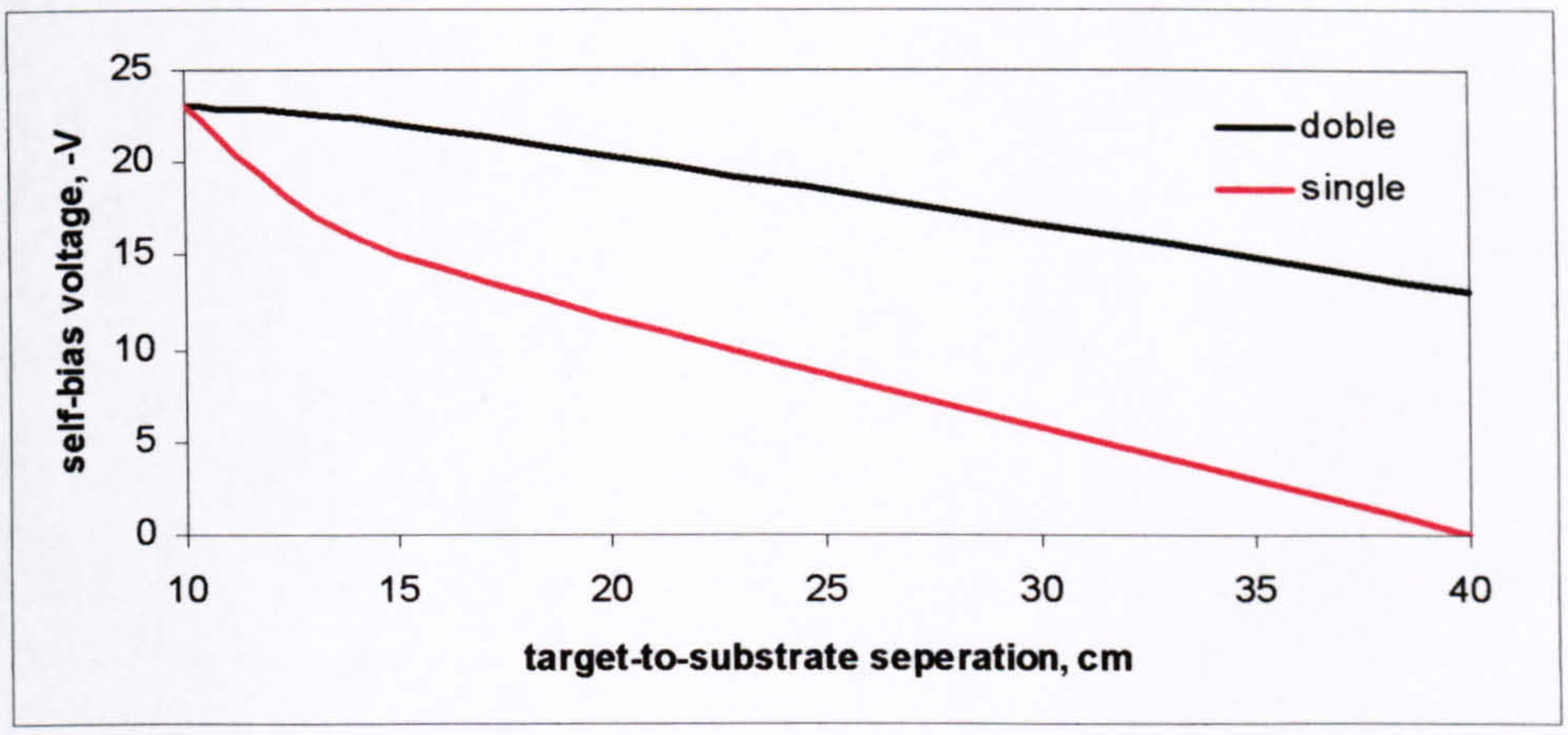

Figure 7.1 The effect of target-to-substrate separation on substrate self-bias potential under double and single magnetron configuration conditions

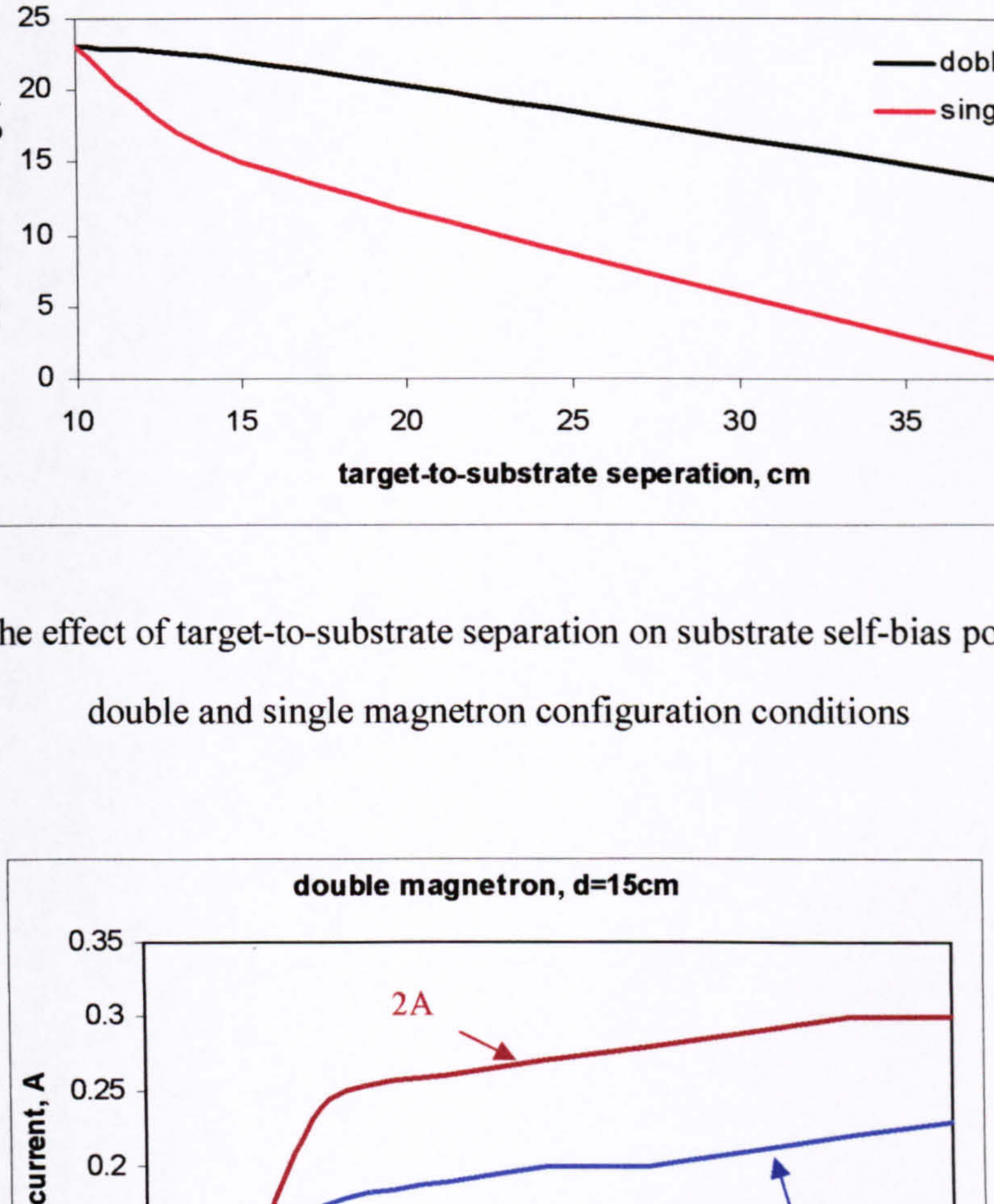

(a)

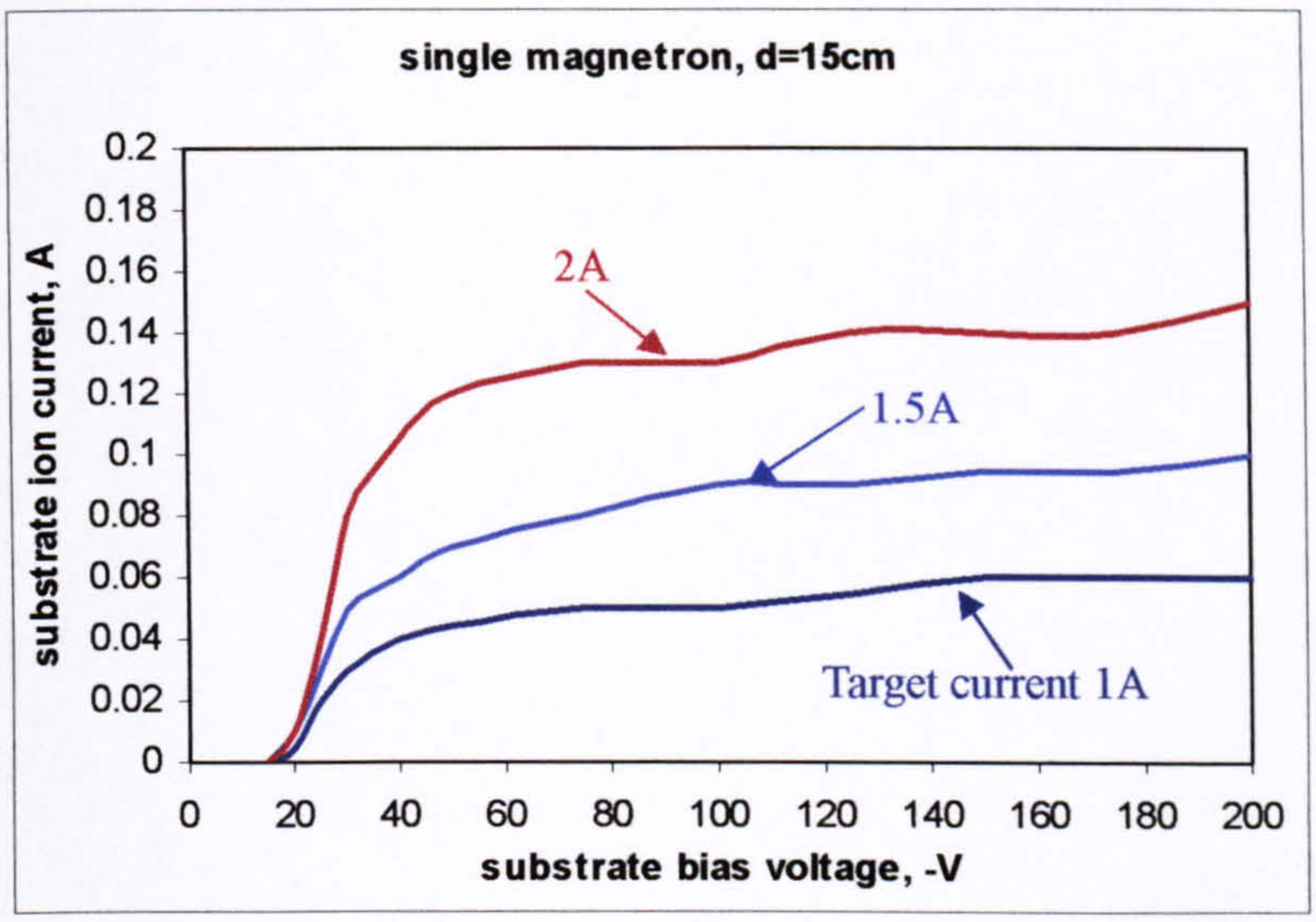
single magnetron, d=15cm
substrate ion current, A
substrate bias voltage, -V
0.2
0.18
0.16
0.14
0.12
0.1
0.08
0.06
0.04
0.02
0
0
20
40
60
80
100
120
140
160
180
200
2A
1.5A
Target current 1A

(b)

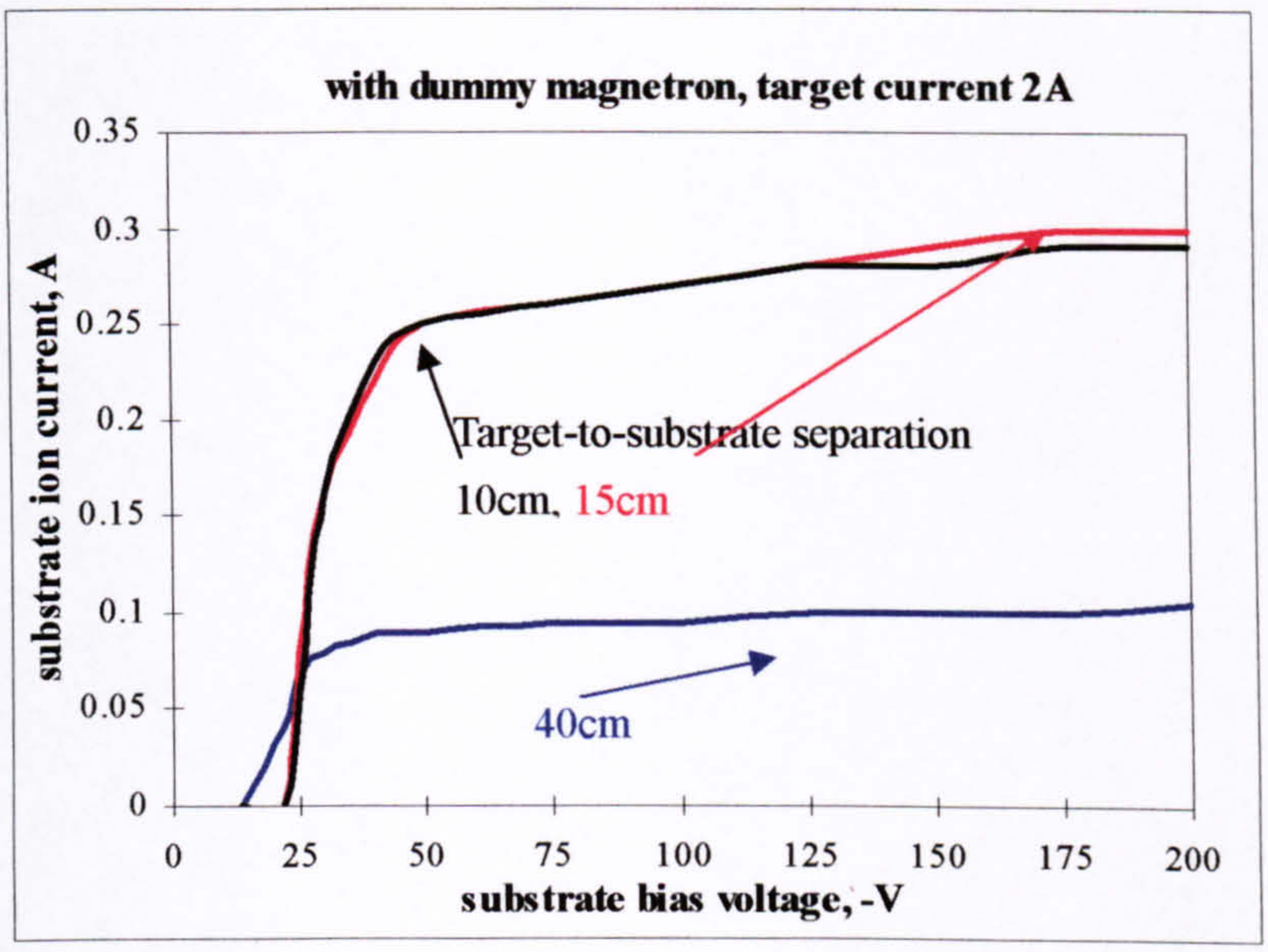
with dummy magnetron, target current 2A
substrate ion current, A
substrate bias voltage, -V
0.35
0.3
0.25
0.2
0.15
0.1
0.05
0
0
25
50
75
100
125
150
175
200
Target-to-substrate separation
10cm, 15cm
40cm

(c)

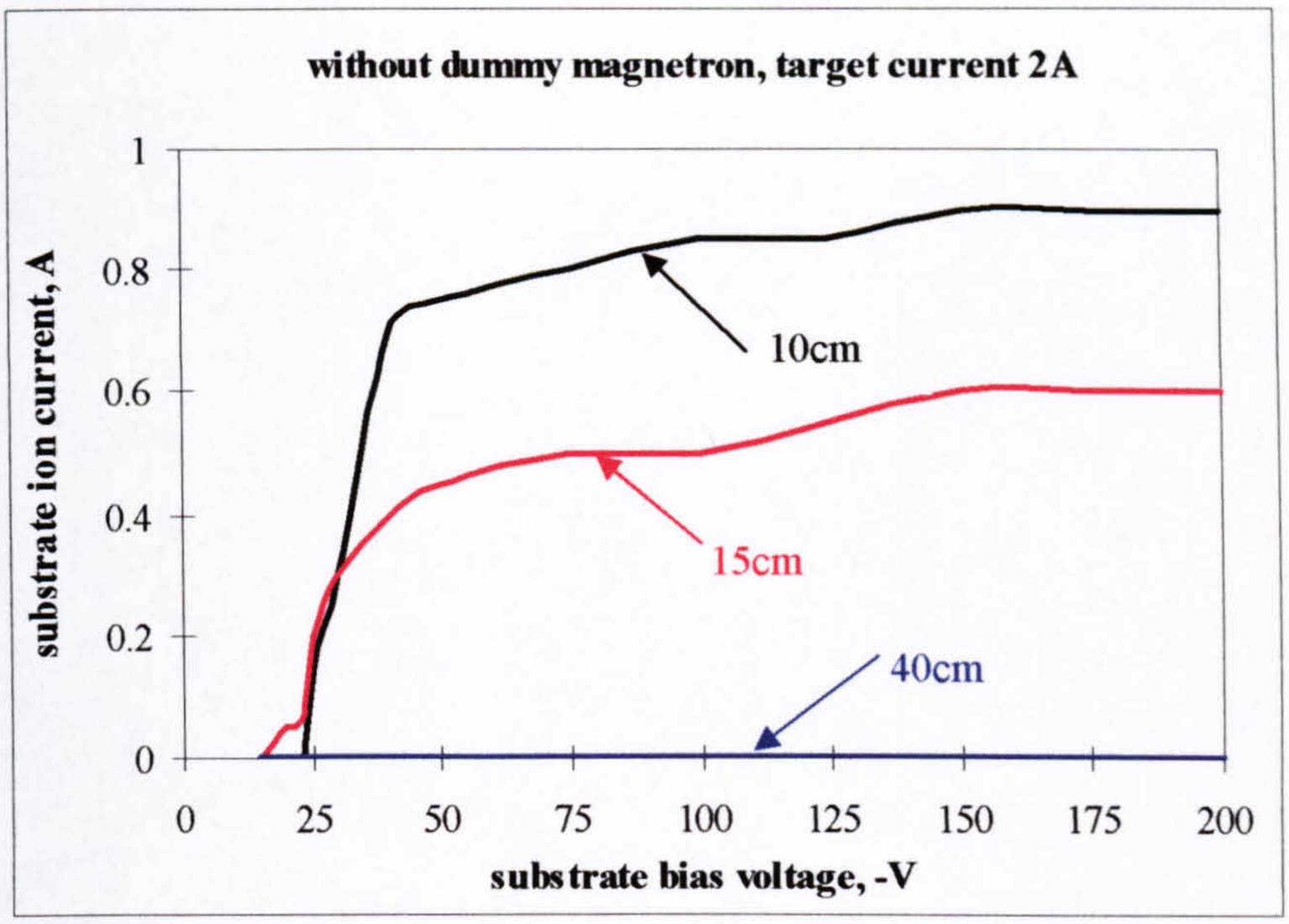

(d)

Figure 7.2 The substrate I-V characteristics under various conditions

The relationships between the substrate bias voltage and the current drawn at the substrate were investigated over the range of target currents and target-to-substrate separations mentioned earlier, and under both double and single magnetron configurations. Figure 7.2 shows the effect of the target current and the target-to-substrate separation on the substrate I-V characteristics under different test conditions. All of the four I-V curves give the same trends: 1) from figures 7.2a and b, the substrate ion current is dependant on the target current – increasing with increasing target current. Also, the substrate current changes as the magnetron configuration and the substrate-to-target separation change, see figures 7.2c and d. The substrate ion current is highest in the double magnetron configuration at the shortest separation. This fact can be true because the target current affects on the ion current flux only, whilst the substrate-to-target separation and magnetron configuration influences the ion energy arrived on the substrate – the self-bias potential. 2) The ion saturation current increases with increasing target current and decreases with increasing substrate-to-target separation. There is an exception that the ion saturation currents are the same when the separations are 10cm and 15cm in the double magnetron condition. Therefore, it can be said that the plasma is more uniform

further away from the target in the double magnetron condition than in the single one. Again, at each target current, the substrate ion saturation current is highest in the double magnetron configuration at the shortest substrate-to-target separation.

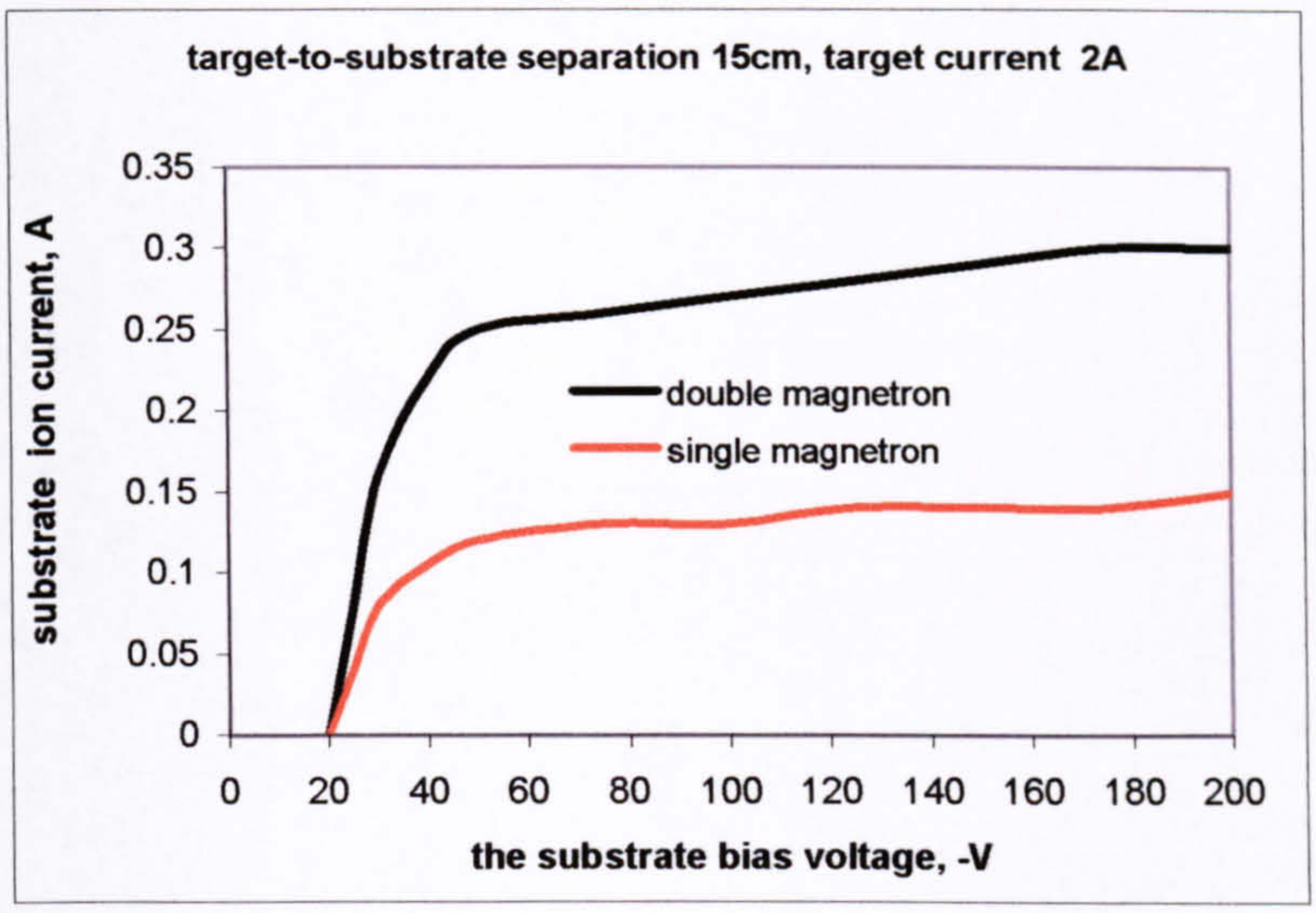

Figure 7.3 the effect of magnetron configuration on the substrate I-V curve

The influence of the magnetron configuration on the substrate I-V curve can be inferred from figure 7.3. As can be seen, the saturation current is a factor of at least two higher in the double magnetron configuration than in the single magnetron configuration at the same target-to-substrate separation, i.e., the installation of the dummy magnetron has more than doubled the effective ion current drawn at the substrate.

The effect of the target-to-substrate separation on the substrate I-V curve is shown in figure 7.4. Again, the closer the substrate to the target is, the higher current drawn at the substrate will be under same conditions.

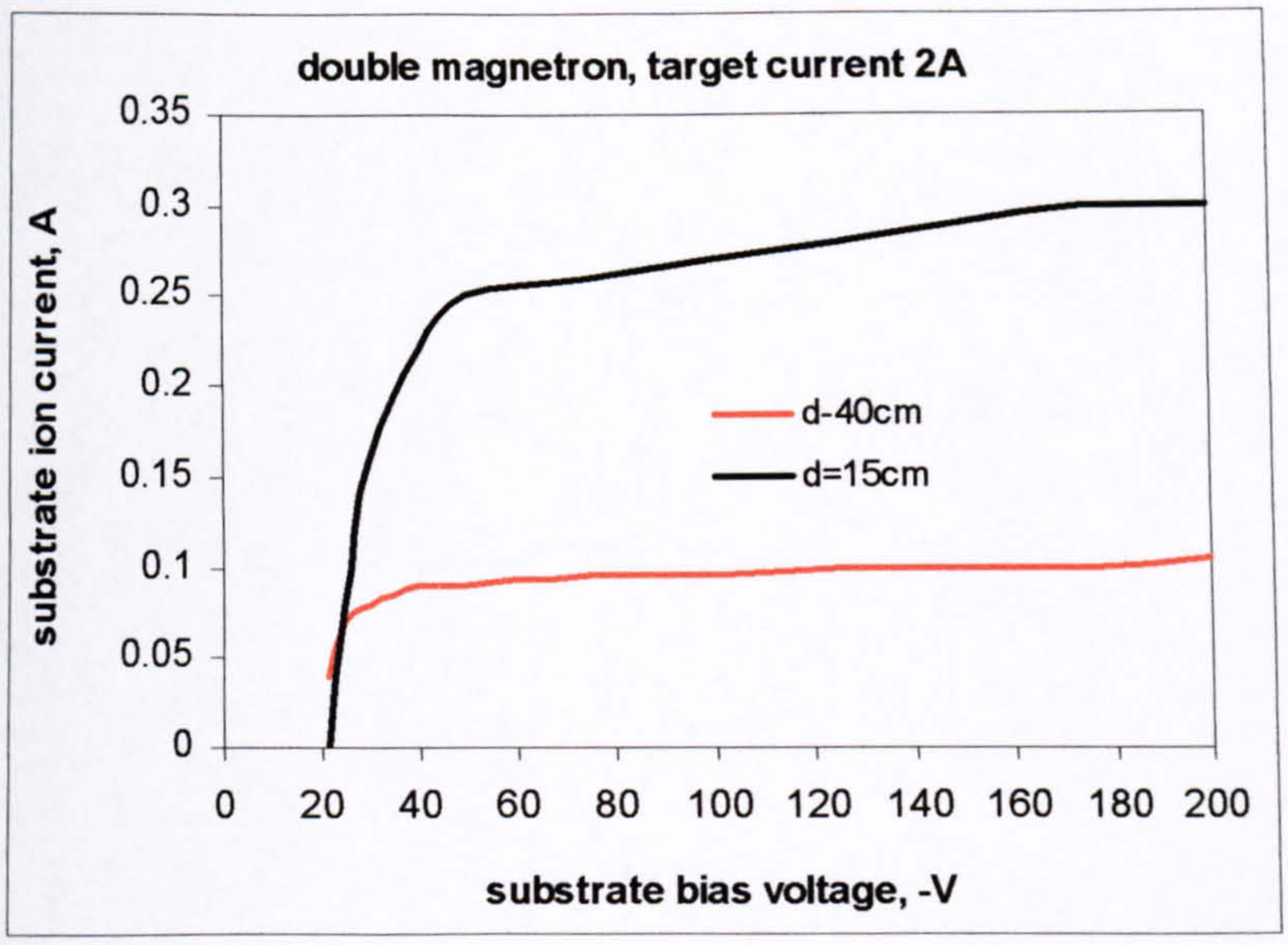

Figure 7.4 the effect of target-to-substrate separation on the substrate I-V curve

The relationship between the target current and the substrate saturation ion current is shown in figure 7.5. It can be seen that the saturation current is proportional to the target current in both double and single magnetron configurations. An empirical formula has been derived to describe this relationship [139]:

$$I_s = n\, I_t \qquad \text{...Eq. (7.1)}$$

in which I_s represents the substrate ion current, I_t, the target current and n, the constant coefficient, which varies with the pressure, the target-to substrate separation and target material. It can also be seen in figure 7.5, that more ions were drawn to the substrate in the double magnetron condition than those in the single one. Therefore, the constant coefficient n also depends on the magnetron configuration.

The gradients of the data lines in 7.5 are 1.5 and 0.8, for double and single, respectively, confirming that the dummy magnetron doubles the current drawn under

any set of conditions.

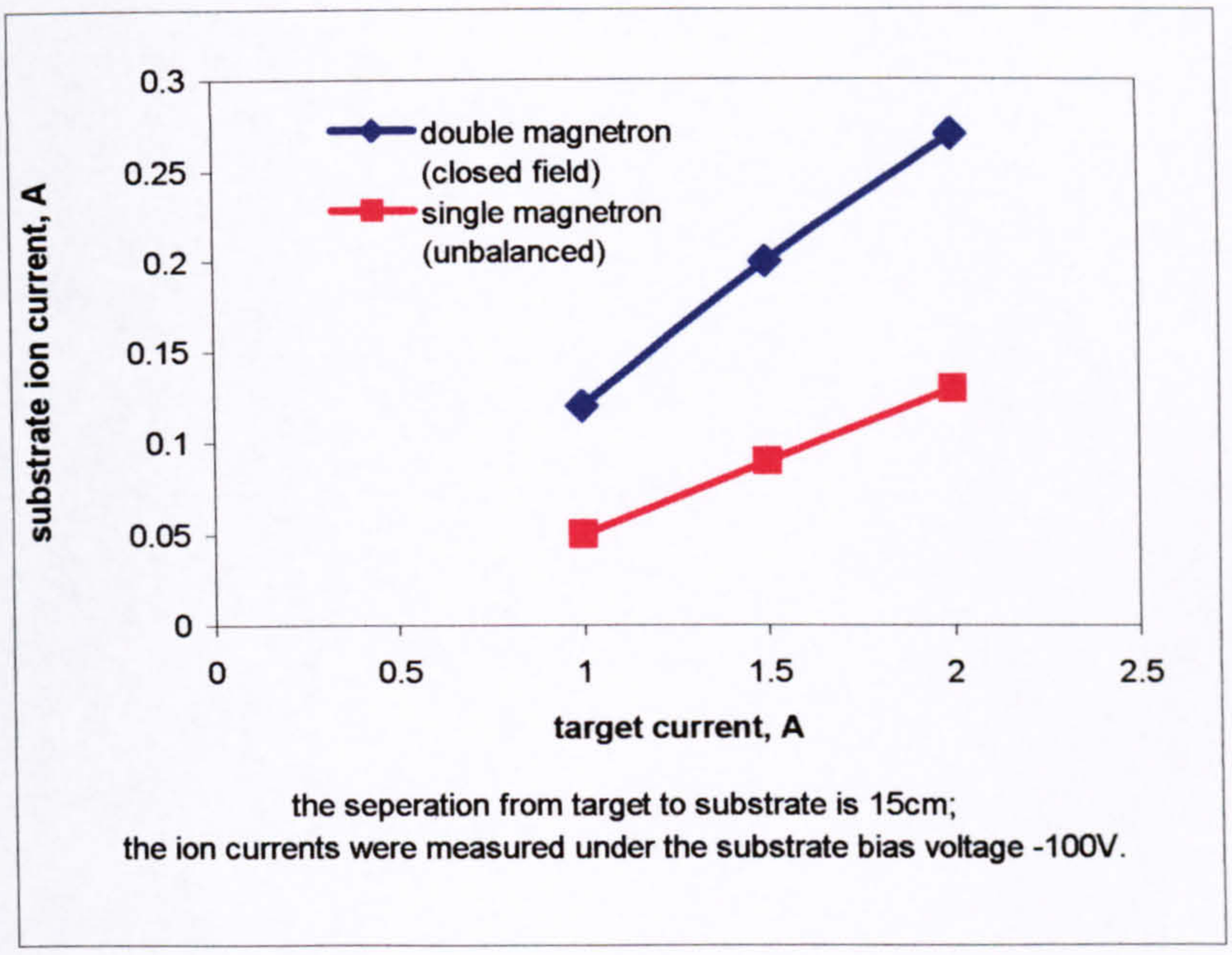

Figure 7.5 the effect of target current on substrate ion current under different magnetron configuration

7.2 The Effect of Pulse Parameters on the Thickness of the Coatings

The investigation was carried out in the current regulation mode of Pulsed DC, and the target current was set at 2A. The variables in this work were pulse frequency and duty, with the response being of thickness. The parameter arrays and the responses are shown in table 7.1. The response was, in turn, analyzed by using the DX 6.0 design expert software, and the results can be seen in figure 7.6. It can be seen clearly that the thicknesses of the coatings increase with the increases of pulse duty and decreases of the pulse frequency.

Table 7.1 The parameter arrays and the results of the response

Std	Run	Block	Factor 1 Frequency KHz	Factor 2 Duty %	Response Thickness (nm)
3	1	Block 1	275	50	400
17	2	Block 1	350	75	837
15	3	Block 1	275	75	936
11	4	Block 1	350	62	503
5	5	Block 1	350	50	280
9	6	Block 1	275	62	690
7	7	Block 1	200	62	962
13	8	Block 1	200	75	1200
1	9	Block 1	200	50	613

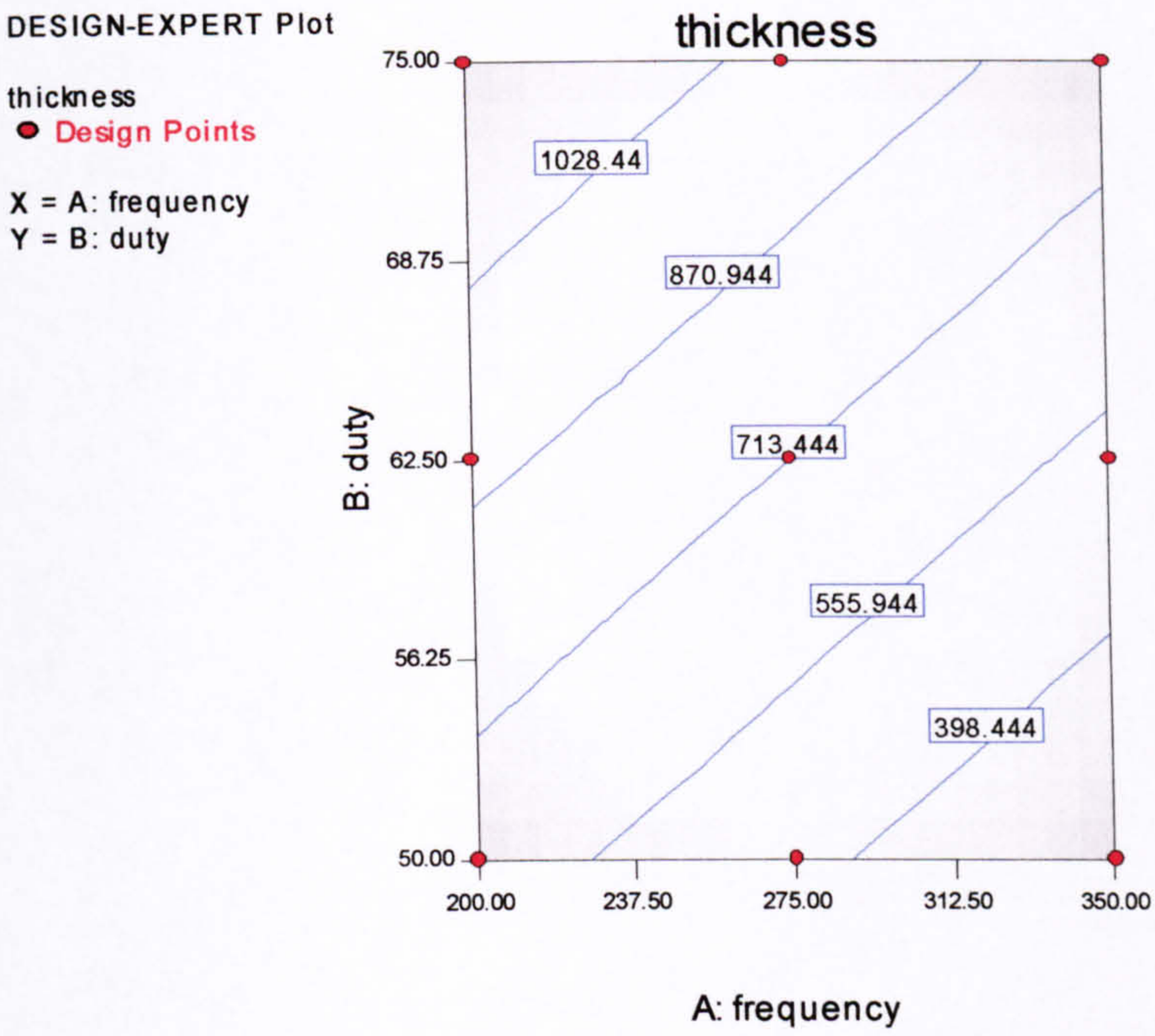

Figure 7.6 the effect of pulsed frequency and duty on the film thickness

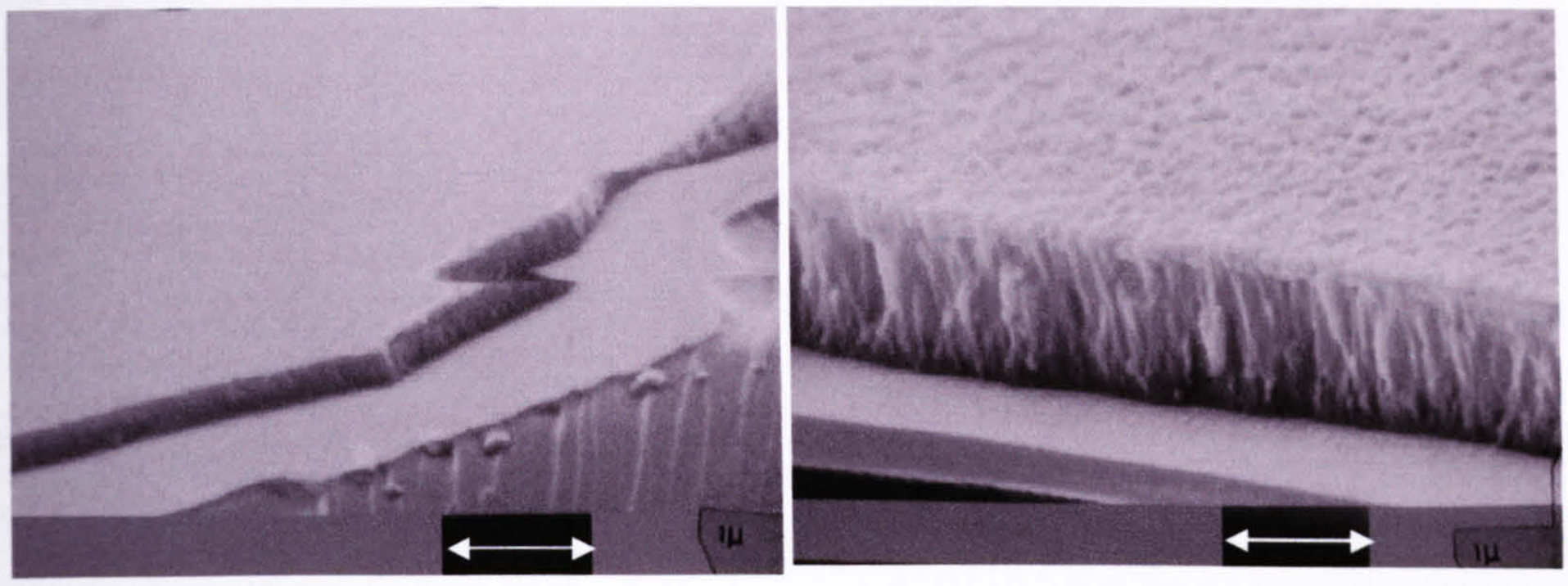

(a) 350kHz frequency+50%duty (b) 200kHz frequency+75%duty

Pictures 7.1 a and b: the effect of pulsed parameters on structure and deposition rate of the ZnO:Al coatings (2A target current for 1h)

From picture 7.1, the difference in the coating thickness can obviously be seen. The design analysis results shown in figure 7.6 also give a clear trend – the thickness of the coating will increase with duty and decrease with pulse frequency. Deposition rate would be expected to increase with duty, as this represents the length of the pulse on time, see figure 7.7, in which the target voltage waveforms were obtained with an oscilloscope. However, the relationship is not straightforward due to the strongly varying target voltage during the pulse on period. The effect of frequency is not immediately clear, but looking at target voltage waveforms, it appears, that at high frequency, the area under the pulse on voltage curve decreases (figure 7.8). Possibly the 'ringing' (very high frequency oscillations) in the waveform leads to losses of energy delivered to the target. Also, it takes a certain amount of time (~ half a microsecond) for the sheath at the target to develop when the target potential reverses, which can be seen in figure 7.9. No sputtering can take place during this time. Thus, as frequency increases, this 'dead time' becomes an increasing proportion of the total on cycle.

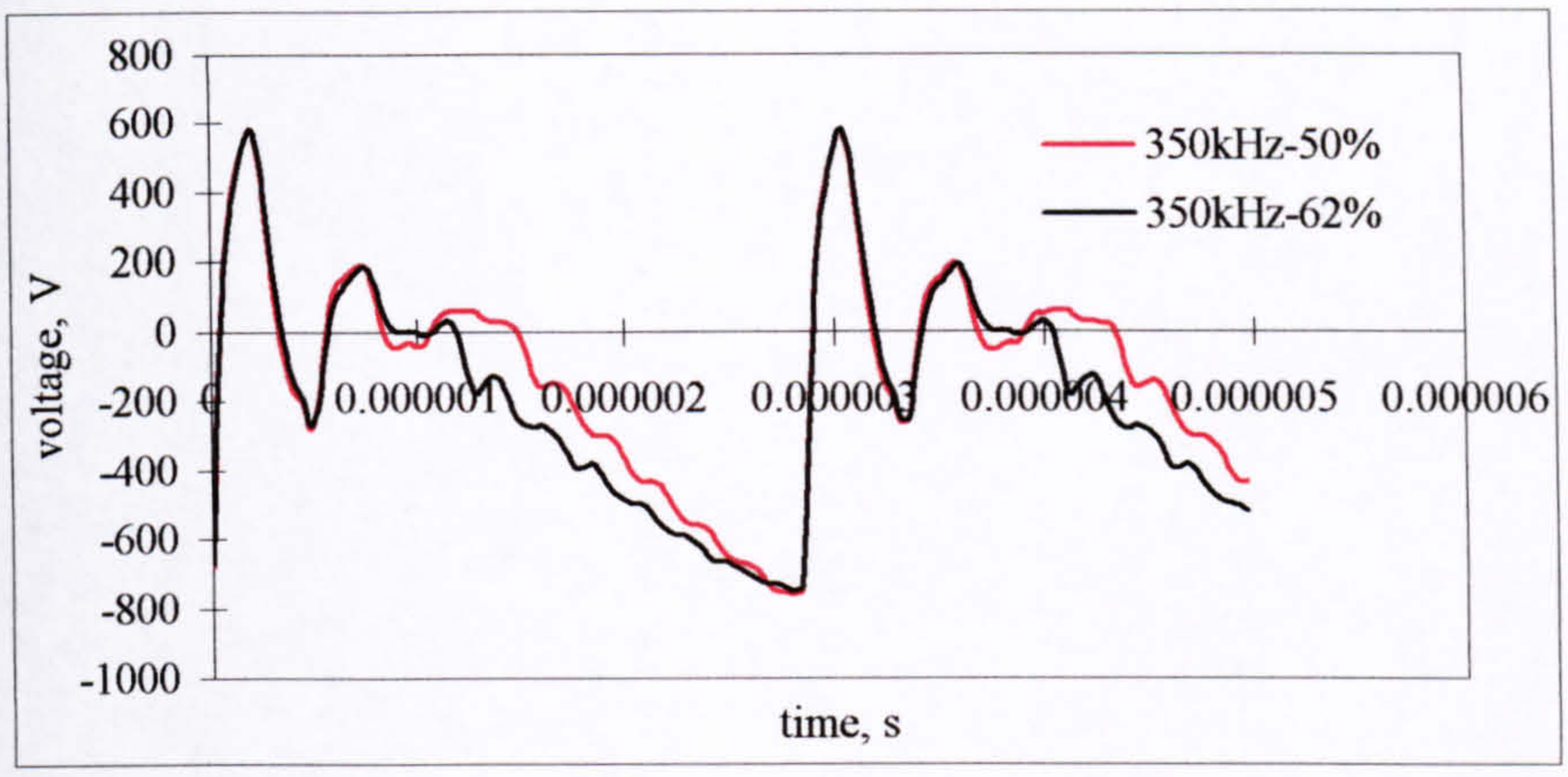

Figure 7.7 the target voltage waveforms with different duty factors

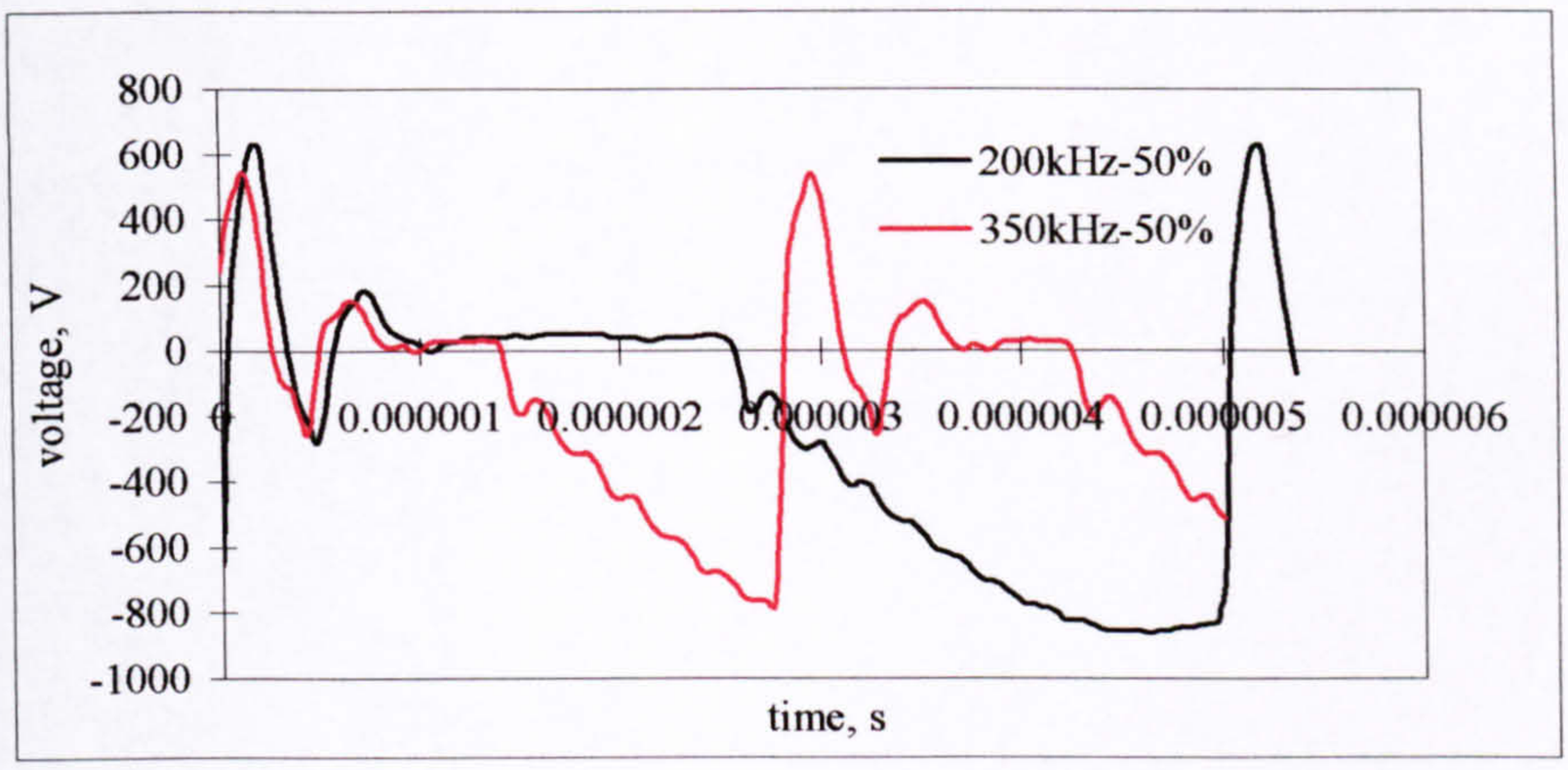

Figure 7.8 the target voltage waveforms with different frequencies

When considering the data, it is clear that the deposition rate increases with duty and decreases with frequency. However, it is possible to explore this further. The reciprocal of frequency is the length of time of each cycle. Multiplying this value by the duty factor gives the proportion of each full cycle that sputtering can take place, named as 'pulse on' factor. This 'pulse on' factor increases with duty and decreases with frequency. Not surprisingly, a strong correlation exists between this 'pulse on' factor and deposition rate, as shown below in figure 7.9. The data crosses the x-axis at

about 0.4 –0.5 μs. This represents the 'dead time' at the beginning of each pulse-on period when the sheath is re-established and no sputtering of the target takes place. This period becomes a more significant proportion of the pulse–on period at higher frequencies and lower duties.

Pulse on factor = duty factor x 1/frequency

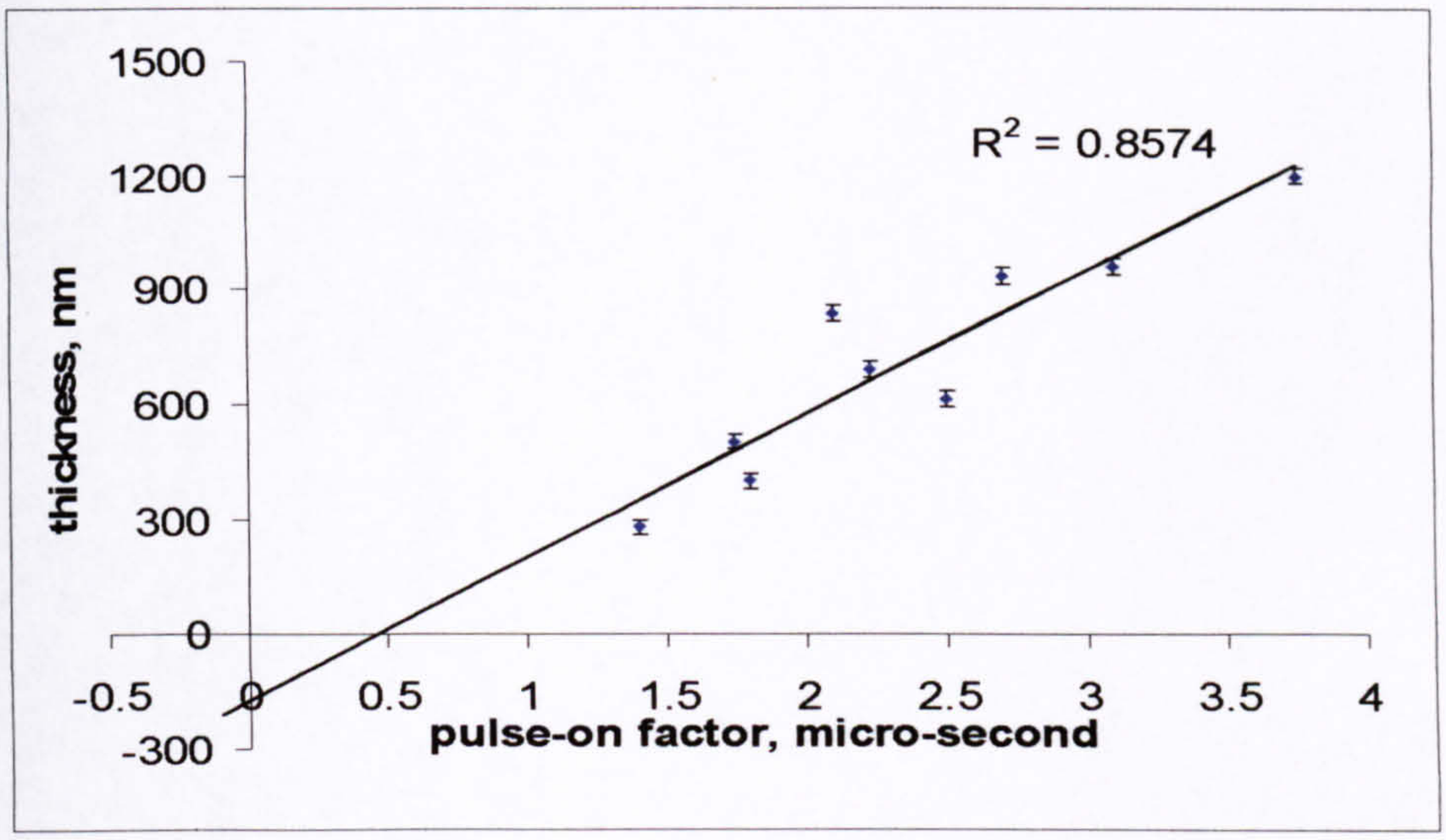

The scatter in the data arises from errors in the measurement of deposition rate, non-constant target voltage during pulse on and resputtering effects at the substrate.

Figure 7.9 The relationship between pulse on factor and deposition rate

In general, the study of pulsed parameters helps to understand more about how they affect the growth of the coatings. This information can be used to develop deposition processes to prepare coatings with specific properties and deposition rates.

7.3 Comparison of the Magnetron Configurations and Power Modes

In order to investigate how the system performed under different magnetron configurations and different power delivery modes, five sets of operating conditions were tested (see table 7.2). The same target material was used in each case (ZnO:3at%Al). The first four runs were carried out in the single magnetron

configuration, i.e., with the dummy magnetron removed. For runs 1 to 3, the coatings were deposited at target-to-substrate separations of 15, 10 and 20 cm, respectively, in pulsed DC mode at 350kHz pulse frequency, 62% duty and at a target current of 2A. The fourth run was carried out at the same conditions as run 1, but with the pulse frequency set to zero, i.e., in DC mode. The samples from these four runs were annealed in vacuum (0.003Pa) at 450^{o}C for 1 hour to achieve low resistivities. To further compare the effect of magnetron configurations, run 5 was carried out in DC mode in the double magnetron configuration. The run time in run 5 was reduced to 1 hour due to target arcing.

Table 7.2: Magnetron configurations and power parameters for comparison experiments

Run number	Separation d_{ts} cm	Magnetron configuration	Power modes	Run time H
1	15	Single	Pulsed 350kHz, 62%, 2A,	2
2	10	Single	Pulsed 350kHz, 62%, 2A,	2
3	20	Single	Pulsed 350kHz, 62%, 2A,	2
4	15	Single	DC, 2A	2
5	15	Double	DC, 2A	1

7.3.1 The effects of target-to-substrate separation on the structure and properties of coatings

The first three runs were carried out at various target-to-substrate separations. Despite the fact that this resulted in large differences in coating thickness, the structures and properties of the as-deposited coatings (crystallinity, morphology and transmittance) are similar. The resistivities of the as-deposited films were too high to be measured by four-point probe. After the annealing treatment, the resistivities reduced to the order of 10^{-3} Ωcm. The relationship between the target-to-substrate separation and the

resistivity of the coatings is shown in figure 7.10. The average transmittance in the visible range of these three samples is around 90% (see figure 7.15 in section 7.3.2). Picture 7.2 shows the SEM morphology of the films, which all have similar dense columnar structure, but big differences in the thickness; the relationship between the thickness of the films and the target-to-substrate separation is shown in figure 7.11.

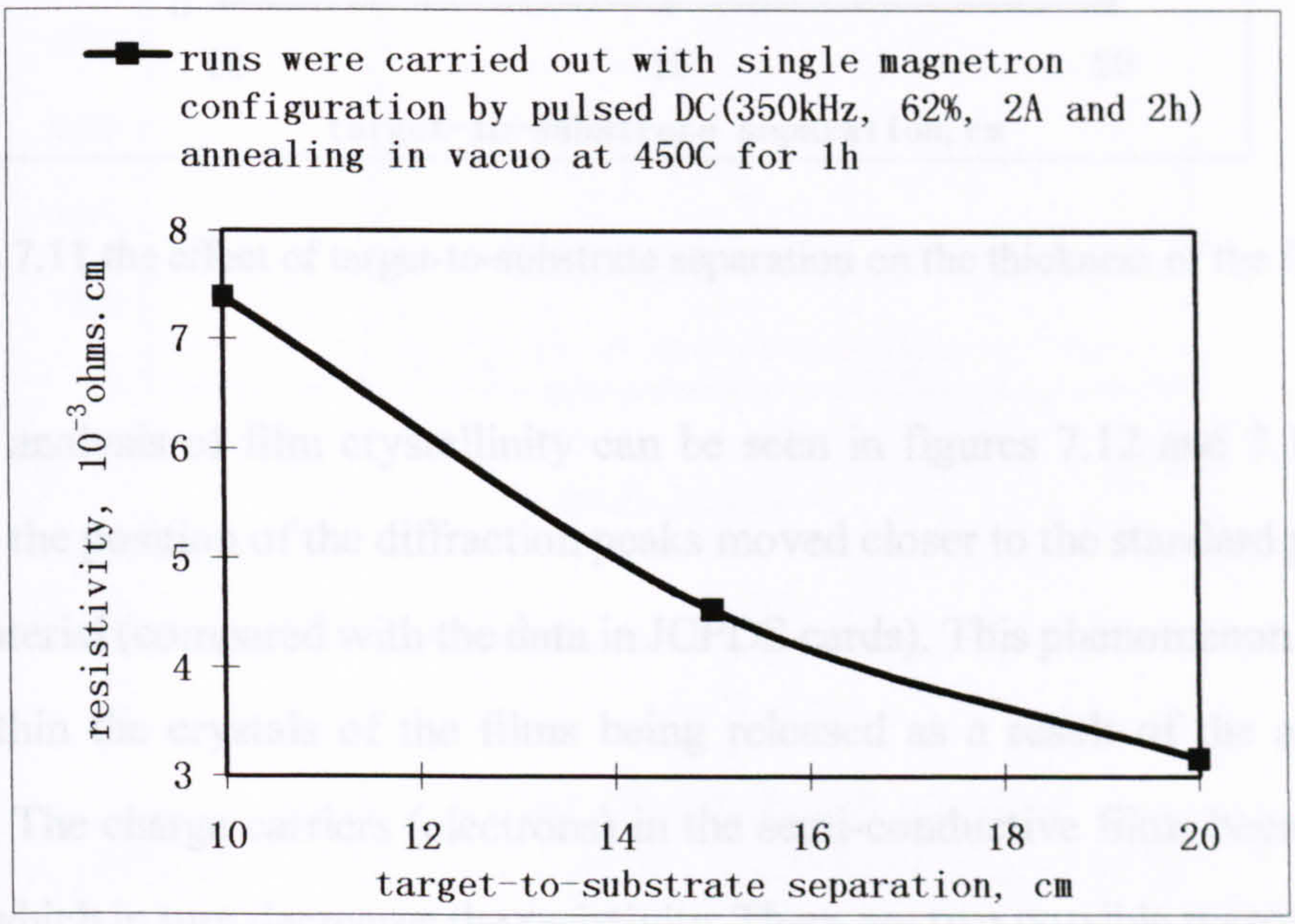

Figure 7.10 the effect of target-to-substrate separation on the resistivity of annealed coatings

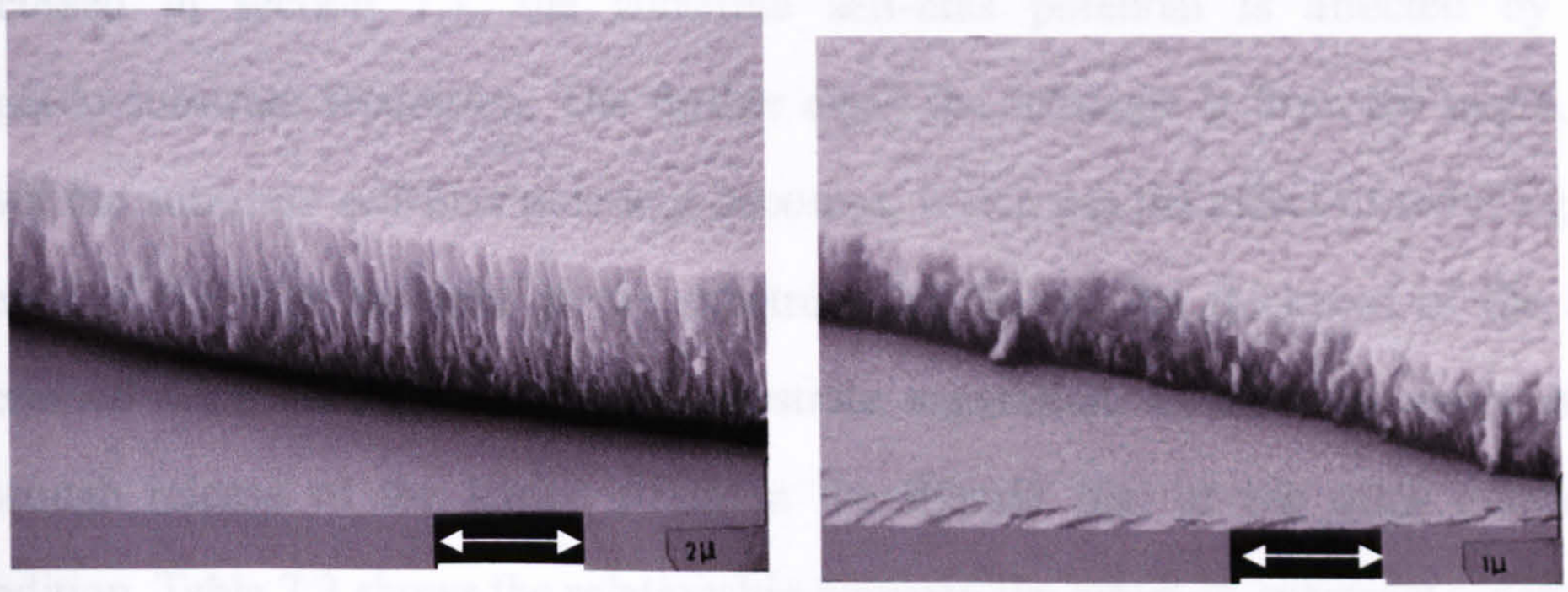

(a) target-to-substrate separation 10cm (run 2)

(b) target-to-substrate separation 20cm (run 3)

Picture 7.2: SEM micrographs showing the morphological structure of the coatings

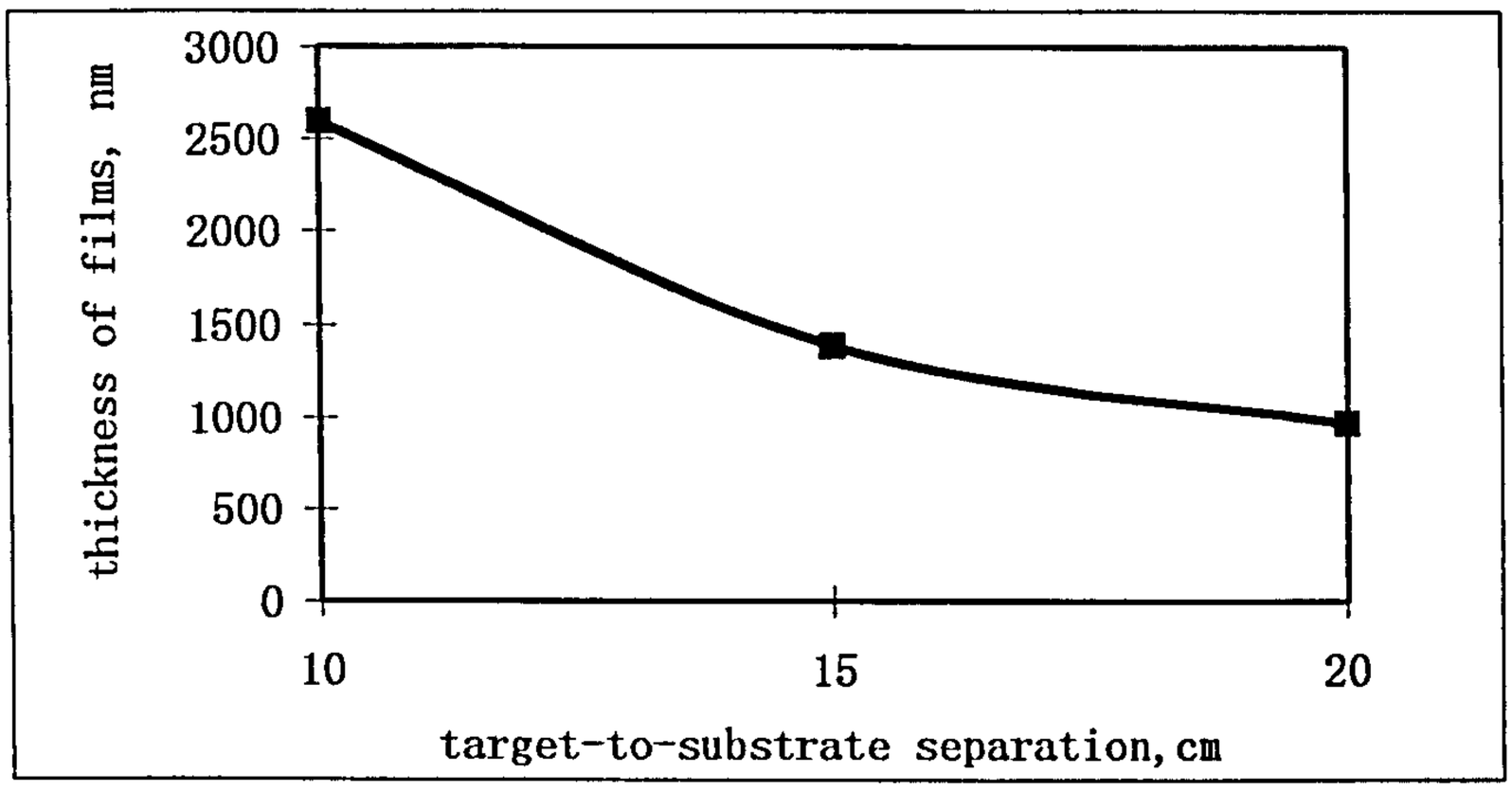

Figure 7.11 the effect of target-to-substrate separation on the thickness of the films

The XRD analysis of film crystallinity can be seen in figures 7.12 and 7.13. After annealing, the position of the diffraction peaks moved closer to the standard positions for this material (compared with the data in JCPDS cards). This phenomenon is due to strains within the crystals of the films being released as a result of the annealing treatment. The charge carriers (electrons) in the semi-conductive films become freer to move, which in turn decreases the resistivity. There are two possible reasons for the reduction in the resistivity of the films at higher target-to-substrate separation. As discussed in section 7.1, the substrate self-bias potential is affected by the target-to-substrate separation. The further away the substrate is from the target, the lower the substrate self-bias potential becomes, which has the effect of reducing the energy of the ions incident at the substrate. Moreover, the thickness of the film decreased with the higher target-to-substrate separation, which may cause more thorough release of the lattice strain in the thinner film at the same annealing condition. Table 7.3 shows the relationship between the target-to-substrate separation and the difference of the crystalline spacings compared with the standard lattice spacings, after the films were annealed. It can be seen that the crystalline traces shifted closer to the standard positions at higher target-to-substrate separations. There are two main diffraction peaks in run 2, which means the lattice strains would be higher although the traces are closer to the standard diffraction peak than those in the

other runs. That may be the reason that the traces shifted less after annealing compared to the other runs.

(100): d_{std}=2.816, d=2.8594, d_{ann}=2.82961

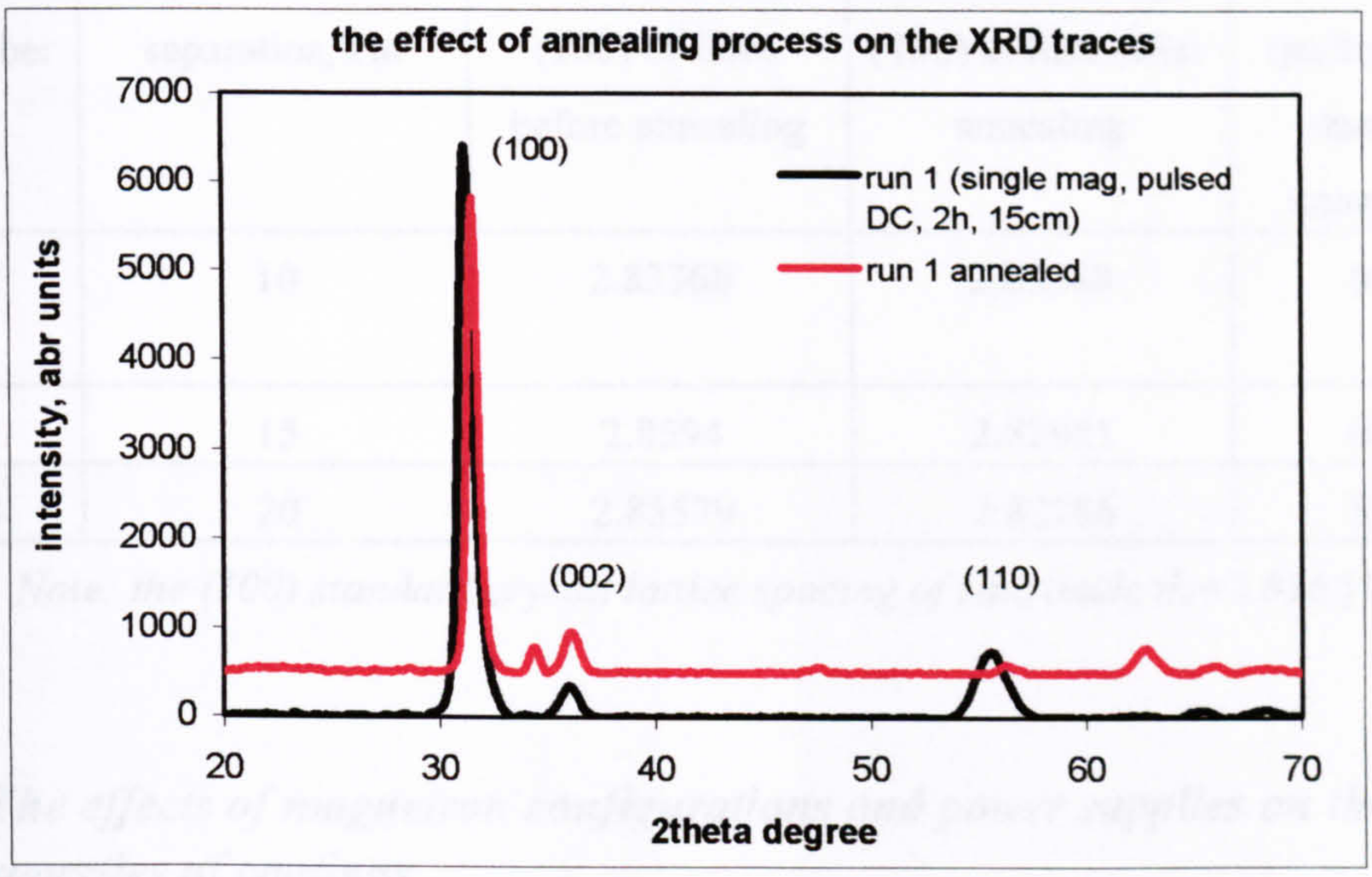

Figure 7.12 the main XRD crystalline traces of the coating before and after annealing

Standard: d (100) =2.816, d (002) =2.602

(100): d_2 =2.8336, d_{2ann}=2.83588; d_3=2.85579, d_{3ann}=2.82786;

(002): d_{2ann}=2.61284

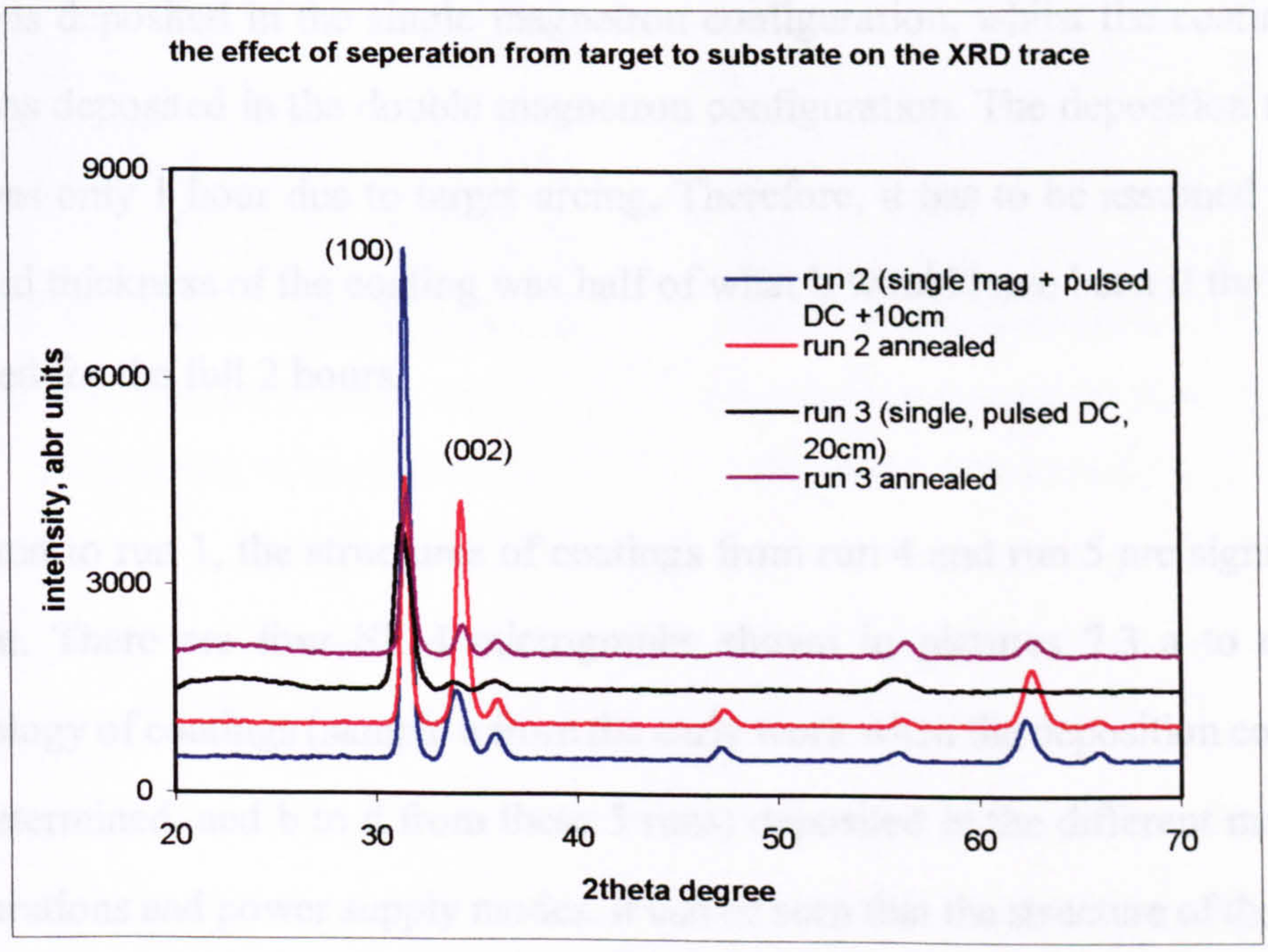

Figure 7.13 the effect of target-to-substrate separation on XRD traces

Table 7.3 the effect of target-to-substrate on the positions of the crystalline traces

Run number	Target-to-substrate separation, cm	Lattice spacing (100) of films before annealing	Lattice spacing (100) of films after annealing	The difference of spacings between standard and annealed films
2	10	2.83368	2.83588	0.01768
1	15	2.8594	2.82961	0.01361
3	20	2.85579	2.82786	0.01186

Note: the (100) standard crystal lattice spacing of zinc oxide d_0=2.816 [147]

7.3.2 The effects of magnetron configurations and power supplies on the structure and properties of coatings

In order to determine the effects of power supply mode on the structure and properties of the coatings, runs 4 and 5 were carried out by DC sputtering at a target-to-substrate separation of 15cm (i.e. the same separation as run 1). Furthermore, the coating from run 4 was deposited in the single magnetron configuration, whilst the coating from run 5 was deposited in the double magnetron configuration. The deposition time for run 5 was only 1 hour due to target arcing. Therefore, it has to be assumed that the measured thickness of the coating was half of what it would have been if the run had continued for the full 2 hours.

Compared to run 1, the structures of coatings from run 4 and run 5 are significantly different. There are four SEM micrographs shown in pictures 7.3 a to d of the morphology of coatings (sample a from the early work when the deposition conditions were determined, and b to d from these 5 runs) deposited in the different magnetron configurations and power supply modes. It can be seen that the structure of the coating deposited by pulsed DC within a closed magnetic field (double magnetron configuration, picture 7.3a) visually appears the densest, whilst that of the coating

deposited by DC in the single magnetron mode (picture 7.3d) is the most porous. The SEM micrograph of the surface topography of the coating from run 4 (picture 7.4b) shows pores, of holes running through the full thickness of the coating. The other two coatings deposited by pulsed DC within unbalanced magnetic field and by DC within closed magnetic field revealed intermediate densities.

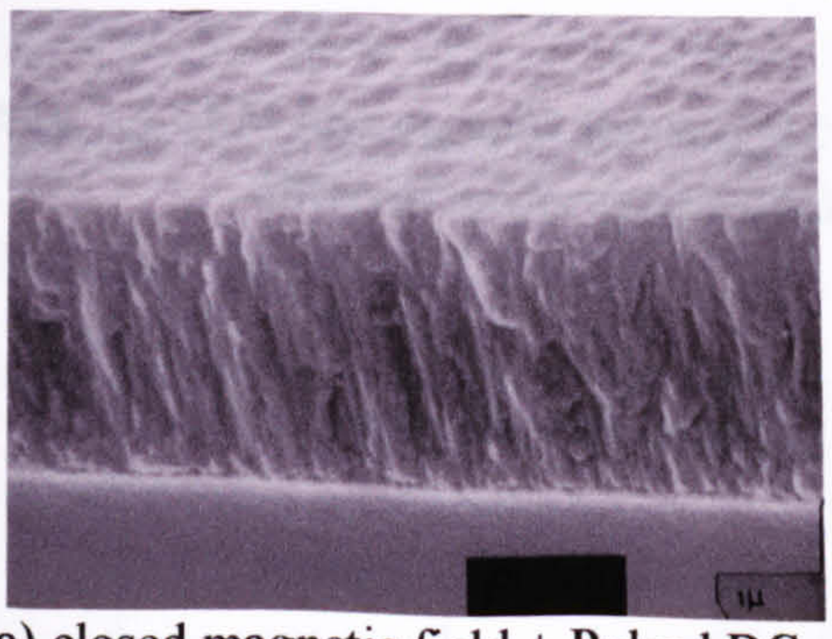

(a) closed magnetic field + Pulsed DC (deposited 4 hours)

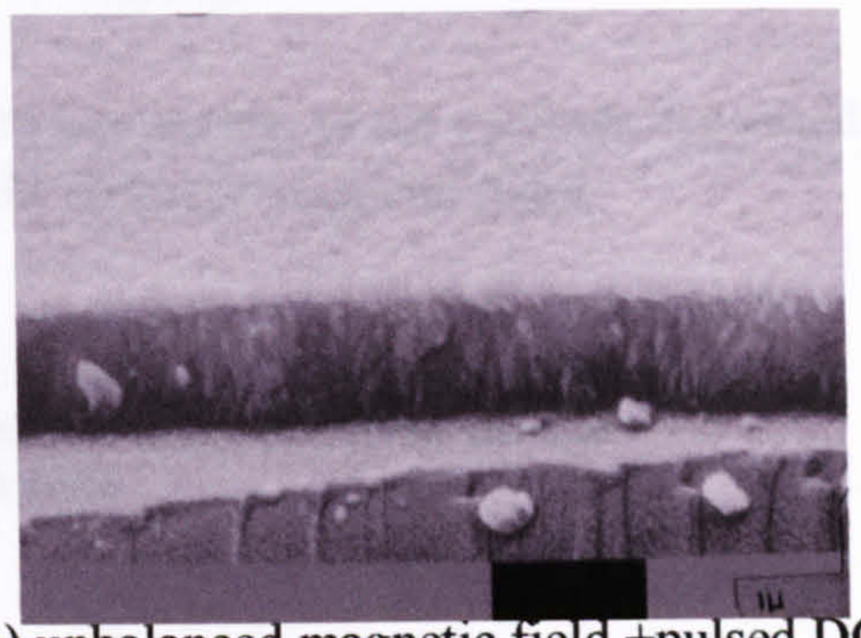

(b) unbalanced magnetic field +pulsed DC (deposited 2 hours) (run 1)

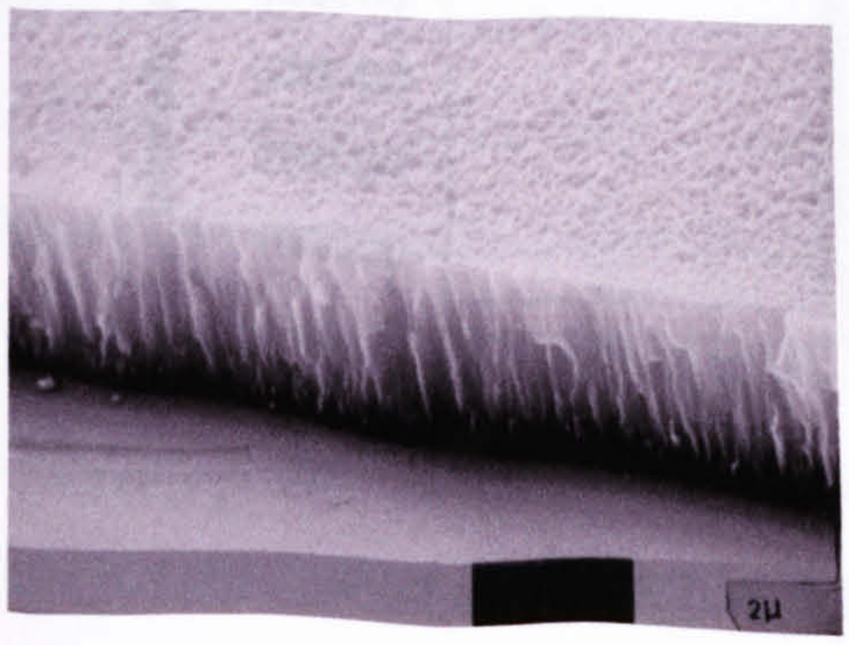

(c) closed magnetic field +DC (deposited 1 hour) (run 5)

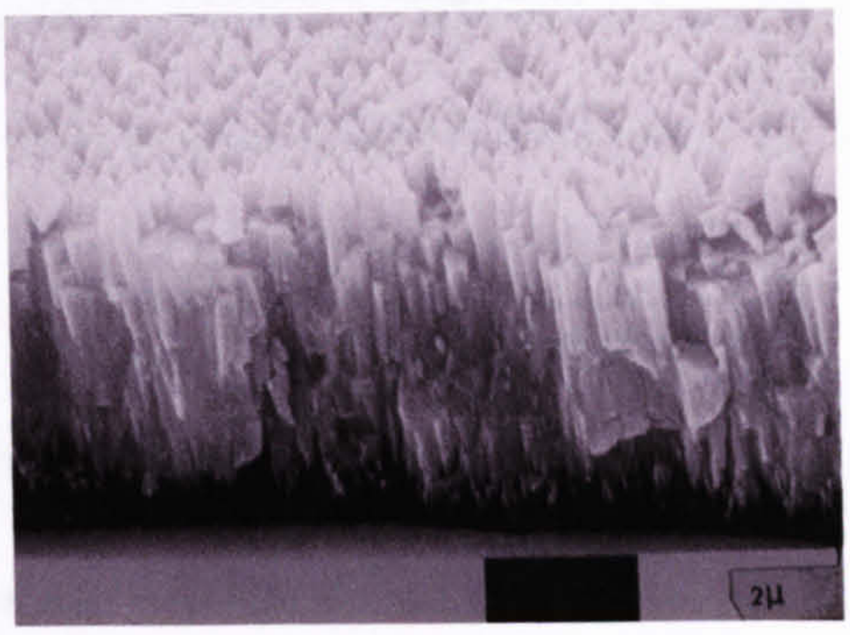

(d) unbalanced magnetic field +DC (deposited 2 hour) (run 4)

Picture 7.3 SEM micrographs showing the fracture sections of the coatings deposited by different power supplies and within different magnetic fields

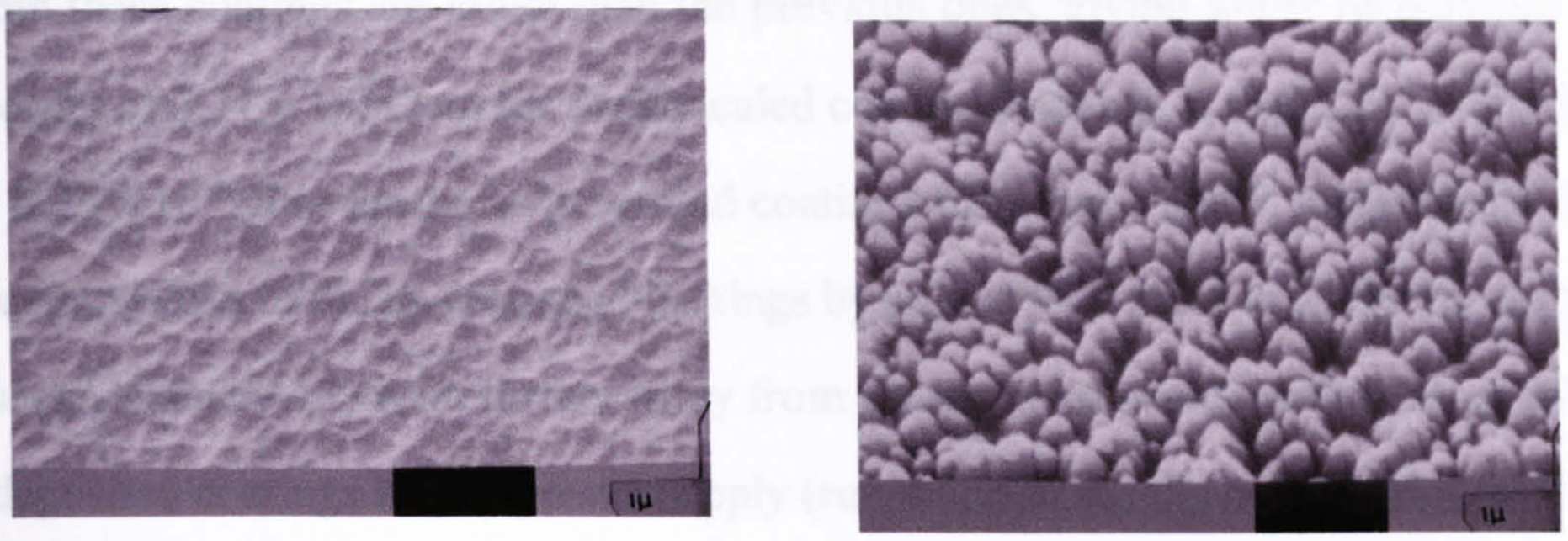

(a) closed magnetic field + pulsed DC (4h) (b) unbalanced magnetic field + DC (2h) (run 4)

Picture 7.4 SEM micrographs showing the surface topography of the coatings deposited by different power supplies and within different magnetic fields

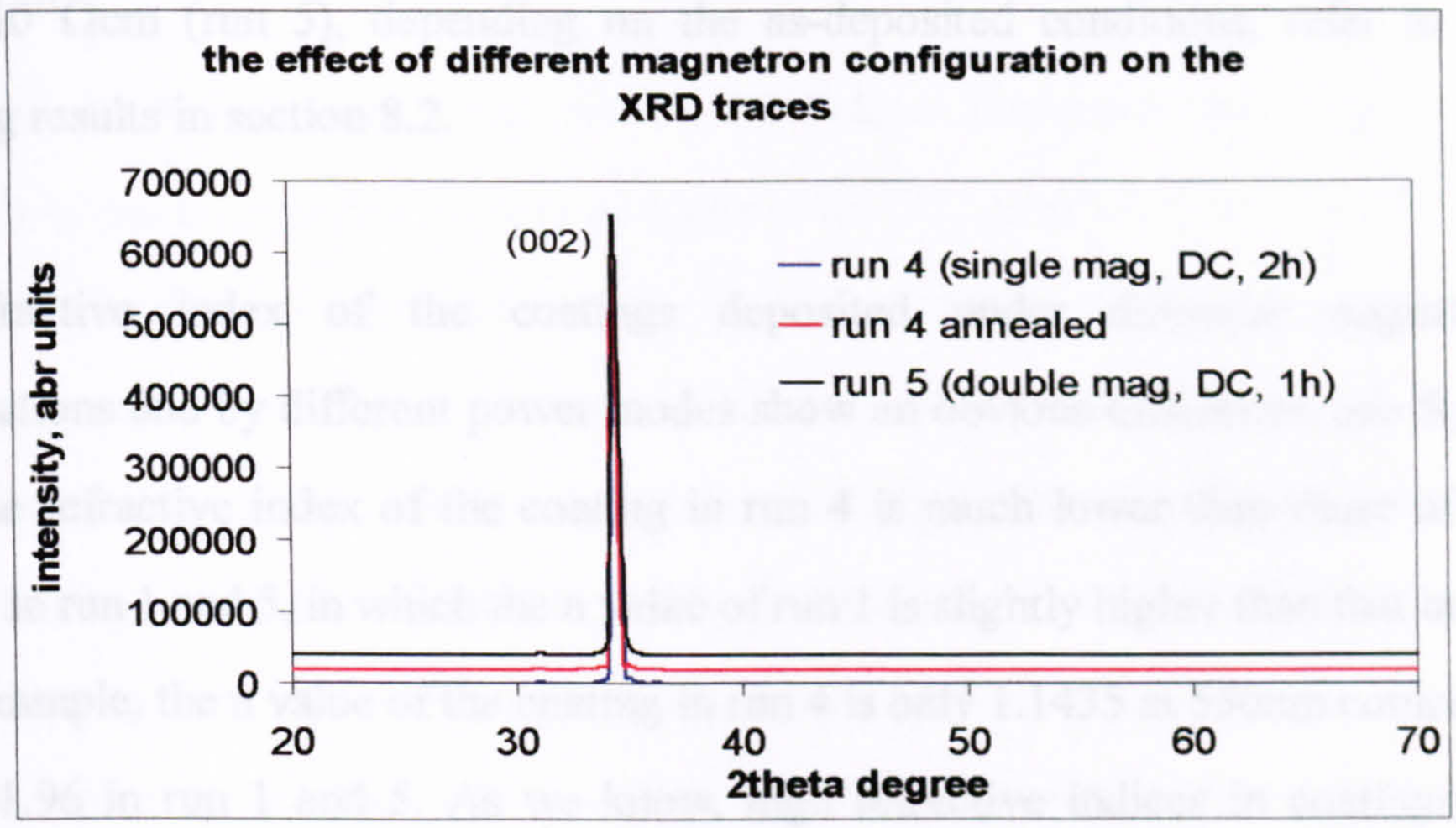

(002) $d_{std} = 2.6.2$; $d_4 = 2.6039$, $d_{4ann} = 2.603$; $d_5 = 2.6039$

Figure 7.14 the XRD crystalline traces of the coatings from run 4 and run 5

Figure 7.14 shows the crystalline structures of the coatings from run 4 and run 5, both of which were deposited by DC sputtering. Compared to the traces of the coatings deposited by pulsed DC (figures 7.12 and 7.13), the crystalline patterns were noticeably different. Only the (002) peak appeared in the coatings deposited by DC instead of the (100) and (002) peaks, in the case of the pulsed DC coatings. More importantly, the crystal lattice spacings of the DC coatings are much closer to the

standard one, even before the annealing treatment. Presumably, therefore, the strains within these coatings are lower than the previous ones, giving lower resistivities (of the order of 2.31 x $10^{-3}\Omega$cm for the annealed coating from run 4, and 2.04 x $10^{-2}\Omega$cm, and 8.24 x $10^{-3}\Omega$cm for the as-deposited coatings from run 4 and 5, respectively. The reflection peaks of the as-deposited coatings by pulsed DC (run 1 to 3, see the notes in figures7.12 and 7.13) were further away from the standard positions than those of the as-deposited coatings by DC power supply (run 4 and 5, see the notes in figure 7.18). After the annealing treatment, though, the differences of the lattice spacings between those annealed films and the standard spacing reduced, see table 7.2. Therefore, the resistivities of all the annealed coatings were in the order of 5-1.8 x $10^{-3}\Omega$cm, despite the fact that they varied from being too high to be measured by four-point probe to 8.24 x $10^{-3}\Omega$cm (run 5), depending on the as-deposited conditions, refer to the annealing results in section 8.2.

The refractive index of the coatings deposited under different magnetron configurations and by different power modes show an obvious difference, see figure 7.15. The refractive index of the coating in run 4 is much lower than those of the coatings in run 1 and 5, in which the n value of run 1 is slightly higher than that in run 5. For example, the n value of the coating in run 4 is only 1.1435 at 550nm compared to 1.94-1.96 in run 1 and 5. As we know, high refractive indices in coatings are associated with dense structures. Therefore, it can be said that the dense coatings have been produced by the pulsed DC power supply or in the closed-field magnetron configuration from powder targets, whilst porous coatings were produced when operating in DC mode with a single unbalanced magnetron (run 4).

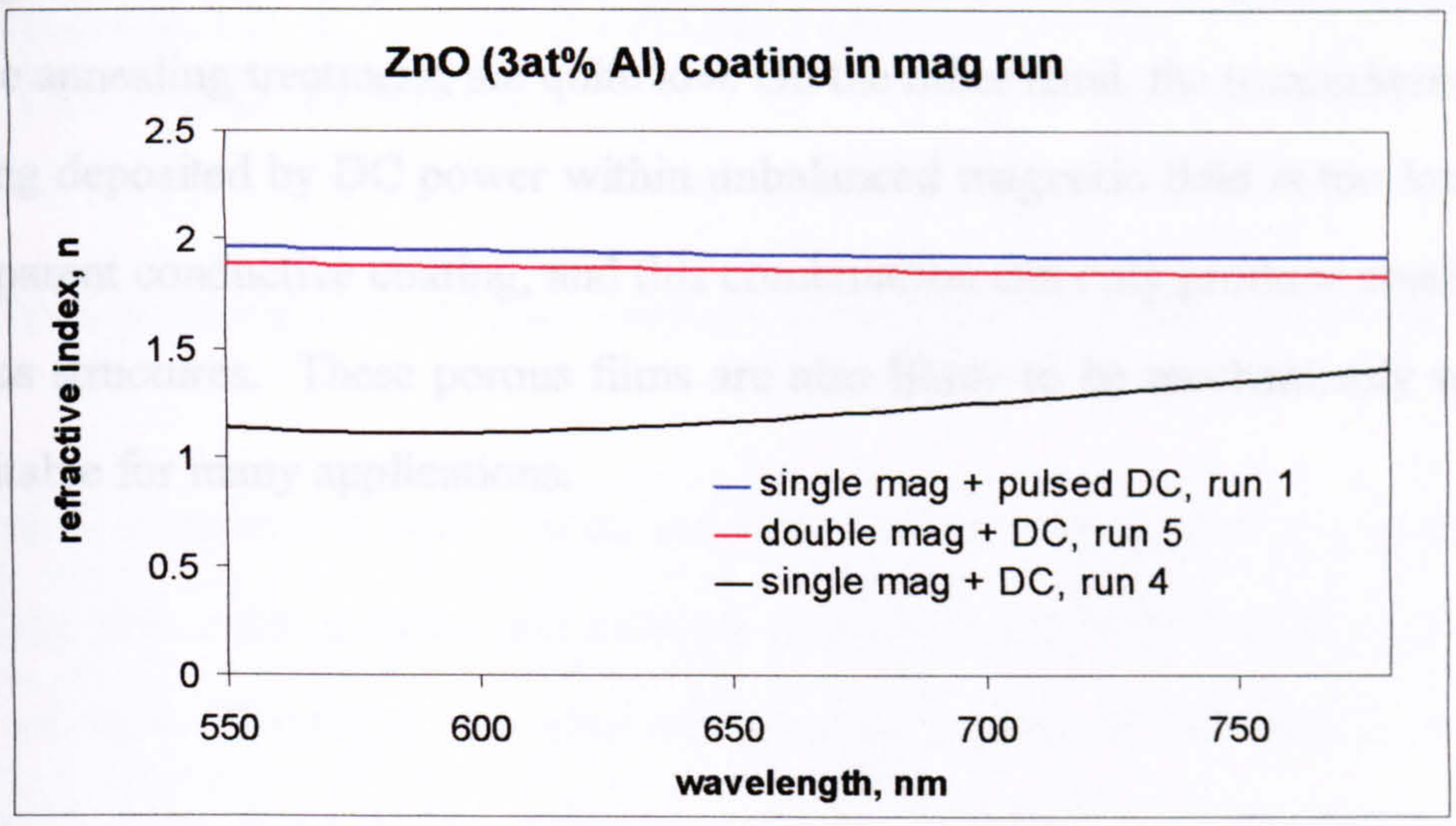

Figure 7.15 the refractive index of the coatings deposited by different power modes within different magnetic fields

J. Bradley and P Kelly etc. from UMIST and Salford University have studied the behaviour of pulsed plasmas for several years [148-151], which showed that the ions energies can be divided into three levels -- the high energy level produced during the very short positive voltage overshoot time, the middle energy level within the steady-state pulse-off time and low energy level within the pulse-on time. According to the studies in UMIST [148-151], the overshoot ion energies make a major contribution to the total ion energy flux when the frequency equal to 350kHz, although the overshoot time is too short to influence the average plasma ion energy when frequency is lower, for example, 100kHz. Therefore, the higher energies that can be delivered to the growing film when operating in pulsed DC mode at high frequency, such as 350kHz, may well be responsible for the dense coatings observed in this study.

In general, the coatings deposited by pulsed DC within a closed magnetic field have dense columnar structures and high transmittance. Also, they show high strain within the crystals of the coatings before the annealing treatment. Annealing treatments can help to release the strain, therefore decreasing the resistivity of the coatings. The coatings deposited by DC sputtering with both single and double magnetron

configurations have very low lattice strains, and the resistivity of these coatings, even before annealing treatment, are quite low. On the other hand, the transmittance of the coating deposited by DC power within unbalanced magnetic field is too low to be a transparent conductive coating, and this combination can only produce coatings with porous structures. These porous films are also likely to be mechanically weak and unsuitable for many applications.

8. RESULTS 2: THE STRUCTURES AND PROPERTIES OF TCO COATINGS

8.1 As-deposited Zinc Oxide Doped Aluminium (ZAO) Coatings

The initial experiments were carried out using ZnO:Al targets, which were formed by blending zinc oxide powder and alumina powder (both 99.99% pure) at the weight ratio of 96:4. Therefore, the aluminium metal content of the targets was about 2.08wt%. Also, some of the optical results were obtained from the ZnO target with 3at% Al. The targets were sputtered in Pulsed DC mode at a frequency of 350 kHz 62% duty and 2A current mode. These conditions were chosen because they were found to provide a readily ignitable, stable plasma. Target currents in excess of 2A resulted in the target material glowing red hot. Deposition times were varied from 1-4 hours depending on the thickness required by particular analysis techniques.

8.1.1 Composition and structures of as-deposited ZnO:Al coatings

An electron probe micro-analyser (EPMA) was used to analyse the compositions of the ZAO coatings. The coatings were deposited for 4 hours because the technique requires the coating thickness to be of the order of 2μm. The results are shown in table 8.1.

Table 8.1 Composition of ZAO coatings (EPMA)

Composition, wt%	Zn	Al	O
Coatings	74.91	2.41	22.68
	74.89	2.16	22.95
	75.50	2.16	22.34
Targets	Weight ratio: Zinc oxide: aluminum oxide = 96:4 Or 2.08wt% Al metal element in the targets		

It can be seen that the compositions of the coatings relatively correspond to those of the targets, and that this is reproducible over several runs. Therefore, the zinc oxide and alumina mixed powder targets can be compared with solid targets made from the same material.

The typical morphological structure of the ZAO coatings is shown in picture 8.1, which was obtained by scanning electron microscopy (SEM) of a gold-coated fracture section of the coating. The micrograph shows a dense columnar and defect-free structure, which is desirable for most PVD coatings.

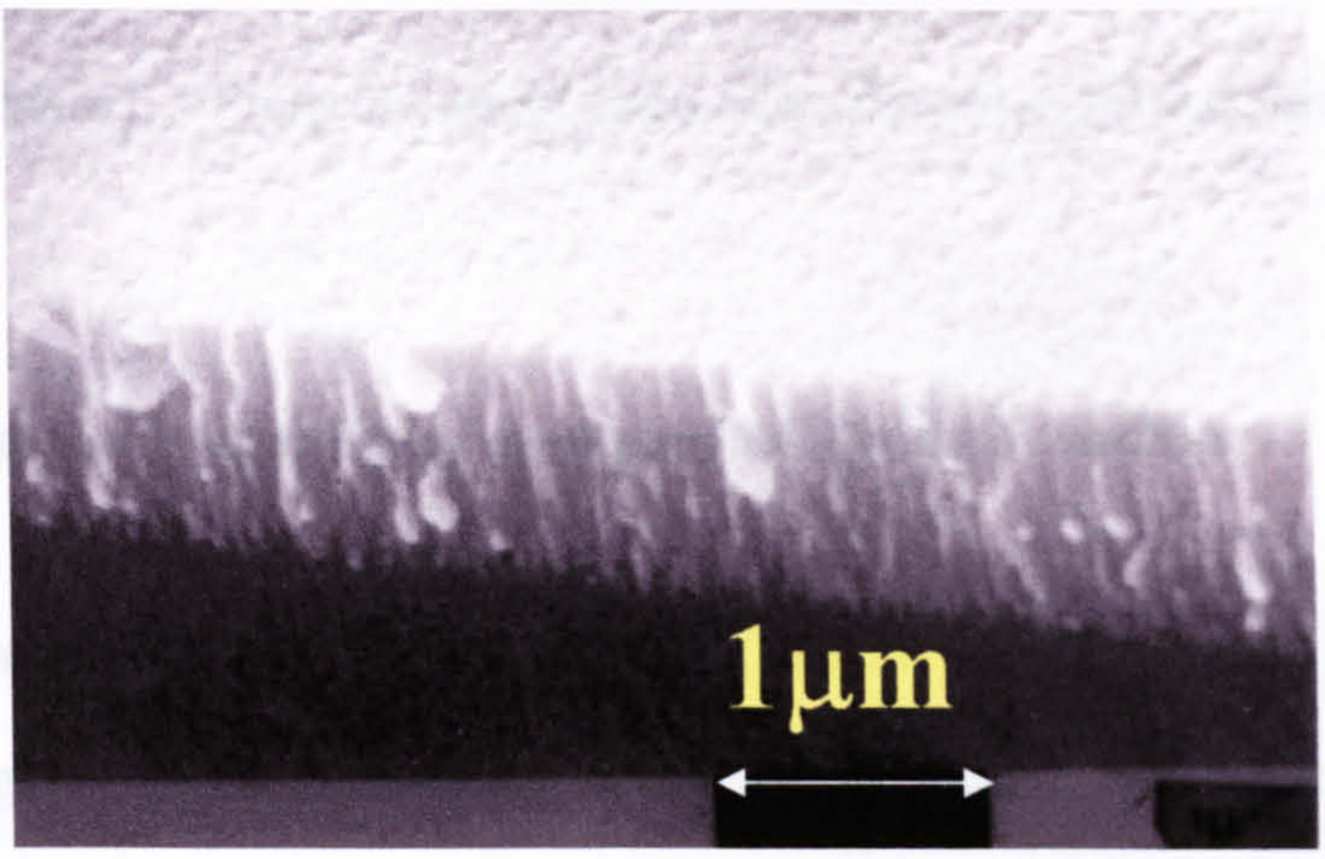

Picture 8.1 SEM micrograph showing typical structure of the as-deposited ZAO coatings

The X-ray diffraction (XRD) technique was used to analyze the preferred orientations of the ZnO:Al coatings both as-deposited under argon and oxygen atmosphere and argon only atmosphere, other deposition conditions, such as pulsed parameters etc., were the same. Strong (002) and (100) zinc oxide diffraction peaks could be observed, although there were also some other smaller peaks, such as the (110) peak. The diffraction peaks were normally broad and shifted away from the standard default positions for ZnO, as shown in the powder diffraction JCPDS cards. The XRD results can be seen in figure 8.1, in which the diffraction peaks shown are mainly the (002), (100) and the low intensity (110) peak.

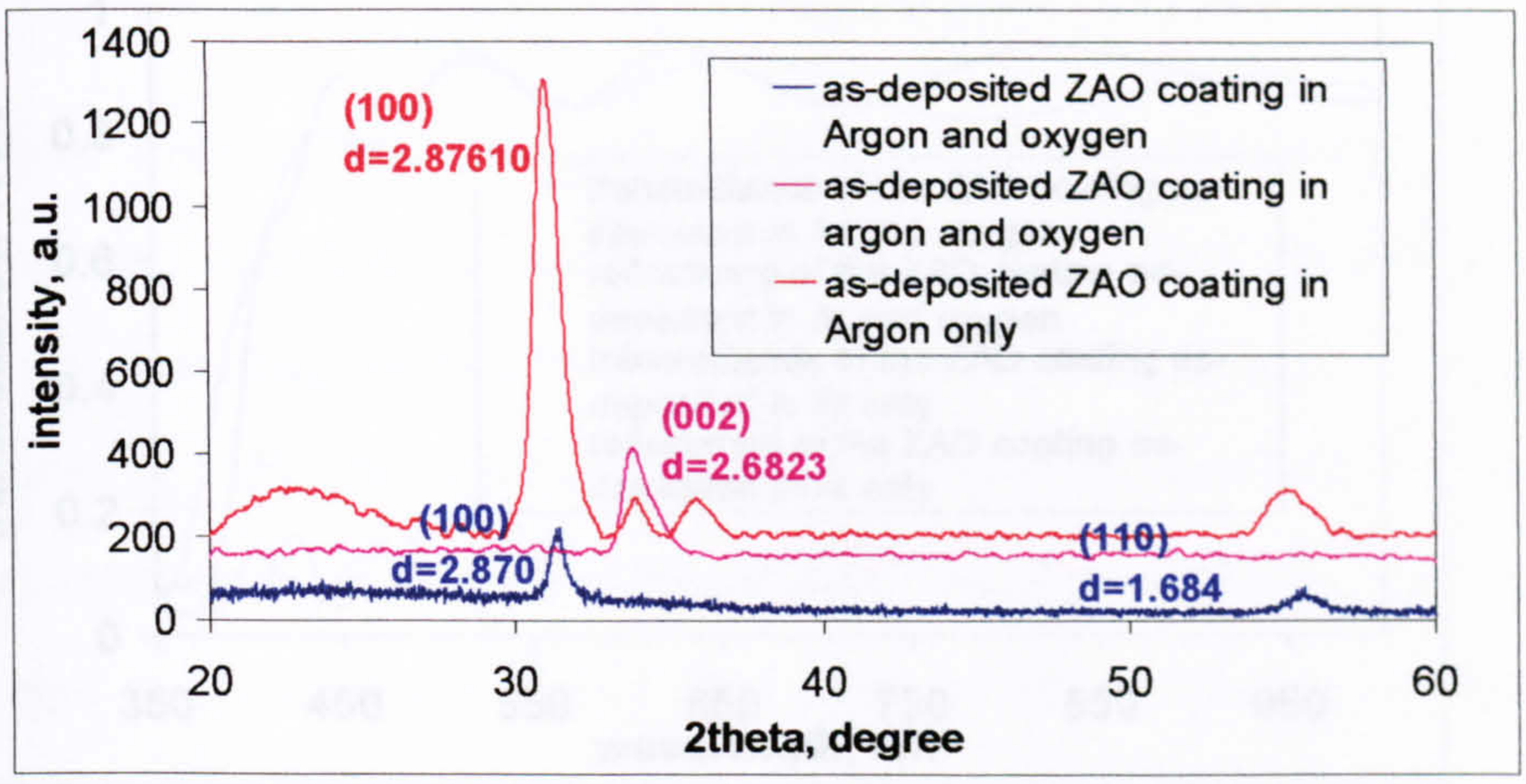

Note: ZnO standard lattice spacings of the diffraction peaks are d(100)=2.815, d(002)=2.602, d(110)=1.626

Figure 8.1 Preferred orientations of as-deposited ZAO coatings

8.1.2 Initial optical properties of as-deposited ZnO:Al coatings

The optical properties of the as-deposited ZAO coatings were determined and analyzed using the Aquilla nkd8000 spectrophotometer. Typical transmittance and reflectance spectra of the coatings are shown in figure 8.2. The refractive index (n) and absorption coefficient (k) were derived from modelling these spectra and are shown in comparison with those of standard ZnO bulk material in figures 8.3a and 8.3b. The negative part of the absorption coefficient in figure 8.3 (a) was due to the spectrophotometer used; it indicates that the k value can be considered were very low in that region. The average transmittance of the coating within the visible wavelength range is about 90%. The coating deposited in an argon only atmosphere showed a lower cut-off wavelength. The refractive index of the coating is only slightly lower than that of the bulk zinc oxide, which implies that the coating is reasonably dense. Also, the absorption coefficient of the coating is low enough to let the visible light transmit through without significant absorption occurring.

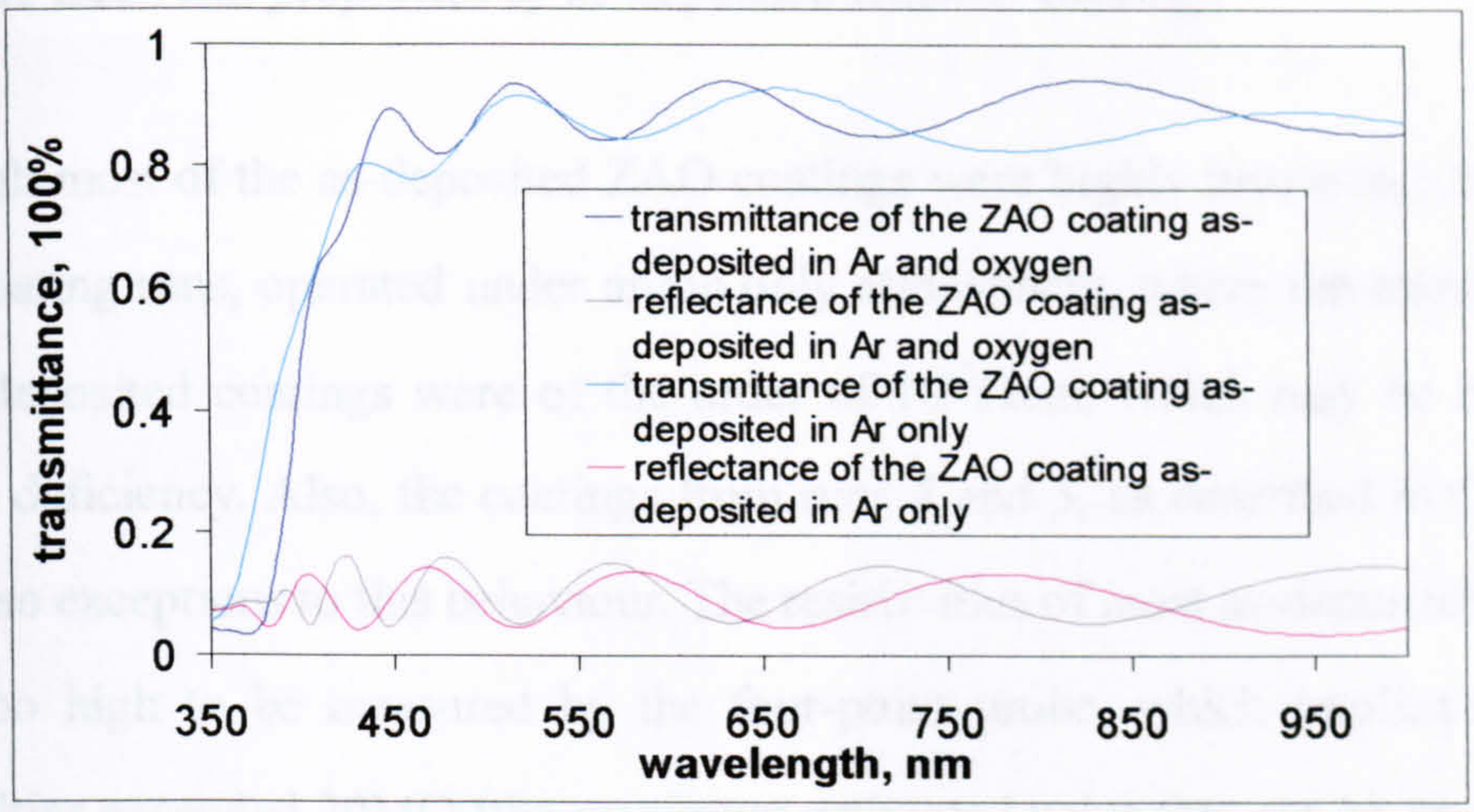

Figure 8.2 Typical transmittance and reflectance of as-deposited ZAO coatings against the wavelength spectra

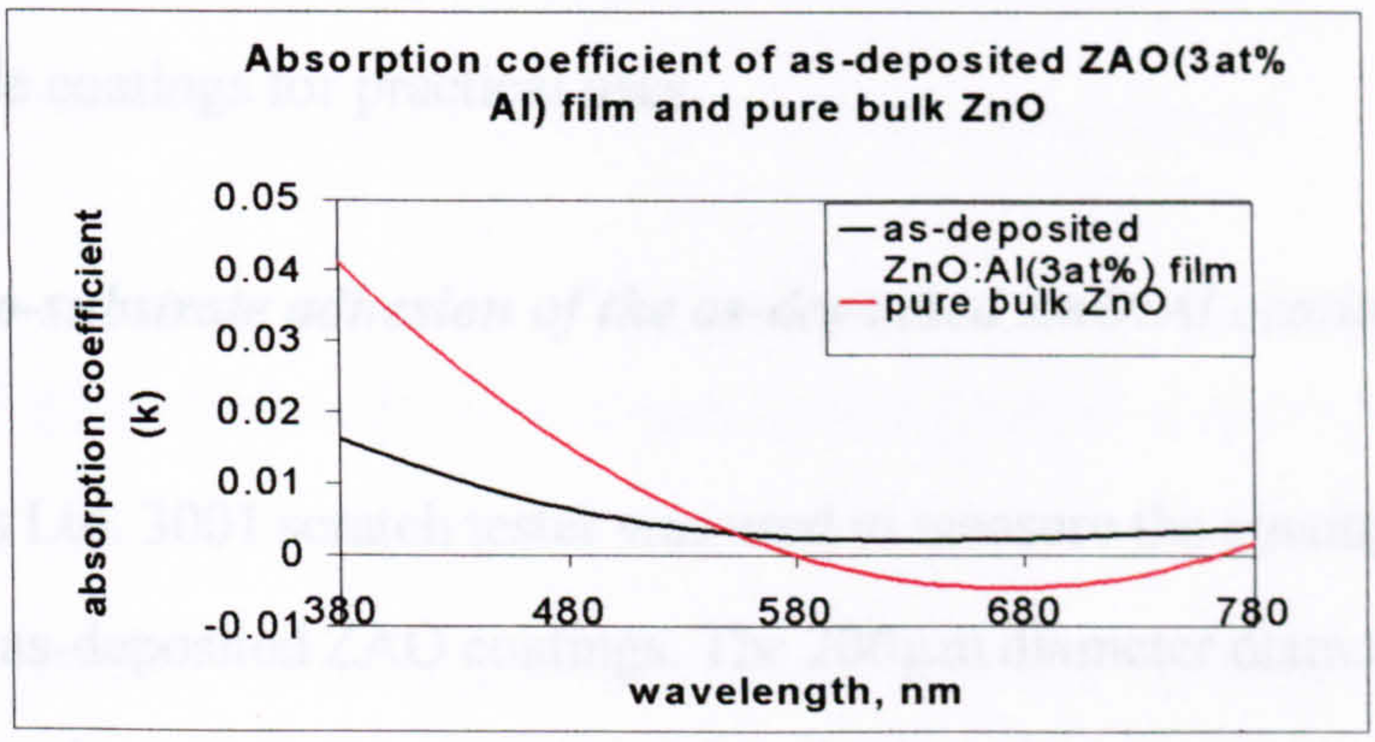

(a)

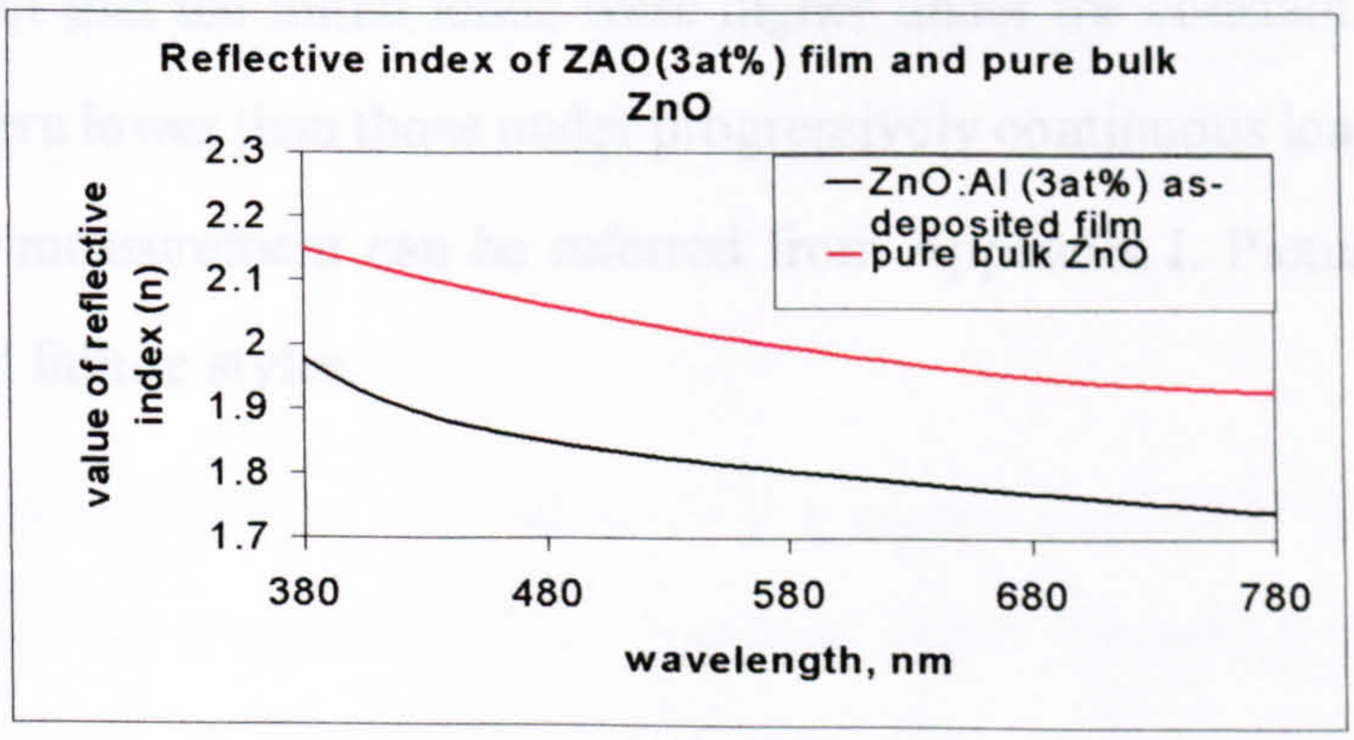

(b)

Figure 8.3 Typical a) k and b) n of the ZAO coatings compared with those of bulk ZnO

8.1.3 The electrical properties of as-deposited ZnO:Al coatings

Although most of the as-deposited ZAO coatings were highly insulating, there were three coating runs, operated under argon only atmosphere, where the resistivities of the as-deposited coatings were of the order of $10^{-2}\Omega$cm, which may be caused by oxygen deficiency. Also, the coatings from runs 4 and 5, as described in Chapter 7, were also exceptions to this behaviour. The resistivities of most as-deposited coatings were too high to be measured by the four-point probe, which implies that their resistivities exceeded 20MΩ (the maximum estimated value that can be measured by this technique). Therefore, the post-deposition treatment is essential to achieve low resistivities in the ZAO coatings, which will make them effective as transparent conductive oxide coatings for practical uses.

8.1.4 Coating-to-substrate adhesion of the as-deposited ZnO:Al coatings

A Teer Coatings Ltd. 3001 scratch tester was used to measure the coating-to-substrate adhesion of the as-deposited ZAO coatings. The 200μm diameter diamond stylus was employed whilst the measurements were taken both under progressively increasing loads to find out the failure points, and under single constant loads to confirm the failure points. The failure loads were in excess of 12N, which are acceptable. It might be due to the fact that the initial loads were higher under the constant loads that the failure points were lower than those under progressively continuous loads. The details of the adhesion measurement can be referred from Appendix I. Pictures 8.2a and b show the typical failure styles.

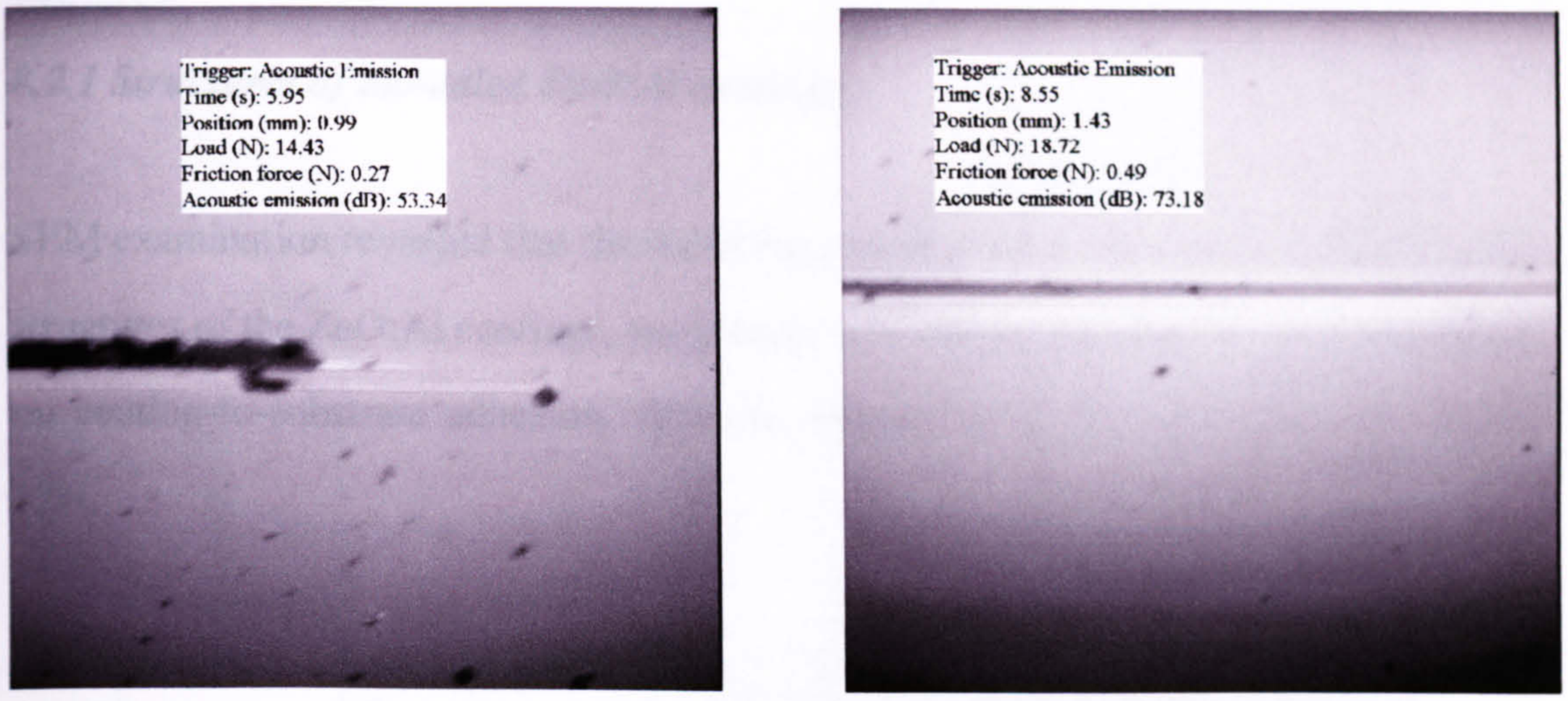

non-cleaned sample sample cleaned by HCl

under single continuous progressive load by diamond stylus

Picture 8.2 Typical failure styles of the adhesion testing

8.2 Annealed Zinc Oxide Doped Aluminium (ZAO) Coatings

As mentioned above, the as-deposited ZnO:Al coatings were generally highly insulating. To permit these coatings to act as transparent conductive oxides, therefore, it is essential to post treat the coatings to achieve lower resistivities.

Post deposition annealing under the controlled annealing temperature, time and atmosphere was considered to be a way to solve the conductivity problem of the coatings.

As a trial, two coated samples were annealed in a normal furnace at 400°C and 500°C for 1 hour in air. Both annealed coatings remained highly insulating, which indicates that the resistivities of the zinc oxide coatings are sensitive to the annealing atmosphere, i.e. oxygen concentration. Therefore, a systematic experimental array (see chapter 6.3) was designed with the variables of annealing temperature, time and

atmosphere. The results are detailed in the following sections.

8.2.1 Structures of annealed ZnO:Al coatings

SEM examination revealed that the annealing process had no discernible effect on the structures of the ZnO:Al coatings, see picture 8.3. It was also found to have no effect on coating-to-substrate adhesion, with the critical load at failure remaining above 12N.

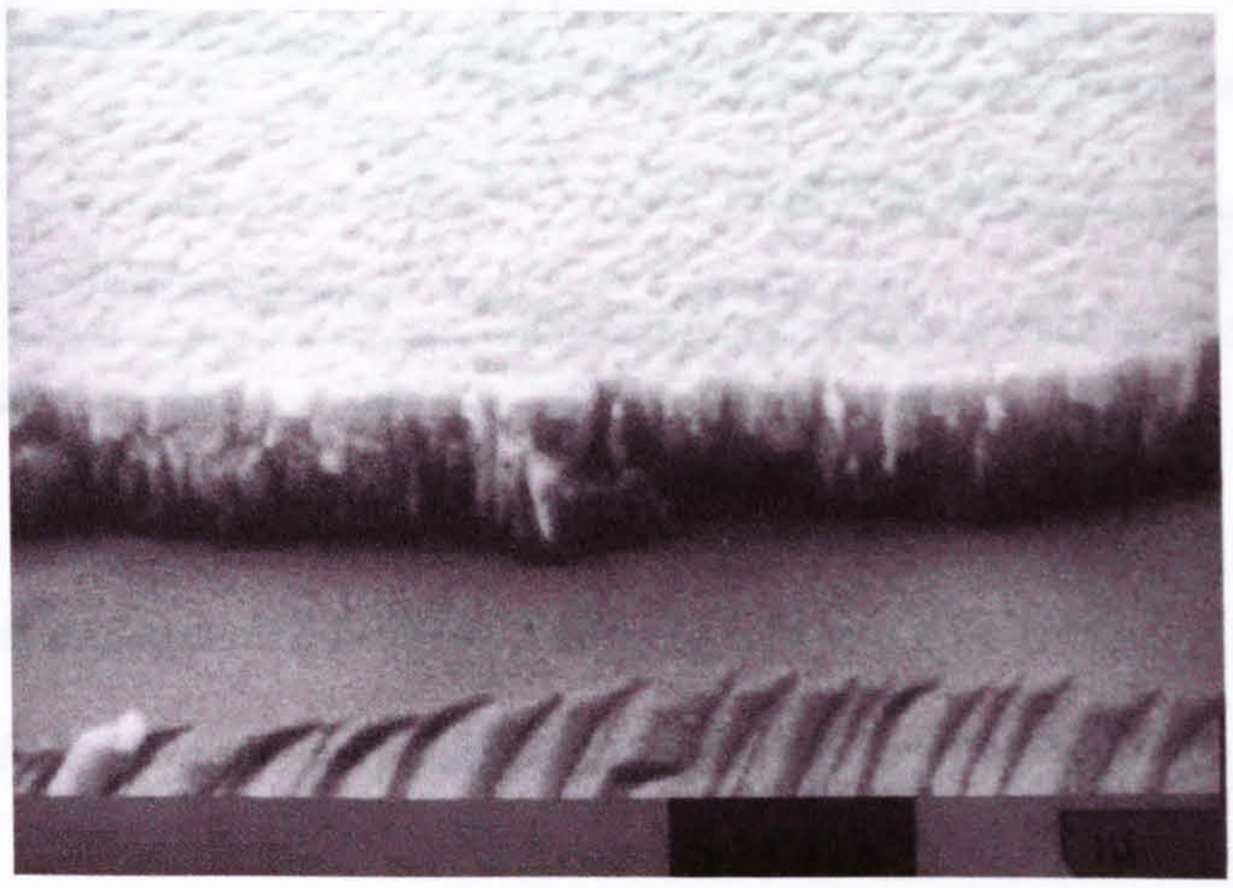

Picture 8.3 SEM micrograph of the fracture section of an annealed ZnO:Al coating

However, annealing was found to have a significant influence on the crystallinity of the coatings, with the XRD diffraction spectra generally showing a strong peak, corresponding to the (002) ZnO reflection. In comparison to the as-deposited coatings, the intensities of the (002) peaks of the annealed coatings tended to increase and were shifted closer to the standard ZnO position. The longer the annealing time was, the closer the peaks shifted to the standard ZnO position. In some cases, the diffraction traces changed from as-deposited (110) and (100) peaks to annealed (002) peak, which was the close-packed orientation of ZnO material. By way of example, figure 8.4 compares the θ-2θ traces of two as-deposited coatings with a coating annealed for 1 hour at 470°C in vacuo and another one annealed for 2 hours at 470°C in nitrogen. It has to be stated that the changes of preferred orientations of the coatings were not always the cases. In the matter of fact, some of them did retain their (100) diffraction

peak after annealing, see figure 8.4. The reason was not clear, but it was impossible to anneal the samples at higher temperatures due to the limitation of the glass substrate.

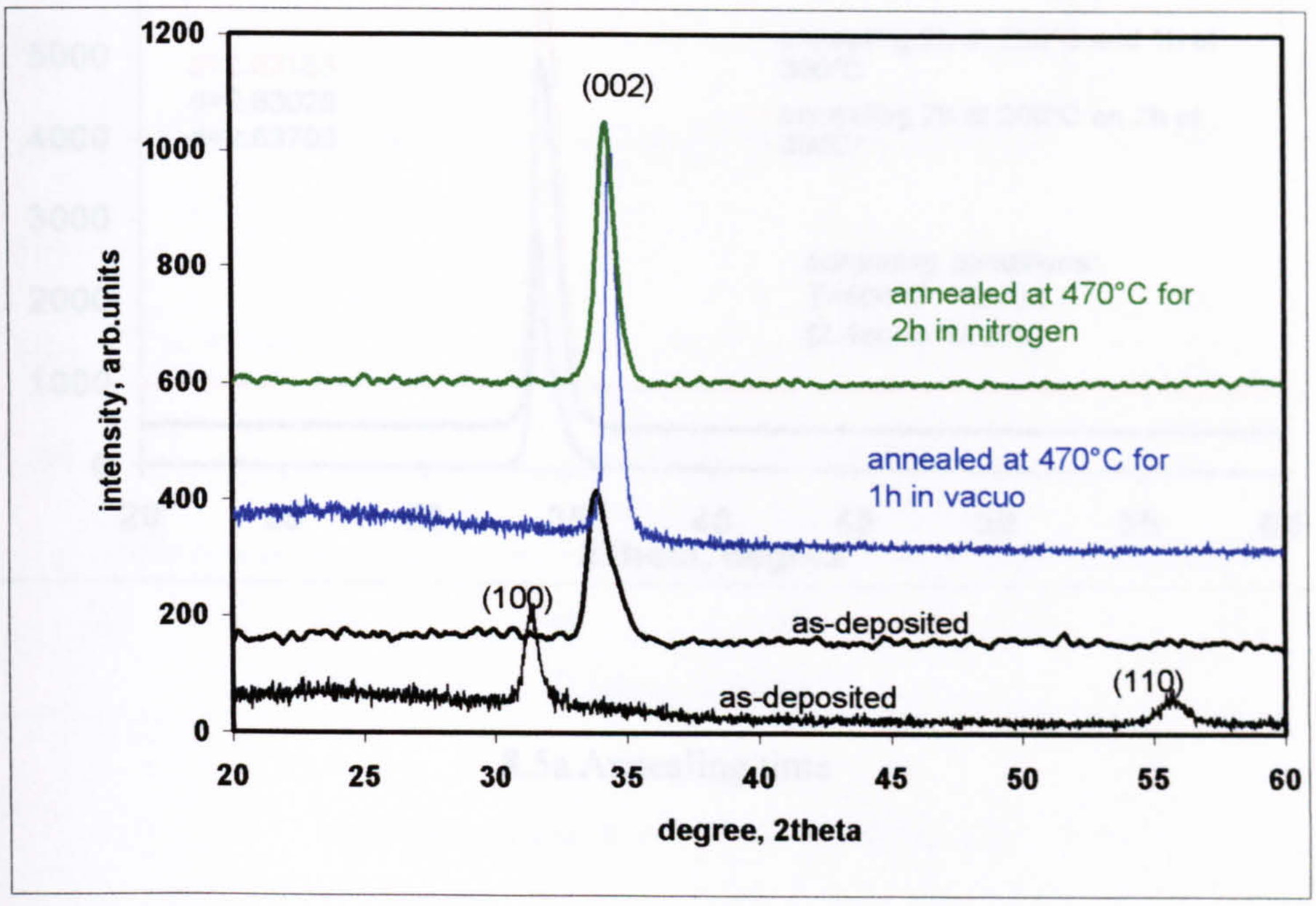

Notes: as-deposited: d (100) = 2.870, d (110) = 1.684, d (002) = 2.6823

annealed: 1h in vacuo d (002) = 2.62026; 2h in N2 d (002) = 2.6006

Figure 8.4 XRD diffraction spectra for the as-deposited and annealed ZnO:Al coatings

The effect of annealing variables, i.e. time, temperature and atmosphere, on the crystallinity of the coatings is shown in figures 8.5a, 8.5b and 8.5c. High annealing temperature, long annealing time and pure nitrogen or vacuo in the annealing atmosphere leads to peak shifts towards the reflection peak positions of standard zinc oxide powder, taken from JCPDS cards. For example, the d spacing of the (002) peak changes from 2.682 before annealing to 2.621 after annealing, compared with 2.602 showed by JCPDS cards. Finally, there were two runs where the crystalline peaks were different from the other coatings. Not only the (002) peak appeared, but also the (100) and (101) peaks could be seen, although the (002) peak remained the most significant. The reason for this is not known at this time.

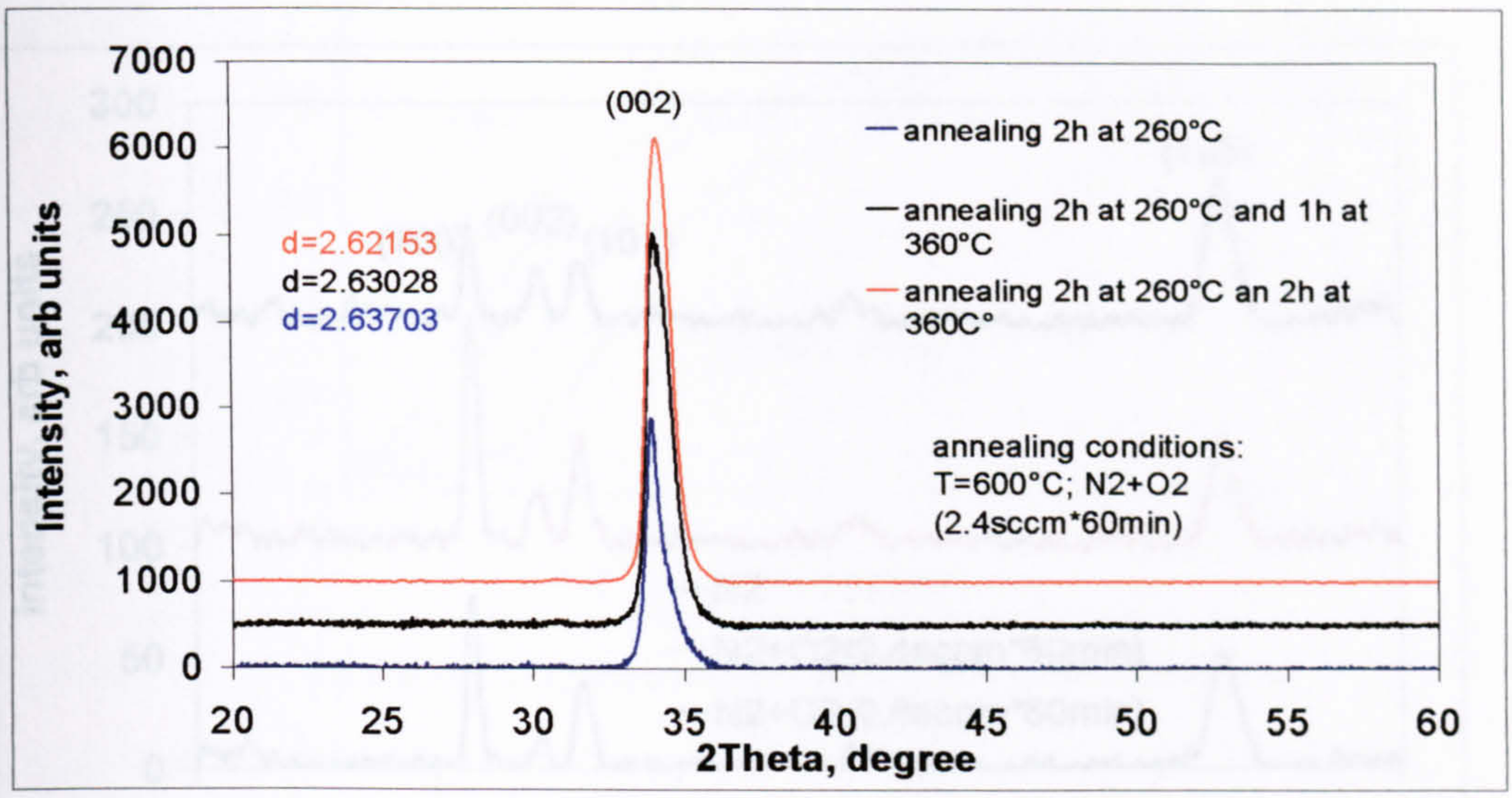

8.5a Annealing time

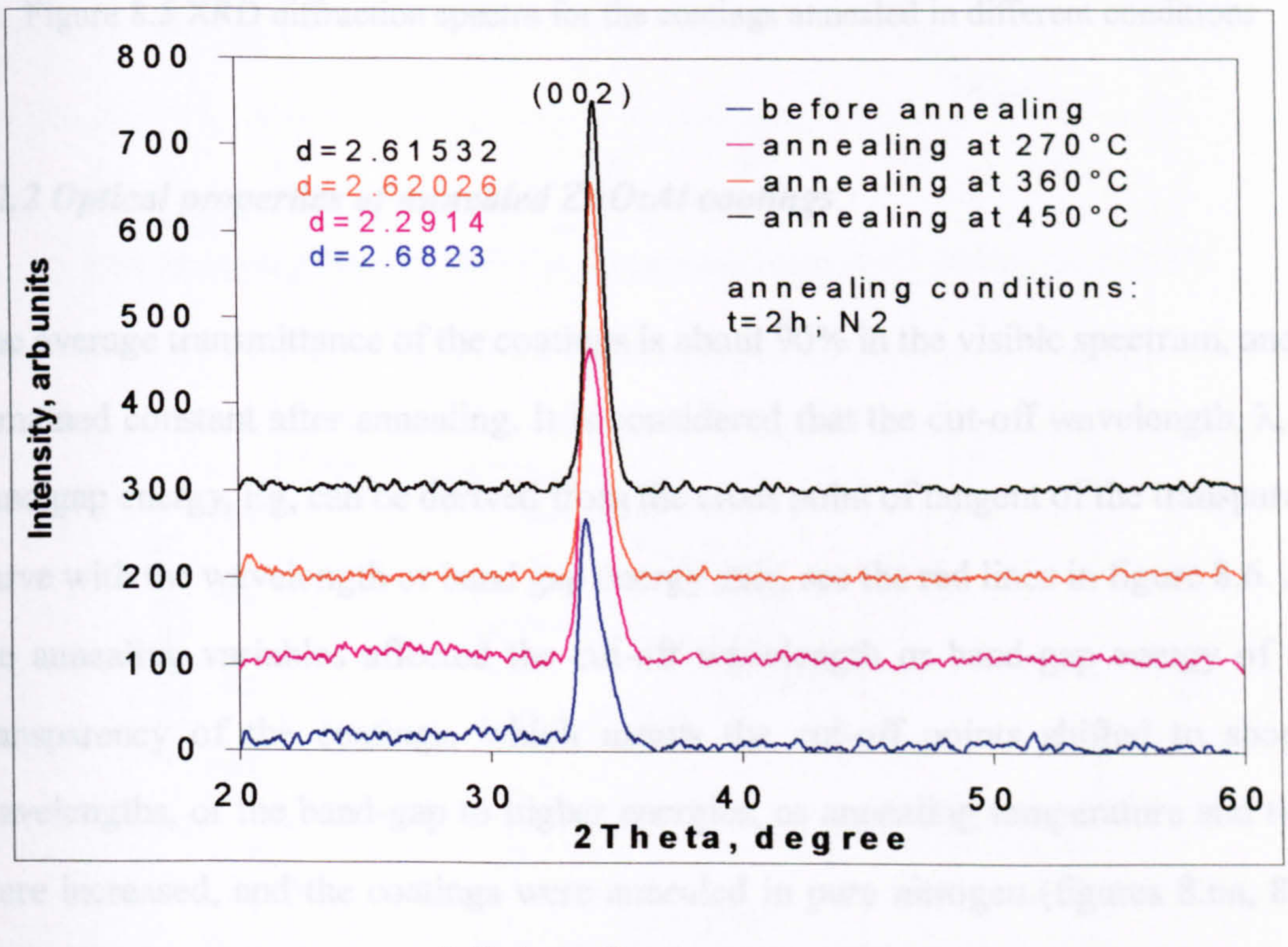

8.5b Annealing temperature

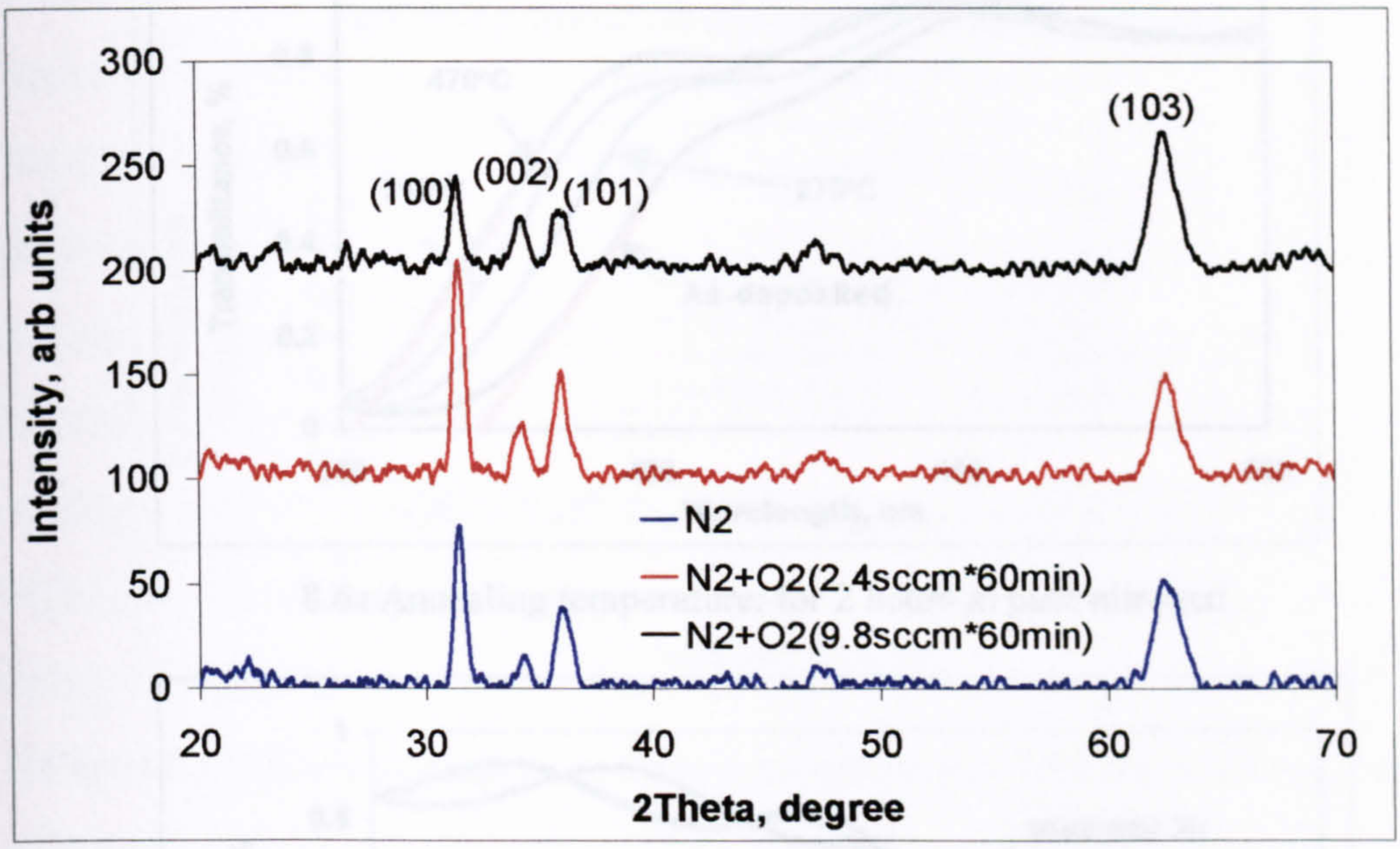

8.5c Annealing atmosphere (@360^{0}C 2h)

Figure 8.5 XRD diffraction spectra for the coatings annealed in different conditions

8.2.2 Optical properties of annealed ZnO:Al coatings

The average transmittance of the coatings is about 90% in the visible spectrum, and it remained constant after annealing. It is considered that the cut-off wavelength, λ, or band gap energy, Eg, can be derived from the cross point of tangent of the transparent curve with the wavelength or band gap energy axis, see the red lines in figure 8.6. All the annealing variables affected the cut-off wavelength or band-gap energy of the transparency of the coatings, which means the cut-off points shifted to shorter wavelengths, or the band-gap to higher energies, as annealing temperature and time were increased, and the coatings were annealed in pure nitrogen (figures 8.6a, 8.6b and 8.6c). For example, the band gap shifted from 3.3eV to 3.49, which corresponded to the wavelength from 375nm to 355nm (Eg=hc/λ =1240eV.nm/ λnm) according to figure 8.6a.

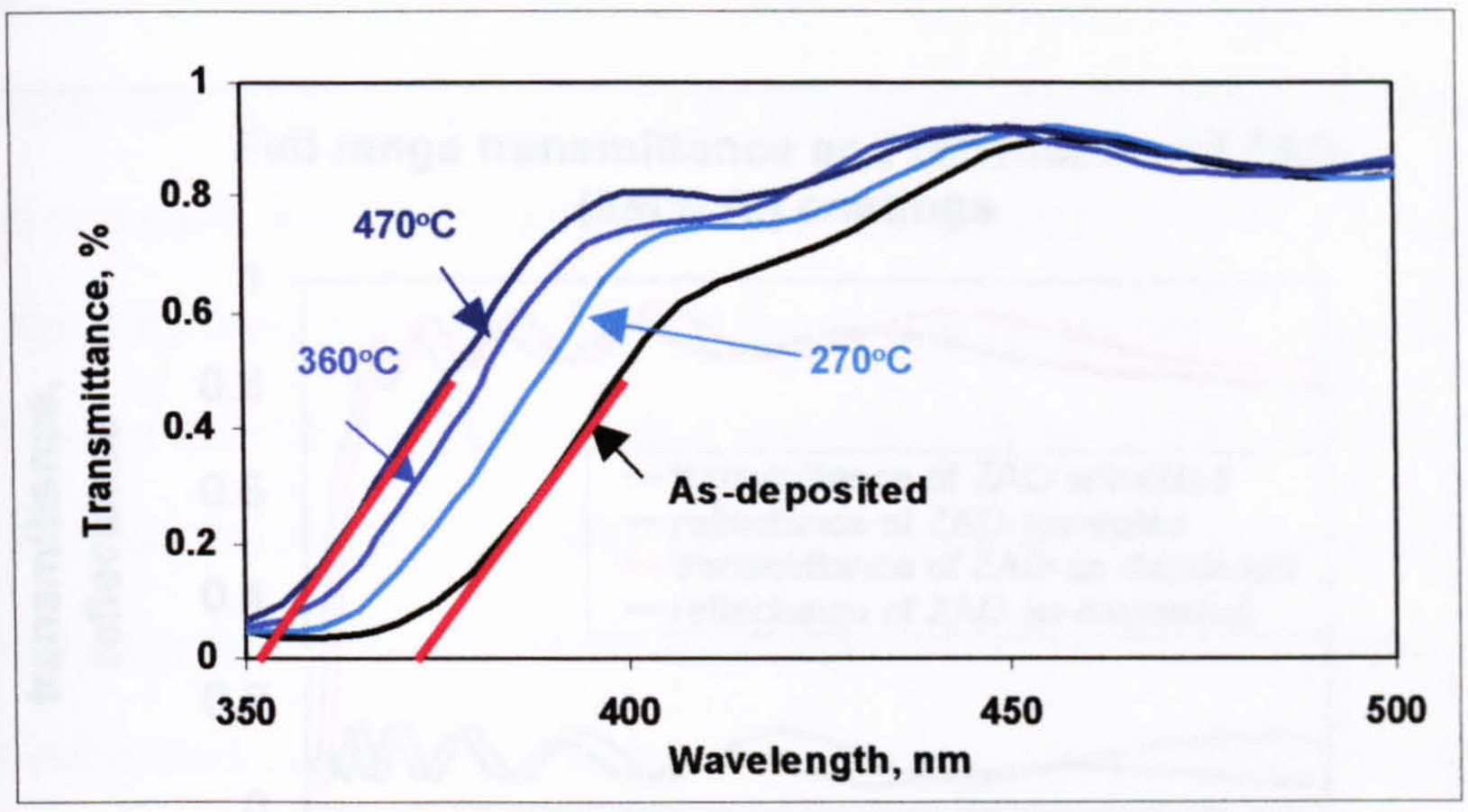

8.6a Annealing temperature: for 2 hours in pure nitrogen

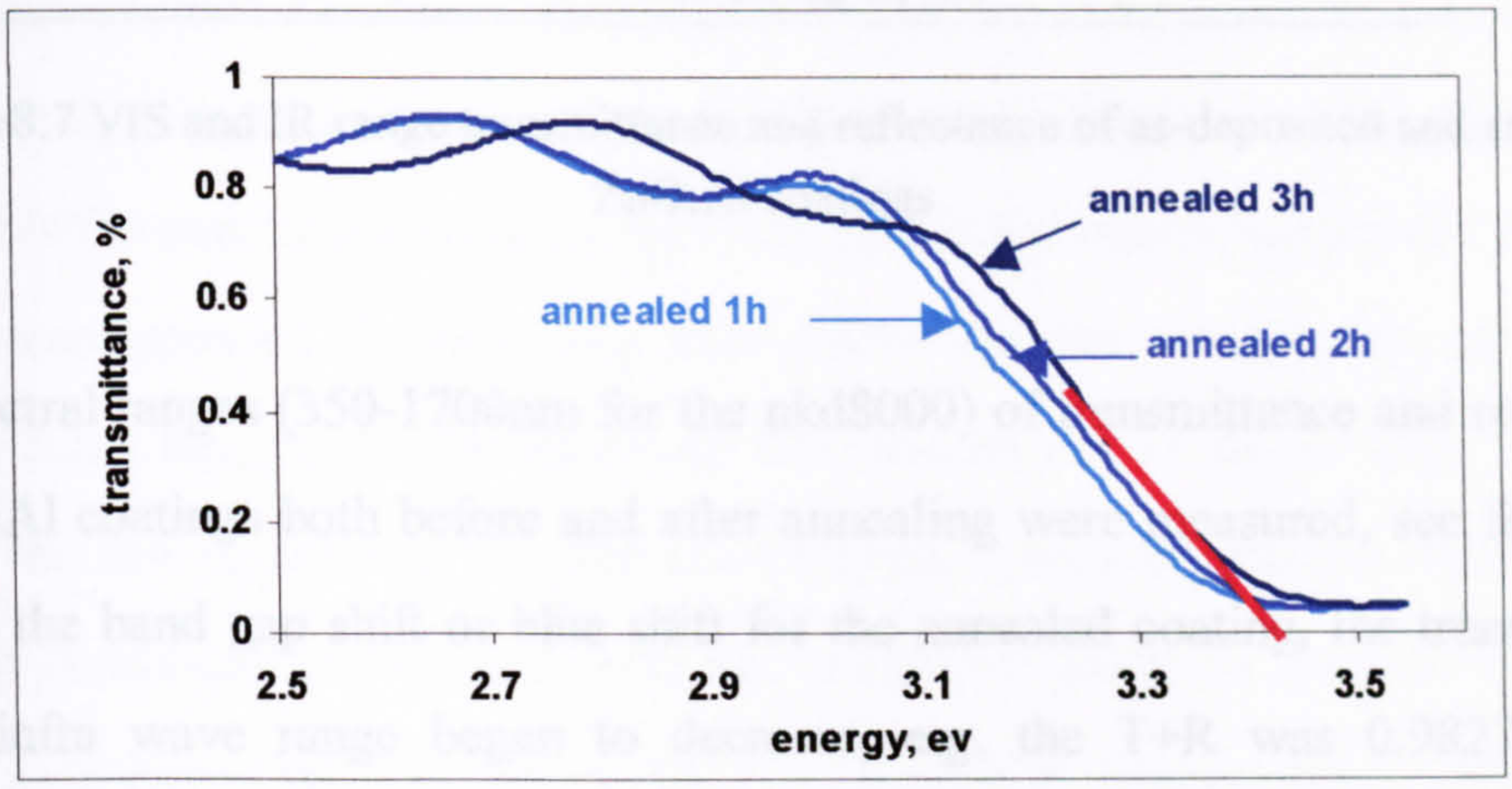

8.6b Annealing time: @360°C in nitrogen and oxygen (2.4sccm) mixture gas

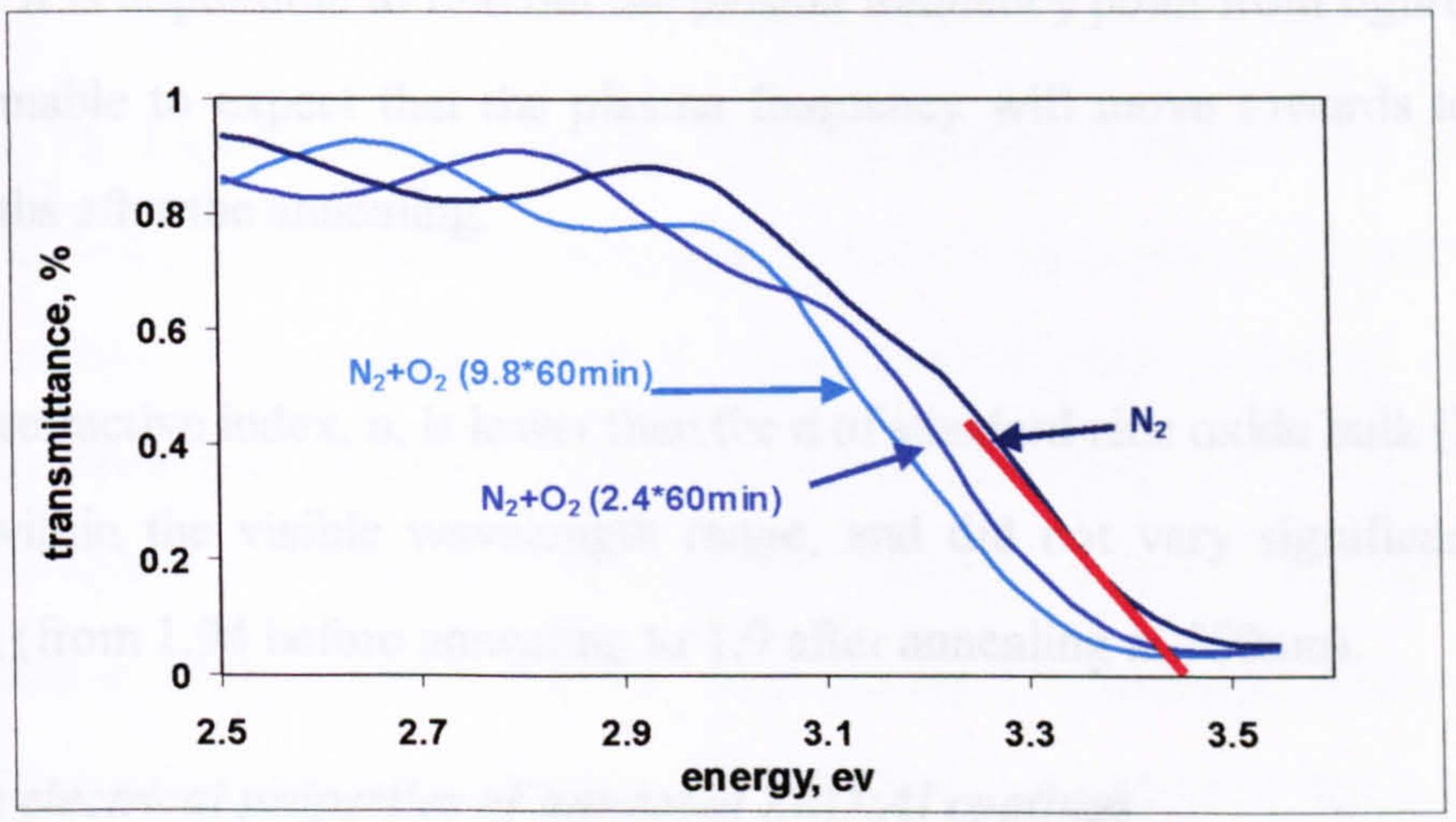

8.6c Annealing atmosphere: @360°C for 2h

Figure 8.6 Transmission spectra or band gap energy for annealed ZnO:Al (2wt%) coatings

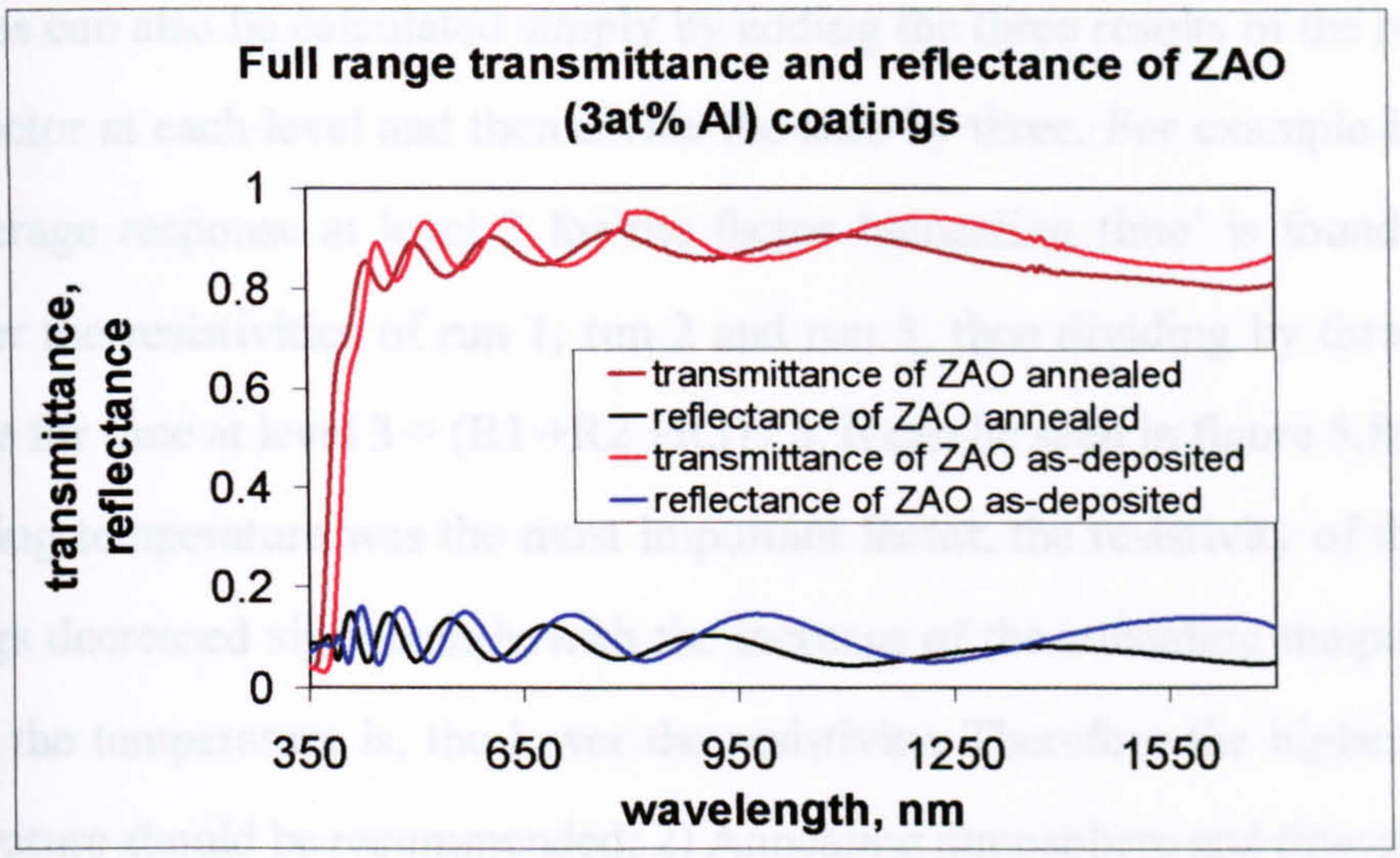

Figure 8.7 VIS and IR range transmittance and reflectance of as-deposited and annealed ZnO:Al coatings

Full spectral ranges (350-1700nm for the nkd8000) of transmittance and reflectance of ZnO:Al coatings both before and after annealing were measured, see figure 8.7. Besides the band gap shift or blue shift for the annealed coating, the transmittance within infra wave range began to decrease, e.g. the T+R was 0.98275 before annealing, and 0.861425 after annealing at 1700nm, which means the IR absorption increased. It is impossible to find out the plasma frequency point from figure 8.7, but it is reasonable to expect that the plasma frequency will move towards to shorter wavelengths after the annealing.

Also, the refractive index, n, is lower than the n of standard zinc oxide bulk (2.0145 at 550nm) within the visible wavelength range, and did not vary significantly after annealing (from 1.94 before annealing to 1.9 after annealing at 550nm).

8.2.3 The electrical properties of annealed ZnO:Al coatings

A detailed study of the influence of annealing time, temperature and atmosphere on coating resistivity has also been carried out, by using resistivity as the response of the Taguchi array when analysed using the ANOVA-TM software package. This gave the

level averages for each array factor at each level, shown in figure 8.8a. The level averages can also be calculated simply by adding the three results of the response for each factor at each level and then divide the sum by three. For example in table 6.3, the average response at level 3 for the factor 'annealing time' is found by adding together the resistivities of run 1, run 2 and run 3, then dividing by three, i.e. level average for time at level 3 = (R1 +R2 +R3) / 3. It can be seen in figure 8.8a that 1) the annealing temperature was the most important factor, the resistivity of the annealed coatings decreased significantly with the increase of the annealing temperature. The higher the temperature is, the lower the resistivity. Therefore the highest annealing temperature should be recommended; 2) Annealing atmosphere and time also affected the resistivity, but to a lesser extent; 3) The lowest resistivity of the coating was obtained in the pure nitrogen atmosphere. Oxygen in the annealing atmosphere should not be recommended in annealing atmosphere for the coatings deposited from ceramic oxide targets; 4) The annealing time should not be longer than 2 hours to achieve the low resistivity. The Taguchi analysis, therefore, predicts that, from the range of conditions tested, the operating conditions likely to produce the lowest coating resistivity ($3x10^{-3}\Omega cm$) would be an annealing temperature of 470°C for 2 hours in pure nitrogen atmosphere.

To confirm the Taguchi analysis results, further annealing treatment was carried out by changing only one of the three factors at a time for each process. Limited by the available samples, the samples used in these confirmation annealing runs were selected from previous annealed samples in Taguchi annealing runs. For example, the annealed sample at 270°C in pure nitrogen for 2 hour, from run 6, was cut into three and annealed at 360°C, 420°C and 470°C, respectively. The annealed sample from run 8, annealed in pure nitrogen for 1 hour at 360°C, was cut into three and one of them was annealed in pure nitrogen at 360°C for 1 hour again, the other two at same temperature for two hours in different oxygen atmosphere. The annealed sample from run 9, annealed at 270°C for 1 hour at less oxygen atmosphere, was cut into three, and those three were annealed at 360°C at same atmosphere for 1, 2 and 3h, respectively.

The results were slightly different, see figures 8.8b and c, which may be due to the annealing processes for the factors of time and atmosphere were not carried out at highest temperature and slightly affected by the previous annealing treatment. The resistivity decreased with the increase of annealing temperature at pure nitrogen atmosphere, and the increase of annealing time in low oxygen atmosphere. The rate of decrease of the resistivity became much slow after annealing two hours. The resistivity of the coating annealed in low oxygen was slightly higher than those of the coatings annealed in high oxygen and pure nitrogen atmosphere. Still, the temperature is the most significant factor, and the recommended annealing parameters were high temperature, pure nitrogen and certain long time. For example, the lowest resistivity of the ZnO:Al coating, $3x10^{-3}\Omega cm$, was obtained after the coating was annealed at 470°C in pure nitrogen for 2hours.

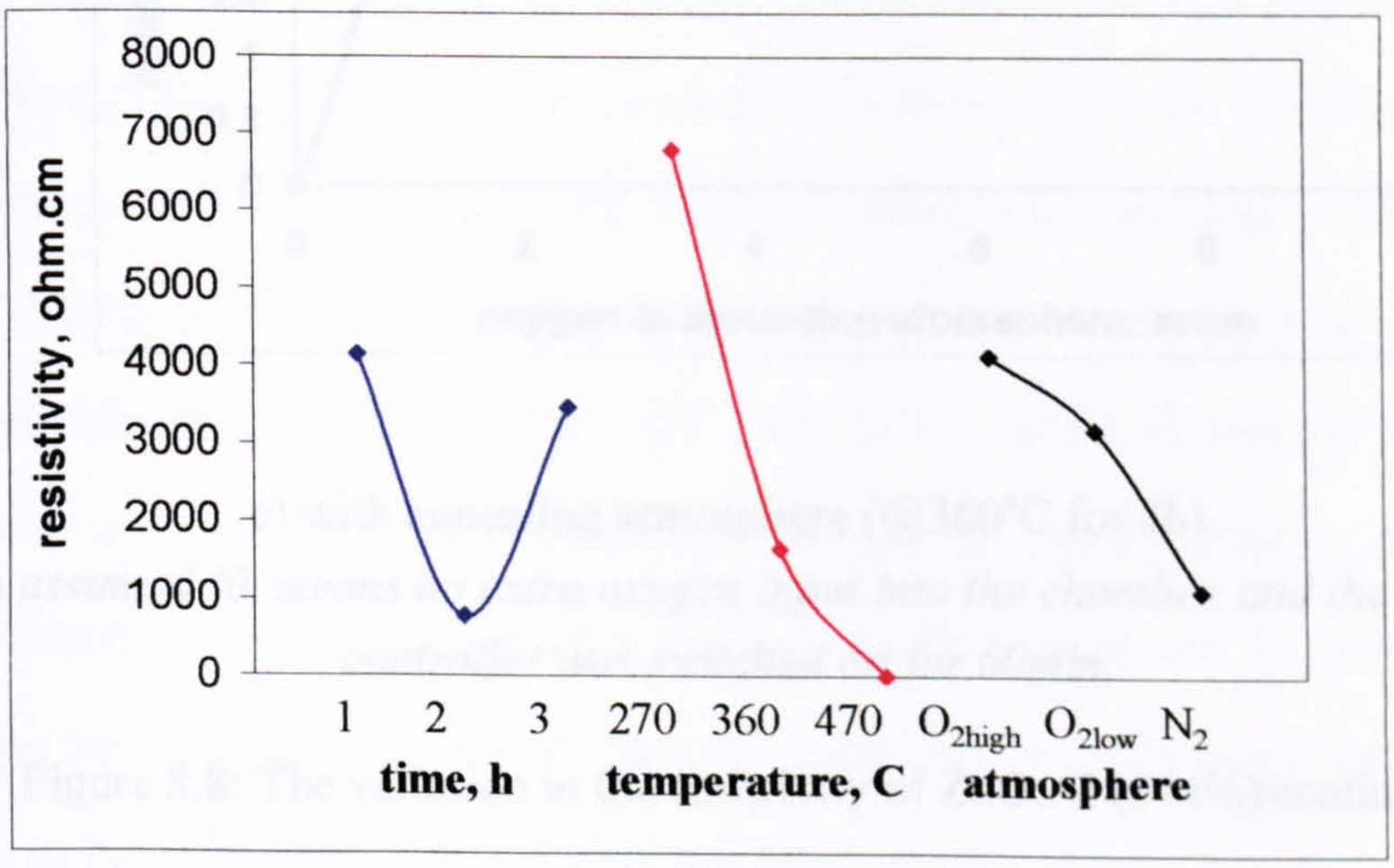

a) the Taguchi array analysis of the resistivity of the annealing coatings

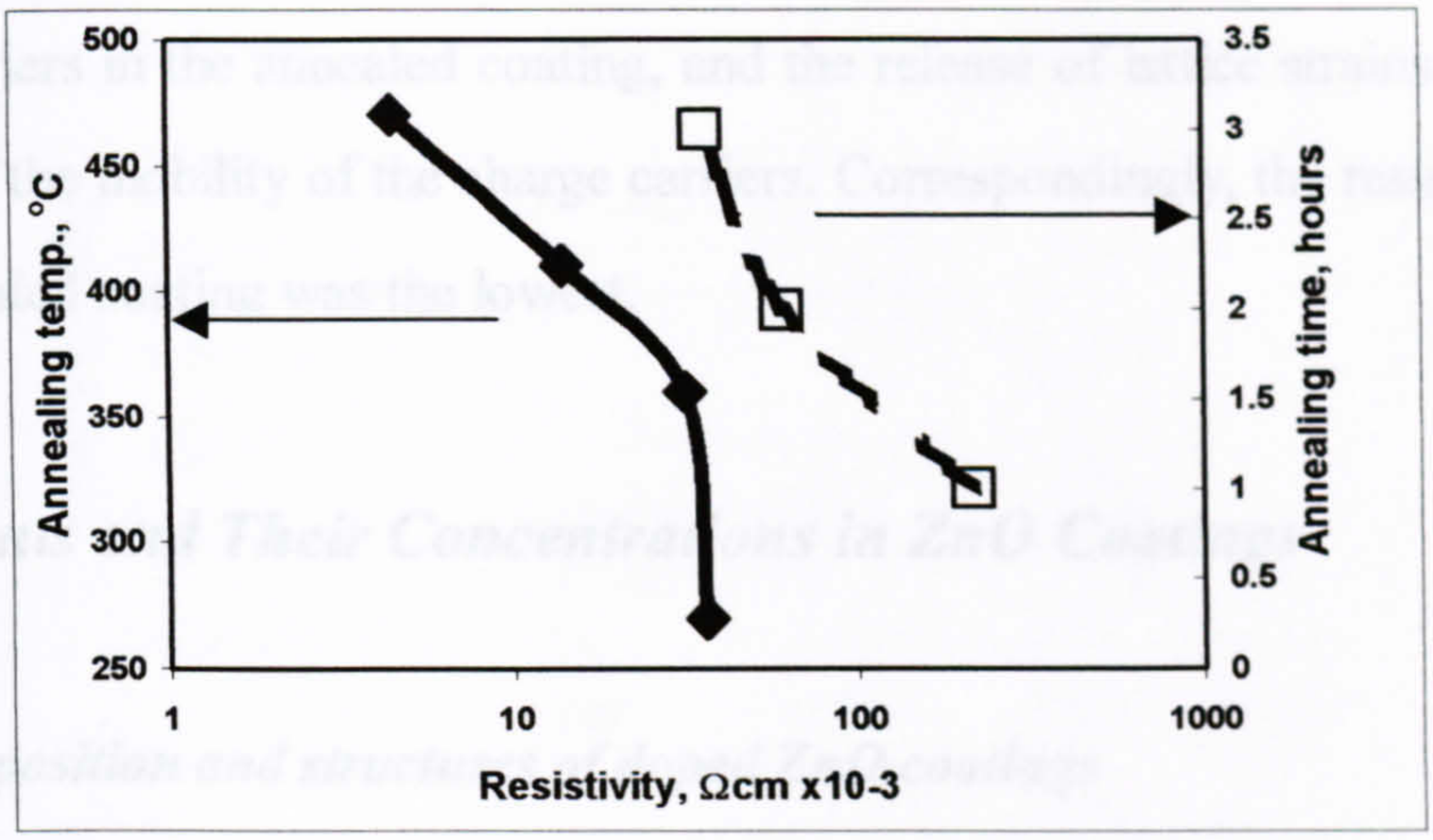

b) with annealing temperature (pure N_2 atmosphere for 2 hours) and annealing time (@360°C in 2.4sccm x 60min O_2 atmosphere)

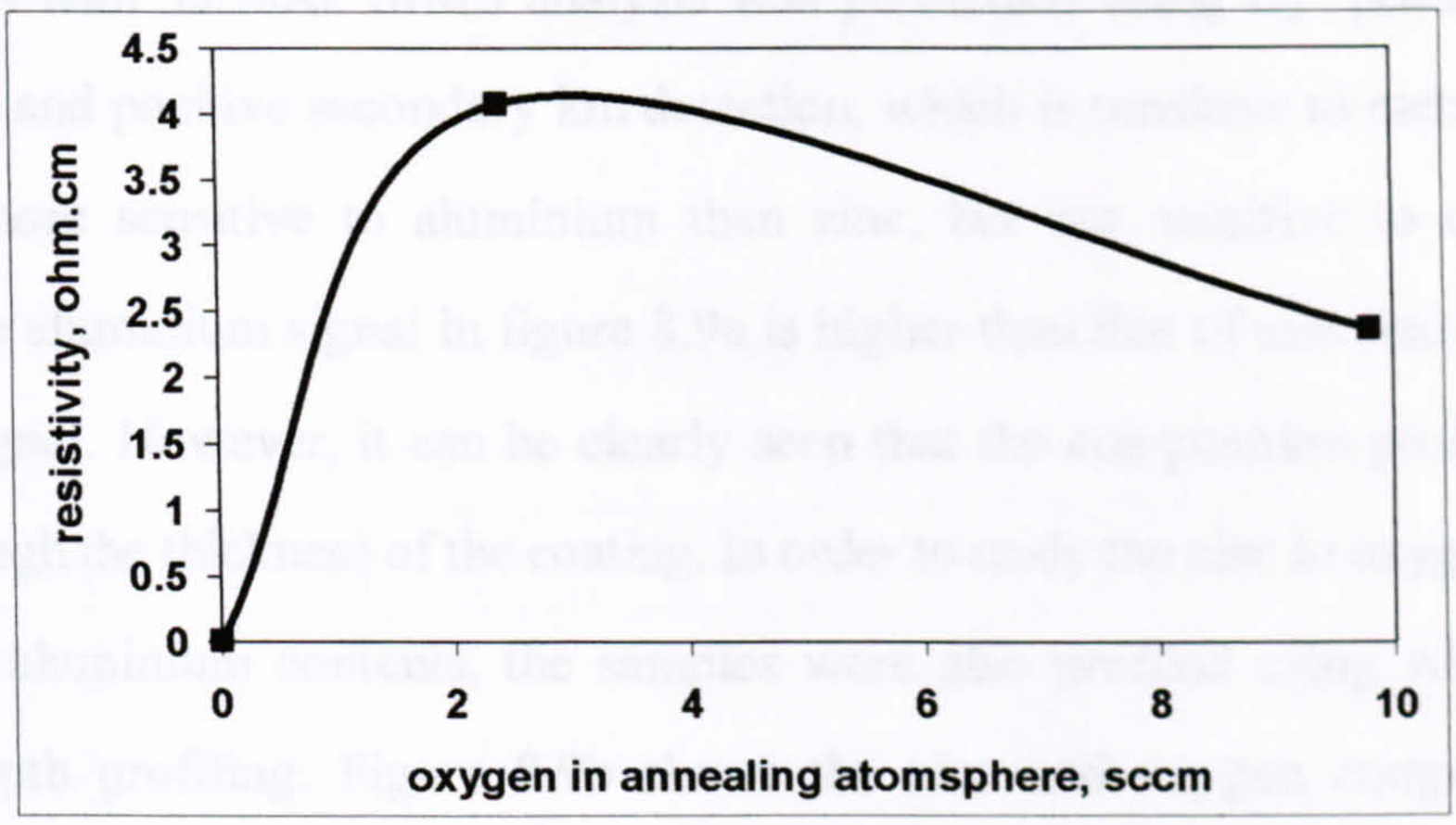

c) with annealing atmosphere (@360°C for 2h)

note: it is assumed '0' means no extra oxygen input into the chamber, and the oxygen flow controller was switched on for 60min.

Figure 8.8: The variation in the resistivity of ZnO:Al (2wt%) coatings

In general, annealing processes did not change the structure of the coatings, and did not deteriorate the coating-to-substrate adhesion. The transmittance of the coatings remained the same as those before annealing. The cut-off point of the coating annealed in pure nitrogen, at the highest temperature and for the certain long, i.e.

2hours, time had the biggest blue shift in the optical spectra, and most complete release of lattice strains. It is believed that the blue shift is due to an increase in the charge carriers in the annealed coating, and the release of lattice strains leads to the increase of the mobility of the charge carriers. Correspondingly, the resistivity of the same annealed coating was the lowest.

8.3 Dopants and Their Concentrations in ZnO Coatings

8.3.1 Composition and structures of doped ZnO coatings

A combination of secondary ion mass spectrometry (SIMS) and Auger electron spectroscopy (AES) was employed to analyze the compositions of samples of zinc oxide coatings with 3at%Al. SIMS analysis was performed using O_2^+ primary ion bombardment and positive secondary ion detection, which is sensitive to metals, and particularly more sensitive to aluminium than zinc, but not sensitive to oxygen. Therefore, the aluminium signal in figure 8.9a is higher than that of zinc and there is no oxygen signal. However, it can be clearly seen that the composition profiles are constant through the thickness of the coating. In order to study the zinc to oxygen ratio and estimate aluminium contents, the samples were also profiled using AES with argon ion depth profiling. Figure 8.9b shows the zinc and oxygen compositions through the thickness of the coating and their ratio. Again, it can be seen that the compositions of the coatings are consistent through the whole range of the thickness. The aluminium signal in AES was too small to be monitored in profiles, but an attempt was made to quantify the Al content about half way through the layer, which was found to be of the order of 2-3at%, see 8.9c.

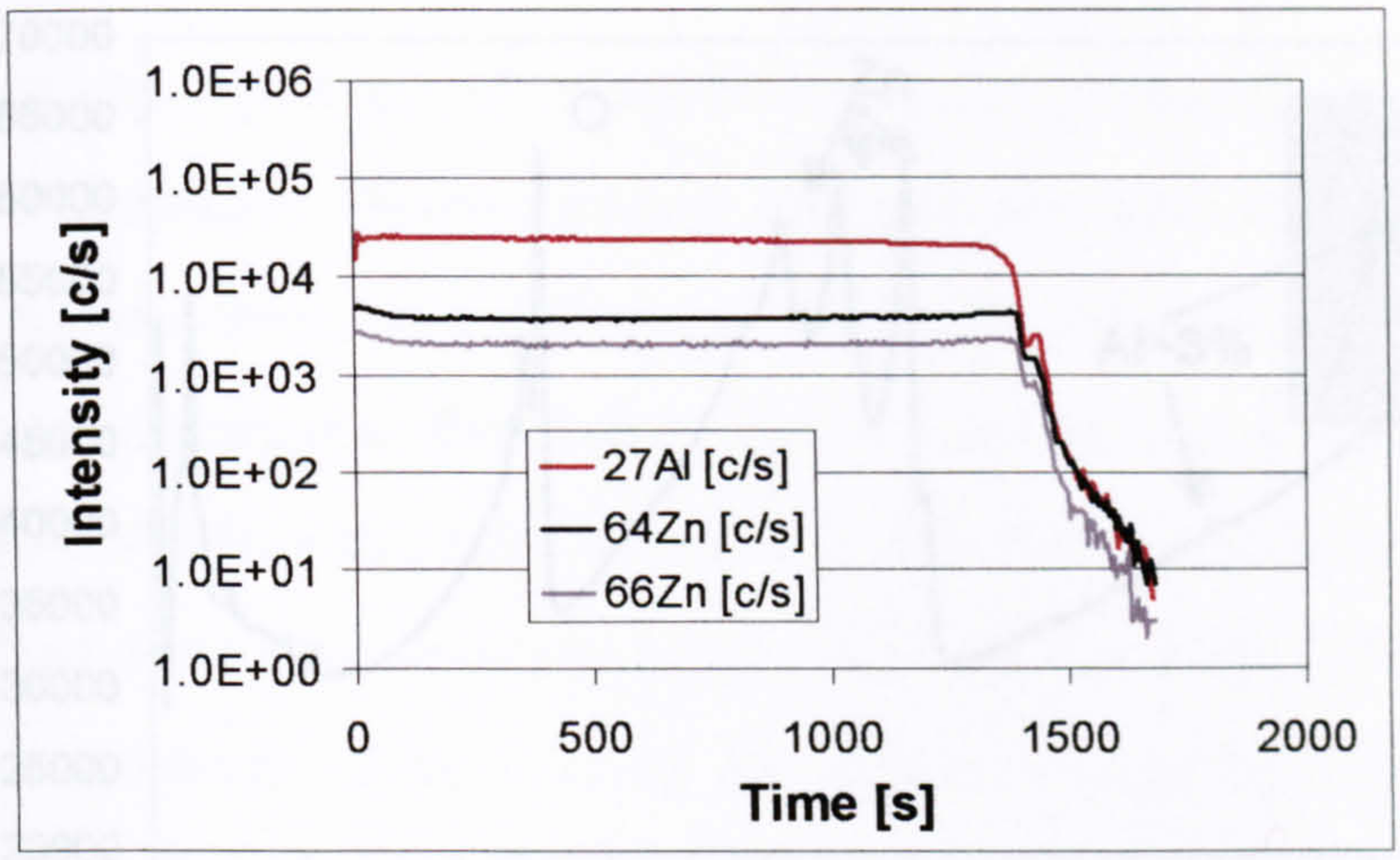

8.9a SIMS profile of zinc and aluminium compositions vs. sputtering time (through thickness of the Al-doped ZnO coating)

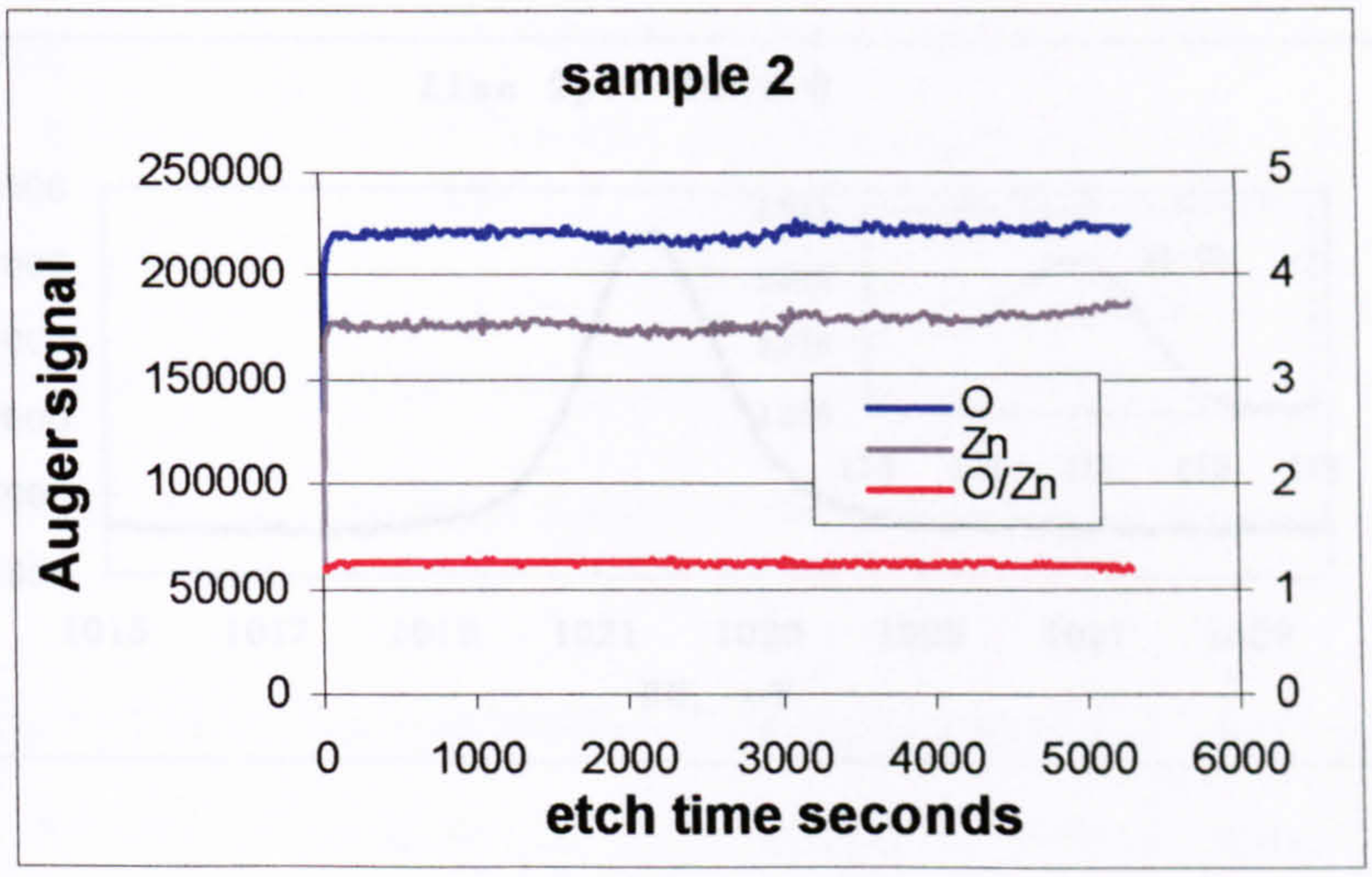

8.9b Auger profile of zinc and oxygen compositions and their ratio vs. sputtering time (through thickness of the Al-doped ZnO coating)

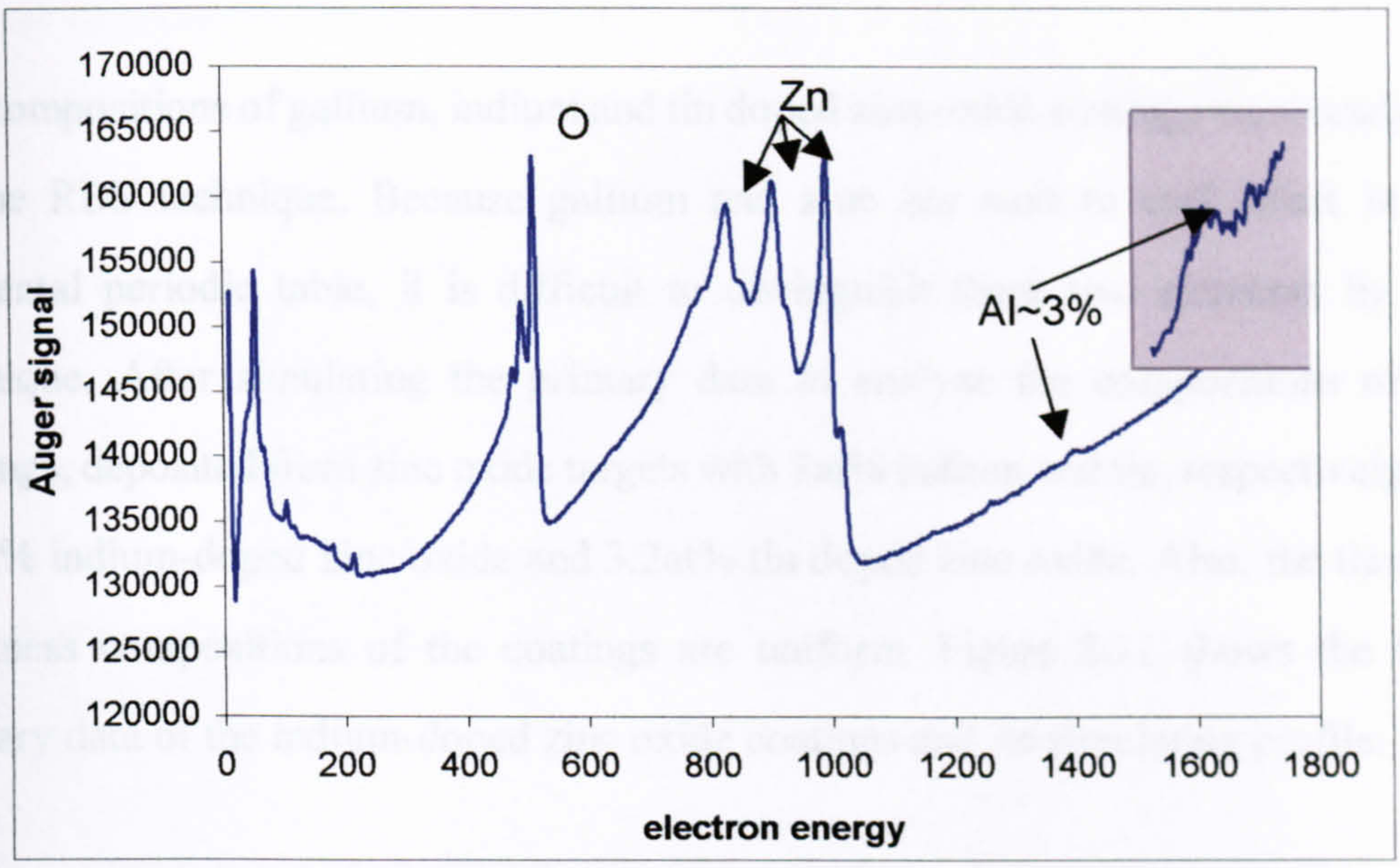

8.9c Auger spectrum of the ratio of aluminium element in the coating

Figure 8.9 Compositions of the coating deposited from the zinc oxide target with 3at% Al analyzed by AES

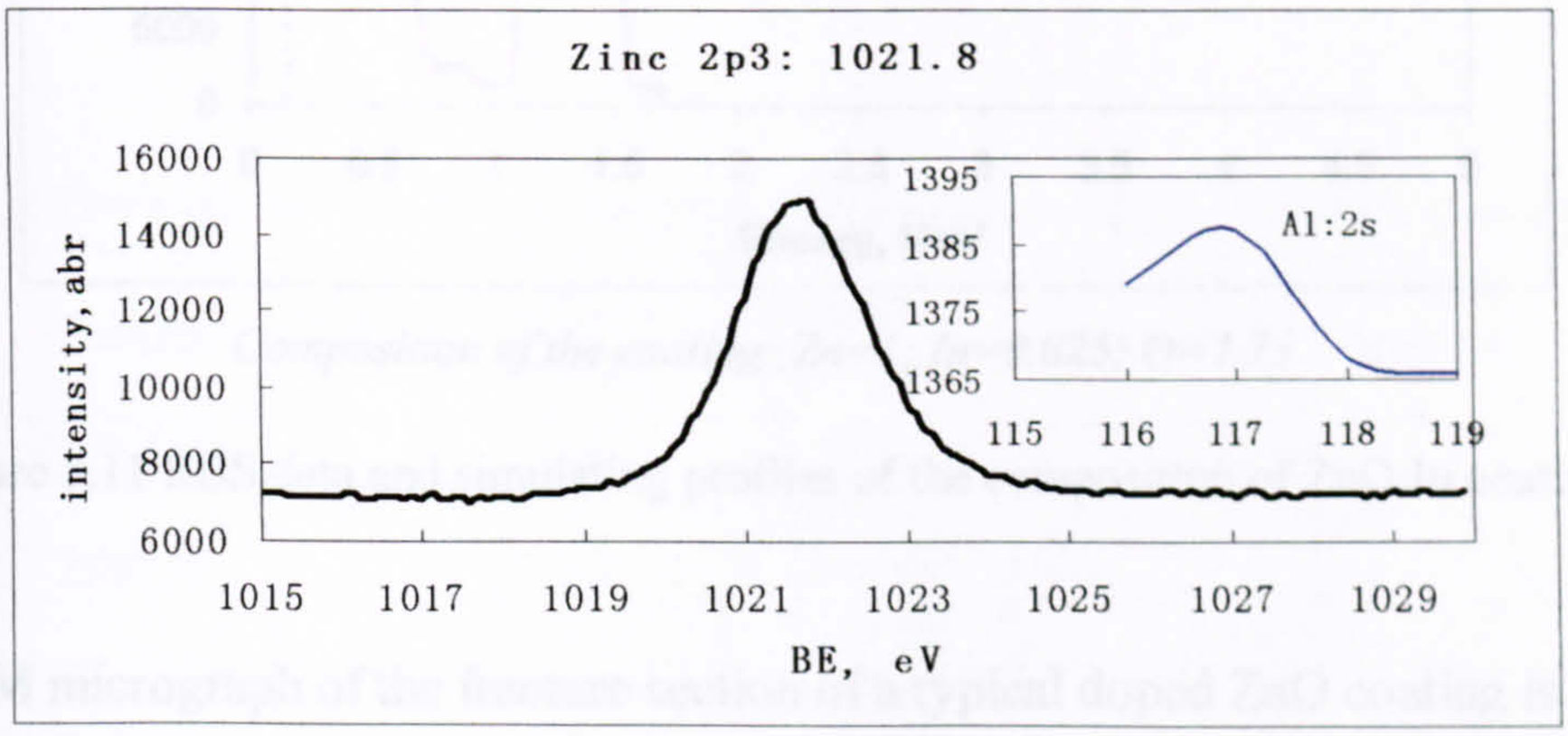

Figure 8.10 Compositions of the coating deposited from Al:ZnO (3at%) target analyzed by XPS

The XPS technique was also used to measure the aluminium doped zinc oxide coating produced from the ZnO:Al (3at%) target. Figure 8.10 shows the zinc 2p3 peak and aluminium 2s peaks, which are located around 1021.8eV and 117.9eV, and their sensitivity factors are 4.8 and 0.23, respectively. The ratio of aluminium and zinc of the coating is about 3.5%, which is roughly consistent with the composition of the

target.

The compositions of gallium, indium and tin doped zinc oxide coatings were analyzed by the RBS technique. Because gallium and zinc are next to each other in the elemental periodic table, it is difficult to distinguish these two elements by this technique. After simulating the primary data to analyze the compositions of the coatings, deposited from zinc oxide targets with 3at% indium and tin, respectively, are 2.5at% indium-doped zinc oxide and 3.2at% tin doped zinc oxide. Also, the through thickness compositions of the coatings are uniform. Figure 8.11 shows the RBS primary data of the indium-doped zinc oxide coatings and its simulating profile.

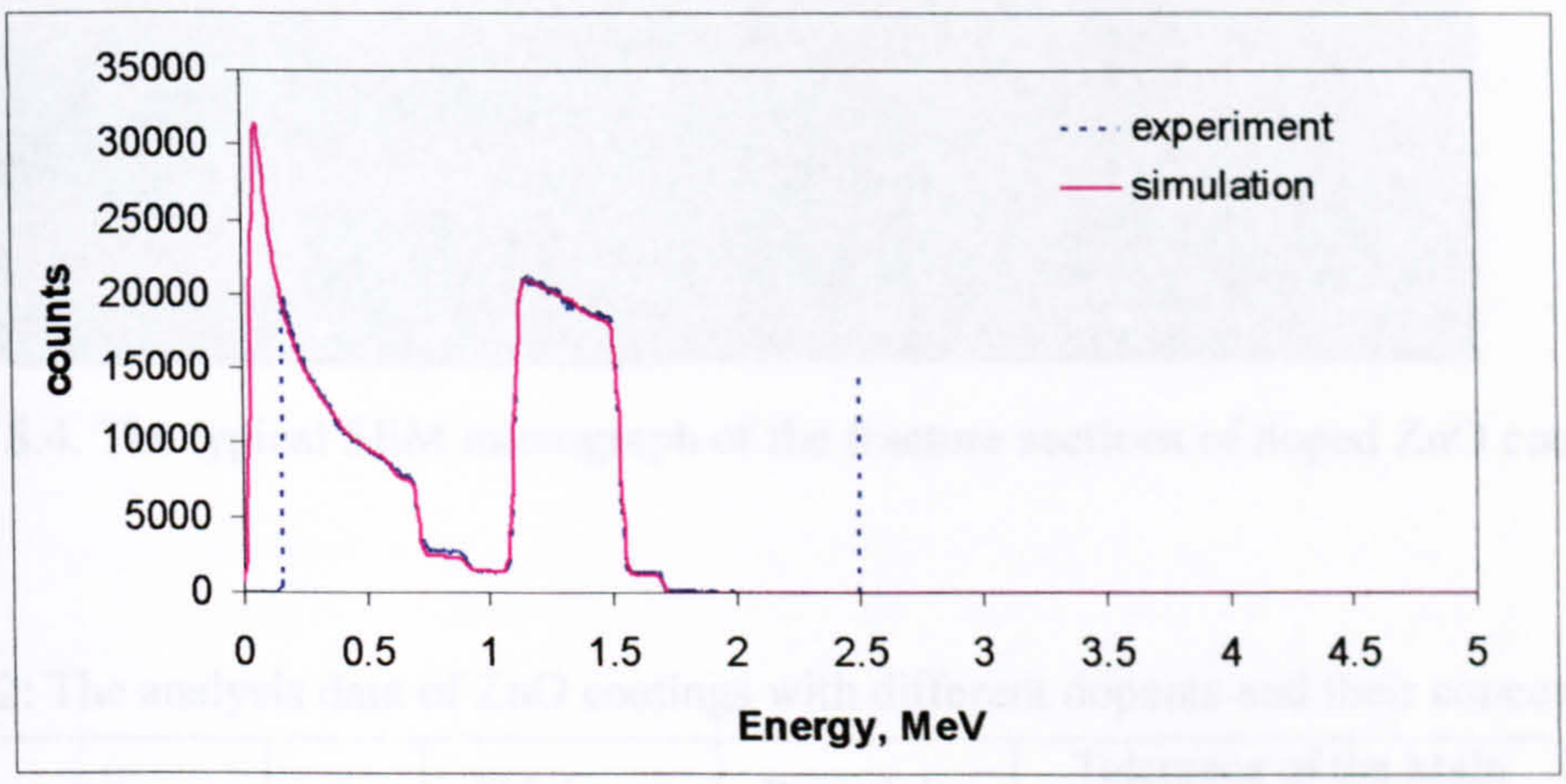

Composition of the coating: Zn=1; In=0.025; O=1.75

Figure 8.11 RBS data and simulating profiles of the composition of ZnO:In coating

The SEM micrograph of the fracture section of a typical doped ZnO coating is shown in picture 8.4. As can be seen, the coating appears to have a dense columnar, defect-free structure. There is no obvious difference between the structures of the coatings with different dopants. The thickness of the coatings, measured by the Dektak ST3, increased as the atomic size of the dopant elements increased, see table 8.2 and picture 8.4, which means that the deposition rates were strongly depended on the dopant elements. Also, the thickness slightly increased with the increase of the doping levels, although there was an exception in 3at% Ga doped coating. The

resistivity of the doped coatings also changed as the changes of dopant elements and their concentrations, see table 8.2.

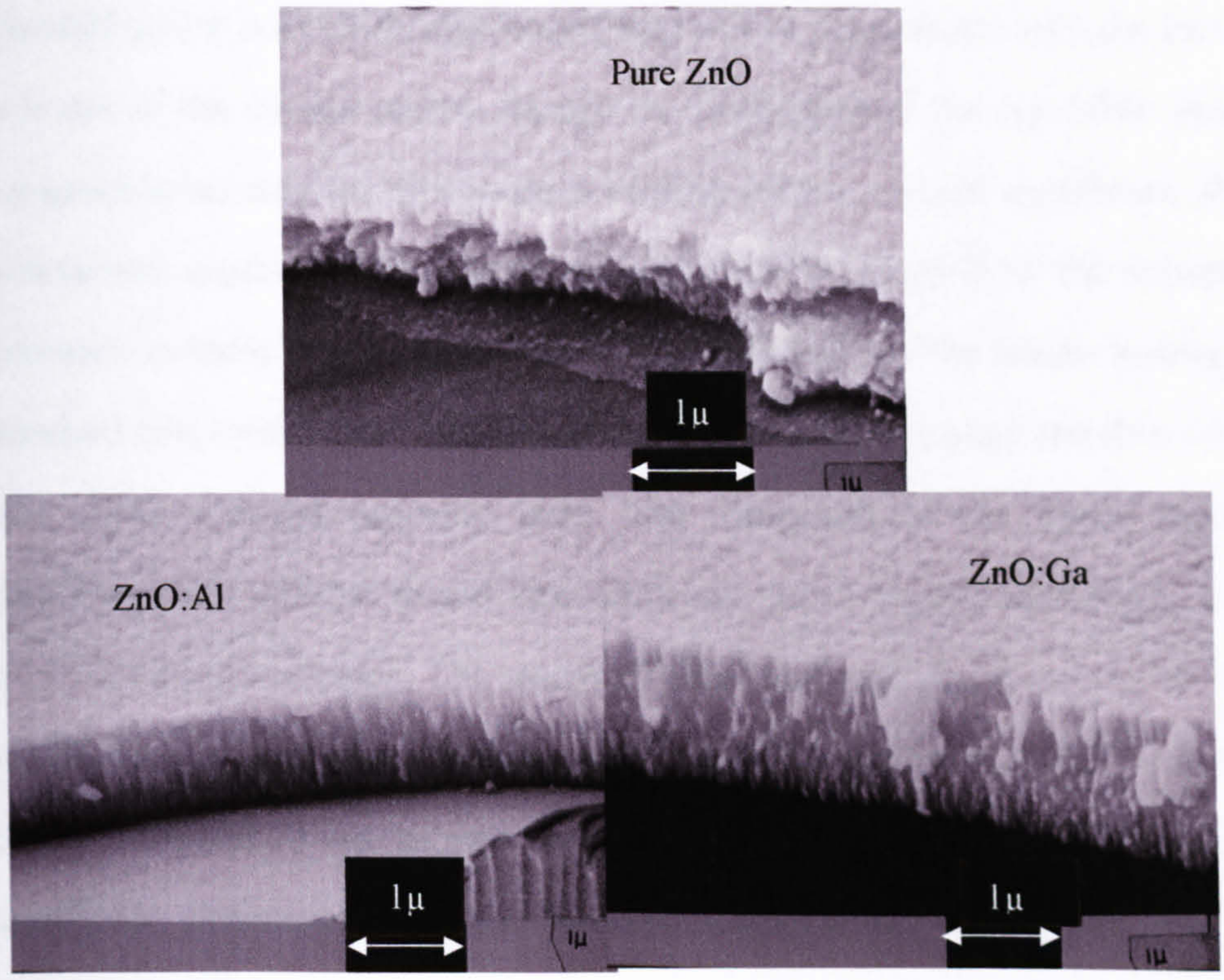

Picture 8.4. The typical SEM micrograph of the fracture sections of doped ZnO coatings.

Table 8.2: The analysis data of ZnO coatings with different dopants and their concentration

Coating	At%	Thickness (d, nm)	Resistivity (ρ, Ωcm)	Tolerance of the Main peaks, $*10^{-3}$ Angstrom Unit
Pure ZnO	-	648	0.14	8.43/3
ZnO:Al	1	680	$3.0*10^{-3}$	7.63/8.57
	3	750	$1.95*10^{-3}$	5/10
	5	840	$5.19*10^{-3}$	6.3/6.3
ZnO:Ga	1	924	$3.6*10^{-3}$	15
	3	826	$2.9*10^{-3}$	11
	5	958	$3.55*10^{-3}$	9
ZnO:In	1	851	$9.6*10^{-3}$	11
	3	956	$6.3*10^{-2}$	48/8
	5	953	-	-
ZnO:Sn	1	950	0.98	12
	3	1100	0.72	56
	5	1036	2.25	89
ZnO:Sb	1	1226	∞	116
	3	1300		130
	5	1325		-

Note: the data were measured from the annealed samples. The tolerances of the main peaks (Angstrom unit) were calculated by subtracting the standard lattice spacing values of the same peaks from the practical lattice spacing data.

Figure 8.12 shows the effect of different dopants on the crystallinity of the coatings. The diffraction peak shifts and broadening can be seen clearly with the increase of the radiuses of the dopant atoms, though the intensities of the crystallite peaks are not comparable because the difference in coating thicknesses are significant, although the parameters, especially the deposition time, were the same in all the dopant runs. The tolerance column in table 8.2 presents the difference of the lattice spacings between standard zinc oxide lattice spacing of the (002) diffraction peak and those of the doped zinc oxide coatings prepared here. The tolerances of the lattice spacings from aluminium and gallium doped zinc oxide are much smaller than those from tin and antimony doped coatings. The reason of these shift and one reason of the broadening are the existence of lattice strains, which cause the deformation of the crystal lattices [139]. Therefore, it can be said that dopant atoms with larger radii can lead to more significant deformation of the lattices, shifts in the diffraction peaks and line broadening.

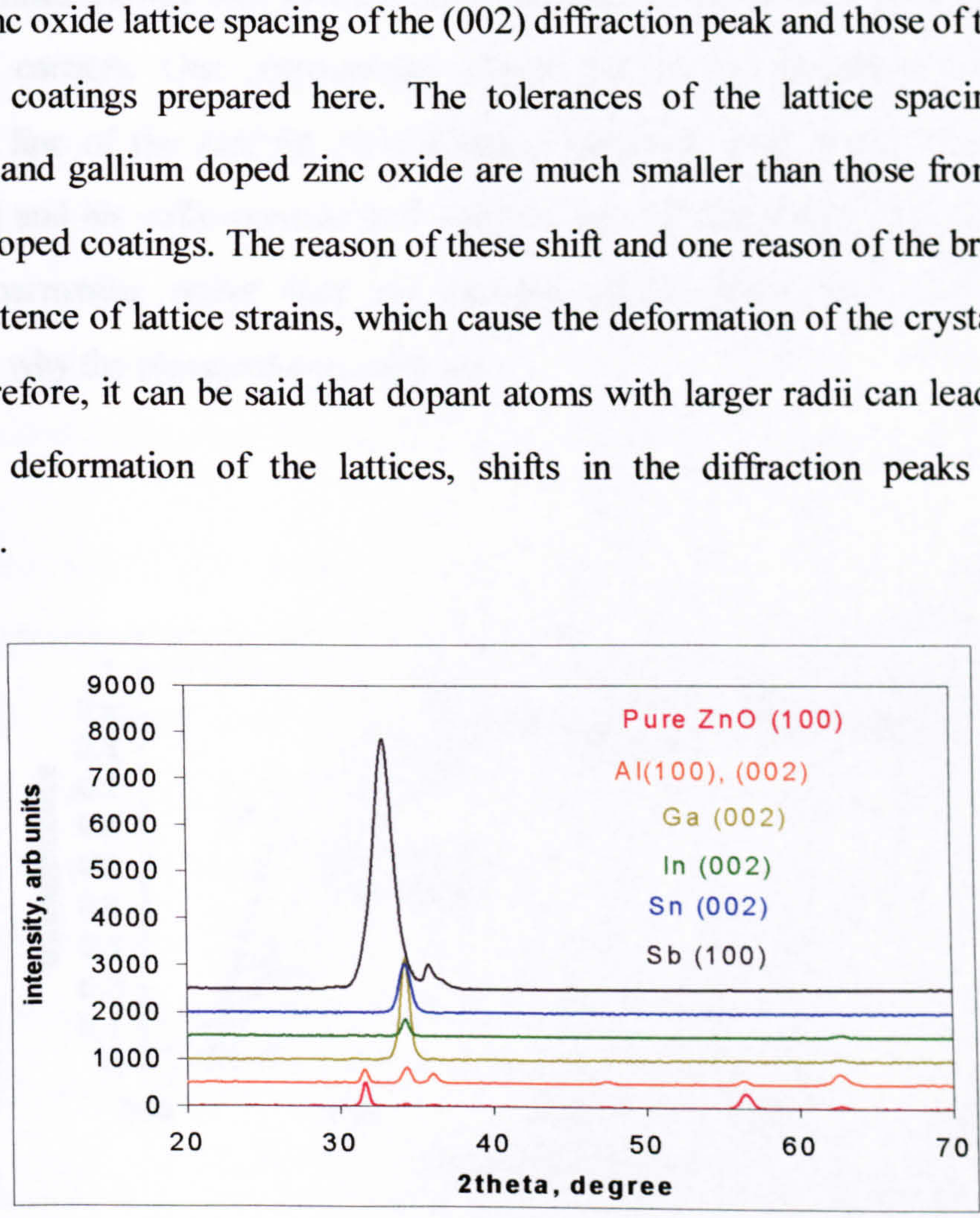

Figure 8.12 Diffraction spectra of zinc oxide coatings with different dopants

The substrate-to-coating adhesion of the doped coatings were all in excess of 12N, under the conditions of continuous progressive load with 200 μm diameter diamond stylus, except that the 5 at% In and Sb doped ZnO coatings fell off after annealing and could not be tested. Therefore, it seems that the concentrations of the dopants with

larger radii might affect the adhesion, which could be due to greater lattice stresses.

8.3.2 Optical properties of doped ZnO coatings

The transmittance of doped ZnO coatings are shown in figures 8.13a and b. Clearly, most of them averaged about 90% transmission within the visible range of wavelengths and none was lower than 80%. Moreover, the cut-off points of the transparent lines showed blue shifts, which correlated to the increase in the number of the charge carriers. One phenomenon which has to be mentioned is that the transparent line of the ZnO:Sn coating had a red shift instead of a blue shift. T. Minami [6] and his colleagues pointed out that the red shift could be caused by the band-gap narrowing rather than the Burstein-Moss effect. But it is not fully understood why the phenomenon occurred.

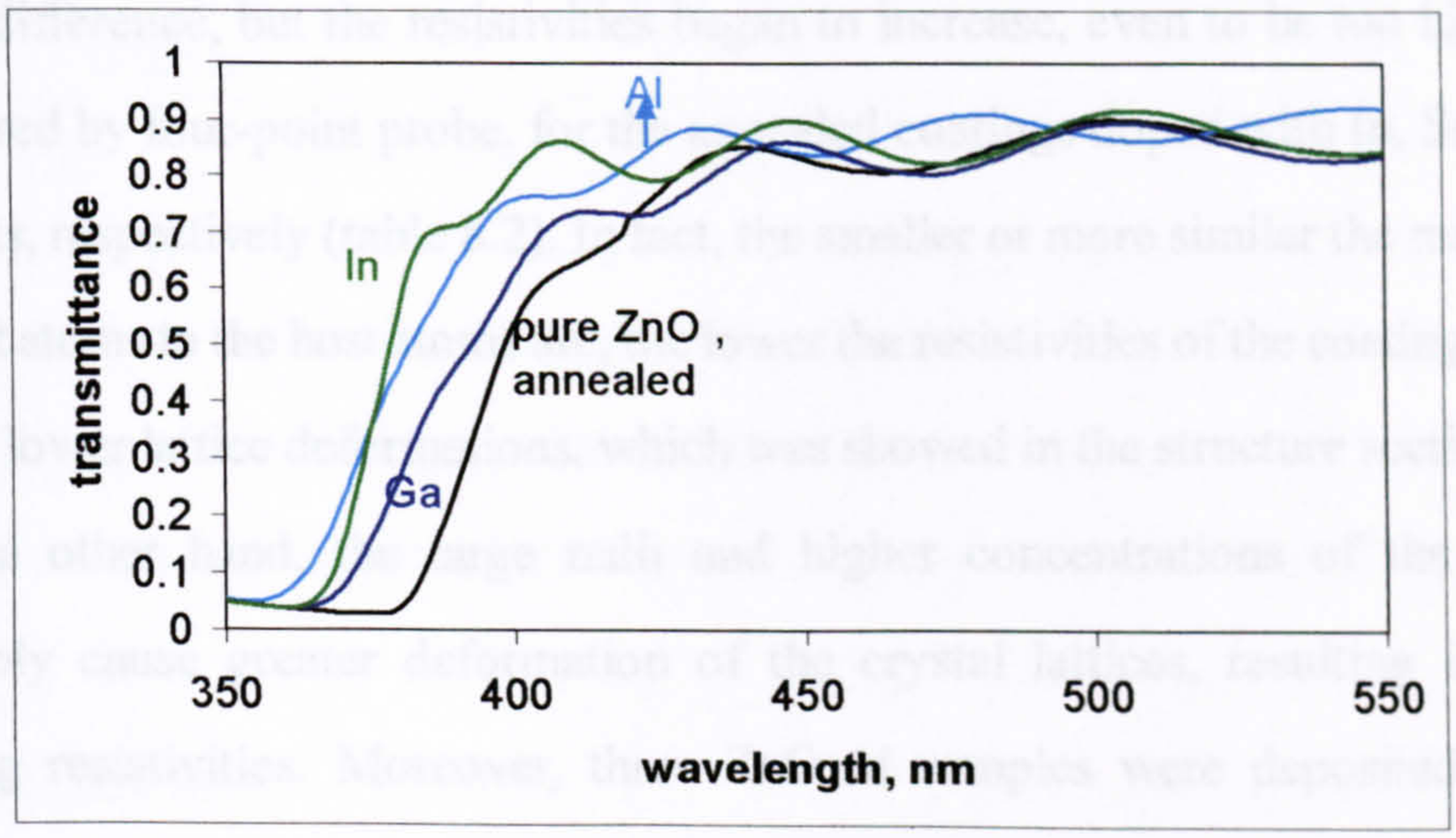

(a)

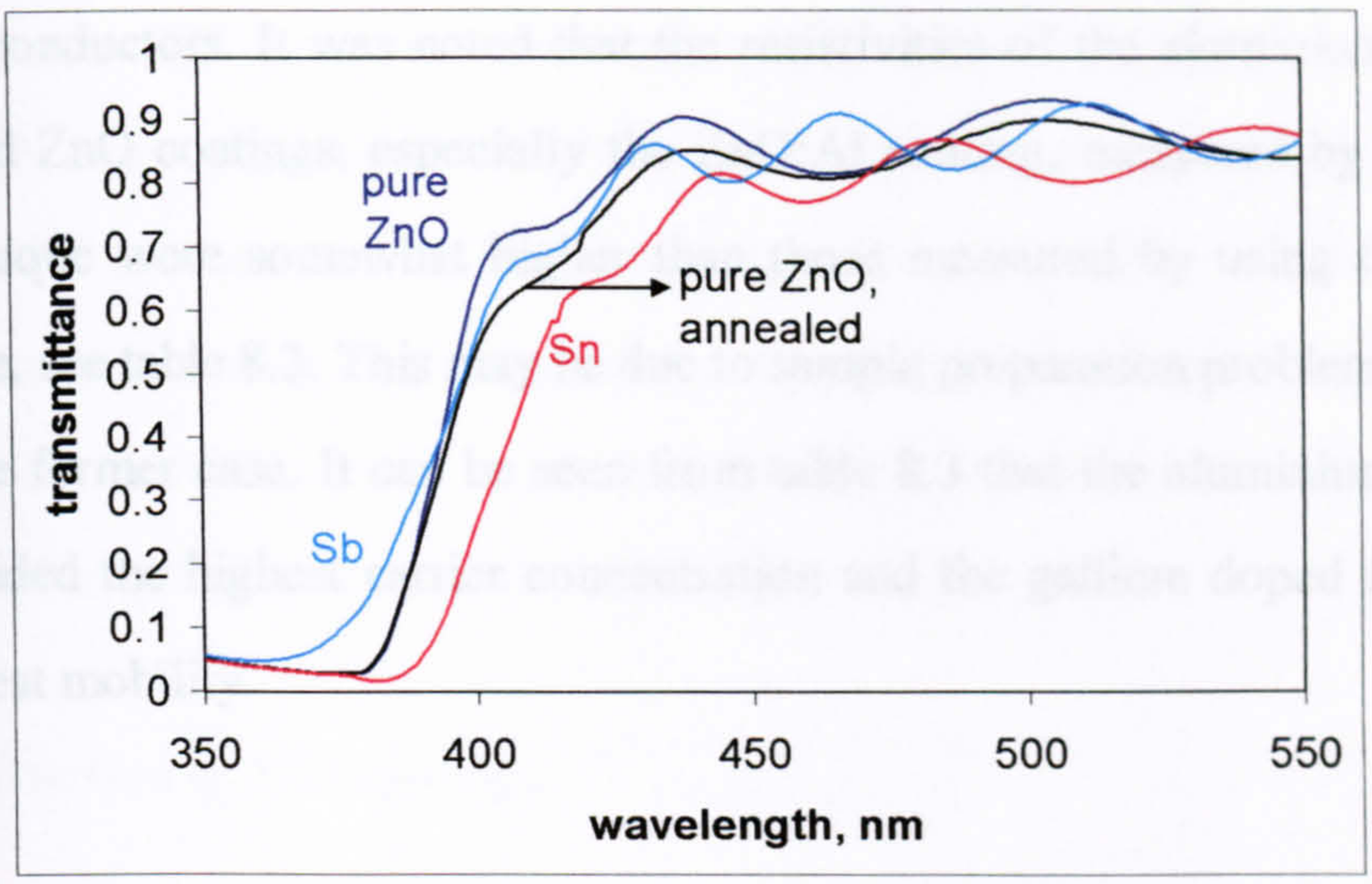

(b)

Figure 8.13 Optical transmission spectra of doped ZnO coatings.

8.3.3 The electrical properties of doped ZnO coatings

The resistivities of the annealed coatings doped by Al and Ga did not show very much difference, but the resistivities began to increase, even to be too high to be measured by four-point probe, for the annealed coatings doped with In, Sn and Sb dopants, respectively (table 8.2). In fact, the smaller or more similar the radii of the dopant atoms to the host atoms are, the lower the resistivities of the coatings will be due to lower lattice deformations, which was showed in the structure section 8.3.1. On the other hand, the large radii and higher concentrations of the dopants probably cause greater deformation of the crystal lattices, resulting in higher coating resistivities. Moreover, three ZnO:Al samples were deposited without extra oxygen supply in the deposition atmosphere. The resistivities of these coatings were in the order of 10^{-2}-$5x10^{-3}\Omega cm$ before annealing. These results cannot be explained at this time.

The charge carrier concentrations and the Hall mobility of Al, Ga and In (3at%) doped ZnO coatings were measured by using an EGK 2000 Hall Effect

Measurement unit. All coatings measured were revealed to be n-type semiconductors. It was noted that the resistivities of the aluminium and gallium doped ZnO coatings, especially the ZnO:Al coating, measured by Van de Pauw technique were somewhat higher than those measured by using the Four-point probe, see table 8.3. This may be due to sample preparation problems experienced in the former case. It can be seen from table 8.3 that the aluminium doped films provided the highest carrier concentration and the gallium doped films gave the highest mobility.

Table 8.3 Hall effect of the doped zinc oxide coatings

Hall Effect	ZnO:Al	ZnO:Ga	ZnO:In
Carrier concentration /cm^3	$-1.35*10^{20}$	$-9.0*10^{19}$	$-8.9*10^{18}$
Carrier hall mobility $cm^2/v*s$	12.6	20.7	12
Resistivity Ohm*cm	$4.3*10^{-3}$	$3.4*10^{-3}$	$4.6*10^{-2}$

Note: "-" means n-type

Overall, the closer or smaller the size of the dopant atom to the host atom, at the correct concentration, the higher the charge carrier concentration and mobility, the larger the blue shift in the optical spectra, and the lower the resistivity of the coatings

8.4 ITO Coatings

For the ITO targets, the powder blends were mixed using the appropriate quantities of 99.9% pure indium oxide and 99.99% pure tin oxide powders in a rotating drum for several hours. The mixtures investigated contained 5at% and 10at% Sn, respectively. Pure indium oxide targets were also investigated for comparative purposes. The Pinnacle Plus supply was operated in current regulation mode (target current = 2A), at

a pulse frequency of 350kHz (62% duty). Sputtering was carried out under pure argon at a flow rate of 27sccm, and mixed argon (27sccm) and oxygen (1sccm) gases. The coating pressure was held at 0.24Pa by varying the chamber pumping speed, the run time was 15minutes, and the target to substrate separation was 170mm. Following deposition, the coatings were annealed at 450 °C for 1 hour under vacuo ($2x10^{-3}$Pa), considering the thickness of the coatings were much thinner than those of the ZnO coatings due to the shorter deposition time.

8.4.1 Structure of ITO coatings

Pictures 8.5a and b respectively show SEM micrographs of the fracture sections of typical examples of as-deposited and annealed ITO coatings, which were deposited onto glass substrates in argon and oxygen atmospheres at 350kHz pulse frequency, 62% duty for 15min, and annealed at 450^{o}C for 1 hour in vacuo. As can be seen, both have very similar dense columnar, defect-free structures. From these figures, it is possible to estimate that a deposition rate of 600 nm/hour was achieved. Independent of deposition conditions, or dopant level, the XRD spectra of the as-deposited coatings all show two main peaks, corresponding to the (222) and (400) reflections for In_2O_3 (see figures 8.14a and b, for examples). Figures 8.14a and b also include the XRD spectra for these coatings after annealing. Again, the same main peaks are present in all cases, but the peaks generally appear somewhat more intense and are sharper (i.e. smaller FWHM), which are more obvious in the case of the coatings deposited in mixed argon and oxygen atmosphere. This may be associated with a decrease in lattice strain and a more periodic arrangement of crystals [141], though no measurements have been made to confirm this.

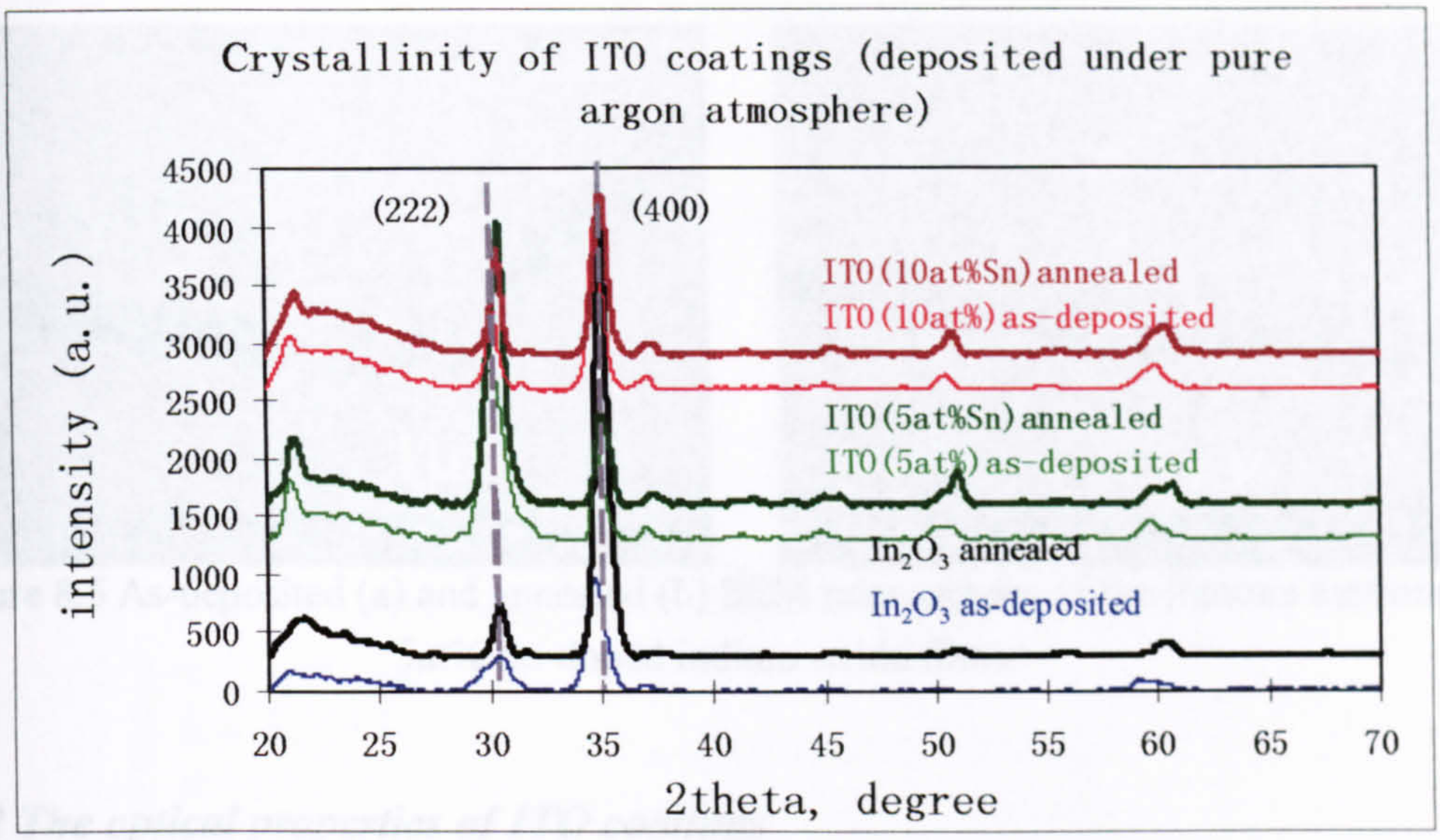

8.14a

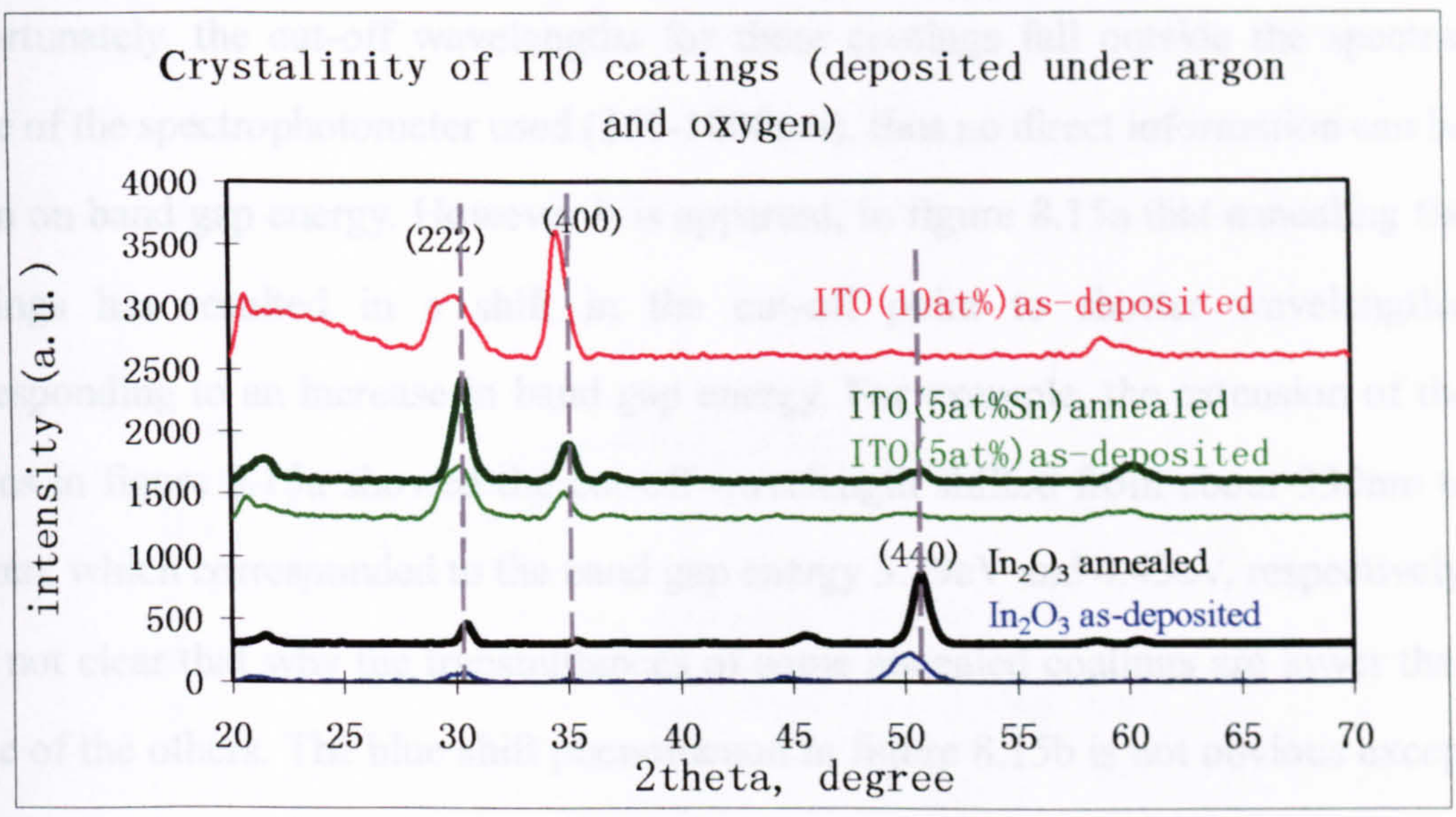

8.14b

Figure 8.14 θ–2θ XRD diffraction spectra for as-deposited (argon, argon and oxygen mixture atmosphere) and annealed (450°C for 1 hour in vacuo) ITO coatings.

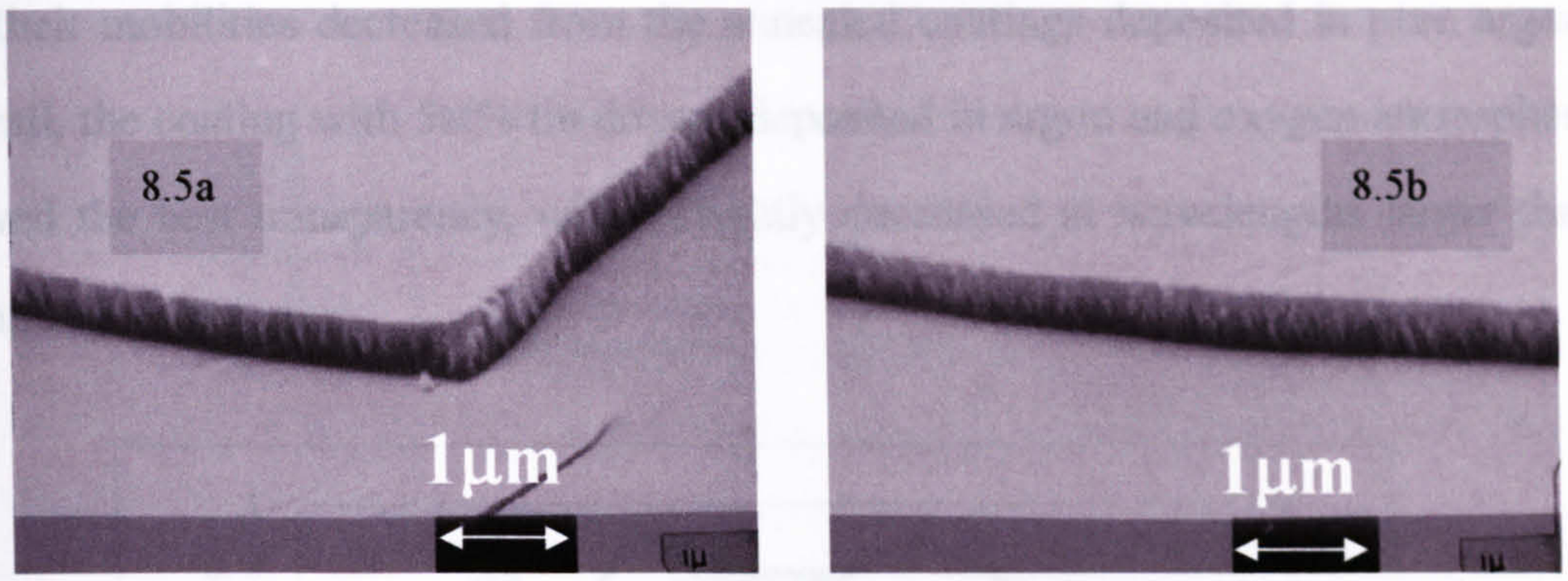

Picture 8.5 As-deposited (a) and annealed (b) SEM micrographs of the fracture sections of 5at% tin-doped indium oxide films.

8.4.2 The optical properties of ITO coatings

Figures 8.15a and b show the optical properties of the ITO coatings in this study. The average transmittances of these coatings were 80-85% over the visible spectrum. Unfortunately, the cut-off wavelengths for these coatings fall outside the spectral range of the spectrophotometer used (350-1000nm), thus no direct information can be given on band gap energy. However it is apparent, in figure 8.15a that annealing the coatings has resulted in a shift in the cut-off point to shorter wavelengths, corresponding to an increase in band gap energy. For example, the extension of the curves in figure 8.15a showed the cut-off wavelength shifted from about 330nm to 280nm, which corresponded to the band gap energy 3.79eV and 4.43eV, respectively. It is not clear that why the transmittances of some annealed coatings are lower than those of the others. The blue shift phenomenon in figure 8.15b is not obvious except for the coating with 5at% tin, of which the coatings were deposited in argon atmosphere. The coatings deposited in pure argon atmosphere may have sufficient oxygen vacancies in the lattices, and further oxygen deficiency caused by annealing in vacuo may lead to serious electron scattering due to the interaction between electrons, ions and lattice deformations. Therefore, the band gap enlarging caused by extra free electrons in the semiconductor might be minimized by the band gap narrowing due to the electron scattering mechanism, which means no obvious blue shift can be seen. It

can be seen in table 8.4 in section 8.4.3, that the number of charge carriers increased and their mobilities decreased from the annealed coatings deposited in pure argon. Overall, the coating with 5at% tin dopant deposited in argon and oxygen atmosphere showed the best transparency, which slightly decreased at wavelengths larger than 870nm.

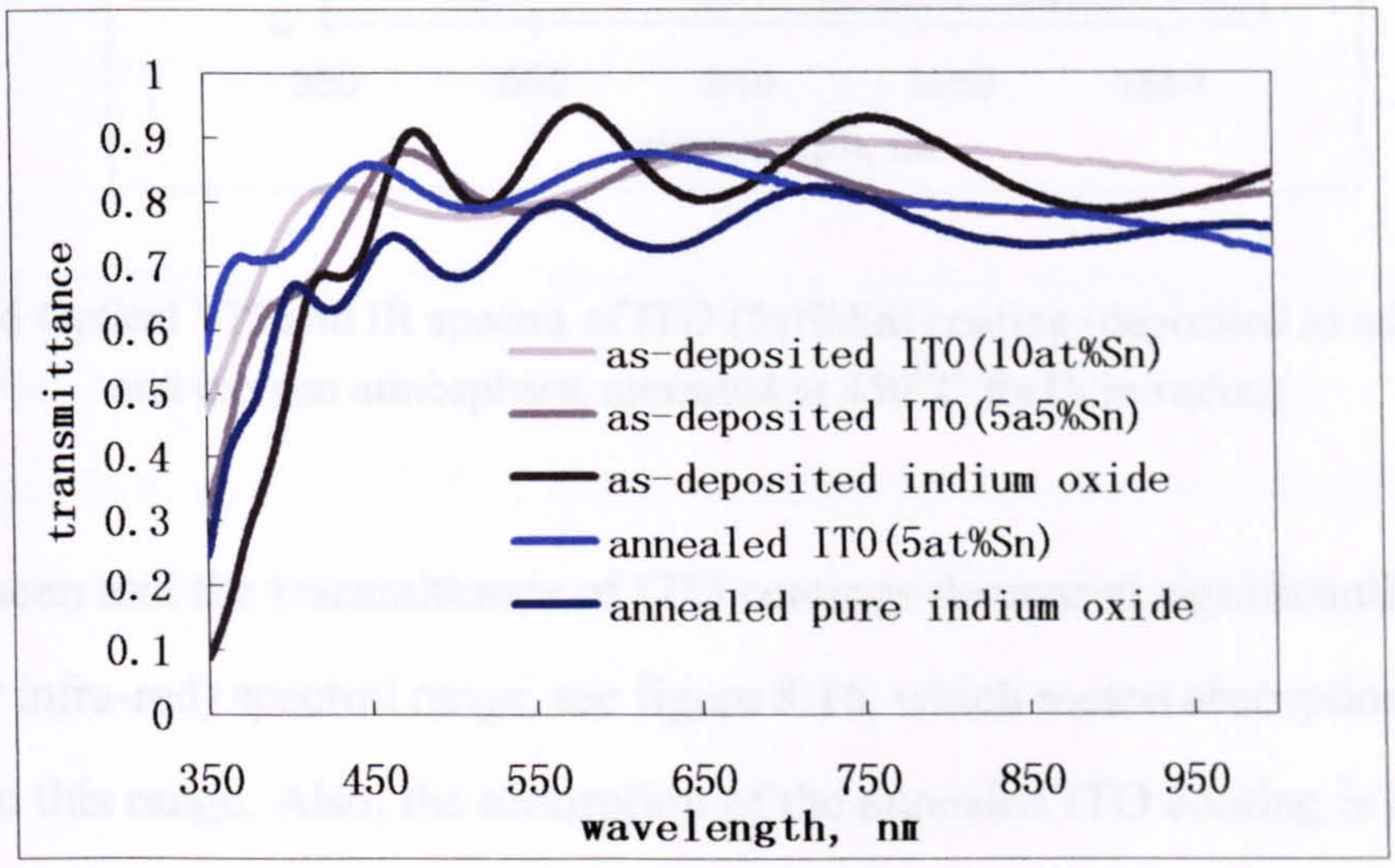

8.15a Coatings deposited under argon and oxygen atmosphere

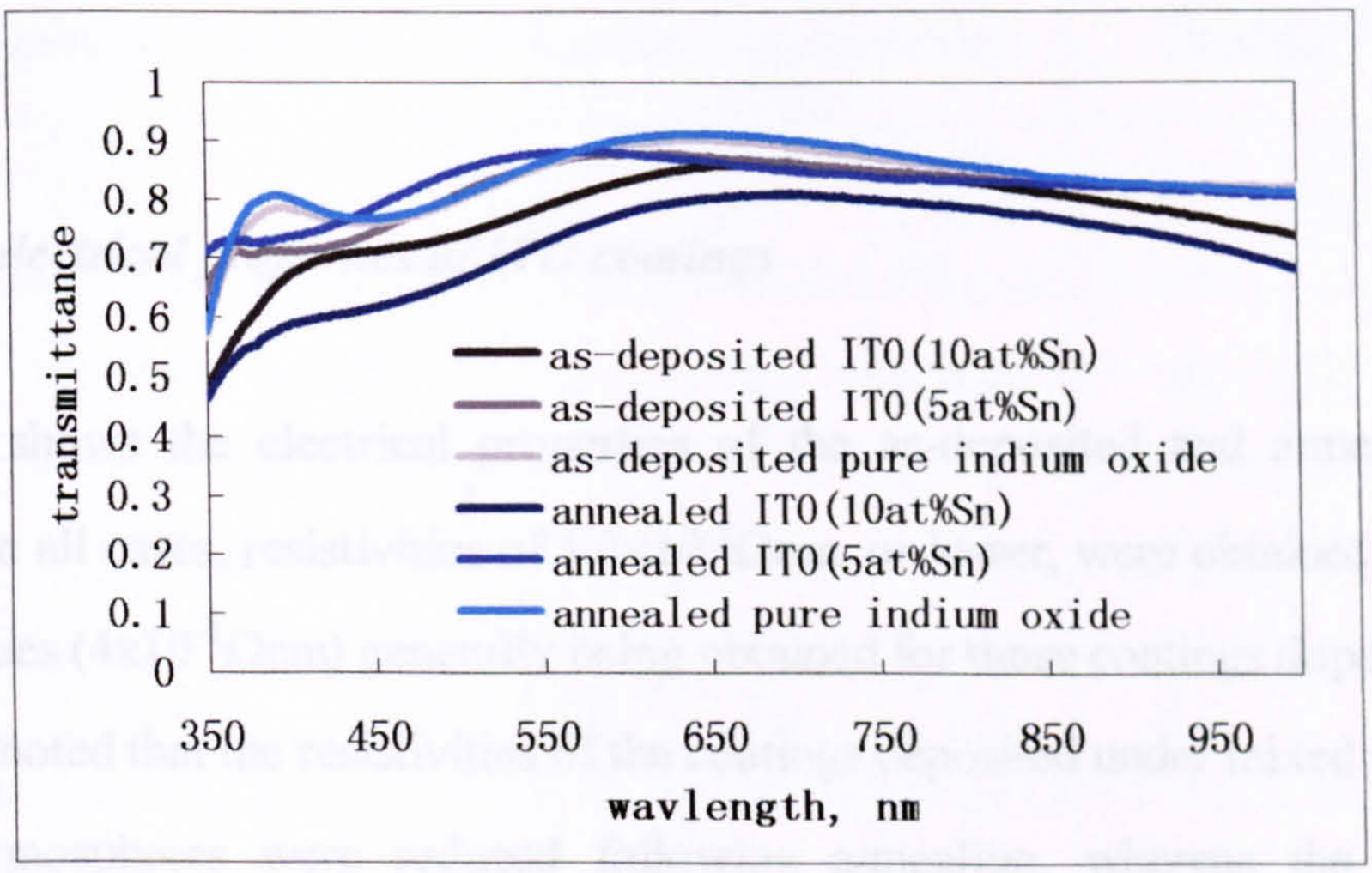

8.15b Coatings deposited under argon atmosphere

Figure 8.15 Optical transmission spectra of ITO coatings

(annealed @450^{o}C, 1h in vacuo)

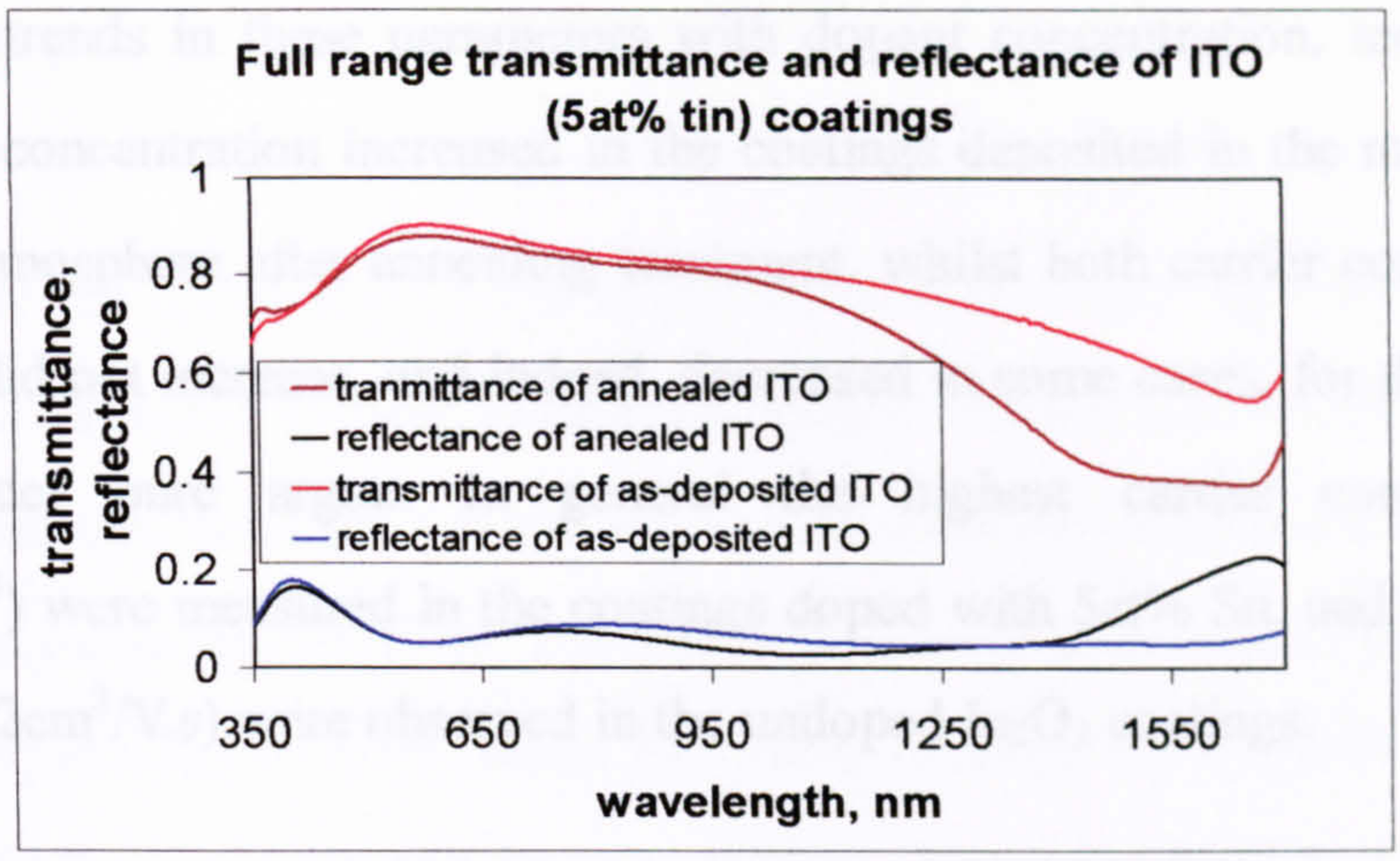

Figure 8.16 Optical VIS and IR spectra of ITO (5at%Sn) coating (deposited in mixed argon and oxygen atmosphere, annealed at 450^{O}C for1h in vacuo)

It can be seen that the transmittance of ITO coatings decreased significantly over the NIR (near infra-red) spectral range, see figure 8.16, which means absorption begins to increase in this range. Also, the absorption of the annealed ITO coating is higher and begins at shorter wavelengths than that of as-deposited ITO coating. It can be explained that the charge carrier concentration increased in the coating after annealing treatment, which moved the plasma frequency to a shorter wavelength (refer to Chapter 3).

8.4.3 The electrical properties of ITO coatings

Table 8.4 shows the electrical properties of the as-deposited and annealed ITO coatings. In all cases, resistivities of $1.3x10^{-3}\Omega cm$, or lower, were obtained, with the lowest values ($4x10^{-4}\Omega cm$) generally being obtained for those coatings doped at 5at% Sn. It was noted that the resistivities of the coatings deposited under mixed argon and oxygen atmospheres were reduced following annealing, whereas the effect of annealing was much less clear for the coatings deposited in an argon only atmosphere. Indeed, in certain cases, annealing appears to have increased the coating resistivity.

Carrier concentration and mobility data are also included in table 8.4. Although there

are no strong trends in these parameters with dopant concentration, mobility and charge carrier concentration increased in the coatings deposited in the mixed argon and oxygen atmosphere after annealing treatment, whilst both carrier concentration and mobility did not increase, and indeed, decreased in some cases, for the coatings deposited under pure argon. In general the highest carrier concentrations (~$10x10^{20}/cm^3$) were measured in the coatings doped with 5at% Sn, and the highest mobilities (~$32cm^2/V.s$) were observed in the undoped In_2O_3 coatings.

The results presented here clearly show that the optical and electrical properties of ITO coatings are strongly influenced by deposition atmosphere, dopant content and post-deposition annealing. Within these experiments the best combination of film properties were obtained for coatings doped at 5at% Sn, followed by annealing in vacuo.

Table 8.4: The electrical properties of indium oxide and ITO films prepared under various conditions.

	Resistivity, $x10^{-3}\Omega cm$			**Carrier concentration, $x10^{20}cm^{-3}$**			**Hall mobility, $cm^2/V.s$**		
	In_2O_3	In_2O_3: 5at% Sn	In_2O_3: 10at% Sn	In_2O_3	In_2O_3: 5at% Sn	In_2O_3: 10at% Sn	In_2O_3	In_2O_3: 5at% Sn	In_2O_3: 10at% Sn
Argon only	0.9	0.4	1.3	*X*	5.3	4.6	*X*	17	12
Annealed	1.1	0.7	1.1	1.9	9.6	7.2	31.8	16	8.6
Ar + 1sccm O_2	212	0.9	0.8	0.001	2.0	3.5	0.4	25	23
Annealed	1.1	0.4	0.6	1.9	5.8	*X*	31	26	*X*

Annealed at 450°C 1hour in vacuo

∞ –>20MΩ *X – not measured*

8.5 ITO/ZAO Coatings

To demonstrate the flexibility of the approach described here the technique has, therefore, been extended to multi-component target compositions. Blended powder targets were prepared by combining the optimum zinc oxide and alumina composition (3at% Al) from earlier studies [140, 152-153], and the optimum indium oxide and tin oxide mixture (5at% Sn) from this study. The initial findings of the new TCO coatings, termed ITO/ZAO, are presented in this section. The deposition parameters and conditions are the same as those used for ITO coatings.

8.5.1 Compositions and structure of ITO/ZAO multi-component coatings

The RBS technique was used to analyze the compositions of ITO/ZAO coatings. The results showed that the average ratio of zinc to indium of the coatings were consistent with the compositions of their targets, but were not very uniform through out the film. This may be because the zinc oxide powders tended to accumulate together themselves other than mix into the indium oxide powder, and it took a long time to mix these blends uniformly. Therefore, not surprisingly, the compositions of the coating through thickness were not consistent, which means that the mixture technique has to be improved for these particular powders. Figure 8.17 shows the RBS data from the ITO/ZAO coating, deposited from the target with In:Zn =1:4, and table 8.5 gives the composition of the film through the whole thickness. The Sn content was estimated by the content of Indium according to the composition of the target. The layer 1 to 3 was about the compositions of the film and layer 4 and 5, the compositions of the substrate. It can be seen that the content of indium in the coating reduces through the thickness and some zinc has apparently diffused into the glass substrate.

Table 8.5 The through thickness compositions of the ITO/ZAO film deposited from the target with In:Zn=1:4

composition / layers	Zn	In	O	Al	Sn	Si	Na	Ca
Layer 1	1	0.25	1.4725	0.06	0.125			
Layer 2	1	0.18	1.367	0.06	0.09			
Layer 3	1	0.1	1.325	0.06	0.005			
Layer 4	0.4		2.6			1	0.4	0.1
Layer 5			2.6			1	0.4	0.1

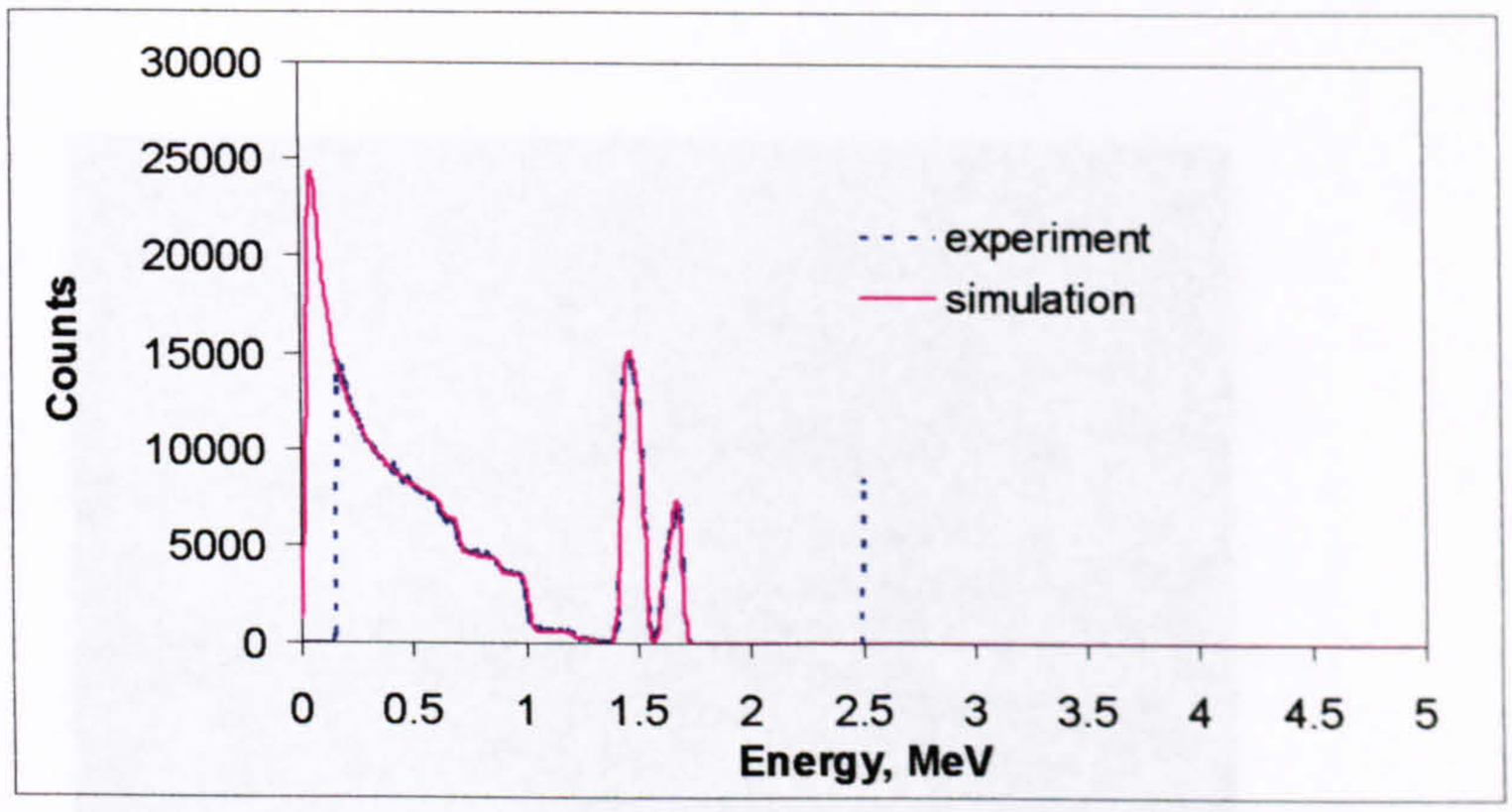

Figure 8.17 RBS simulating result of the coating deposited from the target with the ratio of In:Zn=1:4

The ITO/ZAO multi-component coatings had very similar structures to the ITO coatings. All were dense columnar and defect free: a typical example being shown in picture 8.6 (deposition conditions are summarised in the figure heading). Again, there were no differences discernible from SEM micrographs following annealing. Figures 8.18a and b show the XRD diffraction spectra of the ITO/ZAO coatings deposited under an argon atmosphere and under mixed Ar and O_2 atmospheres. The spectra show a distinct shift from a ZnO-based structure to an In_2O_3-based structure, as the indium content increases. At an In:Zn atomic ratio of 1:4 the spectra reveal single peaks corresponding to the (002) ZnO peak ($2\theta = 34.5^{o}$), but shifted to higher d spacings. For the indium-rich coatings (In:Zn atomic ratio = 4:1), single peaks corresponding to the (222) In_2O_3 reflection ($2\theta = 30.6^{o}$), but shifted to lower d

spacings, are observed. At intermediate compositions the spectra, which consist of single broad peaks lying between the (002) ZnO and (222) In_2O_3 peak positions are harder to interpret. This may be indicative of highly distorted lattice structures. However, it may also be indicative of the presence of the intermetallic compound, $Zn_3In_2O_6$, since the (0015) diffraction peak for this material lies in this region and has been identified in other studies [129]. It is not clear why the intermetallic compound, $Zn_3In_2O_6$, appeared from the coatings deposited from the target with Zn:In ratio 2:3. Annealing may have resulted in marginally sharper, more intense peaks, but the effect was not strong.

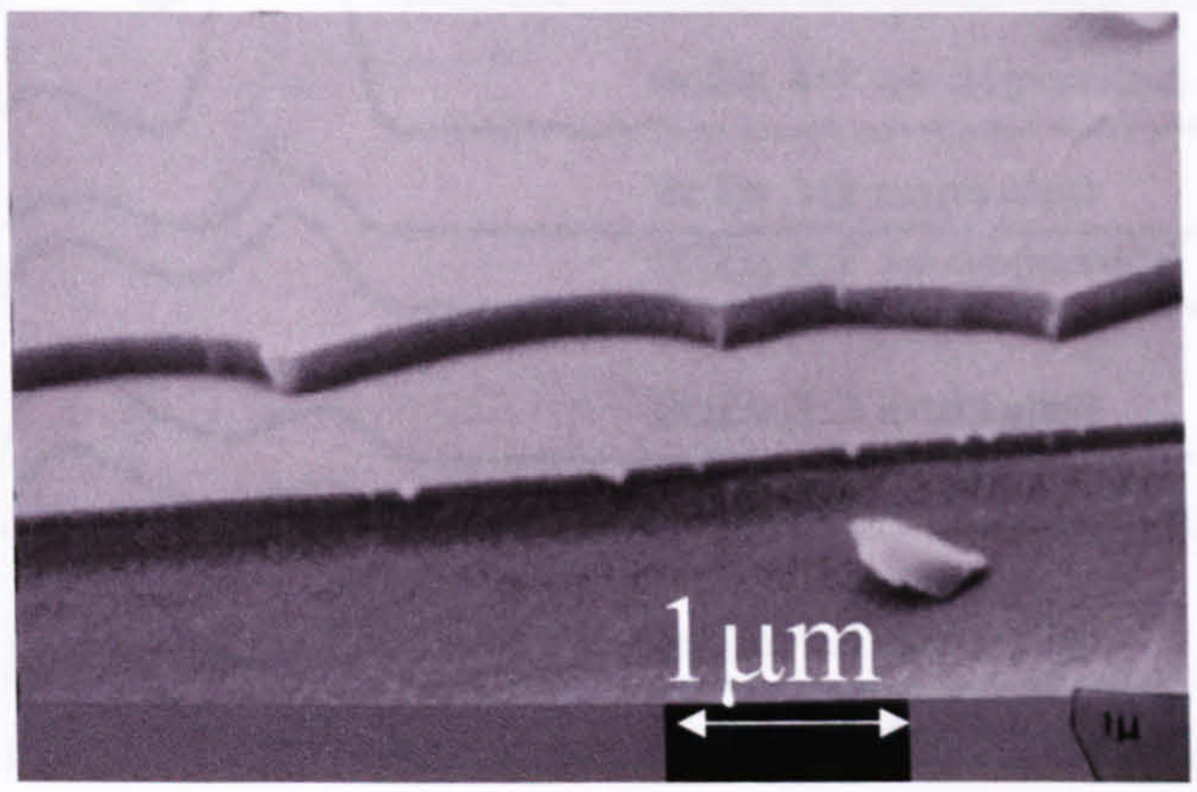

Picture 8.6: SEM micrograph of the fracture section of an ITO/ZAO film (In:Zn atomic ratio = 4:1), deposited in argon and oxygen atmospheres and annealed in vacuo at 450°C for 1 hour.

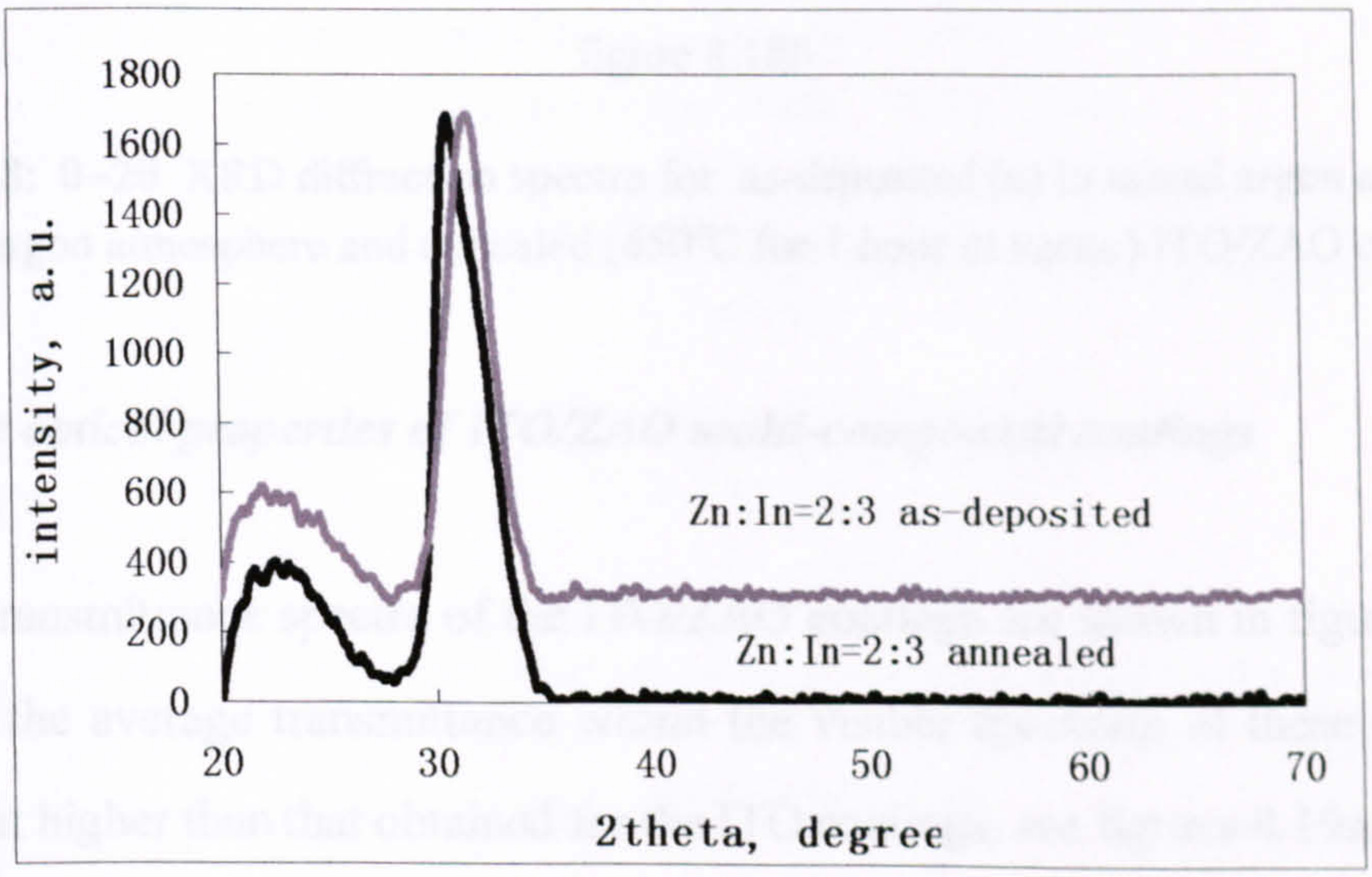

figure 8.18a

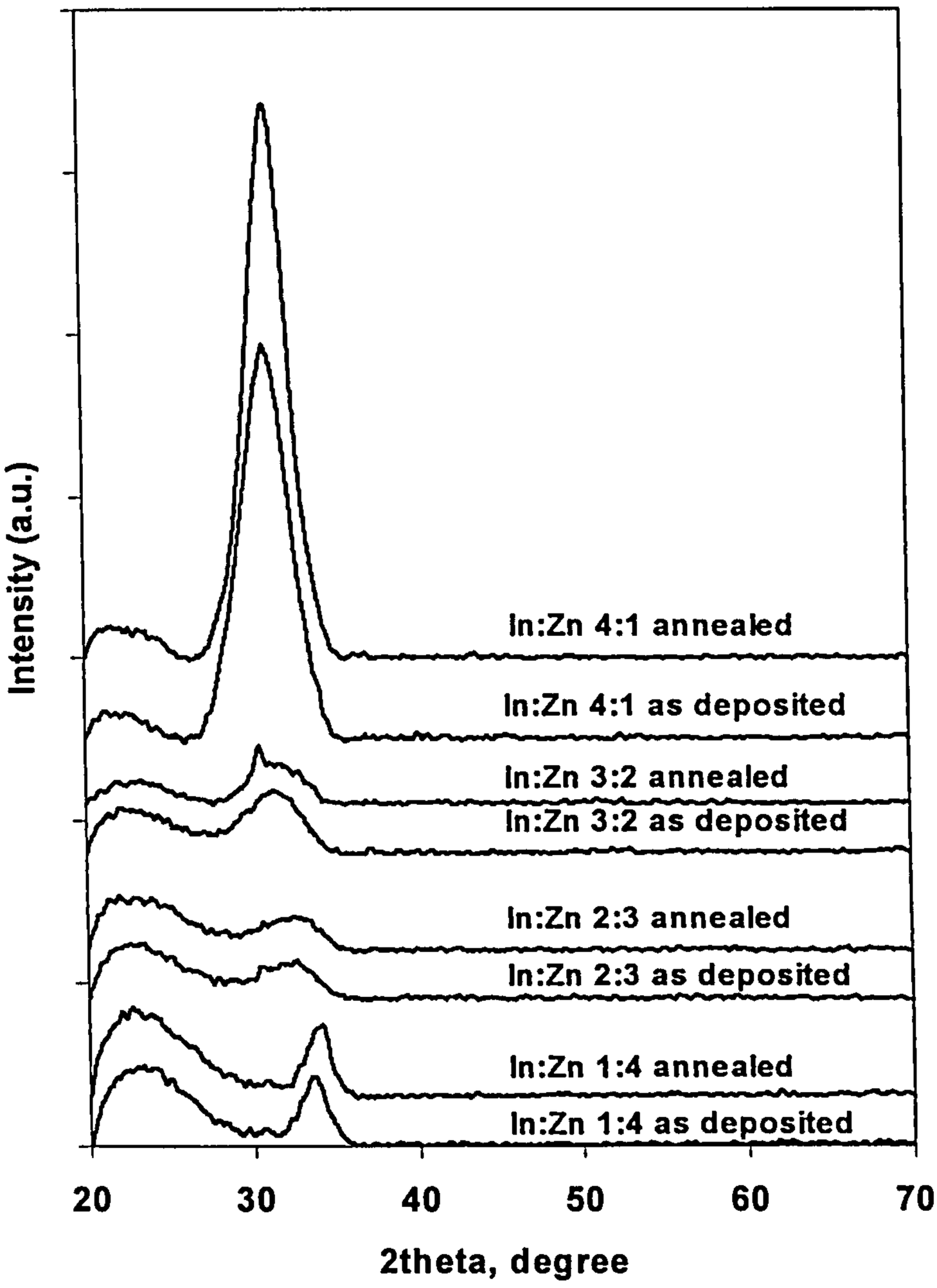

figure 8.18b

Figure 8.18: θ–2θ XRD diffraction spectra for as-deposited (a) in mixed argon and oxygen; (b) in argon atmosphere and annealed (450°C for 1 hour in vacuo) ITO/ZAO coatings.

8.5.2 The optical properties of ITO/ZAO multi-component coatings

Typical transmittance spectra of the ITO/ZAO coatings are shown in figure 8.19. At 85-90%, the average transmittance within the visible spectrum of these coatings is somewhat higher than that obtained for the ITO coatings, see figures 8.19a, b, c and d. There is no big difference among the cut-off wavelengths of the as-deposited coatings under argon and oxygen atmosphere (8.19a), but those of as-deposited coatings under

pure argon atmosphere move to shorter wavelengths as the indium contents in the coatings increase (8.19c). The cut-off wavelengths are longer than the ITO coatings, for all annealed coatings, but show a blue shift with increasing indium content, i.e. a shift to shorter wavelengths/higher band gap energies (8.19b and d). This phenomenon may draw the conclusion that indium tends to provide more charge carriers than zinc does under the same conditions, especially when there is an oxygen deficiency in the deposition or annealing atmosphere.

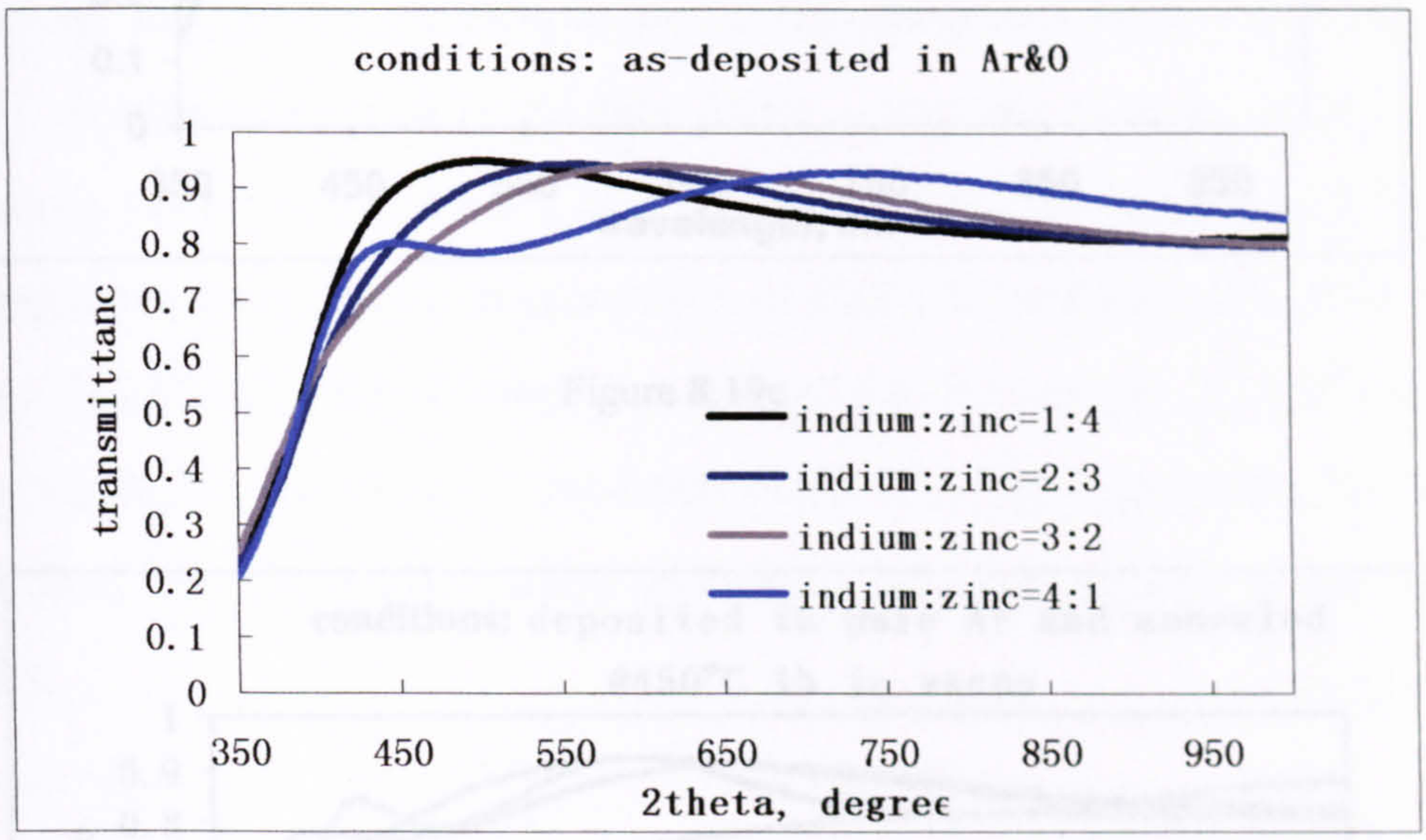

Figure 8.19a

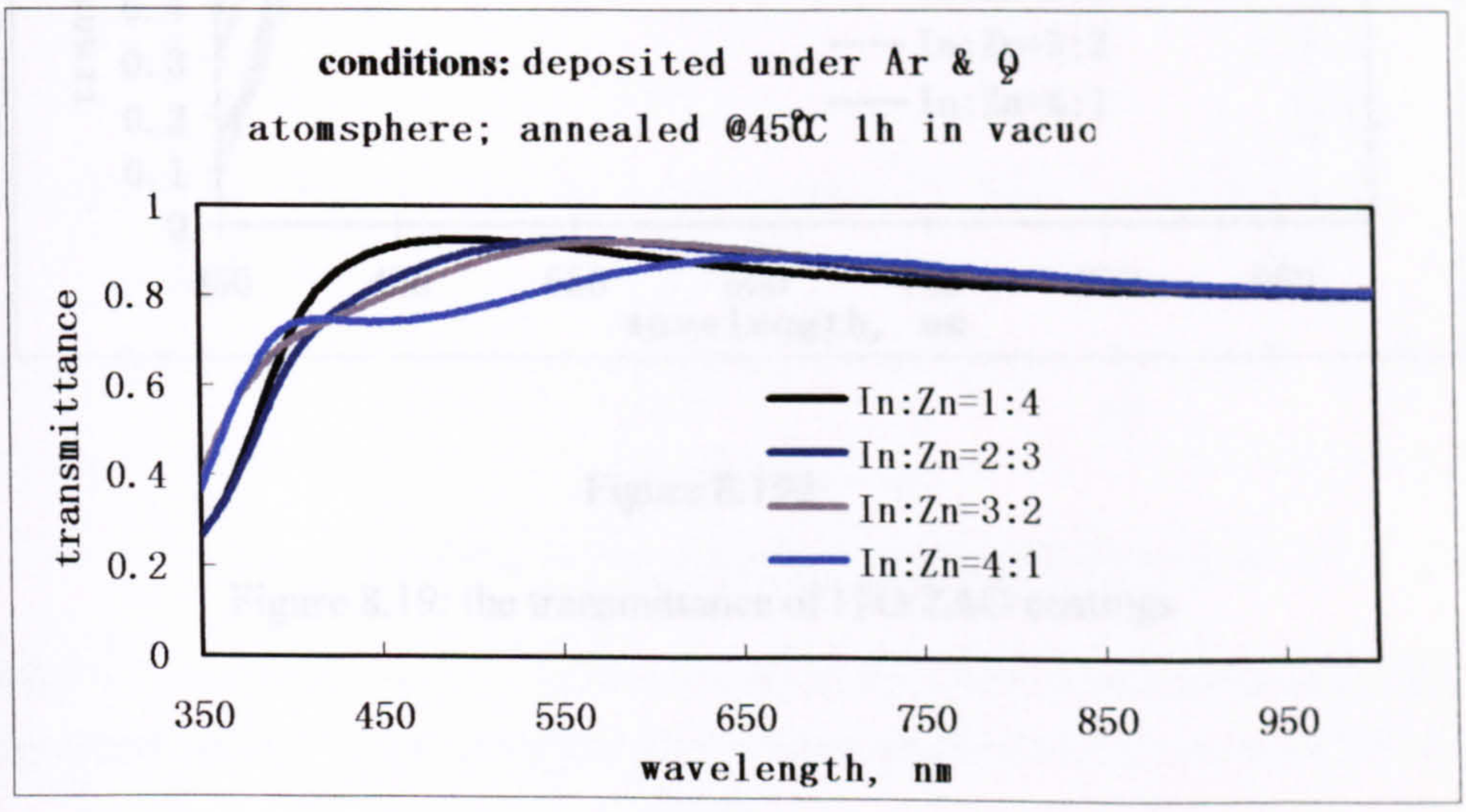

Figure 8.19b

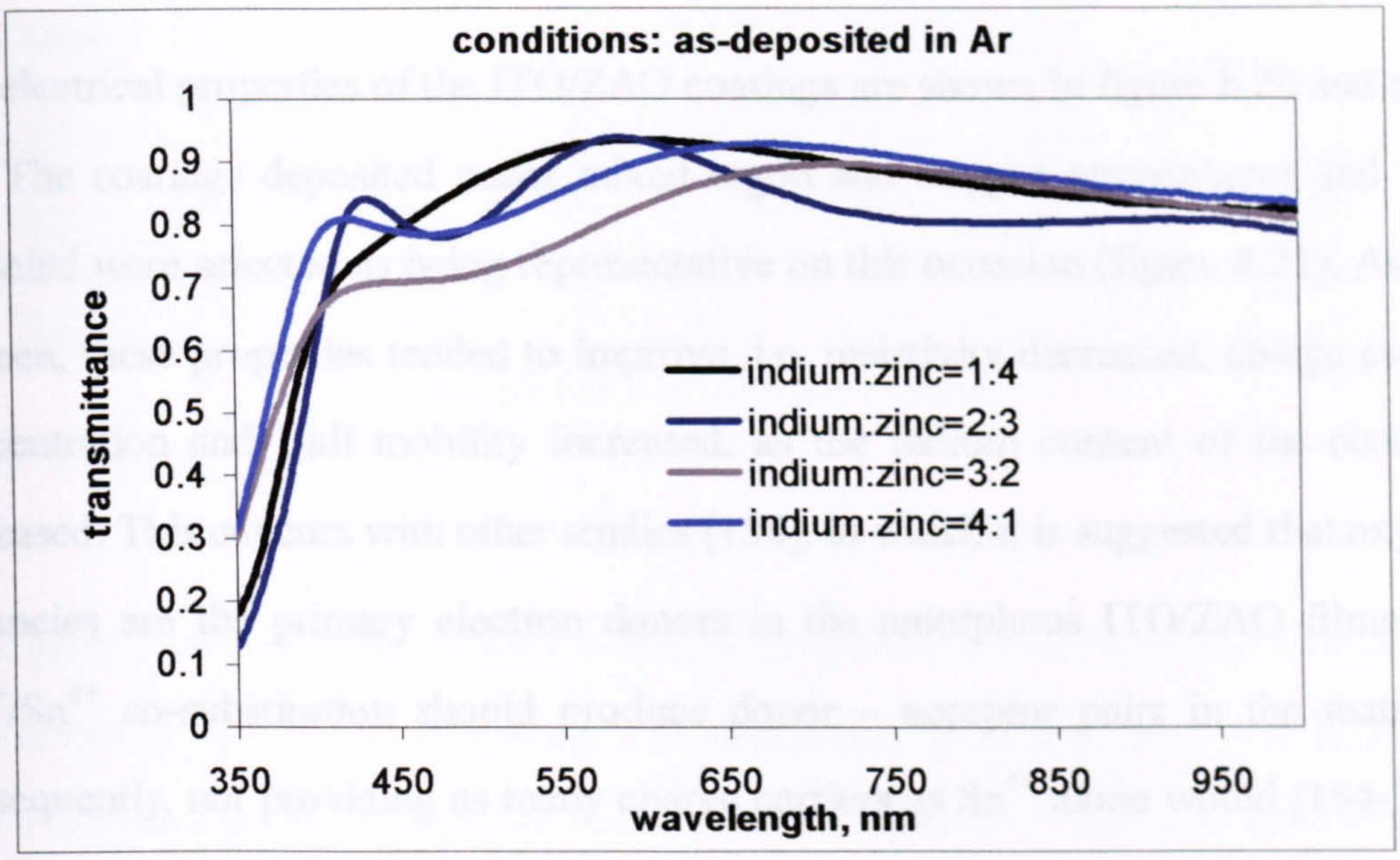

Figure 8.19c

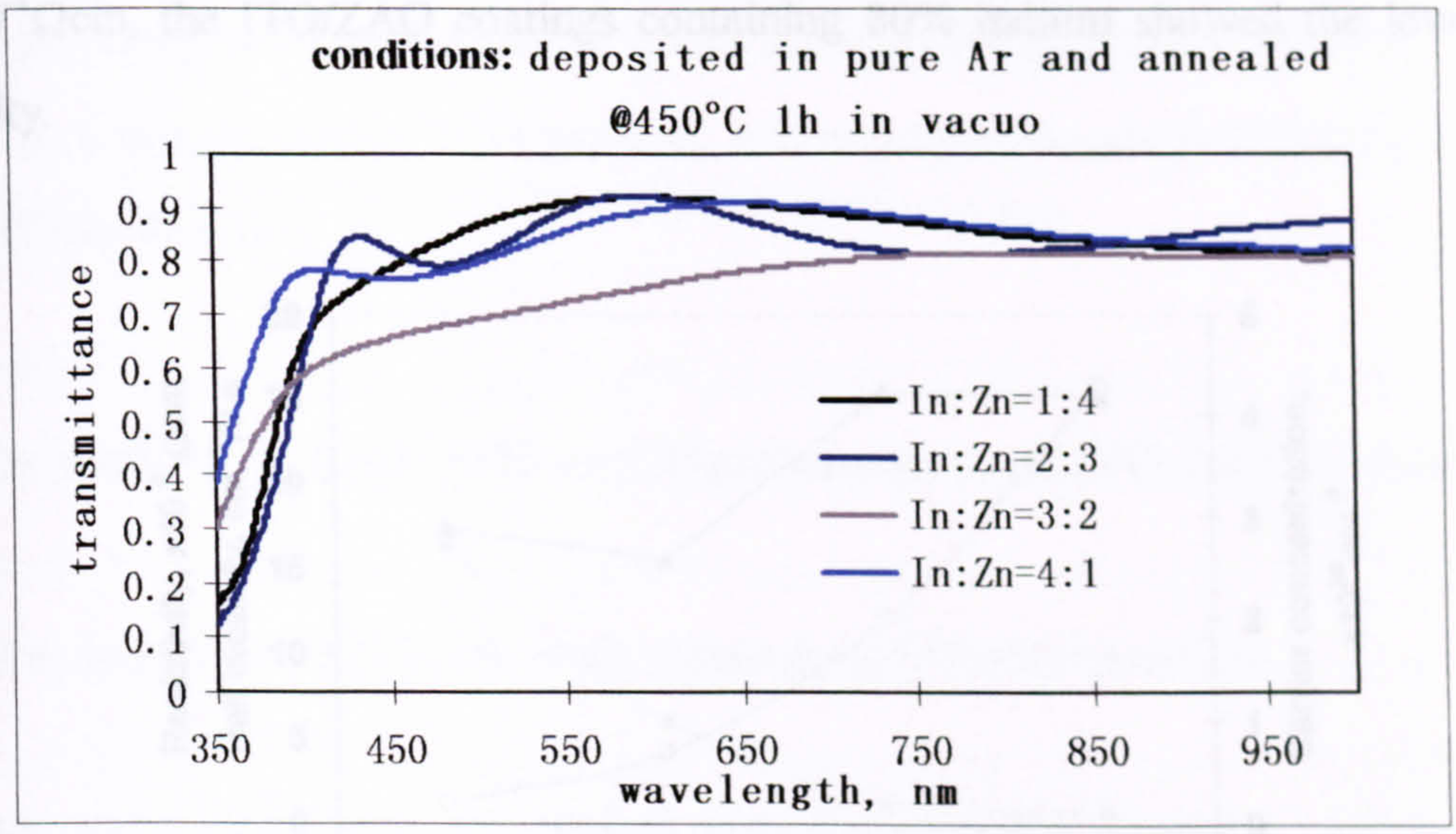

Figure 8.19d

Figure 8.19: the transmittance of ITO/ZAO coatings

8.5.3 The electrical properties of ITO/ZAO multi-component coatings

The electrical properties of the ITO/ZAO coatings are shown in figure 8.20 and table 8.6. The coatings deposited under mixed argon and oxygen atmospheres and then annealed were selected as being representative on this occasion (figure 8.21). As can be seen, these properties tended to improve, i.e. resistivity decreased, charge carrier concentration and Hall mobility increased, as the indium content of the coatings increased. This concurs with other studies [154], in which it is suggested that oxygen vacancies are the primary electron donors in the amorphous ITO/ZAO films and Zn^{2+}/Sn^{4+} co-substitution should produce donor – acceptor pairs in the material, consequently, not providing as many charge carriers as Sn^{4+} alone would [154-155]. For example, the charge carrier concentration of ITO/ZAO coatings with Zn:In ratio 1:4 were $4.2x10^{20}cm^{-3}$, which is lower than those of the ITO coatings, $5.8x10^{20}cm^{-3}$, at the same deposition and annealing conditions (table 8.6). Not surprisingly, therefore, at $6x10^{-4}\Omega cm$, the ITO/ZAO coatings containing 80% indium showed the lowest resistivity.

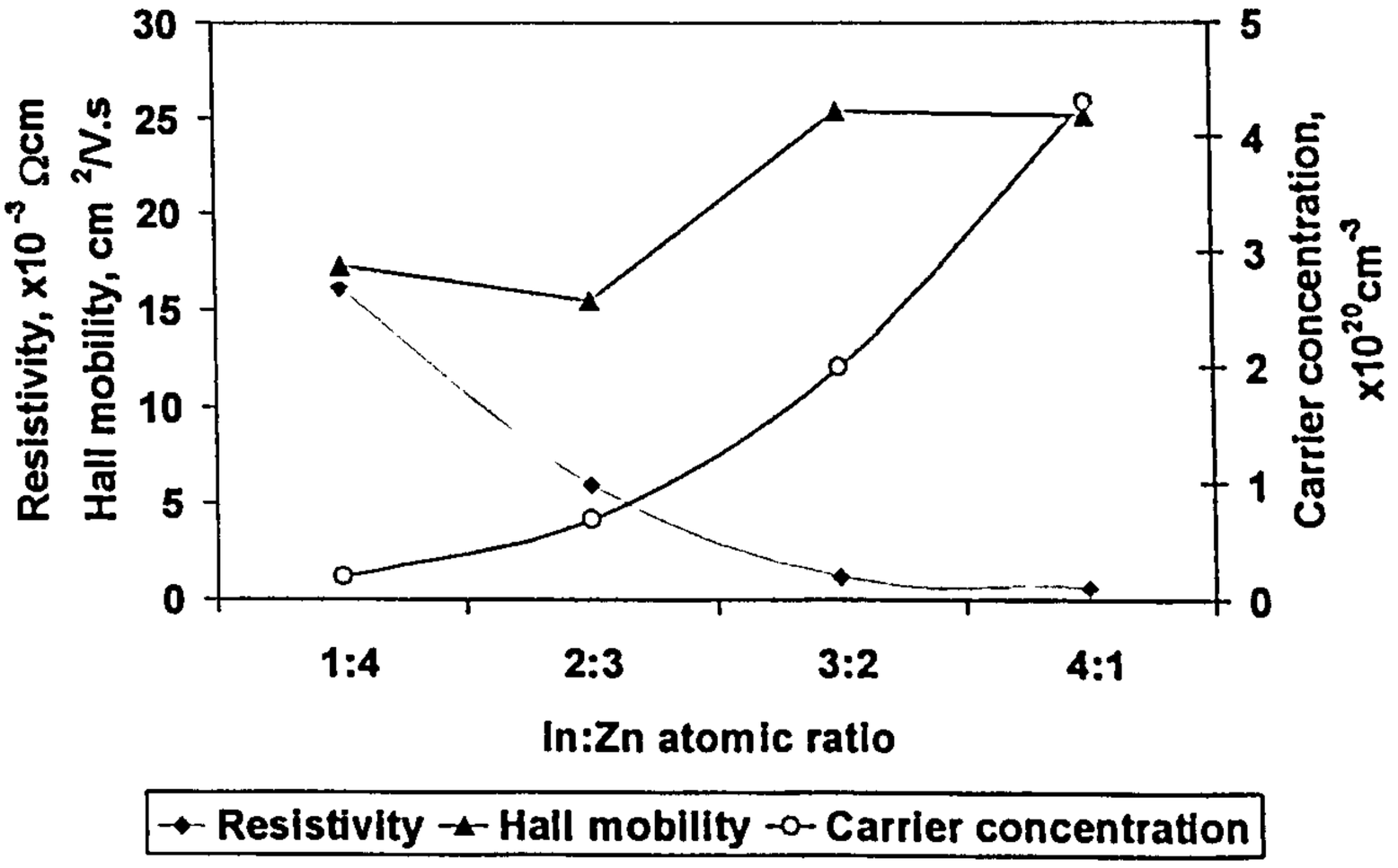

Figure 8.20: The variation with In:Zn atomic ratio in the electrical properties of ITO/ZAO coatings deposited in argon and oxygen atmospheres and annealed in vacuo (450°C for 1 hour).

Table 8.6 ITOZAO coatings resistivity, $10^{-3}\Omega cm$(ZnO:Al (3at%) + ITO (5at%))

Composition / Deposition conditions	4:1 Indium rich	3:2	2:3	1:4 Zinc rich
Ar only	0.7	1.5	4.5	5.8
Annealed	0.6	1.2	3.8	4.3
Ar + 1sccm O_2	5.8	2.7	∞*	∞*
Annealed	0.7	1.2	6.0	16.7

Annealed at 450°C 1hour in vacuo

∞* > *20M Ω*

In general, it is assumed that the electrical properties of the ITO/ZAO coatings are dominated by oxygen vacancies. The deposition conditions and post annealing conditions can be adjusted to produce these vacancies, therefore reducing the resistivity of the coatings. In terms of transmittance, the optical properties of the ITO/ZAO coatings are superior to the ITO coatings. This improvement, though, is obtained at the cost of a small reduction in conductivity of the coatings and their band gap energies. Nevertheless, the results shown here suggest that ITO/ZAO will become a new promising TCO material, whose properties can be tailored to suit specific applications.

8.6 Comparison of ZAO, ITO and Multi-component ITO/ZAO Coatings

8.6.1 Structure of ZAO, ITO and multi-component ITO/ZAO coatings

All these three kinds of TCO coatings had similar dense columnar, defect-free structures both before and after annealing treatment as revealed by SEM micrographs in the above sections. ZAO and ITO showed their strong reflections in XRD spectra, (002) for ZAO and (400), (222) for ITO respectively, which indicated that they had crystalline structures. The multi-component ZAO/ITO showed a zinc oxide-based structure when zinc was rich in the coatings, and an indium oxide-based structure when indium was rich in the thin films. The intermetallic compound, $Zn_3In_2O_6$, might

be present when the contents of zinc and indium in the coatings were similar. In all the coatings, annealing treatments have resulted the diffraction peaks becoming sharper, more intense and closer to standard lattice spacings. Figure 8.21 shows the typical reflections of these three TCO annealed coatings.

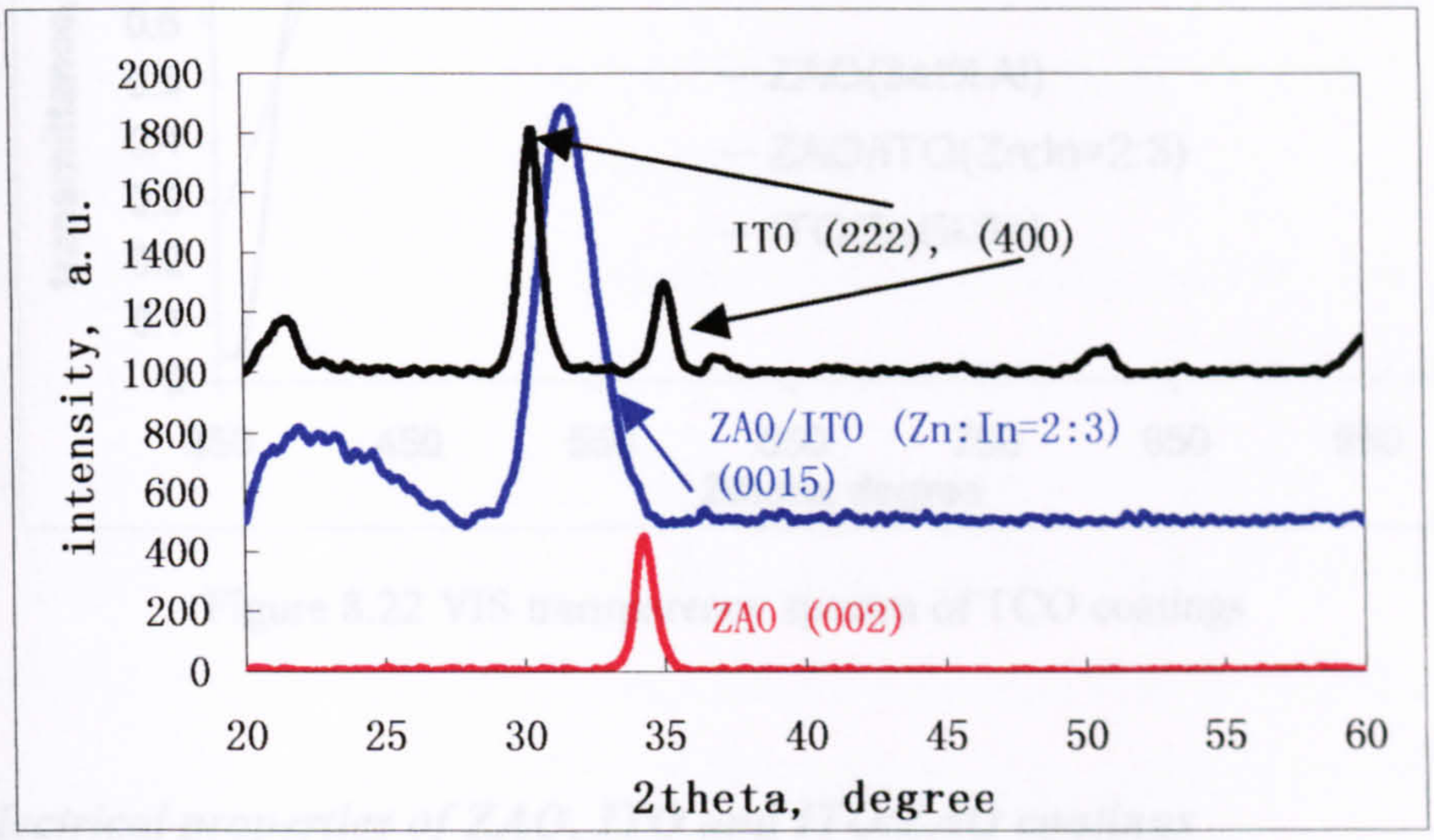

Figure 8.21 XRD spectra of ZAO, ITO and ITO/ZAO annealed coatings

8.6.2 Optical properties of ZAO, ITO and ITO/ZAO coatings

Figure 8.22 shows the transmittance of three kinds of TCO coatings, which were deposited at the same pulse parameters (350kHz, 62%duty), pressure (0.2Pa) and atmosphere (27sccm Ar, 1sccm O_2), and the same annealing processes (at 450^{O}C for 1-2hours in vacuo). The difference was that the deposition time of ZAO coating was 1hour and ITO, ITO/ZAO coatings 15mins. Therefore, the thickness of the coatings were different, with that of the ZAO coating being more than 600nm, ITO 150nm, and ITO/ZAO 140nm.

The transmittance within the visible wavelength of the ZAO coating, at about 90% was slightly higher than those of the other two, of which the transmittance of ITO coating was lower within certain spectra. The interesting phenomenon was that the difference of the cut-off points of these three TCO coatings was obvious, with ZAO

the longest, ITO the shortest and ITO/ZAO between.

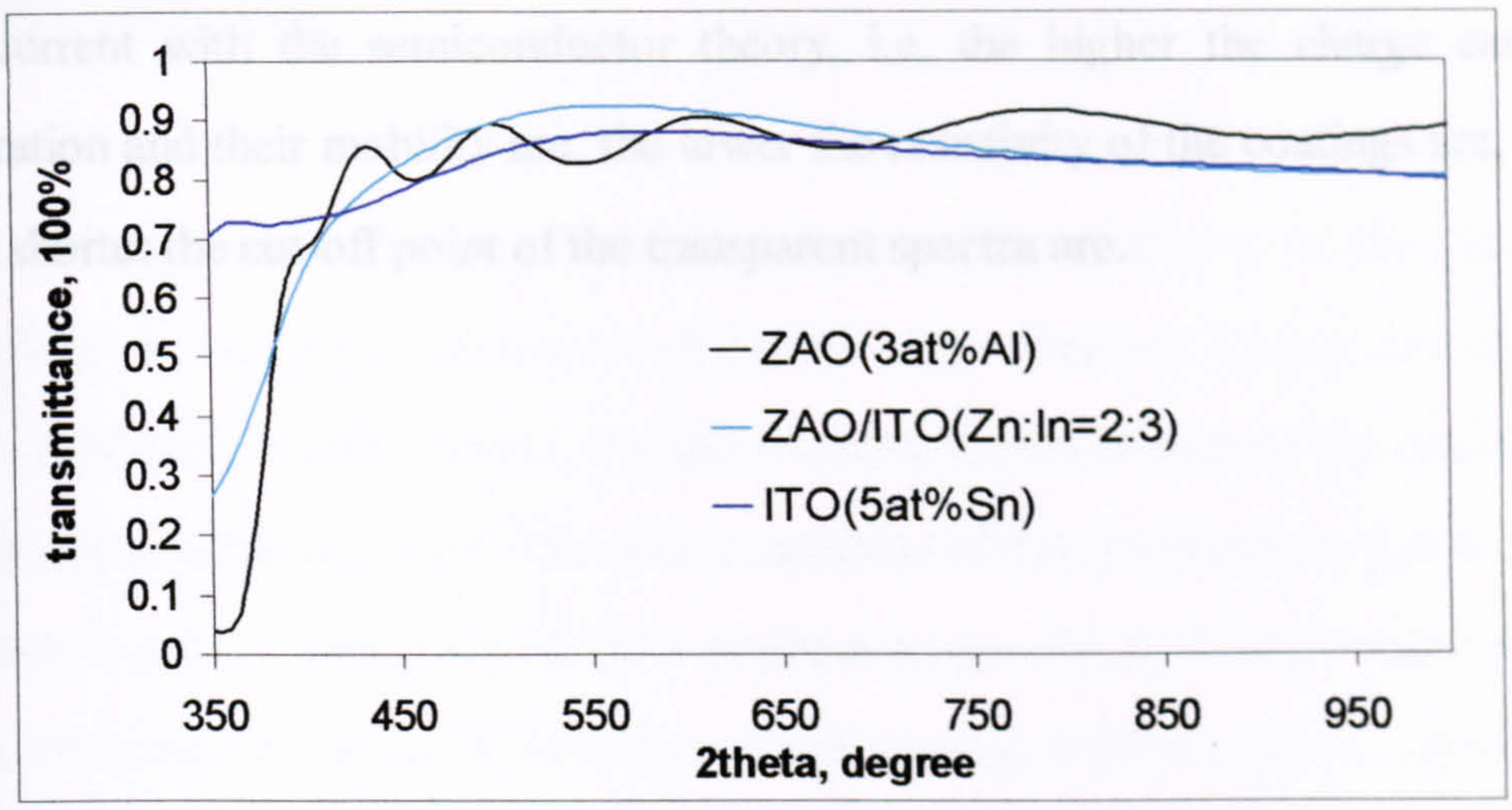

Figure 8.22 VIS transparency spectra of TCO coatings

8.6.3 Electrical properties of ZAO, ITO and ITO/ZAO coatings

Table 8.7 shows the electrical properties of these three TCO coatings. It can be seen that the ITO coating possesses the best electrical properties -- the lowest resistivity, highest charge carrier concentration and mobility. The electrical properties of ZAO and ITO/ZAO coatings are in the same order, although those properties of ITO/ZAO coatings depend on the indium to zinc ratio in the coatings (see section 8.5.3).

Table 8.7: The electrical properties of ZAO, ITO and ITO/ZAO films

	Resistivity, $x10^{-3}\Omega cm$ Deposited in Ar		**Resistivity, $x10^{-3}\Omega cm$ Deposited in $Ar+O_2$**		**Carrier concentration, $x10^{20}cm^{-3}$**		**Hall mobility, $cm^2/V.s$**	
	Before	annealed	before	annealed	before	annealed	before	annealed
ZAO(3at% Al)	8	3.0	∞	2.0	X	1.35	X	12.6
ITO(5at%Sn)	0.4	0.7	0.9	0.4	2.0	5.8	25	26
ITO/ZAO (In:Zn =2:3)	4.5	3.8	∞	6.0	X	0.67	X	15

Annealed at 450°C 1hour in vacuo

∞ – >20MΩ *X – not measured*

In general, the optical and electrical properties of these three kinds of TCO coatings are concurrent with the semiconductor theory, i.e. the higher the charge carrier concentration and their mobility are, the lower the resistivity of the coatings are, and then the shorter the cut-off point of the transparent spectra are.

9. DISCUSSION

The aim of the project was to prepare TCO coatings on glass substrate by the 'Salford methodology' – i.e. the combination of pulsed magnetron sputtering and closed magnetic field with powder targets. For this purpose, a special powder rig was set up and used all through this project. The characterization of the powder rig was described in Chapter 7, and the properties of TCO coatings prepared from this powder rig has been demonstrated in Chapter 8. Therefore, the discussion will be given to explain the reasons behind any trends found in these two chapters, in terms of magnetron configuration, pulsed power supply, deposition parameters, post-annealing treatment, the dopants and the properties of the TCO coatings. The conclusions will be then drawn from this discussion, and the recommendations for further work will be made following on the conclusions.

This chapter will be divided into two parts. The discussion will be concentrated on the effect of the deposition methodology on the properties of the TCO coatings in the first part. The discussion will then go to the relationships between the deposition parameters, post treatment, dopants and their concentrations, and the properties of TCO coatings.

9.1 Configuration of the Powder Rig and Sputtering Power Supply

The influence of the magnetron configuration and power delivery mode (DC, or pulsed DC) on the characteristics of the plasma and the properties of the TCO coatings was described in Chapter 7.

The powder rig was specially set up for use with powder targets. It incorporates an

unbalanced magnetron with a strong magnetic field (maximum 2.2kG), which is formed by rare earth magnets, and a dummy magnetron on top of the chamber to form a 'closed-field' system (refer to Chapter 4). The combination of this strong closed magnetic field with pulsed DC power supply performed very well on sputtering the oxide powder targets to produce good quality TCO coatings. One advantage of the use of pulsed DC is the neutralization of the built-up ions on the surface of the target by highly mobile electrons during the pulse-off phase, which means arcing events caused by a build up of ions can be suppressed. Therefore, no arcing or outgassing occurred during the pulsed magnetron sputtering. Arcing events only occurred when DC power was used to sputter the oxide powder target (Chapter 7 run 4 and 5). Since electrons in the plasma travel along the lines of magnetic flux, the stronger magnetic field can prevent electron losses from the plasma more effectively than a weak magnetron, therefore the sputtering of the target in a stronger magnetic field should provide a higher plasma density than in the weaker one. Furthermore, the higher field strength is also likely to reduce the ignition voltage required to strike a discharge with these poorly conducting targets.

Speaking of the magnetron configuration, it has already been proven that the closed-field unbalanced magnetron configuration is superior to single unbalanced magnetron configurations in confining electrons in the plasma and transporting greater substrate ion currents. A previous study in Salford [65] showed that the ion currents were 1, 8.9 and 21.8A/m^2 in type I, type II unbalanced magnetron configurations and closed-field unbalanced magnetron configuration, respectively, at the same operating conditions. As described in chapter 2, electrons in the presence of a magnetic field tend to travel along the magnetic field lines, which means more electrons are confined in the plasma and are available to take part in ionization in the closed-field magnetron configuration. Therefore, a dense uniform plasma, which fills in the space between the target and substrate, can be created. Also the plasma provides high ion to atom arrival ratio and high ion bombardment energy on the growing film. In this project, closing the magnetic field with the dummy magnetron significantly

increased the ion current drawn at the substrate.

It can be seen, in this project that: 1) the substrate ion currents and self-bias potentials in the double magnetron configuration are about double those in the single magnetron configuration at the same substrate-to-target separations (figure 7.2 and 7.3), which are the expected results according to the theory [139]; 2) The substrate ion currents are proportional to the target currents, and the coefficient of proportionality is larger in the double magnetron condition than that in the single case (figure 7.5); 3) Self-bias potentials are independent of the target current (figures 7.2). In the same magnetron configuration, the number of the secondary electron in the plasma, which cause the gas atom ionization, should be proportional to the target current. Therefore, the ion to atom arrival ratio will correlate to the target current. That is why high target currents lead to high substrate ion currents. On the other hand, the self-bias potential, which controls the energy of the ions incident at the substrate, is only dependent on the magnetron configuration. Increasing the target current does not increase the ion energy, but only means a higher ionization ratio in the plasma. The substrate-to-target separation strongly influences the substrate ion current and the self-bias potentials in both double and single magnetron conditions (Figures 7.4, 7.2 and 7.1). The further away the substrate from the target is, the lower the substrate ion current and the self-bias potential are. This should be true because the longer the electrons travel in the plasma, the more the energy they lose, which in turn means fewer gas atoms will be ionised and the ion energy will be low. Therefore, both the substrate ion current and self-bias potential decreased as the substrate-to-target separation increased. There is an important trend, which is that the self-bias potential decreases at a lower rate with increasing separation in the double magnetron condition, than in the single one. The idea of the formation of closed-field unbalanced magnetron is to provide a dense, relatively uniform plasma between the substrate and the target. In contrast, in single unbalanced magnetrons the plasma density is high close to the target and decreases significantly with increasing separation. Therefore, the loss of electron energy should be less in the double magnetron condition at the same substrate-to-target separation

than in the single one, and the decrease of the self-bias potential is less with increasing separation.

The ZnO:Al (3at%) films were prepared with different pulse parameter conditions. The effect of pulse parameters on the films is that the thickness of the film increases and density slightly decreases as the pulse frequency decreases and pulse duty increases. This is partly because the total deposition times ('pulse-on' factors) are higher at higher duty and low frequency. Also, research at UMIST [148-151] proved that the ion energy flux delivered to the growing film increases with increasing pulse frequency. Therefore, less energy is delivered to the growing film at lower pulse frequencies. This is why the films are thicker but less dense under these conditions.

ZnO:Al films were also prepared by DC and pulsed DC (350kHz and 62% duty) under both single and double magnetron configurations. The films deposited by pulsed DC with the closed-field configuration had the densest structures, and then the densities were lower for the films prepared by pulsed DC with a single unbalanced magnetron and DC with the closed-field configuration, and the most porous film was prepared with a single magnetron in DC mode, see pictures 7.3 and 7.4. This seems reasonable because it is believed, by researchers [17-19, 148-151] who have studied the plasma of the closed-field unbalanced magnetron and pulsed DC power, that the closed unbalanced magnetic field is able to form a uniform plasma further away from the target, and pulsed DC at high frequency is able to produce high energy ions in the plasma with high ion-to-atom ratio. Therefore, the energy delivered to the film was greatest when operating in pulsed mode in the closed field configuration, and least when operating in DC mode with a single magnetron. In the former case, the high ion bombardment caused high lattice strain and deformations in the films, indicated by the shift of the diffraction peaks away from default positions (see the figures 7.12, 7.13 and 7.14). Also, it can be seen from the above figures that the lattice strains in the films were released after the annealing treatment, and the diffraction peaks shifted back closer to their standard positions, which in turn gave the charge carriers more

freedom to move within the crystal lattices, as discussed in Chapter 3. Therefore, the resistivities of the annealed films became lower to the order of 6-1.8x10^{-3}Ωcm, although the resistivities of as-deposited coatings varied due to the different deposition conditions. The major influence of the magnetic field and power supply, though, is on the transparency of the films. The transmittance of the film prepared by DC power with unbalanced magnetic field was as low as 45% at 550nm, compared with those of 85-90% of the films prepared by pulsed DC within unbalanced and closed field magnetrons (figure 7.15). As detailed in Chapter 2, the density of thin films are less than those of the bulk materials. Generally, the denser the film is, the higher the refractive index is, and the closer it is to that of the equivalent bulk material. Porous films tend to show lower refractive indices, higher absorption coefficient, and lower transmittances.

The effect of substrate-to-target separation on the thickness and resistivities of films is given in figures 7.10 and 7.11. It is already discussed above that both substrate ion current and self-bias potential decrease with increasing separation due to the energy losses while the electrons, and other species travel in the plasma. Therefore, the films were thinner, but also suffered less ion bombardment when the substrate was fixed further from the target. The resistivities of the films decreased as the separation increased after annealing treatment. Of course, the ion energy could be the reason for the differences in the resistivity because the high energy delivered to the film would lead to high lattice strains, but it is reasonable to expect that the difference would become less if the annealing time were longer or the temperature higher, because long annealing treatments at high temperatures should help further release the strain within the lattice and give high mobility to the charge carriers.

9.2 Properties of TCO Films

Three types of TCO coatings, i.e. aluminium-doped zinc oxide (ZAO), tin-doped

indium oxide (ITO) and the multi-component TCO combining ITO and ZAO (ITO/ZAO), were prepared, under varying conditions of deposition atmosphere, post-annealing treatment, dopants and their concentrations. The properties of these three types will be compared in the following section, which has been split into four sub-sections.

9.2.1 Deposition atmosphere

It is known that the mean free path (λ) of the species in a plasma is dependent on the pressure in the chamber. Also, it is dependent on the diameters of the species themselves at the same pressure and temperature. The larger the diameter of the species, the shorter the mean free path will be. For example, the mean free path of nitrogen, of which the diameter of a molecule is 3.7Å, is 6.6×10^{-2}m at the pressure of 0.1Pa at room temperature, while that of argon, which has slightly larger diameter, is 5.7×10^{-2}m at the same conditions. In sputtering plasmas, most of the oxygen sputtered from the target should be in the form of atoms or ions. Let us assume that the diameter of an oxygen atom is half of an oxygen molecule, and it is similar to that of nitrogen. Therefore, the mean free path of an oxygen atom or ion at a pressure of 0.2Pa can be estimated to be larger than 13.2×10^{-2}m, according to the formula: $\lambda = KT / 2^{1/2}\pi d^2 p$ (T represents temperature, p pressure and d the diameter of atom or molecule) [39], assuming the temperature will be not lower than room temperature. On the other hand, the mean free path of an argon atom or ion should be larger than 3×10^{-2}m at same conditions, but will not be as long as that of oxygen. The metals, such as zinc and aluminium, have even larger atoms or ions. Therefore, oxygen will be preferentially lost (pumped away, or adsorbed on chamber surfaces) during the sputtering processes. Therefore, extra oxygen has to be input to maintain the stoichiometry. Otherwise, the films will be grown in an oxygen deficient situation.

For the purpose of demonstrating the properties of TCO coatings, the coatings were prepared under argon and oxygen mixture atmospheres and argon only atmospheres.

The transmittance of the films deposited in the argon only atmospheres within the visible wavelength were similar to those of the coatings deposited in argon and oxygen atmosphere (see figures 8.2 and 8.15, 8.19), although the one deposited in argon atmosphere looked a little metal rich when observed by the naked eye. The transmittance lines of TCO coatings as-deposited in argon only atmosphere showed blue shifts compared to those of the coatings as-deposited in argon and oxygen mixture gasses. Therefore, it can be inferred that the cut-off points of the coatings as-deposited in pure argon should be shorter than those of in argon and oxygen atmosphere. For example, the band gap of ZnO:Al coating as-deposited in pure argon is about 3.54 compared to 3.3 (see figure 8.6) for coatings deposited in argon and oxygen. It is difficult to determine the band gaps of ITO due to the limits of the spectrophotometry (350nm to 1700nm) used in this project. The resistivities of the as-deposited films were very different, with the films deposited in argon only atmosphere being about one order higher than the annealed films (see tables 8.4, 8.6 and 8.7), whilst the resistivities of the as-deposited films in argon and oxygen mixture gasses were too high to be measured by the four-point probe, with the exception of some ITO coatings. It is believed [12] that there are two ways to achieve the required low resistivity of TCO coatings: one is to create oxygen vacancies; the other is to add dopants, which provide extra charge carriers. Therefore, it can be said that the TCO films deposited in argon only atmosphere in this project were deficient of oxygen, creating more charge carriers in the films and thus demonstrating lower resistivities.

Moreover, the annealing treatments can result in blue shifts of the transmittance curves and decrease the resistivities of the TCO coatings as-deposited in the argon and oxygen mixture gasses, which can be observed in the figures and tables mentioned above. The annealing treatments were carried out in vacuo, which may have contributed to the low resistivities by degassing the oxygen from as-deposited films to create more oxygen vacancies as well as increasing the charge carrier mobility by releasing lattice strains. In fact, the annealing treatments on the films deposited in argon only atmosphere may have created too many oxygen vacancies, which may

cause electron trapping by dangling bonds (refer to Chapter 3) [72, 155]. As a result, the resistivities of those annealed indium oxide and ITO films were increased and the charge carrier mobility decreased, although the concentrations of charge carriers increased, see table 8.4. In general, both deposition in argon only atmosphere and annealing treatment in vacuo can create oxygen vacancies in the film, which in turn provide free charge carriers and lead to low resistivities for the coatings. On the other hand, the number of oxygen vacancies must be controlled to a suitable level, otherwise it can cause an increase of the resistivities of the films and decrease of the charge carrier mobility.

9.2.2 Annealing parameters

The systematic study of the annealing parameters was carried out according to Taguchi experimental design. The study concentrated on the ZAO coatings. It is obvious that the annealing temperature is the main factor to achieve the required low resistivities. The resistivities decreased faster at relative high temperatures. The resistivities did not show significant changes until the annealing temperature was up to as high as 350°C (see figure 8.8), which meant that the lattice strains began to be released above this point. This should be true because the one aim of annealing treatment is to release the lattice strains, increase the crystallinity and uniformity of the grains, which can be seen from the XRD reflection peak changes in figures 8.4 and 8.5a and b. Also, a certain annealing time is required to achieve the low resistivity according to Taguchi analysis. The rate of change slows down or reverses after a certain time as the optimum values are reached. The results of the changes within the crystal lattices will lead to an increase in the mobility of the charge carriers by relieving the effect of electron scattering (chapter 3), which can be seen from the comparison of the pure indium oxide coatings as-deposited in argon and oxygen atmosphere and their annealed coatings (table 8.4).

The annealing atmosphere is another important factor in the processes of achieving

the required low resistivities. Annealing in air effectively caused the coatings to be re-oxidized, and in turn lose their charge carriers, which means it is impossible to lower the resistivities. It has to be mentioned annealing can be carried out in air for some coatings prepared by Sol Gel processes [1], which may be due to the amorphous metal rich structures of these coatings. The annealing treatments under controlled reduced atmospheres showed that non-oxidizing annealing atmospheres provide a good means of lowering the resistivities of the coatings, which is believed to be due to the extra losses of oxygen from the films, and therefore more charge carriers are produced. This phenomenon corresponds to the blue shift of cut-off points in the optical analysis, as discussed in Chapter 3. On the contrary, the further degassing of oxygen from the coatings may cause more dangling bonds to trap the charge carriers, which in turn lowers their mobility. This is why the resistivity of the ITO coatings, which as-deposited in argon only atmosphere, increased after being annealed in vacuo. Therefore, the results of the resistivities of the coatings annealed in different atmosphere (figure 8.8) may be explained as follows: the annealing process carried out under oxygen and nitrogen mixture atmosphere provided the chance for some oxygen degassing from the coatings and slightly increased the concentrations of charge carriers in the coatings, therefore the resistivities were reduced, but still remained relatively high, which corresponds to the blue shift, see figure 8.6. Using nitrogen only in the annealing atmosphere caused a significant increase of the charge carriers. As a result, the resistivities decreased.

In general, there are two main aspects of the annealing treatment on the properties of the coatings. One is that the annealing treatments help to improve the uniformity of the crystal lattice, which results in an increase of the mobility of the charge carriers. The other is that the annealing treatments, especially in reduced inert atmospheres, provide the chances of degassing the oxygen from the coatings, which in turn results in the increase of the concentration of the charge carriers, also might cause the decrease of charge carrier mobility due to electron trapping. The resistivities of the annealed coatings are dependant on the combined effects of both.

9.2.3 Dopants and their concentrations

I. Hamberg and CG. Granqvist detailed in their paper [72] that there were two opposite effects of adding dopants in a semi-conductor. First of all, the addition of the dopant provides more charge carriers and causes the merging of the dopant band with conduction band when the n-type semiconductor is heavily doped. Therefore, the band gap of the semiconductor is enlarged. On the other hand, there are several types of electron scattering (take n-type semiconductors as an example) which may influence the optical properties by way of narrowing the band gap of the semiconductor, such as electron-defect scattering, electron-lattice scattering and electron-electron scattering, which involve grain boundaries, external surfaces, neutral and ionized point defects, dislocations, precipitations, clusters, local deformation potentials etc. Many of them, except scattering against ionized impurities, can be neglected if the films are strongly crystalline. The ions are necessary because they produce free electrons in the films. Therefore, it is really true that the shift of the band gap of a doped semiconductor is dependent on the concentrations of charge carriers and the scattering mechanisms.

The addition of the dopants of aluminium, gallium and indium, respectively into zinc oxide decreased zinc oxide's resistivity by different amounts by providing extra electrons, see table 8.2. Also, it can be seen in the column of tolerance of lattice spacing in table 8.2 that the lattice strains increased as the radius of the dopant atoms increased, which means that the influence of the electron scattering becomes more serious. Therefore, the resistivities of the coatings increased and the enlarging of the band gaps was small (figure 8.13a) compared to that of pure zinc oxide as the radius of dopant atoms increased. Dopant tin in zinc oxide is an exception, which caused the band gap narrowing – cut-off point red shift (figure 8.13b), and resistivities of the films higher than that of pure zinc oxide. This might be due to complex electron scattering mechanisms dominating the band gap shift. Sb-doped zinc oxide thick films

are normally used in sensors to detect some gasses, such as CH_4. So, we do not give the results of the explanation here, which is beyond the scope of this project – focusing on the optical and electrical properties of the TCO coatings.

The effect of electron scattering mechanisms also is the results of the ITO coatings. The carrier concentration of the pure indium oxide coating is $10^{23}m^{-3}$, and that of ITO coating after being heavily doped reaches the order of $10^{26}m^{-3}$. The conduction band will merge with the dopant band and the band gap will be decided by the highest occupied states in the conduction band if the carrier concentration is larger than 6 x $10^{24}m^{-3}$ [72]. For the ITO films deposited in argon and oxygen atmospheres, which have fewer oxygen vacancies and in turn the electron scattering was less important than those deposited in argon only condition, the trends are obvious, in that the concentration and mobility of charge carriers increased, whilst the resistivity decreased and band gap enlarged as the tin dopant was added into the indium oxide films, see table 8.4 and figure 8.15a.

Dopants in the semi-conductive coatings have to be at a suitable level, which means the electron scattering will not seriously affect the optical and electrical properties of the coatings whilst the dopants provide free charge carriers. It can be seen in table 8.6 that all the electrical parameters, the resistivity, carrier concentration and mobility, of the 5at% tin doped indium oxide coatings are better than those of 10at% ITO coatings after annealing. This is especially true for the coatings deposited in argon only atmosphere. It can be explained that the heavier doped films combined with the more oxygen vacancies in the 10at% ITO coating deposited in argon only atmosphere made the effect of the electron scattering became more serious than the effect of the increase of charge carriers.

9.2.4 Comparison among ZAO, ITO and multi-component TCO coatings – ITO/ZAO

The average transmittance in visible wavelengths of the aluminium-doped zinc oxide (ZAO) coatings is about 90% compared with about 85% for the tin-doped indium oxide (ITO) coatings. Also, the transmittances of the ZAO coatings are very stable through all the processes attempted during this project, whilst those of ITO are more variable; see figures 8.2, 8.15 and 8.19 and 8.22. It is impossible to estimate the band gaps or cut-off points of the ITO coatings due to the limitations of the spectrophotometer used. But it is clear that the band gaps of ITO are larger than those of the ZAO coatings, even the band gaps of indium oxide coatings prepared in this project are larger than those of pure zinc oxide coatings. The ITO coatings show higher concentrations of charge carriers, lower resistivities (table 8.6) and shorter plasma frequencies (figure 8.16) compared with those properties of ZAO coatings (figure 8.7). Pure indium oxide coatings have better electrical properties than those of pure zinc oxide coatings. For example the resistivity of indium oxide coating can be $1x10^{-3}\Omega cm$, but that of zinc oxide coatings only $0.14\Omega cm$. In fact, zinc has a stronger affinity with oxygen, because it has two valence electrons and stronger metallic properties, than indium, which has three valence electrons in its outer shell. So, indium oxide should be more sensitive to the oxygen content in the deposition and annealing atmosphere. As discussed before, oxygen vacancies are one of main reasons for the creation of charge carriers in the coatings during the deposition processes, especially in argon only atmospheres, and in-vacuo annealing processes. Therefore, the oxygen vacancies will be more easily created in indium oxide than zinc oxide, which in turn means the charge carrier concentrations are higher in indium oxide than zinc oxide coatings, see table 8.6.

Dopants in indium oxide and zinc oxide take the same role – to provide free charge carriers, also creating the same side effect – electron scattering. The resistivities of the coatings are dependent on the combined effect of both.

Until now, the multi-component ITO/ZAO coatings have not been mentioned, because their optical and electrical properties relied on their compositions, which are similar to those of ZAO coatings when zinc-rich; and similar to those of ITO coatings when indium-rich. One interesting phenomenon is the electrical properties, such as resistivities, charge carriers concentrations and their Hall mobilities, are only slightly worse (but still acceptable) than those of the ITO and ZAO coatings, even if the crystallinity of the ITO/ZAO coatings are not good (reflection peaks broaden, see figures 8.18). In fact, the structures of some of coatings (indium:zinc atomic ratio = 2:3 and 3:2) may be amorphous or nano-crystalline (grain sizes of the order of a few nm), which is difficult to determine, or resolve by XRD or SEM and would need TEM to investigate this in the future. The reason for the slight changes of the electrical properties, such as the increase in resistivity (table 8.7), should be due to the mixture of large amounts of different materials causing disorder in the crystal lattice, which increases the electron scattering effect. It has been noticed that the charge carriers in the multi-component coatings mainly come from the oxygen vacancies. Therefore, the resistivities of the indium-rich coatings are lower than those of zinc rich coatings.

The optical properties of the ITO/ZAO coatings are also dependant on their compositions; see figures 8.19. Zinc-rich coatings generally have high transmittance within the VIS range. The transmittance of indium-rich coatings are not as high and stable as those of zinc-rich ones, presumably for the same reason as the indium oxide coatings – the affinity of indium to oxygen is weaker than that of zinc to oxygen. Moreover, there should be more charge carriers in the indium-rich ITO/ZAO coatings, which is indicated by the fact that the cut-off points of the transmittance curves of the indium-rich coatings are shorter than those of the zinc-rich coatings.

In summary, there are two ways to create charge carriers in the TCO coatings prepared in this project. One is by adding suitable dopants, the other is oxygen deficiency in the coatings. Both dopant levels and oxygen deficiency levels should be controlled,

because they also cause the electron scattering effect to lower the mobility of the charge carriers. Some of the scattering mechanisms, such as the electron-to-ion scattering, cannot be avoided because they accompany the addition of dopants and the creation of oxygen deficiencies. That means the creation of charge carriers also creates the chance of electron scattering. Therefore, the resistivities of the TCO coatings are the combined results of these two effects.

The effect of electron scattering can be liberated by suitable deposition and post treatment processes, although it cannot be completely eliminated. The powder rig in Salford demonstrates its superior performance on preparing the TCO coatings with required properties. The closed-field magnetron sputtering combined with controllable atmosphere annealing makes the preparation of TCO coatings, with acceptable properties, from powder targets a reality. Furthermore, this rig has become a powerful development tool for the deposition of novel materials.

10. CONCLUSIONS

1. Pulsed magnetron sputtering from powder blend targets is a viable, highly versatile technique for the production of TCO coatings.

2. When operating in the closed field configuration, the saturation ion current at the substrate was double that measured in the single magnetron mode.

3. SEM analysis showed that dense columnar, defect-free TCO coatings could be prepared in the powder rig by this combined sputtering technique.

4. AES and SIMS, XPS and RBS analysis indicated that the compositions of the TCO coatings are consistent with those of their targets. Also, the compositions of the TCO coatings were uniform through the whole thickness of the coatings, except the compositions of the ITO/ZAO coatings.

5. XRD analysis showed that ZAO and ITO coatings had strong crystalline textures. The reflection peaks shifted closer to their standard positions after annealing. The crystallinity of the ITO/ZAO coatings were dependent on their chemical compositions, but their reflection peaks were generally broadened and the structure of some of the coatings were amorphous or possibly nano-crystalline.

6. The properties of the TCO coatings are dependant on the deposition parameters – pulse frequency, duty and current, also the deposition atmosphere and the substrate-to-target separation.

7. Systematic annealing process studies were carried out according to the Taguchi experimental arrays. Optimum annealing parameters were: annealing temperature no lower than 450C; annealing time no shorter than 1 hour; and annealing

atmosphere vacuo.

8. The effects of post annealing treatment on the TCO coatings were the release of the lattice strains, increased crystallinity, and more importantly, creation of oxygen vacancies. Therefore, the concentration and mobilities of free charge carriers increased, which in turn appeared as an enlarging of the band gap of the TCO coatings and a decrease in their resistivities.

9. Dopants are necessary in the TCO coatings, and there are two factors: to select the suitable dopant and control it at a certain level, to achieve the required optical and electrical properties.

10. The aim of the addition of dopants in the semiconductors was to increase the concentrations of the free charge carriers. On the other hand, too heavily doped semiconductors suffer from serious electron scattering effects, which lowers the charge carrier mobilities, therefore increasing the resistivities of the coatings. 3at% aluminium in zinc oxide and 5at% tin in indium oxide coatings, prepared in this project by pulsed magnetron sputtering from powder targets, showed the lowest resistivities.

11. The optical and electrical properties of TCO coatings are dominated by the deposition and post annealing treatments. The combination of suitable deposition and post annealing processes are necessary to achieve the required properties of the coatings.

12. The transmittances of the TCO coatings were measured by spectrophotometry, and electrical properties by four-point probe and Van der Pauw's technique. The best results obtained for the ZnO-3at%Al coatings were resistivities of about $2x10^{-3}\Omega cm$, with average visible transmittances of 90%; those of the 5at% ITO coatings were about $4x10^{-4}\Omega cm$ with visible transmittances of 80-85%; and the

resistivities and transmittances of ITO/ZAO coatings were between those of the ZnO:Al and ITO coatings, dependant on their compositions.

13. The substrate self-bias potentials decrease with the increase of substrate-to-target separations, the rate of the decrease is slow in double magnetron configuration compared to that in single one. The substrate self-bias potentials are independent of the target currents.

14. The substrate ion saturation currents increase with the increases of target currents and the decrease of the substrate-to-target separations. The ion currents are double in closed magnetic field comparison to those in single unbalanced magnetic field at the same substrate-to-target separations.

15. The thickness of the film strongly depends on the pulse parameters, which increases as the decrease of pulse frequency and the increase of the pulse duty, i.e. the increase of pulse on factor.

16. The density of the coating strongly depends on the magnetron configuration and power supply – the film produced in closed magnetic field by pulsed DC power is the densest one, and the film produced in single unbalanced magnetic field by DC power is the most porous one among all the experimental runs.

11. RECOMMENDATIONS FOR FUTURE WORK

1. Production of different coatings by utilizing the flexibility of the powder targets. The non-oxide coatings or metal coatings are strongly recommended because it will help to know if the air trapped among the loose target material will influence the properties of the coatings, or not.

2. Production of multi-layer coatings. One of the applications of TCO coatings is to act as an electrode in certain electronic devices, such as photovoltaic solar cells. Therefore, it would be useful if the multi-layer coatings with desired properties can be produced from the powder targets.

3. High temperature superconductive oxide films using powder targets.

4. Further modifications of the rig are recommended. First of all, it will be much more efficient if a liquid nitrogen baffle can be used on top of the diffusion pump instead of the water cooling system. This will help in the production of super-pure coatings with high quality. Secondly, another two magnetrons can be installed in the bottom of the rig, which will allow the multi-layer coatings to be prepared during the same run without exposure of the coatings to air.

5. Additional analytical techniques would be useful – TEM, for example.

6. Analysis and comparison of the compositions of new and used targets.

REFERENCES

1. *MJ Alam and DC Cameron, J, Vac, Sci. Technol., A19(4) 2001, 1642.*
2. *O Kluth, et al, Thin Solid Films, 351 (1999) 247.*
3. *P Nunes, D Costa, E Fortunato and R Martins Vacuum, 64(2002) 293.*
4. *B Szyszka, Thin Solid Films, 251 (1999) 164-16.*
5. *T. Minemoto, T. Negami, S. Nishiwaki, H. Takakura and Y. Hamakawa Thin Solid Films 372 (2000), p. 173-176.*
6. *T. Minami, etc.,Thin Solid Films 270 (1995) 22-28.*
7. *T. Minammi, T. Kakumu and S. Takata, J. Vac. Sci. Technol. A 14(3) May/Jun (1996) 1704.*
8. *T. Minammi, Y. Takata, S. Takata and T. Kakumu, Thin Solid Films 308-309 (1997) 13.*
9. *T. Minammi, Y. Takata, T. Kakumu, S. Takata, and I, Fukuda, J. Vac. Sci. Technol. A 15(3) May/Jun (1997) 958.*
10. *T. Minammi, T. Kakumu, K. Shimokawa and S. Takata, Thin Solid Films 317 (1998) 318.*
11. *T. Munami, T. yamanoto, H. Toda and T. Miyata, Thin Solid Films 373 (2000) 189.*
12. *K Ellmer J.Phys.D: Appl. Phys. 33 (2000) R17-R32.*
13. *B. Window, N. Savvides, J. Vac, Sci. Technol. A4 (2) Mar/Apr 1986 p196-201.*
14. *B. Window, N. Savvides, J. Vac, Sci. Technol. A4 (2) May/Jun 1986 p453-456.*
15. *N. Savvides, B. Window, J. Vac, Sci. Technol. A4 (2) May/Jun 1986 p504-508.*
16. *D.G Teer, UK patent No. 2258 343, USA patent No. 5 554 519, European Patent No. 0 521 045.*
17. *P.J. Kelly, R.D. Arnell, Surf. Coat. Technol. 86-87 (1996) 425-431.*
18. *P.J. Kelly, R.D. Arnell, Surf. Coat. Technol. 108-109 (1998) 317-322.*
19. *P.J. Kelly, R.D. arnell, J. vac. Sci. Technol. A 16(5), Sep/Oct 1998, 2858-286842-43.*
20. *Bell and Deamley, Surface Engineering 1994, Vol. 10, No.4, P123-128.*
21. *Hutchings, 'Tribology, Friction and Wear of Engineering materials', Edward Arnold, London, 1992.*
22. *K Holmberg and A Matthews, 'Coatings Tribology; Properties, Techniques and Applications in Surface Engineering', Elsevier 1994.*
23. *Park Ridge, N.J., 'Deposition Technologies for Films and Coatings: Developments and Applications', Noyes Publications, 1982.*
24. *Donald M. Mattox, 'The History of Vacuum Coating Technology', Management Plus. Inc 2002.*
25. *John L. Vossen, Werner Kern, 'Thin Film Processes II', Academic Press Ltd., 1991.*
26. *D.M. Mattox, 'Educational Guides to Vacuum Deposition Technology, Society of Vacuum Coaters, 1998.*
27. *NAG Ahmed, 'Ion Plating Technology: Developments and Applications', Chichester, Wiley, 1987.*
28. *Philip S. Henderson, PhD Thesis, the University of Salford, 2002.*
29. *D.M. Mattox, G.J. Kominiak, J.Vac.Sci.Technol. 9, (1971), p528-532.*
30. *D.M. Mattox, PVD Processes—SVC, (1997). P380-394.*
31. *S Rossnagel, 'Use of Plasmas in Deposition Technology,' in DS Rickerby and A Matthews,*

'Advanced Surface Coatings – A Handbook of Surface Engineering.' Blackie, Glasgow, 1991.

32. *A Matthews, 'Advanced Surface Coatings – A Handbook of Surface Engineering.' Blackie Glagow, 1991.*
33. *P.Eh. Hovsepian, W.D. Munz, 'Thin Film Deposition and Surface Modification by Sputtering and Ion Implantation', IoP Plasma Training School, (1999).*
34. *M Venugopalan and R Avni, 'Analysis of glow discharges for understanding the process of film formation,' in KJ Klabunde (ed), 'Thin films from Free Atoms and Particles.' Academic Press, New York, 1985.*
35. *RM Clements, J. Vac. Sci. Technol., 13(2) March/April 1978, 193-198.*
36. *D.M. Mattox J. Vac. Sci. Technol. 10 (1973), 47.*
37. *B Chapman 'Glow Discharge Processes,' John Wiley & Sons, New York, 1980.*
38. *H.K. Pulker, Wear and Corrosion Resistant Coatings by CVD and PVD, Ellis Horwood Ltd., Chichester (1989).*
39. *A Chambers, R K Fitch and B S Halliday, 'Basic Vacuum Technology', 2nd Edition, IOP publishing Ltd 1989.*
40. *M. Ohring, 'The Materials Science of Thin Films', academic press, London, (1991).*
41. *B A Movchan and A V Demchisin, Phys. Met. Metallogr., 28, 4, (1969), 83-90.*
42. *J A Thornton, J, Vac. Sci. Technol. A4 (6), (1986), 3059-3065.*
43. *J A Thornton, J. Vac. Sci, Technol., 11, No.4 Jul/Aug, (1974), 666-670.*
44. *Y Enomoto and K Matsubara, J. Vac. Sci. Technol., 12(4) Jul/Aug, (1975), 827-829.*
45. *R. F. Bunshah and R S Juntz, J. Vac. Sci. Technol., 9(6), (1972), 1404-1405.*
46. *R C Ross and R Messier, J. Appl. Phys., 52(6), 1981, 5329k-5339.*
47. *R Messier, R P Giri and R A Roy, J. Vac. Sci. Technol., A2(2), Apr-Jun, 1984, 500-503.*
48. *C Fountzoulas and B Nowak, J. Vac. Sci, Technol., A9(4), Jul/Aug, 1991, 2128-2137.*
49. *J Musil, S Kadlec, V. Valvoda, R Kuzel and R Cerny, surf. Coat. Technol., 43/44 (1990) 259-269.*
50. *S Kadlec, JMusil and J vyskocil, Surf. Coat. Technol., 54/55 (1992), 287-296.*
51. *J. Musil, V Poule,, V Volvoda, R Kuzel, H A Jehn and M E Baumgartner, Surf. Coat. Technol., 60(1993) 484-488.*
52. *V Poulek, J. Musil, V Valvoda and R Kuzel, Thin Solid Films, 196(1991) 265-270.*
53. *P.J. Kelly, R.D. Arnell, Vacuum 56 (2000) 159-172.*
54. *R.V. Stuart, Vac. Tech. Thin films and sputtering, Academic press Inc, 1983.*
55. *John E. Mahan 'Physical Vapor Deposition of Thin Films', Colorado State University, John Wiley & Sons, 2000.*
56. *J. S. Chapin Res. Dev. 25, 37 (1974).*
57. *R,P. Howson, Glass International, June (1966), 56-58.*
58. *J.A. Thornton, J. Vac. Sci. Technol. 15(2) March/April (1978), 171-177.*
59. *R.Hill, F. Jansen, J. Non-crystalline Solids 218(1997), 35.*
60. *S.M. Rossengel, J.J. Cuomo, Vacuum 38, 2(1988), 73-81.*
61. *J. Musil and S. Kadlec, J. Vac. Sci. Technol. A9(3) May/Jun 1991.*
62. *R.P. Howson, H.A. Ja'afer A.G Spencer, Thin Solid Films (1990), 193-194, 127-137.*
63. *W.D. Sproul, Vacuum, 51(4), (1998), 1379-1376.*
64. *J. O'Brien, R.D. Arnell, Surf. Coat. Technol. (1996) 86-87,p200-206.*

65. *J. O'Brien, PhD thesis, University of Salford, 1998.*
66. *S.L. Rohde, L. Hultman, M.S. Wong, W.D. Sproul, Surf. Coat. Technol. (1992), 50, 255-262.*
67. *I. Petrov, F. Adibi, J.E.Greene, W.D. Sproul W.D. Munz, J. Vac. Sci. Technol. A10(5) (1992), 3283-3287.*
68. *Richard Turton, 'The Physics of Solids', Oxford University Press, 2000.*
69. *John Allison, 'Electronic Engineering semiconductors and Devices', McGraw-Hall Book Company, Second edition 1989.*
70. *J. Wilson, J.F.B. Hawkes, 'Optoelectronics: An Introduction', Prentice Hall International (UK) Ltd., Second edition 1989.*
71. *Wilson, I. H., 'Engineering Solids', London (etc.): McGraw-Hill, 1979.*
72. *I. Hamberg, C.G. Granqvist, J.Appl.Phys. 60(11) 1 Dec. 1986 R123.*
73. *Adir Bar-Lev, 'Semiconductor and Electronic Devices', Prentice Hall, Third Edition, 1993.*
74. *A. Sarkar, et al, Thin Solid Films, 204(1991) 255-264.*
75. *J.D. Perkins, et al, Thin Solid Films, 411 (2002) 152-160.*
76. *Elais Burstein, Phy. Rev. 93(1954) 623.*
77. *P Nunes, E Fortunato, F Tonello, Fbraz Fernandez, P Vilarinho and R Martins, Vacuum, 64 (2002) 281.*
78. *K.Y. Cheong, et al, Thin Solid Films, 410 (2002) 142-146.*
79. *Tae Young Ma, Dae Keun Shim, Thin Solid Films 410 (2002) 8-13.*
80. *O. Vigil, F. Cruz, G. Santana, L. Vaillant, A. Morales-Acevedo and G. Contreras-Puente Appl. Surf. Sci. 161 (2000), p. 27-34.*
81. *Toshinhiro Miyata, et al, Thin Solid Films, 411(2002) 76-81.*
82. *M. de la L. Olvera, et al, Thin Solid Films, 394 (2001) 241-249.*
83. *C.H. Lee, L.Y. Lin, Applied Surface Science 92 (1996) 163-166.*
84. *G.H Lee et al., Thin Solid Films 386 (2001) 117-120.*
85. *J. Tsujino, et al, Thin Solid Films, 407 (2002) 86-91.*
86. *K. Kaiya, et al, Thin Solid Films, 409 (2002) 116-119.*
87. *Guojia J. Fang, et al, Thin Solid Films, 418 (2002) 156-162.*
88. *Y. Nakanishi, A. Miyake, H. Kominami, Appl. Surf. Sci. 142 (1999) 233.*
89. *B.J. Jin, H.S. Woo, S. Im, S.H. Bae and S.Y. Lee Appl. Surf. Sci. 169/170 (2001), p. 521-524.*
90. *S. Jager, et al, Surface and Coatings Technology 98 (1998) 1304-1314.*
91. *B. Szyszka, Thin Solid Films, 351 (1999) 164-169.*
92. *Dengyuan Song, et al, Solar Energy Materials & Solar Cells 73 (2002) 1-20.*
93. *Guojia Fang, Vacuum 68 2003 363-372.*
94. *J.F. Chang, M.H. Hon, Thin Solid Films, 386 (2001) 79-86.*
95. *T. Schuler, M.A. Aegerter, Thin Solid Films, 351 (1999) 125-131.*
96. *XT Zhang, YC Liu, ect. Thin Solid Films, 413(2002) 257-261.*
97. *FD Parguay, M Miki-Yoshida, J. Morales, J Solis, WL Estrada, Thin Solid Films 373 (2000) 137-140.*
98. *N Jayadev Dayan, SR Sainkar, RN Karekar, RC Aiyer, Thin Solid Films 325 (1998) 254-258.*

99. *JB Lee, HJ Lee, SH Seo, JS Park, Thin Solid Flms, 398-399 (2001) 641-646.*
100. *T Yamamoto, Thin Solid Films 420-421 (2002) 100-106.*
101. *KY Cheong, N Muti, SR Ramanan, Thin Solid Films 410 (2002) 142-146,*
102. *TY Ma, DK Shim, Thin Solid Films 410 (2002) 8-13.*
103. *T Minami, T Yamamoto, T Miyata, Thin Solid Films 366 (2000) 63-68.*
104. *K Agura, A Suzuki etc., Thin Solid Films, 445 (2003) 263-267.*
105. *Z.C. Jin,I Hamber, and CG Granqvist, J. Appl. Phys. 64(10), 15 Nov. 1988,5117*
106. *E. fortunate, P Nunes, etc. Vaccum 64 (2002) 233-236.*
107. *M. Bender, et al, Thin Solid Films, 418 (2002) 45-50.*
108. *D.M. Gostantini, H.G. Limberger, and T. Lasser, Optics Letters, Oct. 1, 2000 / Vol. 25, No. 19, 1445-1447.*
109. *Hisashi Ohsaki, Yoshinori Kokubu, Thin Solid Films, 351 (1999).*
110. *RB Hadj Tahar, T Ban, Y Ohya and Y Takahashi, J. Appl. Phys. 83, 5 (1998) 2631.*
111. *BG Lewis and DC Paine, MRS Bull. Aug. (2000) 22.*
112. *H Yeom, N Popovich, E Chason and D Paine, Thin Solid Films 411 (2002) 17.*
113. *WJ Lee, YK Fang, J. Mater. Science: Materials in Electronics 13 (2002) 751.*
114. *C May, J Strumpfel, Thin Solid Films 351 (1999) 48.*
115. *AK Kulkarni, KH Schulz, T–S Lim and M Khan, Thin Solid Films 308-309 (1997) 1.*
116. *TC Gorjanc, D Leong, D Py and D Roth, Thin Solid Films 413 (2002) 181.*
117. *T Minami, S Ida, T Miyata, Thin Solid Films 416 (2002) 92*
118. *M Penza, S Cozzi, MA Tagliente, L Mirenghi, C Martucci, A Quirini, Thin Solid Films 349 (1999) 71.*
119. *J Vetrone, YW Chung, J. Vac. Sci. Technol. A9 (1991) 3041.*
120. *D Yu, W Yu, D Wang and Y Qian, Thin Solid Films 419 (2002) 166.*
121. *SH Keshmiri, M Rezaee-Roknabadi and S Ashok, Thin Solid Films 413 (2002) 167.*
122. *J Vetrone, YW Chung, J. Vac. Sci. Technol. A9 (1991) 3041*
123. *M Wakagi, K Chahara, K Onisawa, Y Kawakubo, T Kichikawa, T Satoh and T Minemura, Thin Solid Films 411 (2002) 46.*
124. *H Morikawa and M Fujita, Thin Solid Films 359 (2000) 61.*
125. *M Kamei, H Enomoto and I Yasui, Thin Solid Films 392 (2001) 265.*
126. *M Quaas, H Steffen, R Hippler and H Wulff, Thin Solid Films 420-421 (2002) 306.*
127. *DS Ginley and C Bright, MRS Bull. Aug. (2000) 15.*
128. *CG Granqvist and A Hultaker, Thin Solid Films 411 (2002), 1-5.*
129. *N. Naghavi, A. Rougier, C. Marcel, C. Guery, J.B. Leriche and J.M. Tarascon, Thin Solid Films 360 (2000) 233.*
130. *N. Naghavi, L. Dupont, C. Marcel, C. Maugy, B. Laik, A. Rougier, C. Guery and J.M. Tarascon, Electrochimica Acta 46 (2001) 2007.*
131. *N. Naghavi, C. Marcel, L. Dupont, /c. Guery, C. Maugy and JM. Tarascon, Thin Solid Films 419 (2002) 160.*
132. *L. Dupont, C. Maauggy, N. Naghavi, C. Guery and JM. Tarascon, J. Solid State Chemistry 158 (2001) 119.*
133. *Y Zhou, PJ Kelly, A Postill, O Abu-Zeid and AA Alnajjar, Thin Solid Films, 447-448 (2004) 33-39.*
134. *Toshihiro Miyata, Tadatsugu Minami, Thin Solid Films, 355-356 (1999) 35-40.*

135. *T. Minami, et al, Thin Solid Films, 373 (2002) 1189-194.*
136. *T. Minami, et al, Thin Solid Films, 398-399 (2001) 53-58.*
137. *T. Minami, et al, Surf. Coat. Technol. 108/109 (1998) 318.*
138. *Alan Postill, MPil. Thesis, the University of Salford, 2004.*
139. *Peter J. Kelly, PhD Thesis, the University of Salford, 1997.*
140. *Peter Kelly, Y.Zhou, Thin Solid Film 426 (2003) 111-116.*
141. *BD Cullity, 'Elements of X-ray Diffraction.' Second edition, Addison-Wesley. London, 1978.*
142. *TH de Keijser, JL Langford, EJ Mittemeijer and ABP Vogels, J. Appl. Cryst., (1982) 15, 308-314.*
143. *D. P. Woodruff, T. A. Delchar, Modern techniques of surface science, Cambridge Universiyt Press, 1986.*
144. *Leslie Davies, Efficiency in Research, Development, and Production, The Royal Society of Chemistry, 1993.*
145. *R. Roy, 'A Primer on the Taguchi Method', Van Nostrand Reinhaold, New York (1990).*
146. *Design of Experiments for Optimisation and Mixtures, Q D Consulting, 68 Station Rd, Steeple Morden Royston, Herts, SG* 0NS.*
147. *Index of the powder diffraction file (inorganic) 1966, Powder diffraction file (inorganic), Joint Committee on Powder diffraction Standard, 1601 Park lane, Swarthmore, Pennsylvania, 19081, USA.*
148. *J.W. Bradley, H. Baecker, P.J Kelly, R.D. Arnell, Surf. Coat. Technol. 135 (2001) 221-228.*
149. *J.W. Bradley, H. Baecker, P.J. Kelly, Surf. Coat. Technol. 142-144 (2001) 337-341.*
150. *J. W Bradley, H. Baecker, Y Arada - Gonzalvo, P J Kelly, R. D. Arnell, Plasma Sources Sci. Technol. 11 (2002) 165-174.*
151. *Martin Misina, J.W. Bradley, etc., Vacuum 68 (2003) 171-181.*
152. *Y Zhou, PJ Kelly, Proc. 7th International Symposium on Sputtering & Plasma Processes, ISSP2003, 11th-13th June 2000, Kanazawa Japan, pp145-148.*
153. *Y Zhou, PJ Kelly, ICMCTF, April 19- 23, 2004, San Diego, United States.*
154. *G. B. Palmer and K. R. Peoppelmeier, Chem. Mater. 9 (1997) 3121.*
155. *Ibrahim EI Fallall, PhD thesis, the university of Salford, 1995.*
156. *B. Lewi and J.C. Anderson, 'Nucleation and Growth of Thin Films,' Academic Press London (1978).*
157. *Leslie Davies, Efficiency in Research, Development, and Porduction, Royal Society of Chemistry, 1993.*
158. *K. Tominaga,,etc., Surf. Coat. Technol. 62 (1993), 683-687.*
159. *C. May, etc., SVC 2000, Denver, USA, Apr. 17-20 2000.*
160. *C. May etc., SCV 2002, Lak Buena Vista, Florida, USA, Apr. 14-17, 2002.*
161. *D. Song, etc., Thin Solid Films, 422 (2002), 180-185.*
162. *A.E. Delhoy, etc., J. Vac. Sci. Technol. A22(4), Jul/Aug 2004, 1-8.*
163. *C. R. Wuethrich, etc., Sensors and Actuators, A66 (1998), 114-117.*
164. *S. Ishibashi, etc., J. Vac. Sci. Technol. A8(3), May/Jun 1990, 1403-1408.*
165. *Ho-Chull Lee, etc.,Vacuum 72(2004), 269-276.*

Appendix I

Investigation into Glass Substrate Cleaning Techniques

Y. Zhou, A Postill and P Kelly

Abstract: Cleaning techniques for glass substrates before PVD processing, both external and internal methods, are investigated systematically in this paper. To estimate the degree of cleanliness using scratch test method, a transparent semi-conductive coating was deposited by sputtering Al_2O_3 doped ZnO powder target. The results of the scratch test are compared considering both the critical failure loads and styles. Finally, the cleaning methods of RF, along with HCl acid solution or 'Windolene', are suggested as the optimum techniques.

1. Introduction

Cleaning, in general, is considered to be the removal of sufficient amounts of contaminant to obtain the desired surface properties (1). The cleaning of glass is important in the process of Physical Vapour Deposition (PVD) in which a glass substrate is used, because the degree of cleanliness influences directly the adhesion between substrate and thin film. The effect of the cleaning methods is normally judged by experience, rather than by systematic analysis. Historically several different cleaning techniques have been used to prepare glass substrates in the Salford Surface Engineering Laboratory. Results have been variable. Consequently, in order to evaluate a range of different cleaning techniques a set of systematic experiments was designed to investigate cleaning techniques. The experiments were designed using the Design Expert 6 software.

Glass is made from a concentrated solution of oxides by melting controlled amounts of mixed raw materials (2). With suitable modifying oxides—TeO_2, V_2O_5, Al_2O_3, MoO_3, WO_3 and TiO_2, glass formers, such as SiO_2, B_2O_3, P_2O_5, GeO_2 and Al_2O_3, form glassy networks. Glass can be classified into soda-lime glass, borosilicate glass, phophosilicate glass, aluminosilicate glass and lead-silicate glass, etc. in terms of the compositions. Also, the composition of the surface of a glass can be different from that of the body, and corroded by the environment. Therefore, the contaminants on the surface of a glass substrate may come from the processes of glass manufacture, during storage, and all the processes before it is coated by a film. Contaminants, which interrupt the film formation process, may cover the whole surface such as oxide reaction layer or an adsorbed hydrocarbon layer, or be restricted to areas such as with soils and fingerprints (3).

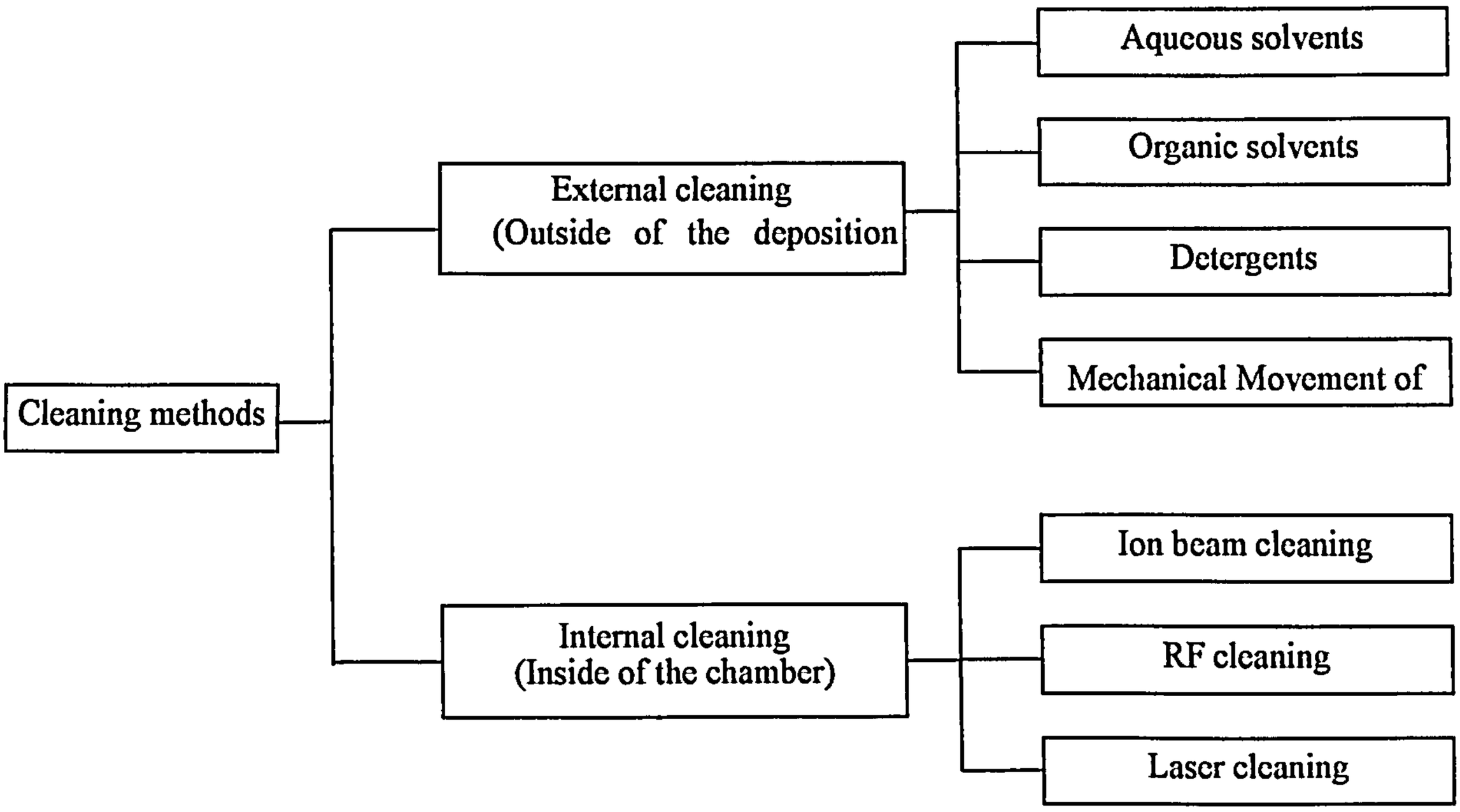

Figure 1 Cleaning methods

The aim of glass cleaning is to reduce the contaminants to an acceptable level and improve the adhesion between coating and glass substrate. Figure 1 shows the different categories of cleaning methods available (4, 5 and 6).

No one product is likely to satisfy all cleaning requirements. The cleaning agent must be matched to the contaminant, the substrate (the component or part to be cleaned), the cleaning requirements, and other performance and environmental constraints. Inorganic contaminants, referred to as hydrophilic, often dissolve effectively in water. On the other hand, hydrophobic organic contaminants tend to dissolve more effectively in organic solvents (1). Each cleaning process must cope with the particular requirement of the contaminant. The following factors should be considered: 1) glass composition, 2) contaminants that are undesirable, and 3) requirements of the surface of the finished part (7). For example, glass funnels can be cleaned by sulphuric acid-hydrogen peroxide mixtures effectively (8), *silica-rich layer* film can be obtained after boroaluminosilicate glass is cleaned by RCA cleaning (A hydrogen peroxide-based cleaning method developed by RCA laboratories) (9).

The "Water break Test" and "Atomizer Test" can be used to evaluate the degree of glass cleaning (10). Also, scratch testing can be used to determine the adhesion between the deposited film and the glass substrate, which indicates the efficiency of cleaning. With a constant or continuously progressive load, scratch testing is performed by drawing a hard stylus over a coated sample. The failure point is determined by examining the scratch track under an optical microscope (11). Special signals such as the applied load, the friction force and the acoustic emission are recorded, these signals are used to indicate when a failure event has occurred. The critical load at failure point is normally used to compare the degree of adhesion of a film.

2. Experiments

The glass slides used in these experiments are soda-lime silicate, which are cut from a sheet of glass that has been vertically drawn in its molten state. To achieve the ground edge effect, the slides are bundled tightly and the edges are 'painted' with an etching

solution, followed by being washed in hot water and rinsed in distilled water before being dried by filtered air to remove minute fragments and residual chemicals. The composition of the glass slide is shown in table 1.

Table 1 the composition of the soda-lime silicate glass slide

Chemical Analysis	SiO_2	Al_2O_3	CaO	MgO	Na_2O	K_2O	B_2O_3	BaO	Fe_2O_3
Microscope Glass as %	69.4	4.3	4.1	3.3	14.4	2.3	1.3	0.8	0.08

Note: the seller provides the data above.

The cleaning methods were chosen from those used in the Salford laboratory, and the systematic experiments were designed as follow.

Table 2 the design for organic solvent cleaning runs

Std.	Run	Block	Factor 1 A: Cleaning type
3	1	Block 1	IPA
6	2	Block 1	ACETONE
7	3	Block 1	METHANOL
12	4	Block 2	CONTROL
9	5	Block 2	METHANOL
11	6	Block 2	CONTROL
2	7	Block 3	IPA
1	8	Block 3	IPA
10	9	Block 3	CONTROL
8	10	Block 4	METHANOL
4	11	Block 4	ACETONE
5	12	Block 4	ACETONE

Note: Control -- no cleaning has been done on the surface of the glass slide.

The best solvent was chosen according to the result from scratch testing to go into the next runs.

Table 3 design for other external cleaning runs

Std.	Run	Block	Factor 1 A: Cleaning type
5	1	Block 1	Solvent +USC
9	2	Block 1	Rouge +water +solvent
12	3	Block 1	Windolene
7	4	Block 2	Rouge +water
16	5	Block 2	HCl
2	6	Block 2	Windolene
11	7	Block 3	Windolene
10	8	Block 3	HCl
1	9	Block 3	Rouge +water
3	10	Block 4	Solvent +USC
17	11	Block 4	Rouge +water
4	12	Block 4	Control
18	13	Block 5	Solvent +USC
15	14	Block 5	Control
6	15	Block 5	Rouge +water +solvent
14	16	Block 6	Control
8	17	Block 6	Rouge +water +solvent
13	18	Block 6	Control

Note: HCl-- The glass slide is cleaned by 1 Concentrated HCl acid +3 de-ion water, then rinsed by de-ion water, finally dried by acetone and air; USC—ultrasonic jetting

The best cleaning method and an alternate one from the external run were chosen for the internal (RF) runs. The internal runs were designed by using centre surface response from design expert DX6.5. The analysis result might tell the best region of combined parameters on the response surface.

Table 4 design for RF cleaning runs

Std.	Run	Type	Factor 1 A: RF power (W)	Factor 2 B: Time (Min)
5	1	Center	150	16.5
4	2	Fact	250	25.0
7	3	Center	150	16.5
6	4	Center	150	16.5
1	5	Fact	50	8.0
3	6	Fact	50	25.0
2	7	Fact	250	8.0
8	8	Axial	10	16.5
12	9	Center	150	16.5
9	10	Axial	290	16.5
13	11	Center	150	16.5
11	12	Axial	150	29.0
10	13	Axial	150	5.0
14	14	Center	150	16.5

The films were deposited on the surfaces of cleaned glass substrates in the chamber using a powder target – Al-doped zinc oxide. Power was supplied by an Advanced Energy Pinnacle Plus Pulsed DC power supply, and plasma in the chamber was confined by an unbalanced magnetic field. The parameters of deposition, such as the current, interval between two current pulse and frequency of the power, as well as the distance between target and substrate, were kept constant. Also, the composition of the powder target was unchanged in order to make sure that all coatings were deposited under the same conditions, so that results of the scratch tests could be compared.

The adhesion of the coatings was evaluated using a Teer ST-3001 scratch test machine. A 200μm diamond stylus was used for both the continuous progressive and constant loads. Critical loads were determined according to the adhesive coating failure. Then the critical loads and the different failure styles of the scratch traces were compared to assess the adhesion of the films.

3. Results and Analysis

3.1 Organic Solvent Cleaning

Table 5 shows the critical loads of failure by scratch testing in the solvent runs. The failure styles can be seen in figure 4, 5 and 6.

Table 5 the critical loads (N) under single constant load condition of the scratch test in solvent runs

Slide position on the substrate	Cleaning methods			
	control	IPA	Methanol	Acetone
Horizontal	13N	12N	13N	12N
Right	13N	12N	13N	15N
Left	12N	13N	12N	13N
Average load (N)	12.7N	12.3N	12.7N	13.3N

The condition of the scratch test: Single constant load; Linear displacement 5mm;

Diamond: 200μm radius

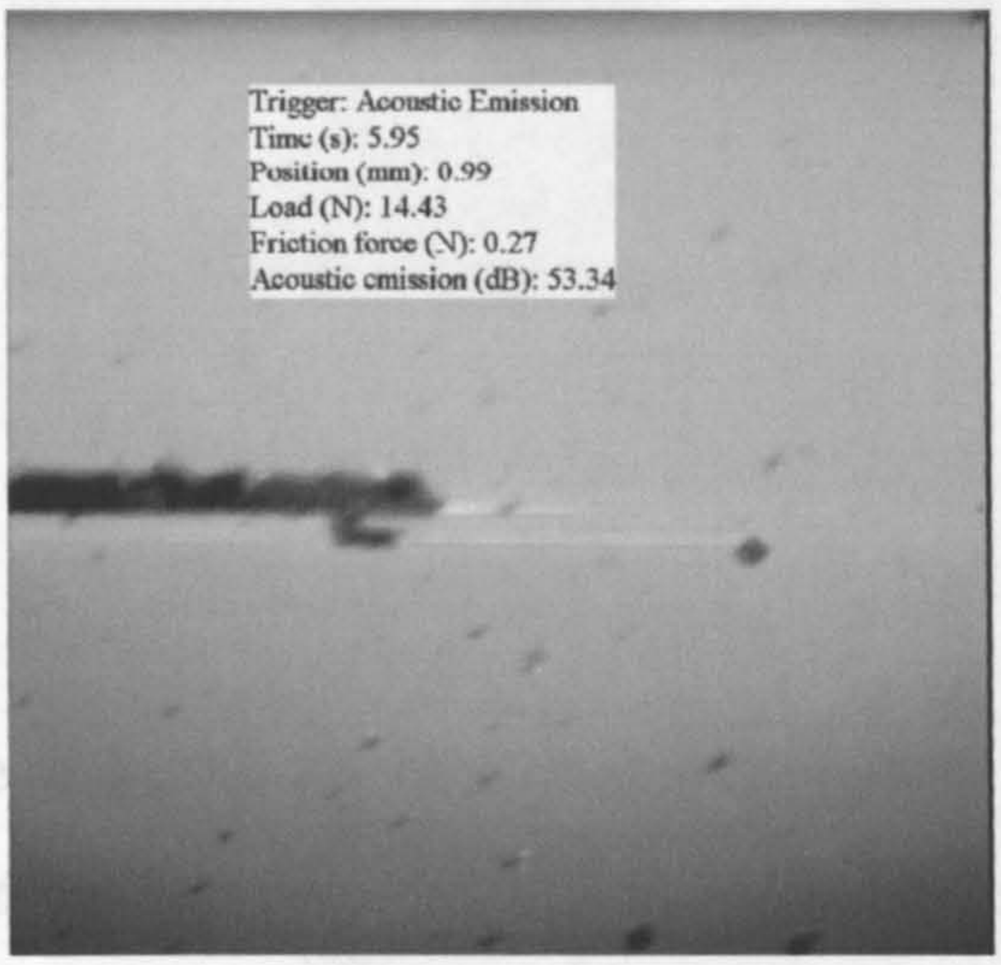

Figure 4 the failure trace of the film on the surface of the control (non-cleaned) sample

(under single continuous progressive load by diamond stylus)

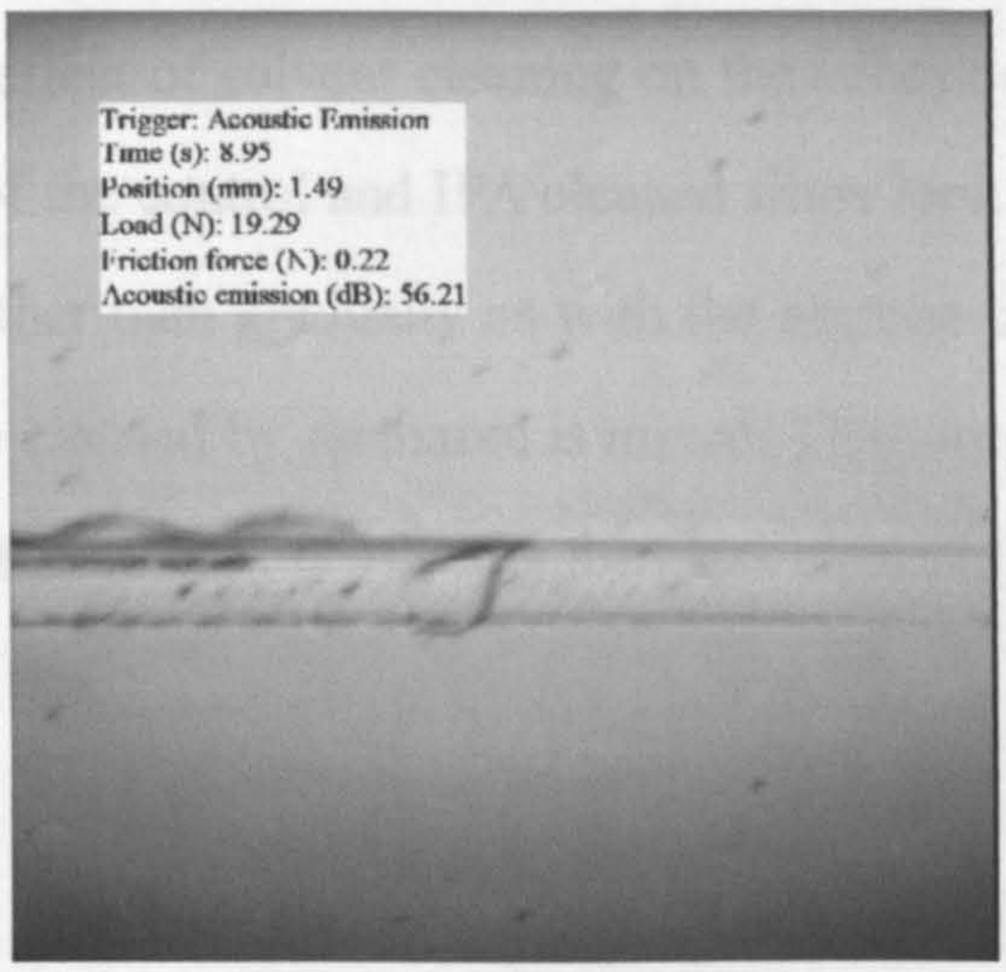

Figure 5 the failure trace of the film on the surface of the sample pre-cleaned by methanol

(under single continuous progressive load by diamond stylus)

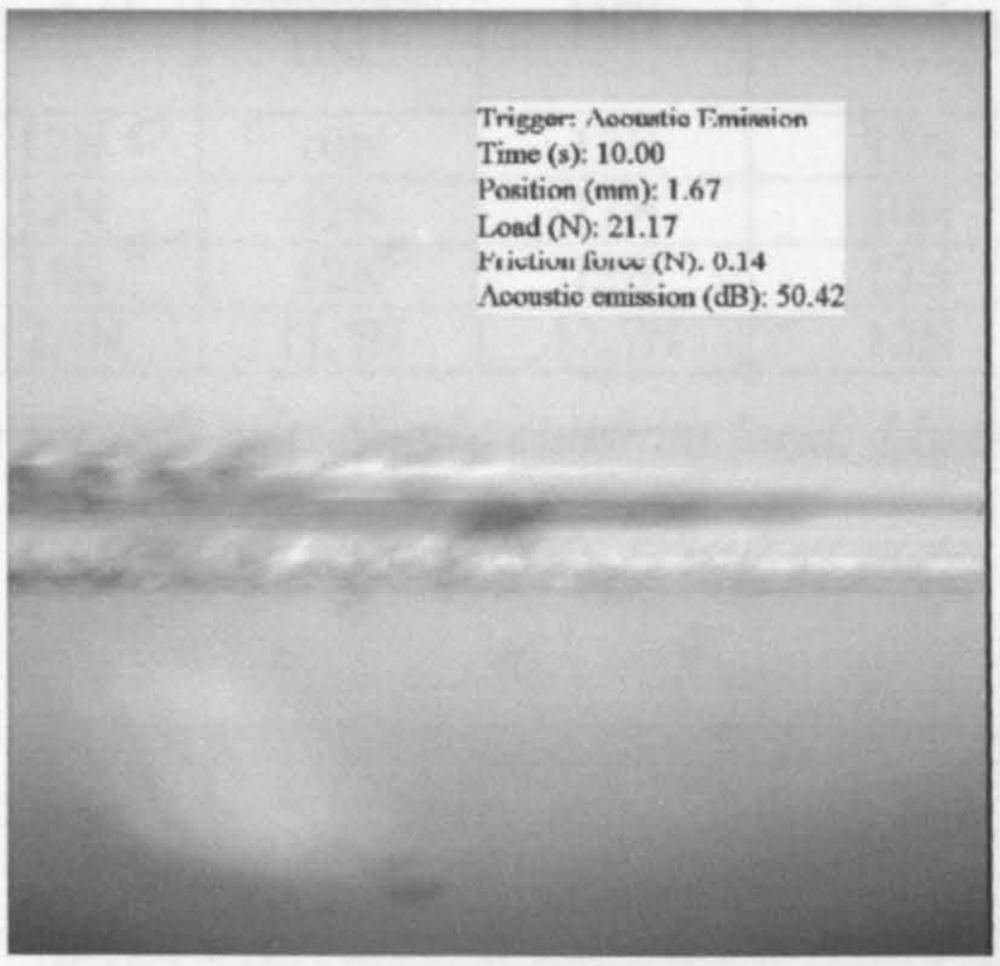

Figure 6 the fail trace of the film on the surface of the sample pre-cleaned by acetone (under single continuous progressive load by diamond stylus)

From table 5, the critical loads of the three solvents and control did not show much difference except that one cleaned by acetone was higher (up to 15N). It may be explained that the glass slides used were in a fairly clean state as confirmed by the manufacturers report. On the other hand, the different failure styles from figure 4-6 still indicate the positive effect of solvent cleaning on the adhesion of the coating to glass. The failure traces of the control and IPA cleaned films look similar in that the coating failed abruptly rather than gradually as with the acetone cleaned slides. The failure style of the sample cleaned by methanol is mixed. Therefore, acetone was felt to be slightly better than the other two solvents for glass cleaning and went forward into the external cleaning run.

3.2 External Cleaning

Table 6 shows the critical loads of failure by scratch test in the external cleaning runs. The failure trace of the coating cleaned by HCl can be seen in figure 7 and 8.

Table 6 the critical loads under single constant condition load of scratch tests in external runs

Slide position on the substrate	Cleaning methods					
	control	Acetone-USC	HCl	windolene	Rouge-water	Rouge-water-Acetone
Horizontal	12N	10N	12N	13N	13N	12N
Right	12N	12N	13N	10N	12N	13N
Left	14N	12N	13N	13N	12N	14N
Average load (N)	12.7N	11.7N	12.7N	12N	12.3N	13N

The condition of the scratch test: Single constant load; Linear displacement 5mm; Diamond: 200μm radiu

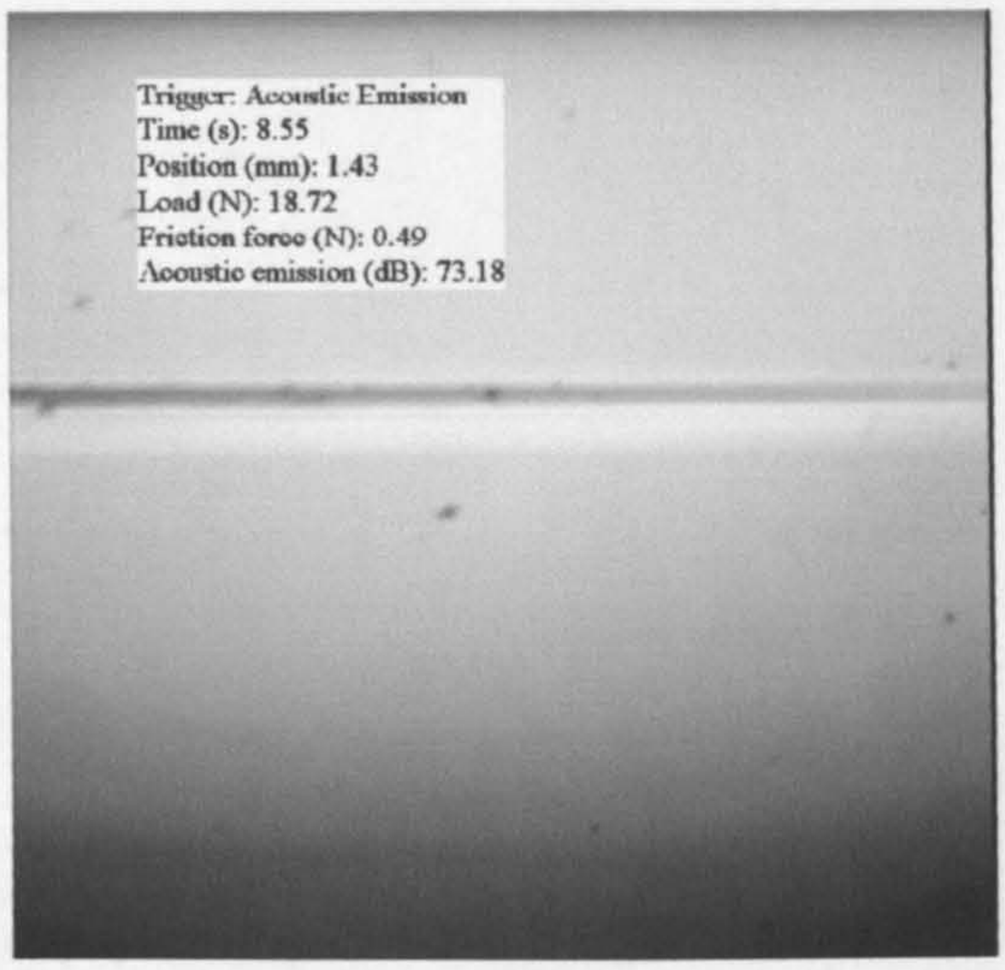

Figure 7 the failure trace of the coating pre-cleaned by HCl (under single continuous progressive load by diamond stylus)

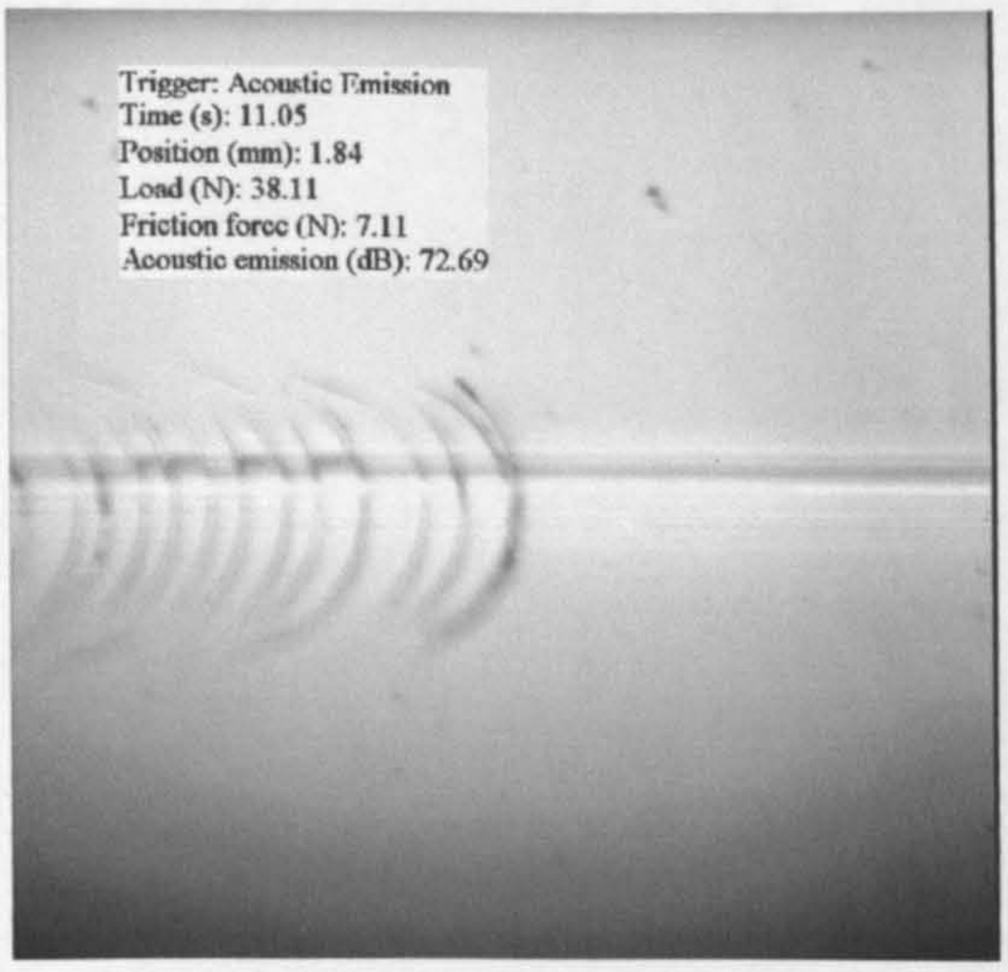

Figure 8 the failure trace of the coating pre-cleaned by HCl (under single continuous progressive load by tungsten carbide stylus)

It can be seen from table 6, that the critical loads do not show much difference. It can also be explained that the glass slides that were used were in a fairly clean state. But the film pre-cleaned by HCl failed much more gradually, as shown in figure 7 and only cracks can be seen in figure 8, than that by other cleaning methods.

Both HCl and Windolene (PH = 5) are acidic and may be more effective in removing the sodium sulphate converted from sodium hydroxide due to sodium ions migrating rapidly to the surface of the glass and reacting with any moisture present. The composition of 'Windolene' is not public knowledge, but its value for cleaning organic contaminants, such as print, is easily proved by experience. The principle of abrasive cleaning is rubbing mechanically on the surface of the substrate using fine abrasives (such as jeweller's rouge), which is useful to remove the extraneous contaminants. Low frequency ultrasonic cleaning depends on the jetting action of collapsing cavitation bubbles in contact with a surface to provide a high pressure jet of fluid against the surface (15). It is more effective to remove large loosely adhering particles than small (such as sub-micron range) absorbed contaminants. But in order to remove water-soluble contaminants and some organic contaminants, the substrates should be cleaned in a good detergent with ultrasonic jetting or scrubbed with an abrasive cleaner (16). Mechanical scrubbing is more effective than ultrasonic agitation for smooth glass surfaces. But the cleaning on the rough or porous surface should be assisted by ultrasonic agitation because jetting increases the rate of *dissolving* or emulsification of contaminants. In general, HCl and Windolene were chosen to go forward into the internal cleaning run programme after due consideration of the principles of all external cleaning methods, the critical loads and failure styles of experiments, as well as the convenience of use of all cleaning methods.

3.3 Internal Cleaning (RF Cleaning)

Internal cleaning, also called plasma cleaning is the process in which ions, along with

electron bombardment, radiation from the plasma and energetic particle bombardment, remove adsorbed surface species (17). The effectiveness of plasma cleaning is well known, but problems, for example, of backscattering of sputtered materials to the surface, especially at high pressure, should be noted. Therefore, a low initial contaminant level should be achieved by external cleaning before the glass substrate goes into the chamber which is under a low pressure discharge and a high system throughput (18). In the cleaning tests, RF power at 13.5MHz frequency was used to create a glow discharge under a 1.0* 10^{-3}mbar pressure in an argon atmosphere.

The RF cleaning results are showed in table 7.

Table 7 Critical load (N) under single constant condition of scratch test in RF cleaning runs

Std.	Run	Type	Factor 1 A: RF power (W)	Factor 2 B: Time (Min)	Response 1 Control (N)	Response 2 HCl (N)	Response 3 Windolene (N)
5	1	Center	150	16.5	14.5	16.17	16.68
4	2	Fact	250	25.0	14.73	14.78	13.87
7	3	Center	150	16.5	13.84	14.93	13.93
6	4	Center	150	16.5	13.82	15.26	13.91
1	5	Fact	50	8.0	13.54	17.91	18.67
3	6	Fact	50	25.0	13.45	15.66	16.86
2	7	Fact	250	8.0	13.90	14.66	15.00
8	8	Axial	10	16.5	12.01	12.89	12.91
12	9	Center	150	16.5	14.78	17.44	16.88
9	10	Axial	290	16.5	12.90	12.10	12.96
13	11	Center	150	16.5	13.46	14.80	15.27
11	12	Axial	150	29.0	13.79	16.77	16.80
10	13	Axial	150	5.0	13.37	17.34	17.30
14	14	Center	150	16.5	13.81	17.74	.16.72
Average					13.71	15.60	15.55

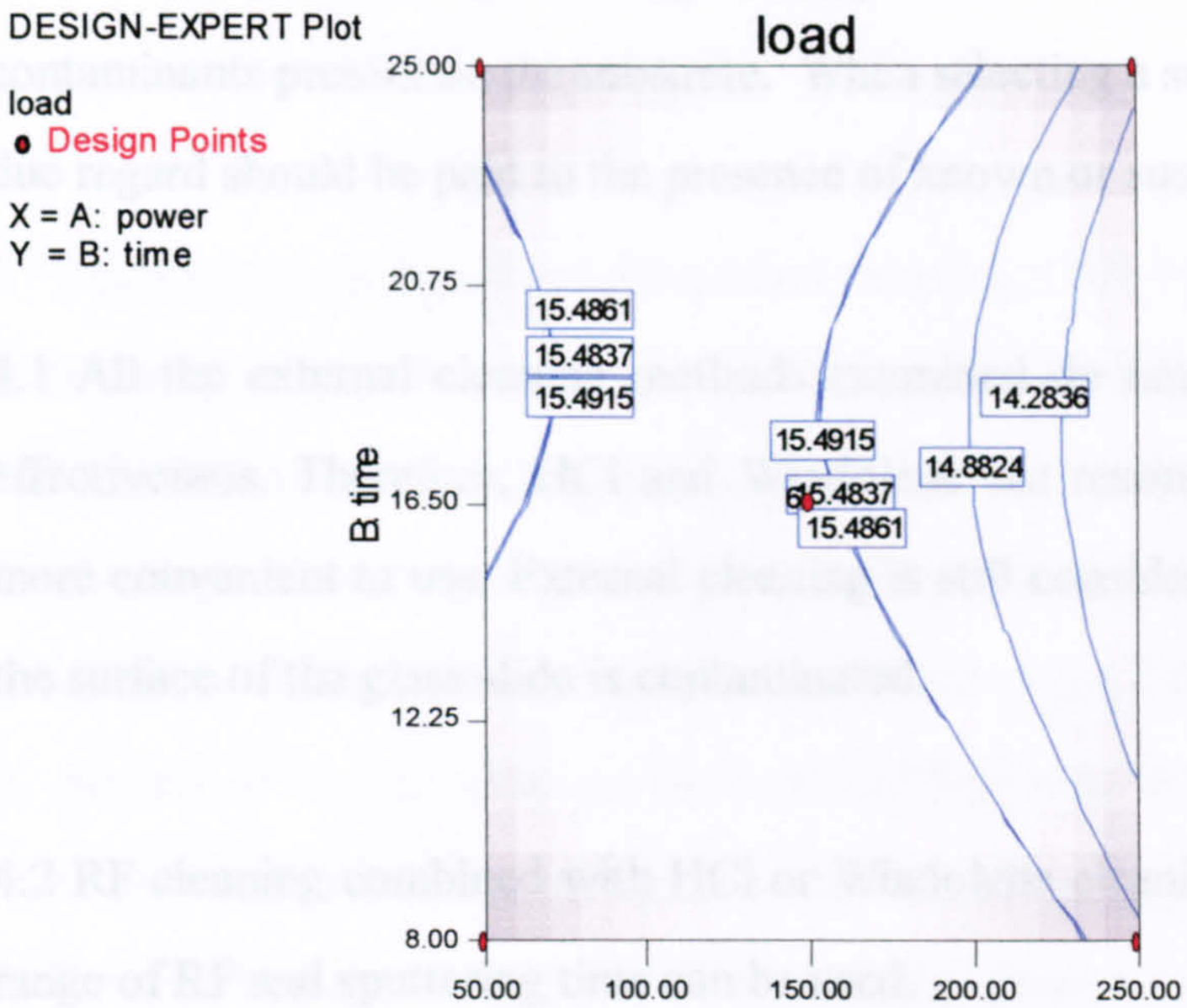

Figure 9: the analysis of the internal RF cleaning

The analysis by Design Expert 6.0 shows (figure 9)that the degree of cleaning or adhesion of the coating is not quite related to the RF power and sputtering time, i.e. a wider range of sputtering cleaning power and time can be chosen without significant effect on the cleaning results. Compared with the average critical loads of organic solvent cleaning and the external cleaning, that of RF were increased by about 3-4N except in control one, which indicates that RF cleaning is an effective cleaning technique. It is worth noting that the RF cleaning combined with HCl or Windolene cleaning is more effective than RF cleaning alone, whilst the critical loads shows no difference among HCl, Windolene and control cleaning in external runs. It is not clear why this happens, but one possible reason maybe that the HCl and Windolene cleaning helps some contaminants to become volatile and flush away from the chamber instead of back-scattering on the surface of the substrate.

4. Conclusion

The effectiveness of any cleaning technique will be influenced by the nature of the contaminants present on the substrate. When selecting a substrate cleaning technique due regard should be paid to the presence of known or suspected contaminants.

4.1 All the external cleaning methods examined do not show much difference in effectiveness. Therefore, HCl and Windolene are recommended because they are more convenient to use. External cleaning is still considered to be necessary in case the surface of the glass slide is contaminated.

4.2 RF cleaning combined with HCl or Windolene cleaning is effective, and a wide range of RF and sputtering time can be used.

5. Acknowledgements

Thanks for the help of all the members in the lab, especially Phil Henderson and Geoff France for scratch testing and SEM analysis.

6. References

1. 'Introduction' in handbook for critical cleaning, CRC PRESS, 2001.

2. Welter H. Kohl, Chapter 1 'glasses' in Handbook of Materials and Techniques for Vacuum Devices, Reinhold Publishing 1967, P5

3. Society of Vacuum Coaters, External cleaning of Surface preparation in Educational Guide to Vacuum Deposition Technology, 1998.

4. Society of Vacuum Coaters, External and Internal cleaning of Surface preparation in Educational Guide to Vacuum Deposition Technology, 1998.

5. Krishna Seshan, Chapter 7 'Contamination Control' in Handbook of Thin-Film Deposition Processes and Technologies—Principles, Methods, Equipment and Applications, William Andrew Publishing, P304.

6. ASTM C912-93, Standard Practice for designing a Process for Cleaning Technical Glasses, re-approved 1997.

7. ASTM C912-93, Standard Practice for designing a Process for Cleaning Technical Glasses, re-approved1997, P5.

8. Cleaning glass funnels in Chemical & Engineering News, June 25, 1990, P2.

9. E.C. Onyiriuka, etc., Effect of RCA cleaning on the surface chemistry of glass and poly-silicon films as studied by ToF-SIMS and XPS, Surface and Interface Analysis, 1998, Vol. 26, Iss 4, P277.

10. Welter H. Kohl, Chapter 1 'glasses' in Handbook of Materials and Techniques for Vacuum Devices, Reinhold Publishing 1967, P45.

11. ST-3001 Operation Manual, P5.

12. J.F. Chang and M.H. Hon, Thin Solid Films 386 (2001) 79-86.

13. P. Nunes, D. Costa, E. Fortunato and R. Martins, Vacuum 64 (2002) 293-297.

14. Tadatsugu Minami, Shingo Suzuki and Toshihiro Miyata, Thin Solid Films 398-399 (2001) 53-58.

15. Donald M. Mattox, 'Cleaning' Chapter 12 in Handbook of Physical Deposition (PVD) Processing, William Andrew publishing / Noyes Publications 1998, P667.

16. Donald M. Mattox, 'Adhesion and Surface Preparation' Chapter 3 in Deposition Technologies for Film and Coatings, edited by R. F. Bunshah, Noyes Publications 1994, P75.

17. 'In situ cleaning of Surface preparation' in Education Guide to Vacuum Deposition Technology.

18. Donald M. Mattox, 'Adhesion and Surface Preparation' Chapter 3 in Deposition Technologies for Film and Coatings, edited by R. F. Bunshah, Noyes Publications 1994, P77.

Appendix II Concepts in Semiconductor Physics and Optical Physics

1. Concept of Semiconductor

Solid materials are classified into three groups according to their conductivity: *conductors, insulators and semiconductors.*

Conductors, to which class most metals belong, have very large conductivities (e.g. copper has a conductivity of $10^7\ \Omega^{-1}m^{-1}$). In conductors, atoms have only a few (one or two in most situations) valence electrons, which are not closely confined to their parent nuclei. The valence electrons form electron clouds and atoms connect with each other by metallic bonds.

The second category is *insulators*, which have very large resistivities and are not conductive. Most non-metallic components, such as NaCl, are part of this group. Insulators normally consist of combinations of metallic atoms with no more than three valence electrons in the outer-shells and non-metallic atoms, which can accept less than three electrons to completely fill their outer-shells. Therefore strong combination forces, known as ionic bonds, are formed between two types of neighbouring atoms. Another kind of combination bond found in insulators is covalent bonds, in which the bonds are formed between non-metallic neighbouring atoms by means of sharing valence electrons around them, but valence electrons are confined firmly to their parent atoms.

The third category, which is of relevance to this project, is *semiconductors*, which have relative low conductivities, such as silicon ($10^{-2}\ \Omega^{-1}m^{-1}$)[2]. The forces between neighbouring atoms of semiconductors are also in the form of covalent bonds. The valence electrons in semiconductors are not as free as those in metals and not as closely bonded as those in insulators. Semiconductors behave like insulators at 0K.

The conductivities of semiconductors can increase with increasing temperatures.

2. *Concept of band gap*

The conduction theory, which assumes that the free electrons behave as classical particles and are available all over the body of a material, can be used very well to explain the conductivity of a metal, but fails to explain the behaviour of materials with covalent bonds, such as semiconductors. Therefore, the so-called *energy band theory* was proposed, which successfully accounts for the differing electrical properties of conductors, semiconductors and insulators. It is suggested in the band theory that the energy of electrons is located only in allowed bands. The electrons within a particular allowed band can behave as free electrons and interact with externally applied fields to show the conductive property of a material.

According to band theory, the electrons in an isolated atom only occupy discrete bands at different energy levels. Also, each energy level can only hold two electrons moving with opposite spins. The atoms in a solid are packed so closely that the energy levels are modified due to the overlapping of the electron orbitals between neighbouring atoms. Figure A1[1] shows a system of three atoms interacting, in which δ represents a width of one-dimensional rectangular potential well, and r the separating distance between two atoms. It can be seen that the electrons occupying the same energy band in their individual atoms are separated in different energy bands. The larger the separating distance between the neighbouring atoms is, the closer the energy bands are. The bands unify to be one if the distance between two atoms is large enough that their interaction disappears, as in the case of isolated atoms. In the example, the band separations are clear, because it shows only the interaction of three atoms. In realistic systems, the number of interacting atoms in a solid is much higher (typically about $10^{22}cm^{-3}$). Therefore, it can be said that the electrons are quasi-continuous within one band. Figure A2 [1] shows carbon energy bands with varying inter-atomic spacing. When the distance between atoms, known as the lattice

constant, is large enough, the electrons stay in their bands as isolated atoms. The electrons begin to interact with each other and separate into variable energy levels when the lattice constant decreases. It can be seen from figure A2 that energy band splitting occurs and electrons possess energies in the *allowed energy bands* in the cases of (ii) and (iv), where the electrons occupy under the quasi-continuous or closely discrete situations. The space between two allowed energy bands is called *forbidden energy band*, in which no electron is allowed or able to stay.

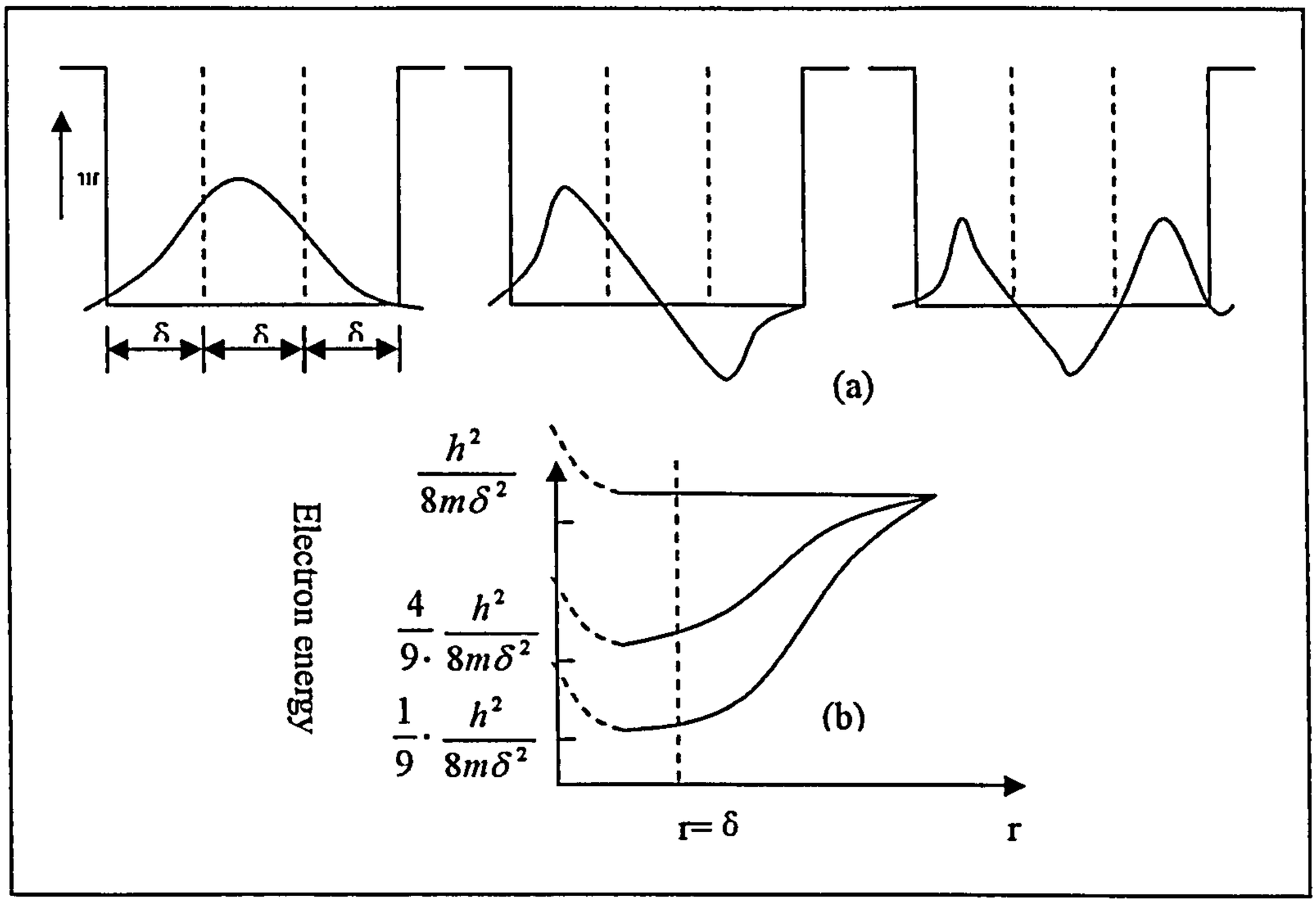

Figure A1 Three-atom system: (a) possible wave-functions for the lowest energy states; (b) electron energy as a function of atomic separation

(u: electron potential)

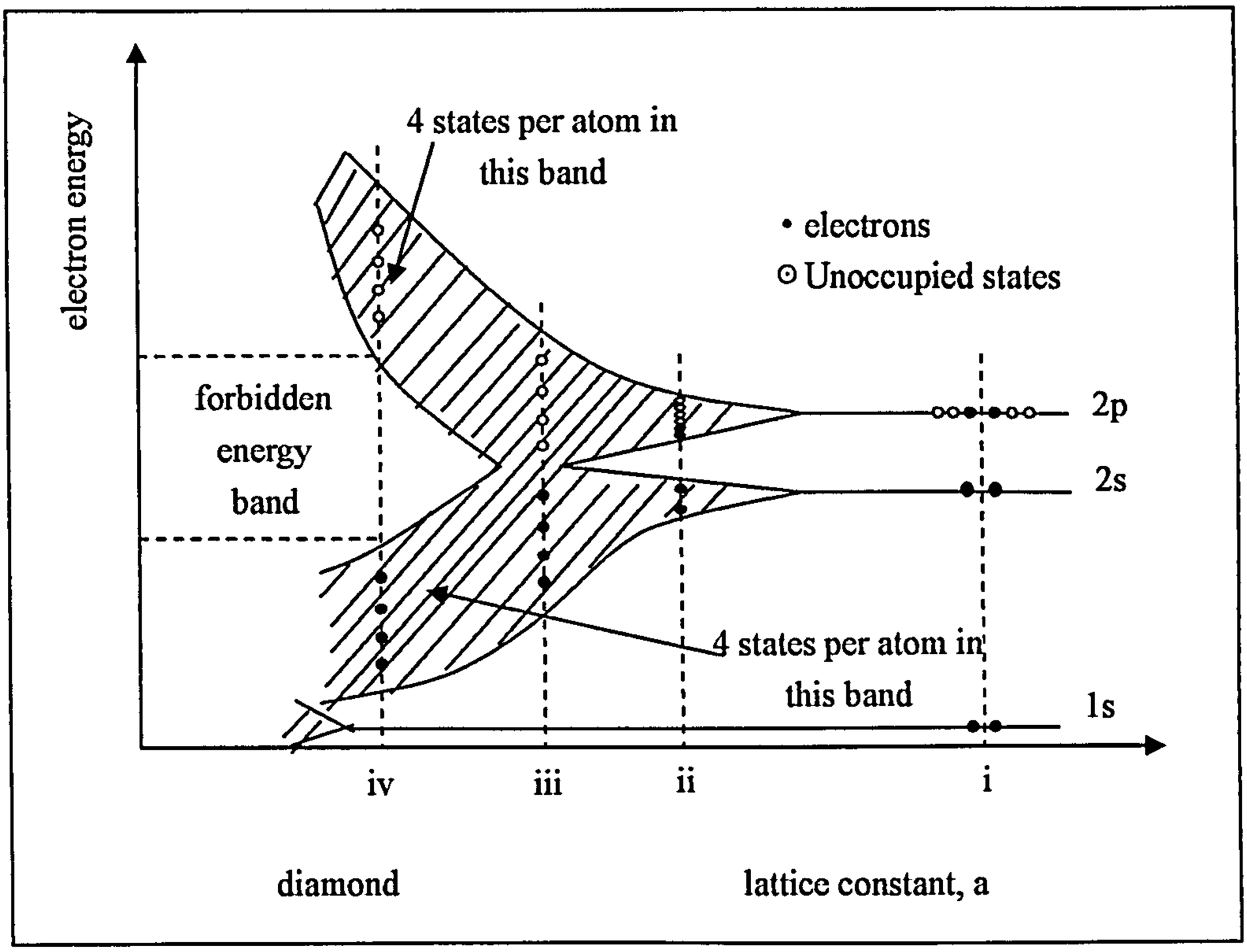

Figure A2 Energy bands for carbon with varying inter-atomic spacing.

In general, the allowed electron energies in a solid are in bands, in which the electron energies are quasi-continuous, actually absolutely discrete. Bands are separated by forbidden energy regions, in which no electron is allowed to be accommodated.

Again, taking the figure A2 as an example. It can be seen in the case (iv) that the electrons in the outer shell occupy the allowed band with a low energy level, which is called the *valence band*. The high empty allowed energy band is called the *conduction band* in which, in this case, also has a capacity of 4N electrons. Electrons in conduction band are relatively free and able to respond to the external electric field to contribute to a current drift. The forbidden region between two bands is referred as the *forbidden band gap* (or often so-called as *'band gap'*). The magnitude of the gap is measured by energy, known as *band gap energy* (E_g), with units of electron-volts (eV). Band gap energy is an important physical concept in semiconductor field because it refers the essential energy for a semiconductor transferring the electrons from the

valence band to conduction band to take part in the conduction.

There is a big different in band structure between metals and non-metals (semiconductors and insulators). It is found that in a metal the highest allowed energy band is only partially filled. The electrons occupying this band are free and can be shared by the atoms in the metal body. When an external electric field is applied, the electrons in the partially filled state can gain small amounts of energy and move to a nearby unoccupied state in the direction of the electric field. While on the other hand, the highest occupied state (at absolute zero) in a non-metallic material is separated from the lowest vacant state, which is empty, by the band gap. Without extra energy, it is impossible for the electrons to be elevated up into the vacant conduction state from the occupied valance state. Therefore the non-metallic material behaves as an insulator.

When considering why a semiconductor has different electric properties from an insulator, it is very important to remember that electrons can gain energy from a temperature above absolute zero and therefore are not necessarily occupying the lowest possible energy levels. We can imagine that some electrons in the valance band may jump into the conduction band if the band gap is sufficiently small and the temperature is above the absolute zero (e.g. 100K). Thus, the so-called semiconductor material is able to conduct current to some degree, but not as efficiently as a metal.

3 Fermi energy level and the band gaps in metal, insulator and semiconductor

Another key physical concept, which can help us to understand the difference between an insulator and a semiconductor, is *Fermi energy level*. *Fermi energy level* is defined as 'the energy for which the probability of electron occupation is equal to one-half in a metal'. This definition is not suitable to a non-metal at absolute zero because the probability of occupation is 1.0 at the valence band and 0.0 at the

conduction band, which means that there is no 0.5 probability of occupation. Considering this, it is assumed that:

Fermi energy level is the position at the centre of the band gap and can be expressed as follow, see figure A3[1]:

$$E - E_F = E_g/2 \qquad \text{...eq (A1)}$$

In which E_F denotes Fermi energy and E the energy of the lowest energy state in the conduction band.

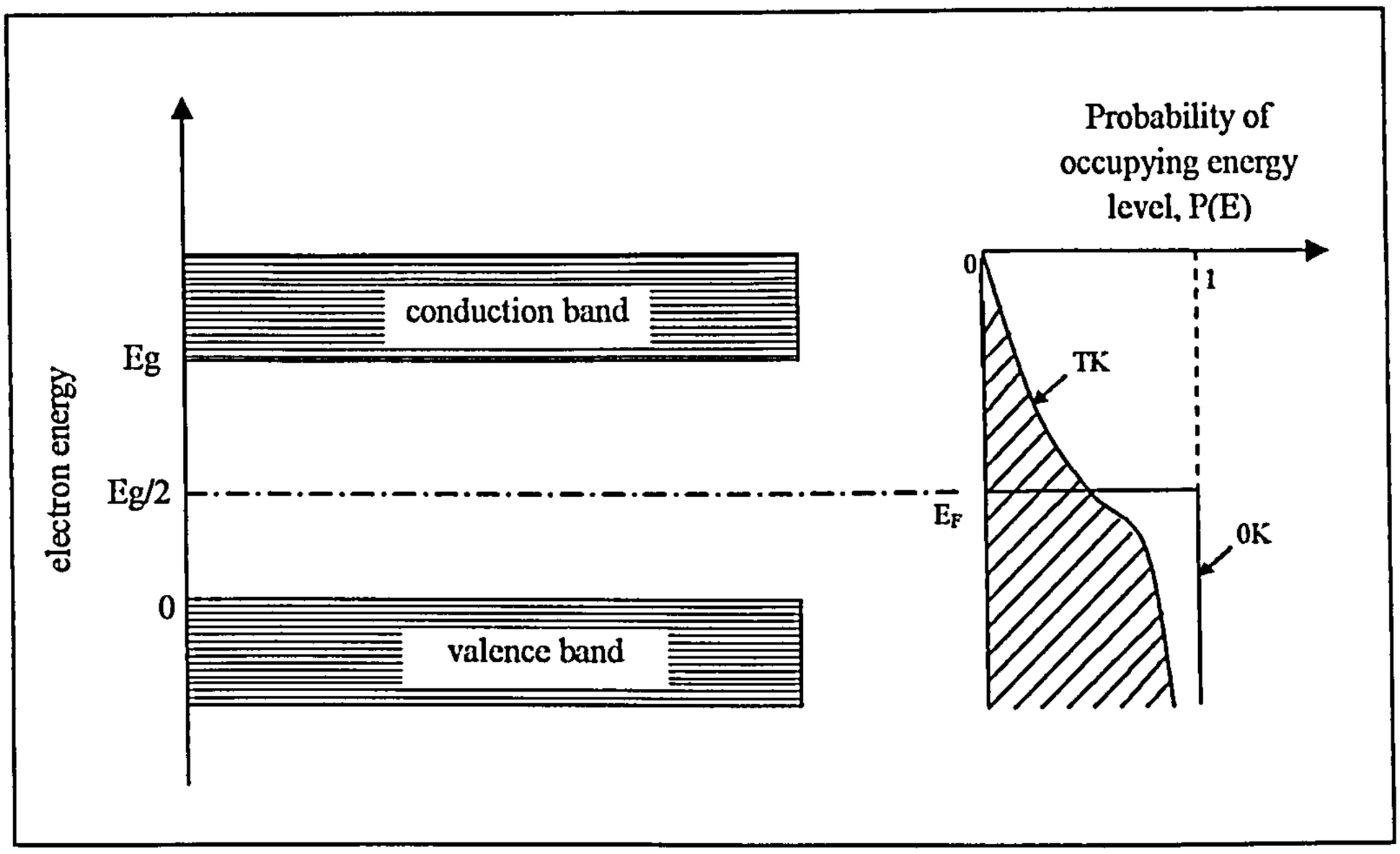

Figure A3 Position of the Fermi level in an intrinsic semiconductor

In Fermi-Dirac distribution theory, it is considered that no two electrons in an atom can have identical quatum numbers, which is called *Pauli exclusion principle*. This is an example of a general principle which applies not only to electrons but also to other particles of half-integer spin – *Fermions*. Fermions incude electrons, protons and neutrons. The wavefunction which describes a collection of fermions must be

antisymmetric with respect to the exchange of identical particles. The fact that electrons are fermions is foundational to the build up of the periodic table of the elements since there can be only one electron for each state in an atom (only one electron for each possible set of quantum numbers).

The Fermi-Dirac distribution can be expressed as:

$$f(E) = [\, e^{Eg/2kT} + 1]^{-1} \qquad \text{...eq (A2)}$$

in which k is Boltzann constant, which equal to $1.38 * 10^{-23} m^2 kg\, s^{-2} K^{-1}$.

Now let us consider the difference of the conductivity among metals, semiconductors and insulators, see figureA4. The electrons in a metal could occupy the top band or the highest two overlapping band partially (figures A4a and b), which allows them to gain energy from an external field easily. In an insulator (figure A4c), the band gap is about 4eV, which is too large for electrons to gain enough energy to overcome it. The band gap of a semiconductor (figure A4d) is as small as 1eV[3], that is why some of the electrons cold be excited into conduction band to contribute the current flow.

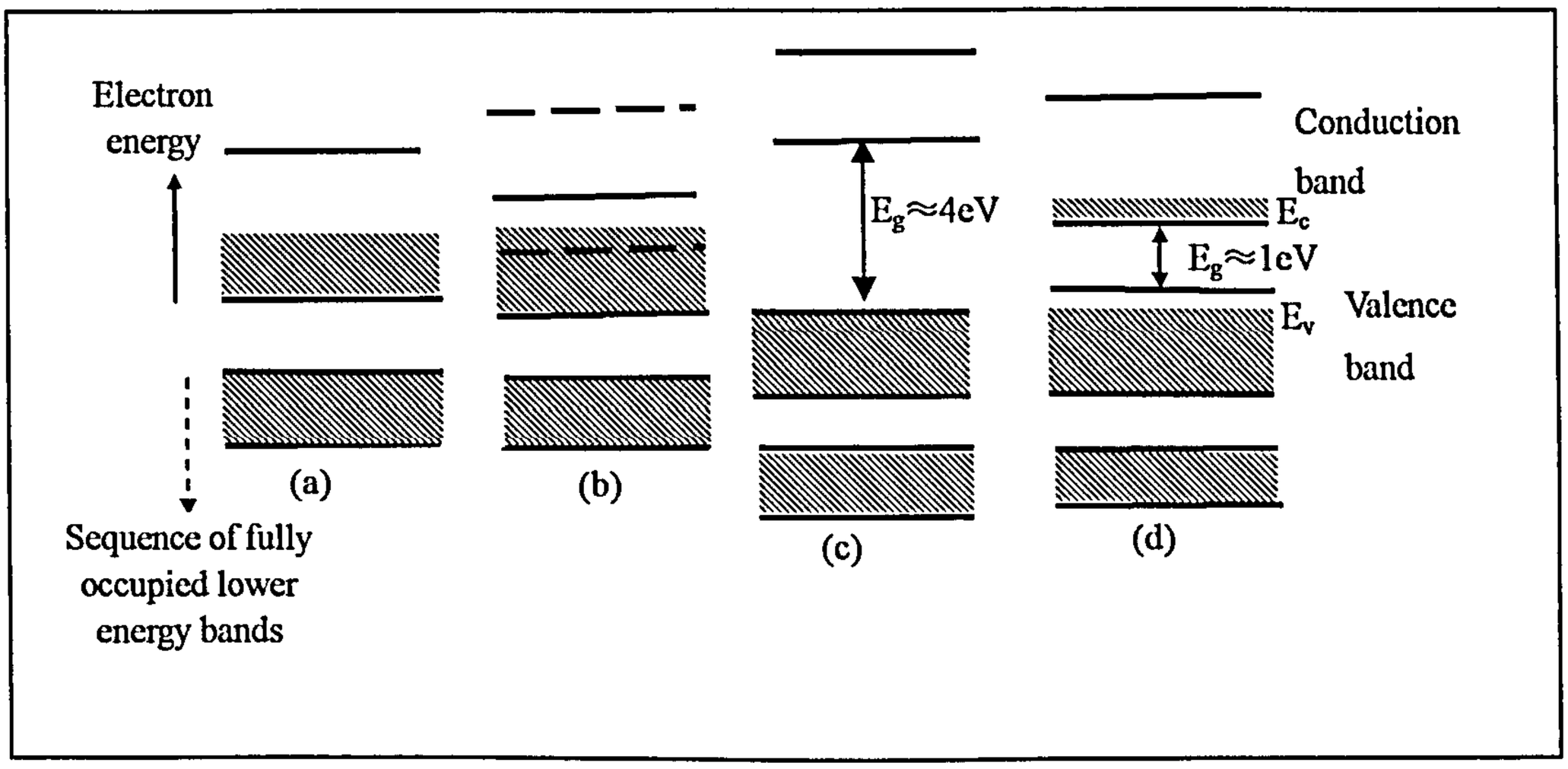

Figure A4 Schematic representation of the energy bands in various materials: (a) with partially filled valence band; (b) a metal with lapping partially filled bands; (c) an insulator; and (d) a semiconductor.

4 Band gaps in semiconductors

In solid state physics, there is an expression for the relationship between electron energy E and wavenumber *k* [3]:

$$E = U(x)e^{jkx} \qquad \text{...eq (A4)}$$

in which x represents the electron position in one dimension, j is integer number. The expression is called E-*k* relationship or energy and momentum relationship because the momentum $p = \hbar k$ ($\hbar$ is Dirac's constant). There are two situations between the conduction bands and valence bands according to the energy-momentum or E-*k* relationship. One is the maximum of the valence band, which occurs at the same k value as the minimum of the conduction band. The band gap in this case is called *direct band gap*. The other situation is that the maximum valence band and minimum conduction band are not in the same step or k. Then the band gap is known as *indirect band gap*. Figure A5 [3] is a schematic representation of the typical direct and indirect band gap semiconductors.

For a direct semiconductor, the electrons accommodated in the highest valence band can be elevated to the lowest conduction band with the minimum of energy (band gap energy) and there is no momentum change needed. Also, the electrons can transfer in the opposite direction by emission of photons without momentum change. In contrast, the electron transition not only needs the external energy as much as the band gap energy in an indirect semiconductor, but also requires a simultaneous momentum change, which comes from the lattice phonon vibrations. The classification of band gap of a semiconductor is important in its particular uses. For example, the direct semiconductors are favourable in solid-state lasers, while indirect one is not.

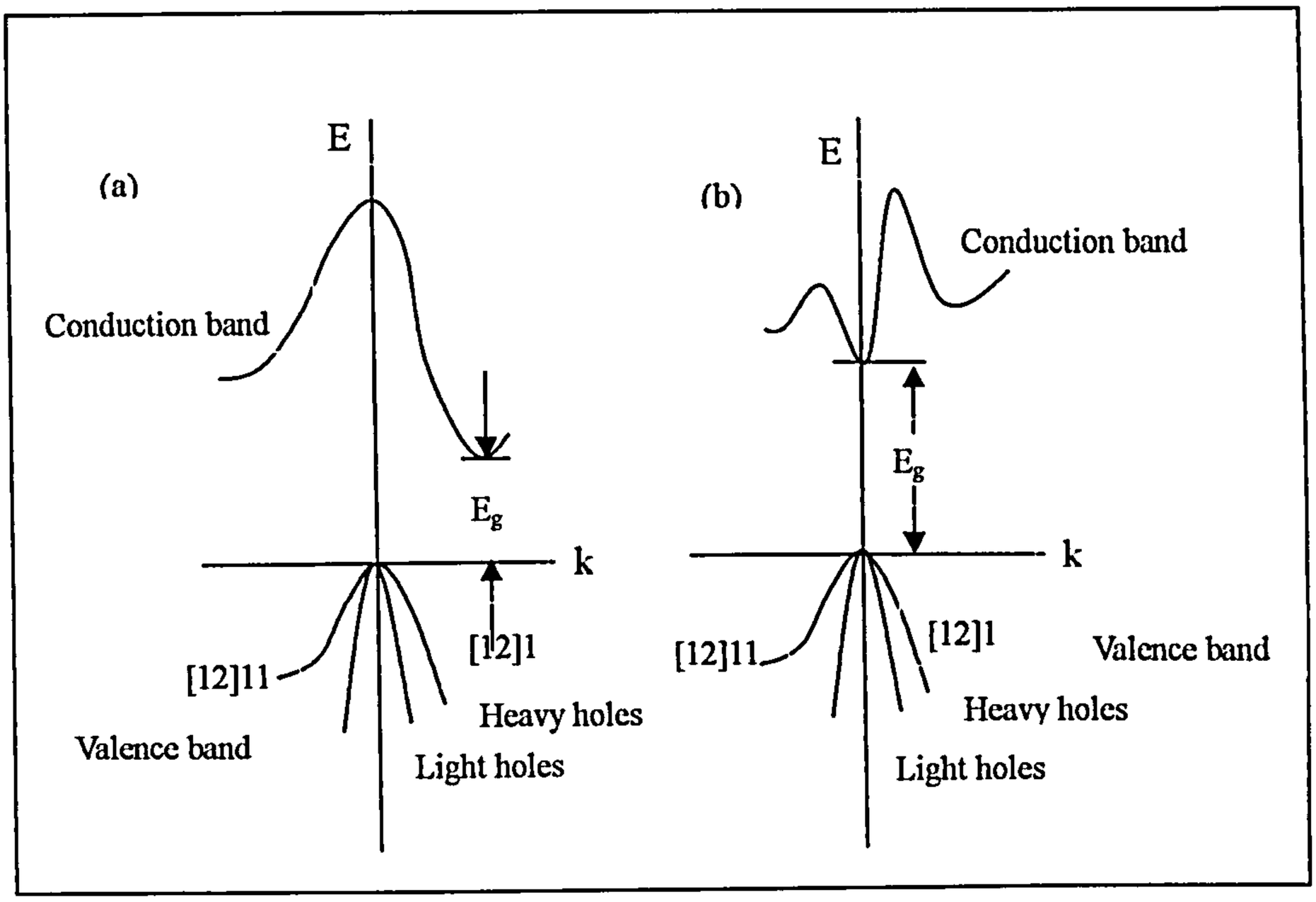

Figure A6 Relationship of E-*k* for real solids: (a) silicon (which has an indirect band gap) and (b) gallium arsenide (which has a direct band-gap).

5 Refractive Index

The behaviour of light entering a crystal is fundamentally controlled by the crystal structure. The refractive index (n) of a substance is defined as:

$$n = V_v / V \qquad \text{eq. (A5)}$$

Where V_v is the velocity of light in a vacuum, and V is the velocity of light in the substance. For our purposes we will assume that the refractive index of light in air is essentially the same as a vacuum, = 1. Light slows down when it enters a substance, so the refractive index will always be greater than 1. Most minerals have refractive indices between 1.32 and 2.40.

6 Absorption

The *Absorption* is the "missing piece", when comparing the total reflected and transmitted energy with the incident energy. The ratio of the total absorbed radiant or luminous flux to the incident flux is called *absorptance*. Standard unit of absorptance is percent (%) or a factor between 0 and1.

The fraction of light absorbed per unit distance in a participating medium is called *absorption coefficient*. Standard unit of the absorption coefficient is fraction per meter (1 / m).

References

1. *J. Allison, 'Electronic Engineering semiconductors and Devices', McGraw-hill book company, second edition, 1989.*
2. *Richard Turton, 'The Physics of Solids', Oxford University Press, 2000.*
3. *J. Wilso, J.F.B. Hawkes, 'Optoelectronics: An Introduction', Prentice Hall International (UK) Ltd., second edition, 1989.*